Electrical and seismic anisotropy of the lithosphere with the focus on central southern Africa

by

Mark Peter Hamilton

A thesis submitted to the
Faculty of Science, University of the Witwatersrand
in fulfilment of the requirements for the degree of

Doctor of Philosophy

School of Geosciences,
University of the Witwatersrand
and
School of Cosmic Physics,
Dublin Institute for Advanced Studies

Johannesburg, 2008

I hereby declare that this thesis is entirely my own work, except where acknowledgement is made in the text. It is being submitted for the Degree of Doctor of Philosophy in the University of the Witwatersrand, Johannesburg, South Africa. It has not been submitted for a degree at this or any other University.

I agree that the Library may lend or copy this thesis upon request.

Signed,

Mark Peter Hamilton

May 12, 2008.

Electrical and seismic anisotropy of the lithosphere with the focus on central southern Africa

by

Mark Peter Hamilton

Abstract

The aim of this study was to gain a better geological understanding of the southern African region through the use of magnetotelluric (MT) and seismic techniques. Specifically, the newly collected southern African magnetotelluric experiment (SAMTEX) data are analysed for directionality using a tensor decomposition technique. Instead of conducting the analysis for given periods, as is commonly done, the data are analysed for approximate depths due to the variable electromagnetic penetration across the region. I also re-analyse previously collected southern African seismic experiment (SASE) data for shear wave splitting of teleseismic events using standard processing techniques. These analyses provide information on the electrical and seismic anisotropy properties of the region, which may then be related to tectonics and geological structure. It is found that MT conductive direction results, for both crustal and lithospheric mantle depths, are significantly more complex than has previously been observed in other regions. The complexity is attributed to be due to strong effects of large-scale conductivity heterogeneities on the conductive directions measured. The reanalysis of some of the SASE stations for shear wave splitting has produced near-identical results to those previously measured, and I was not able to conclusively demonstrate the presence or absence of 2-layer anisotropy. A previously unnoticed relationship is observed between thick lithosphere, and regions of well correlated seismic fast axis directions and plate motion directions. Combined with the observations of vertical variations in conductive directions of the MT results, this has led to a new model being proposed to explain the anisotropy results observed in the region. The model suggests both lithospheric and asthenospheric contributions to seismic anisotropy, with a significantly stronger anisotropic layer below thicker lithosphere, which is proposed to be due to stronger lattice preferred orientation (LPO) of olivine as a result of increased flow velocity below the thicker lithospheric keel. This model is supported by other geoscientific observations, including the results from the lithospheric and asthenospheric MT analysis. No strong correlation between the measured MT and seismic anisotropy parameters is observed, likely because the electrical anisotropy is strongly effected by structure, and the seismic anisotropy is predominantly a result of LPO of olivine (in places, quite strongly vertically varying).

For Mum and Dad

Acknowledgements

As a result of this project I have encountered many kind and helpfull colleagues, many of whom I now regard as friends rather than colleagues, and without whom, my studies would have been far more difficult and far less enjoyable. It would be impossible to name them all here. However, I would like to take this opportunity to thank some who have been of particular help during the last few years.

I would like to thank my supervisors Alan Jones and Susan Webb for their guidance, inspiration, and continual encouragement throughout my studies. They have given me the opportunity to work with scientists around the world and present my work on many occasions. Their doors were always open, and they were constructive and thorough in their advice.

I would sincerely like to thank the many co-workers and helpers we have had during the SAMTEX field work. The level of support and enthusiasm shown has made this project a pleasure and privilege to work on. I have been afforded the opportunity to work at different institutions, and with various scientists, all of whom have been exceedingly helpful and friendly. I would particularly like to thank Rob Evans and Mark Behn at Woods Hole Oceanographic Institute, Dave Eaton who always seemed to drop by at the ideal times, and the geophysics group at the University of Barcelona.

I am sure that everyone at the Dublin Institute for Advanced Studies (DIAS) has helped me in some way or another during my time there. I would particularly like to thank the DIAS MT group for many useful and enlightening discussions, the DIAS technicians for the endless help in the field and in the workplace, the DIAS students for many entertaining times, and everyone in the Blue room (Max Moorkamp, Mark Muller, Marion Miensopust, Van Chuong Do, and CK Rao), which has evolved over the years, but has always been a friendly and lively environment in which to work.

Similarly, I am certain that everyone in the Geophysics department at Wits has helped me in some way during my studies, for which I am very grateful. Particularly, I would like to thank Shawn Letts, Stephen Coomber, and Stephanie Scheiber, who made the Wits field schools endless fun rather than any sort of chore.

I have often pondered how it is, that my housemates have continued to put up with me, never mind support and encourage me, particularly towards the end of my studies when I was sometimes far from being the most pleasent or easy person to live with. Veronica and Christian you are fantastic. I will always be grateful!

I would like to thank all my friends for their continued support, and their persuasion to go for a pint and relax every now and again. To Mom, Dad, Neil, and family, thank you for your continual faith, love, and support, without which this would not have been possible.

Publications

Preliminary results from the work conducted in this thesis were published in Hamilton *et al.* (2006) (Appendix 5). This work has been substantially expanded and will be submitted for future publication. As per the agreement in the SAMTEX consortium, there is a member from each organisation represented on any SAMTEX publications. During the course of my study, the work conducted has been presented to the scientific community as follows:

Peer Reviewed:

- Hamilton, M.P., Jones, A.G., Evans, R.L., Evans, S.F., Fourie, C.J.S., Garcia, X., Mountford, A., Spratt, J.E., and the SAMTEX Team, 2006. Electrical anisotropy of South African lithosphere compared with seismic anisotropy from shear-wave splitting analyses. Physics of the Earth and Planetary Interiors, 158, 226-239.

Conference Talks:

- Hamilton, M.P., A.G. Jones, R.L. Evans, X. Garcia, M.R. Muller, M.P. Miensopust, J.E. Spratt, S.F. Evans, A. Mountford, W. Pettit, P. Cole, T. Ngwisanyi, D. Hutchins, C.J.S. Fourie, and the SAMTEX Team, 22-26 October 2007. Electrical and seismic anisotropy of the southern African lithosphere. 10th SAGA Biennial Technical Meeting and Exhibition, Wild Coast, South Africa.

- Hamilton, M.P., A.G. Jones, R.L. Evans, S.F. Evans, C.J.S. Fourie, A. Mountford, X. Garcia, J.E. Spratt, and the SAMTEX MT Team, 17-23 September 2006. A Comparison of Electrical and Seismic Anisotropy Across the Southern African Region. 18th EM Induction Workshop, El Vendrell, Spain.

- Hamilton, M., Jones, A., Evans, R., Evans, S., Fourie, C.J.S., Garcia, X., Mountford A.,

Spratt, J., and the SAMTEX MT team, 31 August-1 September 2006. A comparison of seismic and electrical anisotropy over the southern African region. British Geophysical Association Postgraduate Meeting, Edinburgh, Scotland.

- Hamilton, M.P., Jones, A.G., Evans, R.L., Evans, S.F., Fourie, C.J.S., Mountford, A., Garcia, X., Spratt, J.E., and the SAMTEX team, 24-26 February 2006. Magnetotelluric studies across the Kaapvaal craton in southern Africa. 49th Irish Geological Research Meeting, University College Cork, Cork, Ireland.

- Hamilton, M.P., Jones, A.G., Evans, R.L., Garcia, X., Fourie, C.J.S., Evans, S.F., Webb, S.J., and the SAMTEX team, 14-16 September 2005. Electrical anisotropy across Southern Africa derived from MT studies and compared with seismic anisotropy results. 9th SAGA Biennial Technical Meeting and Exhibition, Cape Town, South Africa.

Poster Presentations:

- Hamilton, M.P., A.G. Jones, R.L. Evans, M.R. Muller, M. Miensopust, C.J.S. Fourie, T. Ngwisanyi, D. Hutchins, S.F. Evans, A. Mountford, and the SAMTEX MT Team, 16-20 April 2007. Electrical and seismic anisotropy properties over Southern Africa. European Geosciences Union meeting, Vienna, Austria.

- Hamilton, M.P., Jones, A.G., Evans, R.L., Evans, S.F., Fourie, C.J.S., Mountford, A., Ngwisanyi, T., Hutchins, D., Garcia, X., Muller, M., Spratt, J.E., Miensopust, M., and the SAMTEX Team, 2006. A comparison of electrical and seismic anisotropy across the southern African region. American Geophysical Union Fall meeting, San Fransisco, California, USA.

- Hamilton, M.P., Jones, A.G., Evans, R.L., Evans, S.F., Fourie, C.J.S., Mountford, A., Garcia, X., Spratt, J.E., and the SAMTEX Team, 2005. Electrical Anisotropy Across the Kaapvaal Craton Derived from SAMTEX MT Studies Compared with SASE SKS Seismic Anisotropy Results. American Geophysical Union Fall meeting, San Fransisco, California, USA.

Contents

Contents **ix**

List of Figures **xiii**

List of Tables **xvii**

Symbols/Nomenclature **xviii**

1 Introduction **1**

1.1 Motivation and aims of my study 1

1.2 The southern African magnetotelluric experiment (SAMTEX) 3

1.3 Previous MT work in southern Africa. 4

1.4 Geological outline and tectonic framework 6

2 MT theory **13**

2.1 Introduction to the magnetotelluric (MT) method 13

2.2 The physics of the MT method 15

2.3 Assumptions of the MT method 17

2.4 The impedance tensor 22

2.4.1 The tipper vector 22

2.5 Possible cases of the impedance tensor 23

2.5.1 The 1D Earth 23

2.5.2 The 2D Earth, and the fault model 24

2.5.3 The 3D Earth 27

2.6 Electrical anisotropy 27

2.7 Distortion: the problem 29

2.8 Data acquisition 31

2.9 Data processing 33

2.9.1 Pre-conditioning . . . 34
2.9.2 Conversion to the frequency domain . . . 35
2.9.3 Estimation of Transfer Functions . . . 36
2.10 Distortion analysis and removal . . . 37
2.10.1 Groom-Bailey decomposition . . . 38
2.10.2 The MT Phase Tensor . . . 41
2.11 Modelling and Inversion of MT data . . . 44

3 Seismic anisotropy theory 46
3.1 What is seismic anisotropy? . . . 46
3.1.1 What are SKS and shear waves? . . . 47
3.2 Seismic SKS shear wave splitting . . . 49
3.3 Where along the path does the anisotropy occur? . . . 54
3.4 Data preparation and analysis methodology . . . 55
3.4.1 Data Preparation and selection . . . 55
3.4.2 Analysis techniques . . . 58

4 The relationship between MT and Seismic anisotropy 61
4.1 Why are seismic and MT results complementary? . . . 61
4.2 Why would we expect a correlation? . . . 62
4.2.1 Causes of electrical anisotropy . . . 62
4.2.2 Causes of seismic anisotropy . . . 64
4.2.3 How are stress and strain related to anisotropy? . . . 66
4.2.4 Which causes will produce a correlation? . . . 71
4.3 Past studies of MT and teleseismic anisotropy . . . 71

5 Teleseismic shear-wave splitting in southern Africa 78
5.1 Introduction . . . 78
5.2 Southern African Seismic Experiment . . . 79
5.3 SASE shear wave splitting results . . . 79
5.4 Re-analysis of SASE shear wave splitting . . . 83
5.4.1 Event selection . . . 83
5.4.2 Station selection . . . 85
5.4.3 Preparation for splitting analysis . . . 87
5.4.4 Splitting analysis . . . 88
5.5 Results of splitting re-analysis . . . 90

5.6 Comparison with plate motion and mantle flow 96
5.6.1 Seismic anisotropy from mantle flow models 97
5.7 Correlation with plate motion and mantle flow 99

6 MT data analysis 102
6.1 Depth of investigation 103
6.2 GB decomposition analysis 107
6.3 The electrically more conductive direction 112
6.3.1 The more conductive direction across a fault 112
6.4 MT results 114
6.5 Cluster analysis 115
6.6 Correlation of lineaments with MT 122

7 Discussion of MT and seismic results 127
7.1 The MT conductive direction results 127
7.1.1 Crustal MT results 127
7.1.2 Lithospheric mantle MT results 133
7.1.3 Asthenospheric MT results 138
7.2 The SASE shear-wave splitting results 142
7.2.1 Shear wave splitting re-analysis. What have we learnt? 142
7.2.2 Key features of splitting results 143
7.2.3 Further arguments from this study 146
7.2.4 Possible explanations for SASE splitting 148
7.2.5 Mantle flow below thick lithosphere 153
7.3 A model for anisotropy in southern Africa 155
7.4 The correlation between MT and seismic results 161
7.4.1 Correlation between seismic and MT parameters 162
7.4.2 Causes of anisotropy 163

8 Summary and conclusions 166
8.1 Summary and main conclusions 166
8.2 Future work and possible improvements 169

References 171

APPENDICES 192

Appendix 1: Penetration estimates **193**

Appendix 2: Asthenospheric MT analysis **202**

Appendix 3: SASE events **204**

Appendix 4: Permanent station events **210**

Appendix 5: Published manuscript **213**

List of Figures

1-1 Site locations of the SAMTEX and SASE experiments. 5
1-2 Tectonic framework of southern Africa. 7
1-3 Regional magnetic anomaly map of southern Africa. 11
1-4 Regional Bouguer gravity map of southern Africa. 12

2-1 Electrical conductivity of common Earth materials. 14
2-2 An example of typical MT data as it is commonly displayed. 21
2-3 Lines of current flow for the TM mode at a vertical conductivity boundary. . 25
2-4 A graphical description of the EM modes for a 2 quarter-space model. 25
2-5 Photographs of some typical fieldwork. 32
2-6 A typical layout of an MT station. 33
2-7 Recorded time series data at an MT site. 34
2-8 A contrived example of distortion to aid in the understanding of distortion. . 40
2-9 The graphical representation of the phase tensor. 43

3-1 A schematic portrayal of raypaths and their sampling regions for various seismic anisotropy analyses. 49
3-2 (a) Seismic wave paths through the Earth, and (b) Shear wave splitting in the case of two anisotropic layers. 50
3-3 Traveltimes versus epicentral distance. 51
3-4 Predicted splitting parameters as a function of backazimuth, for two layers of seismic anisotropy. 53
3-5 (a) The Fresnel zone argument, and (b) the depth extent of shear anisotropy. 56
3-6 An example of a good shear wave splitting measurement using the method of Silver & Chan (1991). 60

4-1 The effect of parallel vertically aligned fluid-filled cracks on a near-vertically, downward propagating shear wave. 65
4-2 Physical and chemical variations in the Earth's mantle, and their control on seismic anisotropy. 67
4-3 Schematic representation of a lithospheric-scale shear zone. 70
4-4 Amplitudes and azimuths of shear wave splitting and electrical anisotropy over the Grenville front in Canada (Ji *et al.*, 1996). 73
4-5 An MT and teleseismic experiment across the Great Slave Lake shear zone, northern Canada (Eaton *et al.*, 2004). 74
4-6 A comparison of SKS fast axis directions with the geoelectric strike directions across the Grenville Front in Canada (Frederiksen *et al.*, 2006). 75
4-7 Azimuths and magnitudes of shear wave splitting and geoelectric anisotropy in south central Brazil (Padilha *et al.*, 2006). 76

5-1 Location map for the southern African seismic array stations, with re-analysed stations circled. 80
5-2 Results of shear wave splitting study reported in Silver *et al.* (2004). 81
5-3 Arguments for frozen-in lithospheric anisotropy, and not APM anisotropy reported by Silver *et al.* (2004). 83
5-4 Histograms describing the nature of all the events originally selected for shear wave splitting analysis. 85
5-5 Preliminary events selected for the SASE splitting analysis. 86
5-6 An example of seismogram arrivals at the seismic stations for a poor event. . 87
5-7 An example of seismogram arrivals at the seismic stations for a good event. . 88
5-8 Time window selection for split analysis of a SKS trace. 89
5-9 An example of a high quality splitting result at station SA39 for a single event 91
5-10 An example of a medium quality splitting result at station SA18 for a single event 92
5-11 An example of a poor quality splitting result at station SA71 for a single event 92
5-12 An example of a null splitting result at station SA82 for a single event, and a compass plot for the same station. 93
5-13 Splitting parameters as a function of backazimuth for station SA71 94
5-14 Plate motion and mantle flow models. 99
5-15 Correlation between SASE anisotropy, and plate motion and mantle flow models. 101

6-1 Penetration depths for given frequencies across a 2D fault model. 104

6-2 Penetration depth across the Kap03 profile (>1500 km in length) for data at 100 s. 105
6-3 A model response plotted as a function of (a) period, and (b) Niblett-Bostick depth. 106
6-4 Data selection for GB analysis from Niblett-Bostick penetration depth calculations. 107
6-5 RMS values from GB analysis of crustal and lithospheric mantle periods. . . 109
6-6 Twist values from GB analysis of crustal and lithospheric mantle periods. . . 110
6-7 Shear values from GB analysis of crustal (a,c) and lithospheric mantle (b,d) periods 111
6-8 The variation of apparent resistivity and phase for the xy and yx modes for a Niblett-Bostick depth of ≈35 km along a 2 quarter-space model profile. . . . 113
6-9 Crustal MT most conductive directions overlain on regional magnetic data. . 116
6-10 Lithospheric mantle MT most conductive directions overlain on SKS splitting results of Silver *et al.* (2001). 117
6-11 Asthenospheric MT most conductive directions overlain on SKS splitting results of Silver *et al.* (2001). 118
6-12 Elbow criterion (a and b) and silhouette plots (c and d) for 5 clusters using k-means cluster analysis. 120
6-13 Results of k-means cluster analysis for 5 clusters, on the conductive directions from the crustal and lithospheric mantle MT results. 122
6-14 Significant magnetic lineaments across southern Africa, digitised from Jelsma *et al.* (2004). 123
6-15 Rose diagrams of weighted magnetic lineament data (a), crustal MT results (b), and lithospheric mantle results (c). 125
6-16 Rose diagrams of unweighted crustal MT results (a), and lithospheric mantle MT results (b). 126

7-1 Site locations of the SAMTEX and SASE experiments. 128
7-2 Crustal MT most conductive directions overlain on regional magnetic data. . 129
7-3 Schematic diagram describing the different effects of heterogeneity and anisotropy on the electrical conducting directions. 130
7-4 Results of k-means cluster analysis for 5 clusters, on the conductive directions from the crustal MT results (a). Rose diagram of crustal MT results (b). . . 132

7-5 Results of k-means cluster analysis for 5 clusters, on the conductive directions from the lithospheric mantle MT results (a). Rose diagram of lithospheric mantle MT results (b). 134
7-6 Spatial correlation between the crustal and lithospheric mantle MT results. . 137
7-7 Asthenospheric MT results compared with plate motion models, and with shear wave splitting results. 139
7-8 Apparent resistivity and phase for site dmb030 plotted against NB depth as opposed to period. 140
7-9 A model and model MT response calculated for an anisotropic asthenosphere. 141
7-10 Delay time measurements from SASE, compared with other global studies. . 144
7-11 Shear wave splitting results of Silver *et al.* (2001), overlain on the regional magnetic data. 147
7-12 Correlation between SASE anisotropy and plate motion, overlain on a tomographic model of Fouch *et al.* (2004a). 149
7-13 Plots of shear wave splitting delay times plotted against velocity anomaly (akin to lithospheric thickness), and correlation between fast axis direction and plate motion against velocity anomaly. 150
7-14 Schematic models to describe the shear wave splitting observations. 151
7-15 Schematic cross section portraying mantle flow below a lithospheric keel. . . 154
7-16 A proposed model for the anisotropy of southern Africa. 156
7-17 The anisotropy produced by a proposed model for southern Africa. 160
7-18 Azimuthal correlation between MT and seismic parameters. 164
7-19 Magnitude correlation between MT and seismic parameters. 165

List of Tables

3.1 A brief summary of the advantages and disadvantages of various techniques used for calculating continental seismic anisotropy. 48

4.1 A summary of the different causes of electrical anisotropy and the resulting effect on the fast axis split direction and magnitude of SKS shear wave splitting and the electrical most conductive direction. 72

5.1 Table with seismic stations selected for shear wave splitting reanalysis. Splitting parameters are those of Silver *et al.* (2001). 87

5.2 Splitting results from this study, compared with the study of Silver *et al.* (2001). 96

Symbols/Nomenclature

Below is a list of the symbols and nomenclature used in this dissertation and their meaning. Vectors are denoted by a single underline, while matrices/tensors are denoted by a double underline.

Symbol	Description (units)	Relationship
∇	the vector differential	
$\times$	cross product operator	
$\cdot$	dot product operator	
$\underline{E}$	electric field (Vm^{-1})	
$\underline{D}$	electric displacement (Cm^{-2})	$\underline{D} = \epsilon \underline{E}$
$\underline{J}$	total electric current density (Am^{-2})	$\underline{J} = \sigma \underline{E}$
$\underline{H}$	magnetic field strength (Vm^{-1})	
$\underline{B}$	magnetic flux density (teslas, T)	$\underline{B} = \mu \underline{H}$
q	electric charge density (coulombs (C) per unit volume)	
ϵ_0	electric permittivity in free-space ($8.85 \times 10^{-12}\ Fm^{-1}$)	
ϵ	electric permittivity (Fm^{-1})	
μ_0	magnetic permeability in free-space ($1.2566 \times 10^{-6}\ Hm^{-1}$)	
μ	magnetic permeability (Hm^{-1})	
t	time (s)	
f	frequency (Hz)	
T	period (s)	$T = \frac{1}{f}$
ω	angular frequency (s^{-1})	$\omega = 2\pi f$
ρ	resistivity ($\Omega.m$)	
σ	conductivity (S)	
$\delta(\omega)$	skin depth (m)	

Symbol	Description (units)	Relationship
$\underline{\underline{Z}}(\omega)$	Impedance tensor (VA^{-1})	
$\underline{\underline{M}}(\omega)$	Magnetotelluric tensor	
$\underline{T}(\omega)$	Tipper vector	
TE	Transverse Electric (TE) mode / E-polarisation	
TM	Transverse Magnetic (TM) mode / B-polarisation	
$\underline{\underline{R}}_\theta$	Cartesian rotation matrix	
$\underline{\underline{C}}$	Galvanic distortion tensor	
$\underline{\underline{T}}$	Twist distortion tensor (GB decomposition)	
$\underline{\underline{S}}$	Shear distortion tensor (GB decomposition)	
$\underline{\underline{A}}$	Anisotropy distortion tensor (GB decomposition)	
g	gain factor (GB decomposition)	
β	skew angle (Phase tensor)	
Φ_{max}	coordinate invariant (Phase tensor)	
Φ_{min}	coordinate invariant (Phase tensor)	
V_P	P-wave propagation velocity (ms^{-1})	
V_S	S-wave propagation velocity (ms^{-1})	
ϱ	density ($kg.m^{-3}$)	
K	bulk modulus / incompressibility (GPa)	
μ	shear modulus / rigidity (GPa)	
IASP91	standard Earth velocity model (Kennett & Engdahl, 1991)	
δt	delay time (s)	
ϕ	fast-axis direction (degrees clockwise from north)	
Δ	epicentral distance (km)	
APM	absolute plate motion	
SAMTEX	Southern African Magnetotelluric Experiment	
SASE	Southern African Seismic Experiment	
MT	Magnetotellurics	
DC	Direct Current	
NB	Niblett-Bostick depth estimates	
GB	Groom-Bailey decomposition	
ISA	Infinite Strain Axis (Kaminski & Ribe, 2002)	

1 Introduction

This chapter provides an introductory overview to the focus of the research work described in this thesis. It also serves as an introduction to the southern African magnetotelluric experiment (SAMTEX), provides a brief tectonic framework of the region, and describes previous electromagnetic work conducted in the area.

1.1 Motivation and aims of my study

The SAMTEX experiment is a multinational project, comprising a consortium of academic, government, and industry partners. The sheer size of the experiment (figure 1-1) has necessitated this cooperation in order to complete the vast amount of work linked to the collection, processing, analysis, modelling, and interpretation of the data. A strength of an experiment such as this is that it provides access to the expertise from each organisation, as well as the opportunity to get involved in many different aspects of the experiment.

My thesis work was originally planned as an M.Sc. by research, which was subsequently converted to a PhD. project. The conversion has afforded the additional time and opportunity to focus my project on a more comprehensive study: examining the electrical

anisotropy information gained from the MT technique, and comparing the results with seismic anisotropy results from the southern African seismic experiment (SASE). The work of this thesis was originally inspired by the work of Ji *et al.* (1996), who compared MT geoelectric strike directions with the fast axis splitting directions across the Grenville front in Canada (findings discussed later). This is a facet of MT/seismic co-interpretation that has only recently started to be explored in any detail. The SAMTEX experiment has provided an unparalleled opportunity to compare seismic and electrical anisotropy across a very large and geologically diverse region since the large SASE experiment (discussed in depth later) is spatially coincident with many of our profiles (figure 1-1).

There were a number of outcomes that it was hoped would be addressed by this study, although as this was the first time MT data had been collected across the vast majority of the southern African region, it was sure to yield new and exciting data regardless. Past studies of electrical anisotropy from MT have yielded interesting results that have been used to infer geological information, e.g. mantle flow direction, and have proved a very worthwhile analysis. It was hoped that through the correlation of the electrical and seismic anisotropy, we would be able gain even more information than would otherwise be obtained through using either of them alone. One of the more obvious aims was to place more accurate bounds on the depth and extent of the seismic shear wave splitting anisotropy of Silver *et al.* (2001), since this seismic technique has no inherent depth information. Additionally, we expected that the electrical anisotropy could provide information on any distinct electrical fabric in the region, which may be related to geology, and thereby give more insight into the formation and tectonics of southern Africa.

My part in the SAMTEX project has included many different aspects. I have planned and led sections of the field campaign, particularly those in Botswana. I have processed and analysed large portions of the MT data, and have participated in modelling and inversion of some of the MT data during software courses and SAMTEX workshops (SAMTEX, 2004, 2005). The main focus of my work has been on the electrical and seismic anisotropy of the region. This entails the detailed analysis of the MT responses for geoelectric directionality, and since I am comparing the MT results with seismic results, it has been necessary for me to become familiar with the seismic shear wave splitting method. I have reanalysed some of the seismic data from the SASE experiment to look for subtleties that may have been overlooked by the Silver *et al.* (2001) analysis, and also in order to gain a better understanding of the technique. Additionally, in order to try and understand the results of my analysis, it has

been necessary for me to explore other techniques and data sets, such as cluster analysis, as well as plate motion and mantle flow models. We present in this thesis the analysis of the MT data for directionality at different depths, the re-analysis of some of the SASE data for shear wave splitting, and the interpretation of the results taking into account constrains provided by both techniques.

1.2 The southern African magnetotelluric experiment (SAMTEX)

Archean cratons have been the target of geoscientific studies for a long time. Our understanding of them is important because not only are they the oldest parts of the continents, but also because they are major sources of the world's mineral wealth. There are many different hypotheses and models for the formation of continental cratons, primarily because there is a very limited amount of data present that imposes constraints on the deep structure beneath cratons. The different models that have been proposed would likely produce very characteristic structures in the continental lithosphere. Magnetotelluric (MT) studies are able to help identify and characterise many of these features through imaging and analysis of the MT data: for example, the depth and extent of electrical anisotropy, the degree and character of regional variation in the apparent resistivity, and the variation in electrical anisotropy direction. By relating these features to surface structures, such as the orientation of mobile belts, large faults, etc., as well as with the expected results for different models of formation, these data can prove invaluable for the rejection as well as the improvement of hypotheses for the formation of the cratonic roots of the continents (Jones, 1999; Chave *et al.*, 2002).

The SAMTEX project as a whole is intended to compliment the broad geoscientific data that exist over the southern African region by providing added constraints through the measurement of the electrical properties of the region. It has been demonstrated in other studies (e.g. Jones *et al.*, 2001; Jones & Ferguson, 2001; Jones *et al.*, 2003; Davis *et al.*, 2003) that electromagnetic results can combine with other geoscientific results such as geochemical, petrological, geochronological, and seismic results to form a more complete geological picture. The study conducted over the Slave craton in Canada is an example of a very large area MT study, where the primary aim was to map the lithosphere-asthenosphere boundary beneath the craton. That study revealed unexpectedly and serendipitously the presence of a conductivity anomaly, named the Central Slave Mantle Conductor (CSMC) anomaly, that

is a localized region of low resistivity at depths of 80-120 km and is spatially coincident with the Eocene-aged kimberlite field. Given the electrical properties of the conductor, its position, and as well as geochemical information, Jones *et al.* (2003) attribute the anomaly to carbon, as either graphite or as carbon on grain-boundary films.

A large amount of geoscientific information, in particular geochemical, petrological, and seismic, is available for both the Slave and Kaapvaal cratons, making the Kaapvaal craton an ideal region for comparison with the Slave craton. The need for electrical information on the southern African region was one of the main driving reasons for the initiation of the SAMTEX experiment. Originally the proposal was to collect data along four profiles that coincided well with the SASE experiment, thereby providing the opportunity to compare the MT results directly with the seismic results (Chave *et al.*, 2002). After the successful first phase of fieldwork, the project was subsequently extended, with further phases of data collection as a result of interest and funding from government, academic, and industry partners. The SAMTEX experiment has moved further to the northwest into Namibia and covered Botswana extensively. With further phases of data collection planned, the SAMTEX experiment already covers the majority of the SASE station coverage, with the exception of Zimbabwe due to political reasons, as well as large regions to the northwest where there is far less geoscientific information available. The experiment currently consists of over 525 broadband sites along a total of 20 profiles (figure 1-1). Once complete, it will be the largest experiment of its kind yet performed, involving a consortium of academic, government, and industrial partners worldwide.

1.3 Previous MT work in southern Africa.

Small-scale controlled-source MT studies are routinely conducted in South Africa as a tool for late-stage mineral exploration. However, these small-scale shallow studies are of little use for obtaining geoelectric information of lithospheric scale. When SAMTEX was first initiated, the only relatively large-scale MT study carried out in the country was that of Stettler *et al.* (1998) and Stettler *et al.* (1999) (same data). These MT data consisted of 5 soundings, and were combined with reflection seismic, gravity and magnetic data in order to gain a better understanding of the crustal structure of the Kheis tectonic province.

An MT study in northwestern Namibia (≈250 km west of our nearest profile) was carried out by Ritter *et al.* (2003) and Weckmann *et al.* (2003) (same study), which consisted of an

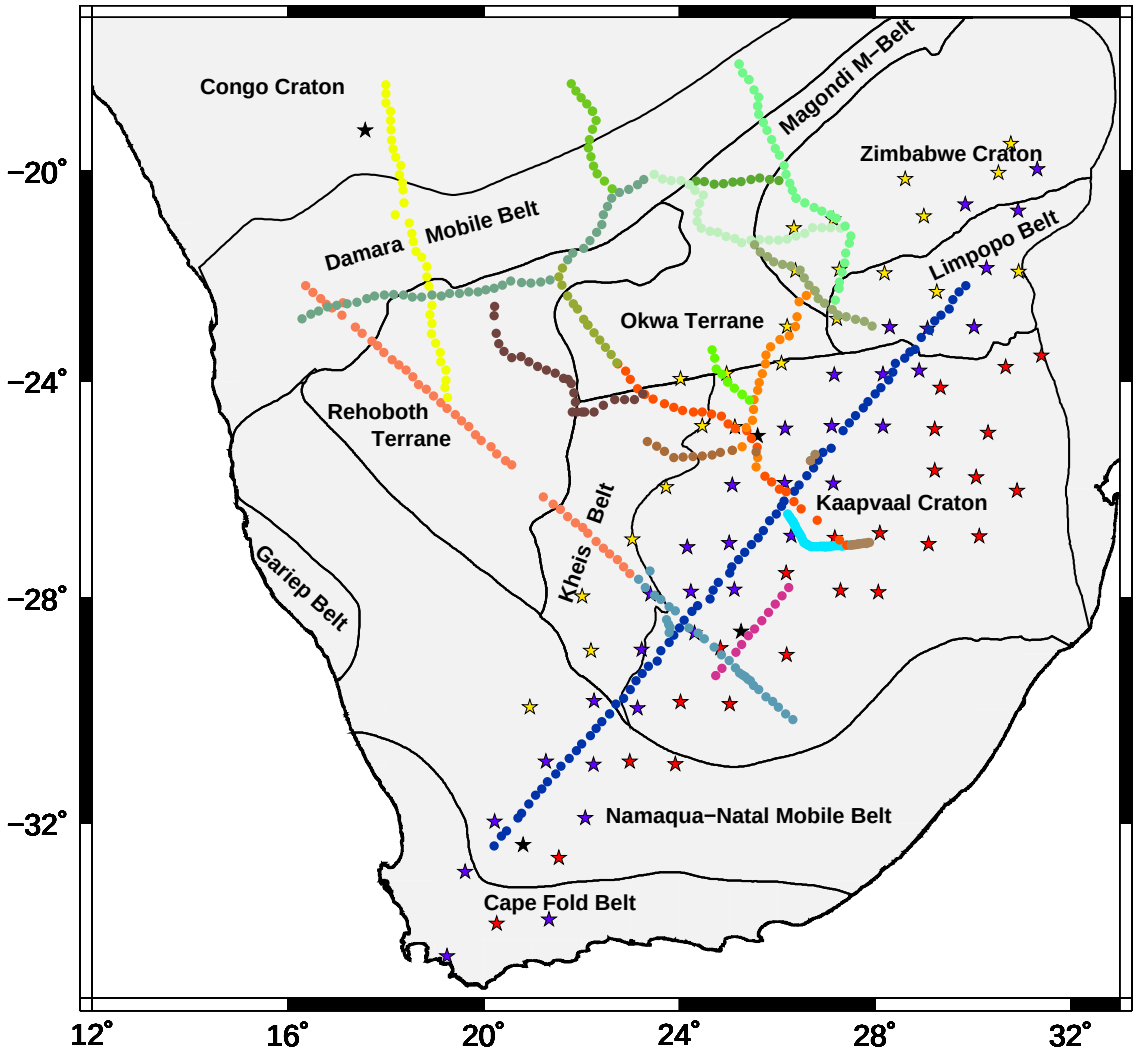

SAMTEX Survey Lines (Phases I, II, & III) and SASE station locations			
WITS04	KAP03	KIM03	
BOT200	BOT400	RTZ200	RTZ400
KIM04	KAP04	KOF04	WITS05
DMB	K2G	MAK	MOF
MOL	OKA	SSO	WIN
ZIM			
1997–1998	1998–1999	1997–1999	Permanent

Figure 1-1: *The southern African magnetotelluric experiment (SAMTEX) profile/site locations, and the SASE seismic array station locations, overlain on a map of southern Africa with schematic geological provinces (after Nguuri* et al.*, 2001).*

≈200 km long profile, the interpretation of which was focused on crustal structure (upper 40km). Subsequent to the start of SAMTEX, there has been further MT work across the Beattie magnetic anomaly (Cape fold belt) funded by the GeoForschungsZentrum in Potsdam, Germany, as part of the German-South African Inkaba yeAfrica project (Bochannon, 2004; de Wit & Horsfield, 2006). Some of this work was recently published (Weckmann *et al.*, 2007), but is also more focused on crustal (upper 25 km) structure, utilising 82 broadband stations, with a station spacing of ≈2 km.

Although not MT studies, it is important to make note of magnetometer array studies undertaken in the region (Gough *et al.*, 1973; de Beer & Gough, 1980), which noted a conductive anomaly in the southern Cape orientated east-west, located in the crust or uppermost mantle. de Beer & Gough (1980) note that the conductive anomaly correlates well with a magnetic anomaly, and is likely not thermally related. Other methods that have been used to gain information on the electrical structure of the region include DC resistivity soundings (e.g. Van Zijl, 2006). Some of these are deep soundings, with current electrode spacings of a few hundred kilometres (e.g. Van Zijl, 1969, 1978), and have provided useful information on crustal resistivity structure. The very deep DC resistivity soundings generally use telephone or power lines to gain large current electrode spacings. However, although MT and deep DC electrical soundings both provide information on the electrical characteristics of the crust, they are not mutually exclusive (Stettler *et al.*, 1999). MT, being an electromagnetic method, is more capable of distinguishing between conductive layers than DC methods, but less capable in distinguishing between different resistive layers than DC methods.

1.4 Geological outline and tectonic framework

There are two major reasons for geological interest in southern Africa. Firstly, contained in this region is the Archean-aged Kaapvaal craton. Our understanding of Archean cratons is essential to our understanding of early Earth and continent formation. Secondly, areas on the Kaapvaal craton contain very significant mineral resources. These two reasons provide both academic as well as industry interest in the region, resulting in an enormous amount of geoscientific information being available. This section is intended as a brief introduction to the geological structure and tectonic framework of the region (figures 1-1, 1-2). More detailed works on the subject are presented by Tankard *et al.* (1982); de Wit *et al.* (1992); Key & Ayres (2000), and James & Fouch (2002).

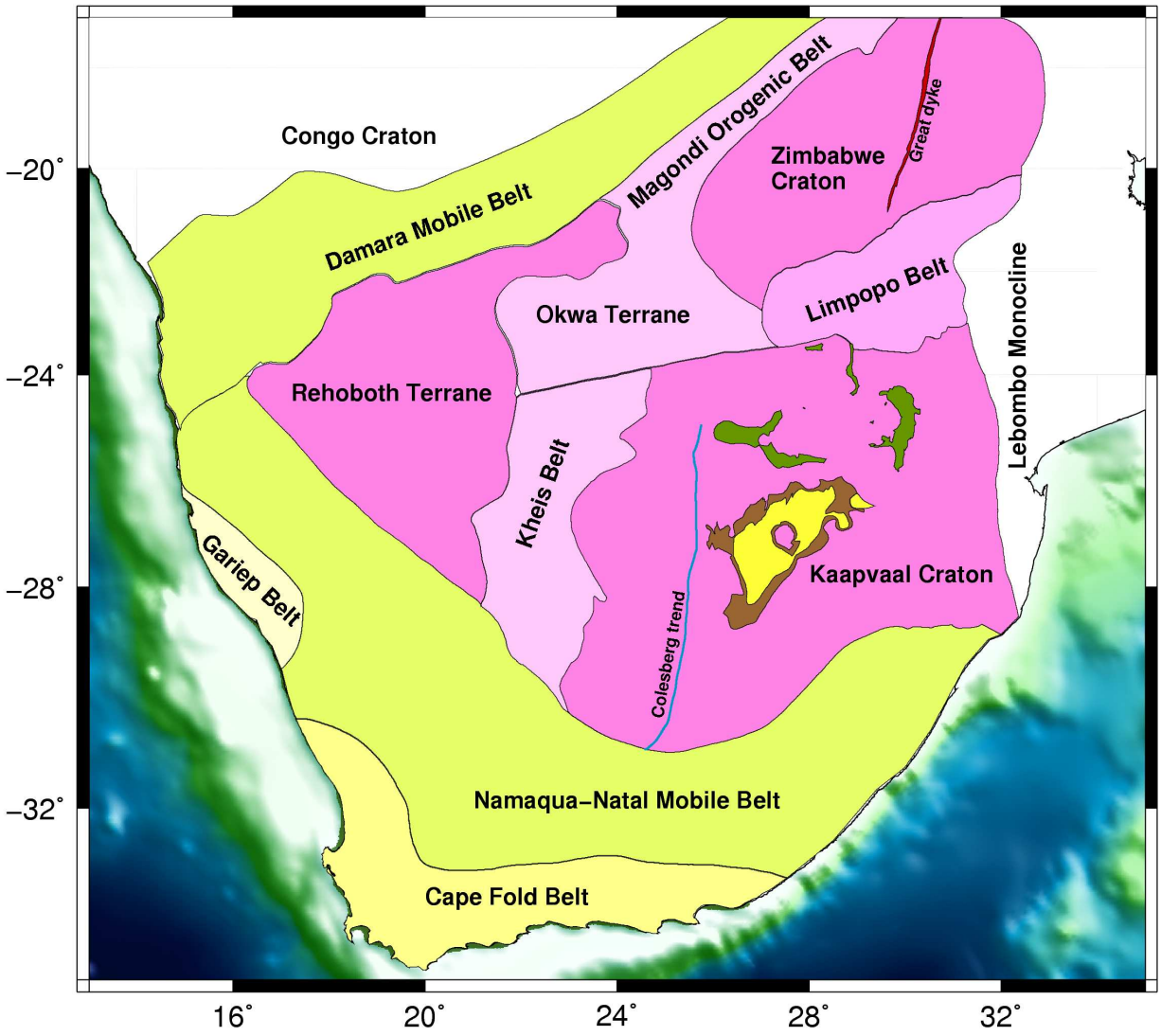

Figure 1-2: *A schematic tectonic framework of the geological provinces of southern Africa, with some other important features (Nguuri* et al.*, 2001). The yellow and brown in the centre of the Kaapvaal craton is the Witwatersrand basin. The green regions on the Kaapvaal craton are the outcrops of the Bushveld complex. Etopo 5 data (freely available at: www.ngdc.noaa.gov/mgg/fliers/93mgg01.html) are used for the bathymetry in the oceans.*

The Kalahari craton, within which is contained the Archean Kaapvaal and Zimbabwe cratons, forms the core of the southern African continent. The Kaapvaal craton, the more thoroughly studied of the two cratons, is composed of various granite-greenstone terranes. It is bounded in the south and west by Proterozoic mobile belts (Namaqua-Natal mobile belt, and Kheis fold and thrust belt), in the east by the Lebombo monocline, which is Jurassic in age, and in the north by the Neoarchean orogenic Limpopo belt (de Wit *et al.*, 1992). At

its surface, the Kaapvaal craton can be divided into Archean subdomains, and it has been suggested that some of these subdomains are also distinct at upper mantle depths (de Wit *et al.*, 1992) within the deep lithospheric keel, or tectosphere (Jordan, 1975), typically found beneath Archean cratons. The Kaapvaal cratonic keel, as observed by James *et al.* (2001) through tomographic analyses of P-wave and S-wave delay times, is a high velocity mantle zone. The eastern part of the craton is host to the oldest known sections of crust (≈3.5 Ga), some of which may represent the remnants of ancient oceanic lithosphere, whereas the more western sections of the craton are generally younger in age (de Wit *et al.*, 1992). The Kaapvaal terranes were assembled over a period of at least 1 Ga, from the early Archean (3.6 Ga) to the late Archean (2.6 Ga). In contrast to the general ENE-WSW trend in the east of the craton, the western section of the Kaapvaal craton, to the west of the Colesberg Magnetic lineament (CML) (figure 1-2) shows a distinctively NS trend both geologically and geophysically, e.g. the Amalia and Kraaipan greenstone belts as well as the CML itself (Corner *et al.*, 1990; de Wit *et al.*, 1992). The CML can be clearly observed in the magnetic data in figure 1-3. The core of the Zimbabwe craton is characterised by north-northeast structural trends, including the Great dyke (Wilson, 1990; Jelsma *et al.*, 2004). The late stages of the Kaapvaal craton evolution included widespread extensional volcanism, followed by the development of very large depositional basins (James & Fouch, 2002). One such basin is the Witwatersrand basin, supplied by sediments originating in the north, and host to what is thought to be the world's largest gold reserves. The end of craton evolution in Archean time was marked by a craton-wide extensional cycle of Ventersdorp volcanism and sedimentation between 2.7 and 2.6 Ga (James & Fouch, 2002). A prominent feature located on the northeastern part of the Kaapvaal craton is the ≈2.06 Ga (e.g. Eglington & Armstrong, 2004) Bushveld intrusion, the world's largest layered mafic intrusion, containing the world's largest reserves of platinum group metals.

The Limpopo belt separates the Kaapvaal and Zimbabwe cratons, and can be divided into three zones; the northern marginal zone, central zone, and southern marginal zone (de Wit *et al.*, 1992). These three zones are geologically distinct, and are separated from each other, and from the adjacent cratons by well defined shear zones (Van Reenan *et al.*, 1992). As a whole, it is a high-grade metamorphic terrane formed through collision between the Kaapvaal and Zimbabwe cratons in the late Archean. There is a large system of roughly ENE-WSW trending ductile shear zones that accommodated crustal shortening during the Limpopo orogeny (McCourt & Vearncombe, 1992). The Thabazimbi-Murchison Lineament (TML), a deformation belt with a long-lived tectonic history, is one such feature ≈25 km

wide that stretches for approximately 500 km across the Kaapvaal craton (Good & DeWit, 1997). The TML has been advocated to be an important controlling structure for the SKS shear-wave splitting results of the region (Silver *et al.*, 2001).

Mobile belts accreted to southern Africa in the mid to late Proterozoic, buffering the cratons from later plate tectonic events (James & Fouch, 2002). The Kaapvaal craton is bounded to the south and east by the Namaqua-Natal Belt, which is Proterozoic in age and thought to be subduction-related (James & Fouch, 2002). To the west, the Kaapvaal craton is bounded by the Proterozoic "thin skinned" Kheis fold and thrust belt (Carney *et al.*, 1994). The Okwa terrane and Magondi orogenic belt lie to the northwest of the Kaapvaal craton, Zimbabwe craton, and Limpopo belt. This region has complex geological relationships, made even more enigmatic due to the extensive Kalahari cover (Carney *et al.*, 1994; James & Fouch, 2002; McCourt *et al.*, 2004). These orogenic belts relate to events around 2 Ga and imposed strong overprinting on the very western parts of the Zimbabwe craton. However, despite Proterozoic overprinting, the mantle beneath some parts of this region are known to be of Archean age (Carlson *et al.*, 2000; Shirey *et al.*, 2001; James & Fouch, 2002). Blue diamonds in figure 1-3 represent model ages >2.5 Ga, calculated from Re depletion models of peridotite xenoliths (note there is one in the Magondi orogenic belt). Red diamonds represent model ages <2.0 Ga, and the green diamond is for a model age of 2.0-2.5 Ga (Carlson *et al.*, 2000).

To the northwest of the Okwa Terrane and Kheis belt is the Rehoboth terrane (or Namibia province), of which very little is known due largely to the thick Kalahari desert sands which cover a large portion of it. It is delineated primarily by potential field (mostly aeromagnetic) data (figures 1-3, 1-4), where it has a characteristically lower frequency, "smoother" response. The Rehoboth terrane can be divided into two subprovinces, the northern Tses Subprovince, which has a weaker magnetic signature than the southern Aroab Subprovince. The change in magnetic signature is considered to reflect a potential transition in the crustal basement across a northeast trending discontinuity (Hoal *et al.*, 1995). The discontinuity, which is not very well understood, is known as the Makgadikgadi line and was originally based on gravity (figure 1-4) and seismicity anomalies (Reeves & Hutchins, 1982), but is also visible in the regional magnetic data (figure 1-3). Northwest of the Rehoboth terrane and Magondi orogenic belt is the Ghanzi-Chobe belt and the Damara orogenic belt (Hoal *et al.*, 1995), outlined as one belt (the Damara belt) in figures 1-2, 1-3, and 1-4. The Damara belt is interpreted to represent the collisional suture separating the Rehoboth terrane from the

Congo craton (sometimes called Angola craton) (Johnson *et al.*, 2006). Most studies place the timing of the collisional tectonics in the central, high-grade metamorphic part of the belt to be ≈550 Ma (Johnson *et al.*, 2006).

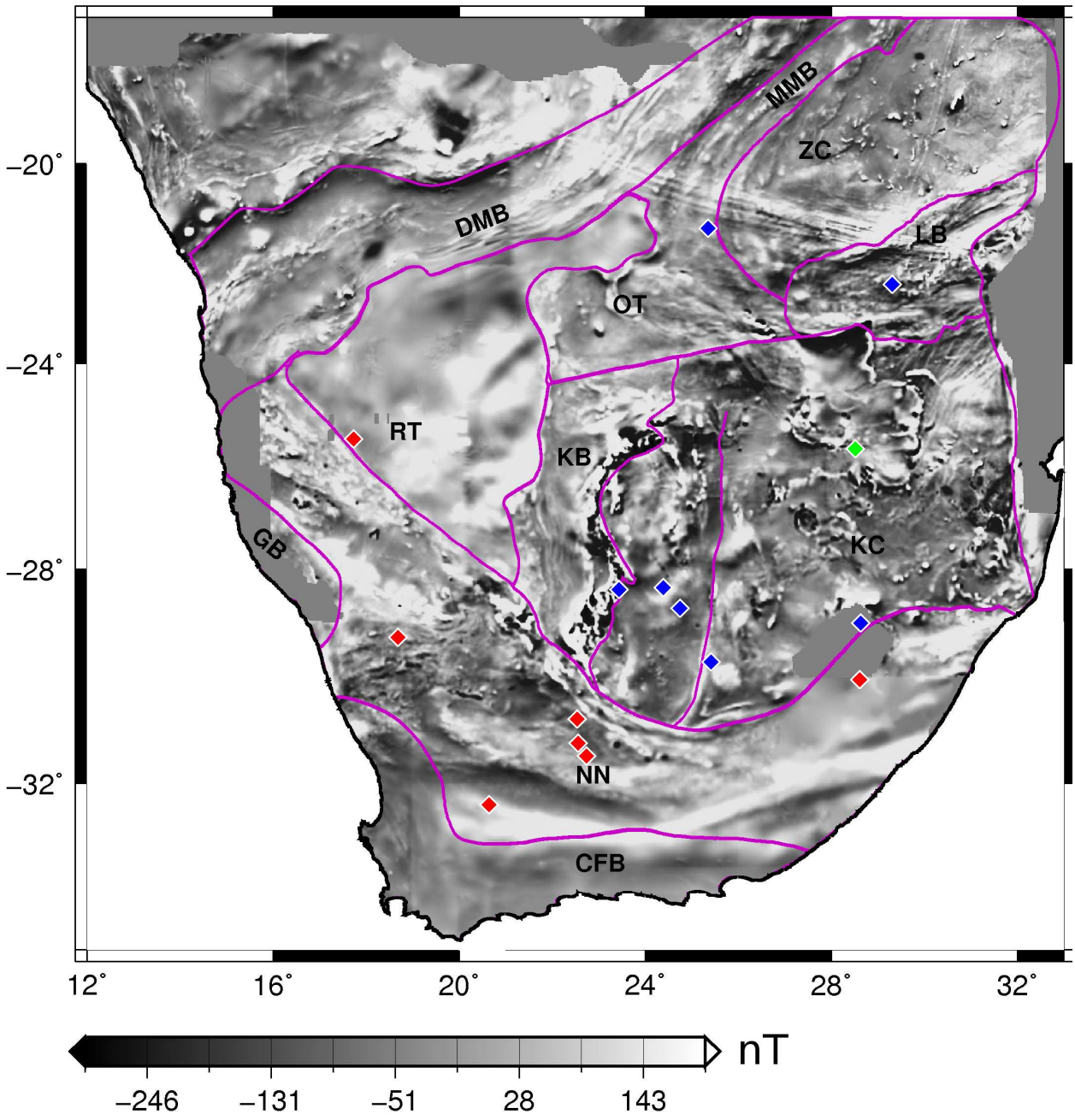

Figure 1-3: *Regional magnetic anomaly map of southern Africa, in nT, with rough framework of geological provinces (Nguuri* et al.*, 2001). KC: Kaapvaal craton. KB: Kheis belt. ZC: Zimbabwe craton. RT: Rehoboth Terrane. DMB: Damara Mobile belt. OT: Okwa Terrane. MMB: Magondi Orogenic belt. NN: Namaqua-Natal Metamorphic belt. CFB: Cape fold belt. GB: Gariep belt. LB: Limpopo Belt. Colesberg magnetic lineament also displayed. Blue, green, and red diamonds represent Re model ages of >2.5, 2-2.5, and <2.0 Ga respectively from peridotite xenoliths, after Carlson* et al. *(2000). Magnetic data courtesy of the Council for Geoscience, Pretoria, South Africa.*

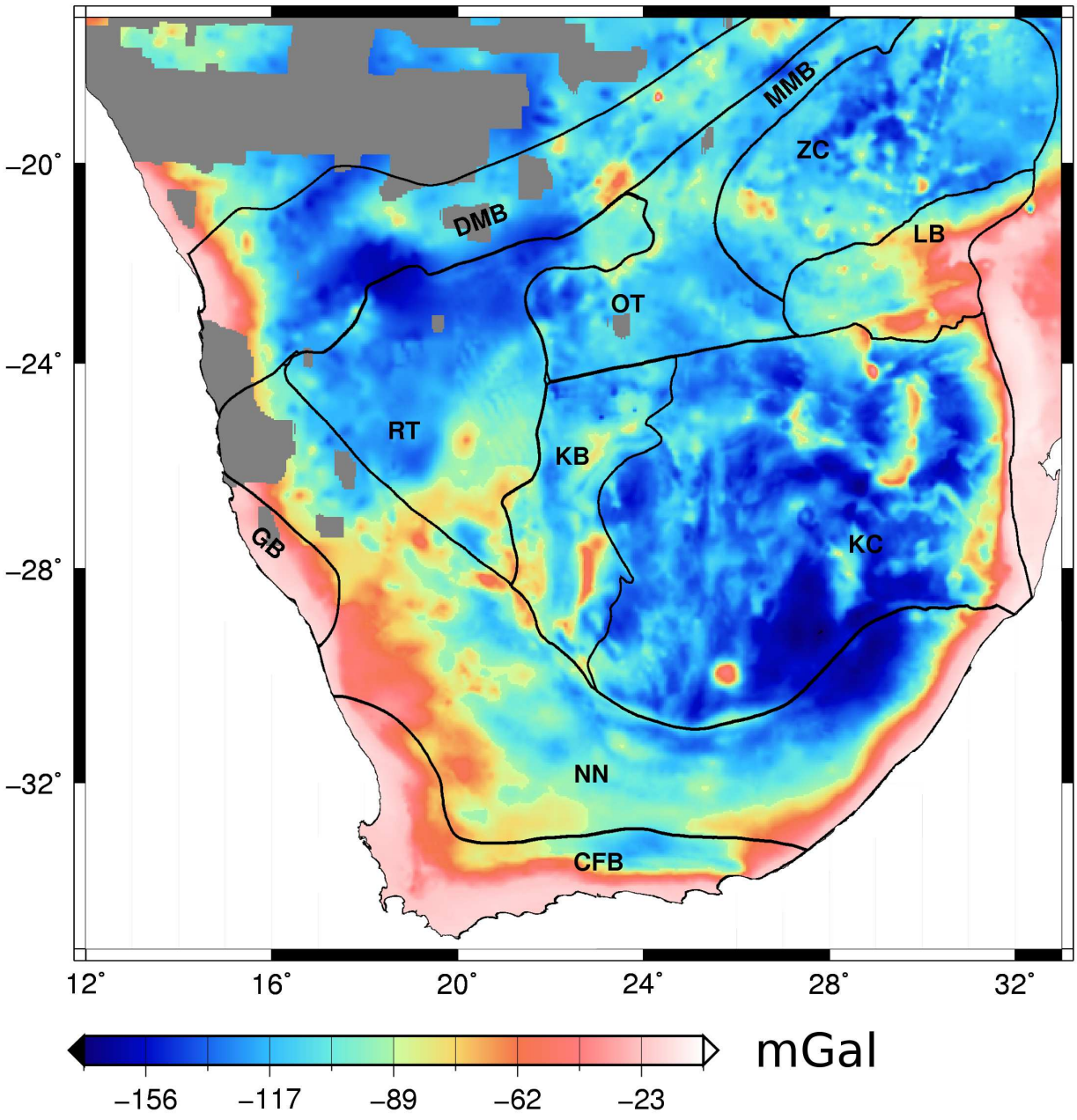

Figure 1-4: *Regional Bouguer gravity map of southern Africa, with rough framework of geological provinces (Nguuri* et al.*, 2001). Terrane symbols as in figure 1-3. Gravity data courtesy of the Council for Geoscience, Pretoria, South Africa.*

2

MT theory

2.1 Introduction to the magnetotelluric (MT) method

The magnetotelluric (MT) method is a natural-source (passive) electromagnetic geophysical technique. The foundations of the technique were described by Cagniard (1953) in the 1950's, and although used sporadically subsequently, its use and development has made massive progress since the 1980's with the aid of modern instrumentation, 24-bit recorders, low-noise sensors, modern robust processing methods, advanced analysis techniques, and multi-dimensional modelling and inversion. MT has the ability to penetrate several hundred kilometres into the Earth, reaching well into the upper mantle. To provide an artificial source large enough so as to allow this depth penetration would be costly and impractical, and would produce additional complications through the necessity of dealing with source geometry (Madden & Nelson, 1986; Jones, 1999). A few studies have used very large sources, mostly power lines, to penetrate depths greater than the middle crust (e.g., Blohm *et al.*, 1977; Lienert, 1979; Kaikkonen *et al.*, 1996; Zhamaletdinov *et al.*, 2007). The source used by the magnetotelluric method is the Earths naturally fluctuating magnetic field. These variations in the magnetic field are produced by a number of different mechanisms; high frequency signals that penetrate several hundred metres to typically ten kilometres into the Earth are

caused largely by world-wide thunderstorm activity. The resulting electromagnetic energy travels around the Earth in a waveguide that is formed between the Earth's surface and the ionosphere. If the thunderstorm activity is too near the station where measurements are being made, say within 5 km, it will not provide an ideal source as it will have non-planar characteristics, and will appear as a spike in the data. Longer period signals (10^3–10^4 s) that penetrate deeper (100 km or more) into the Earth are caused by the interaction of solar plasma with the Earth's magnetosphere (Vozoff, 1991).

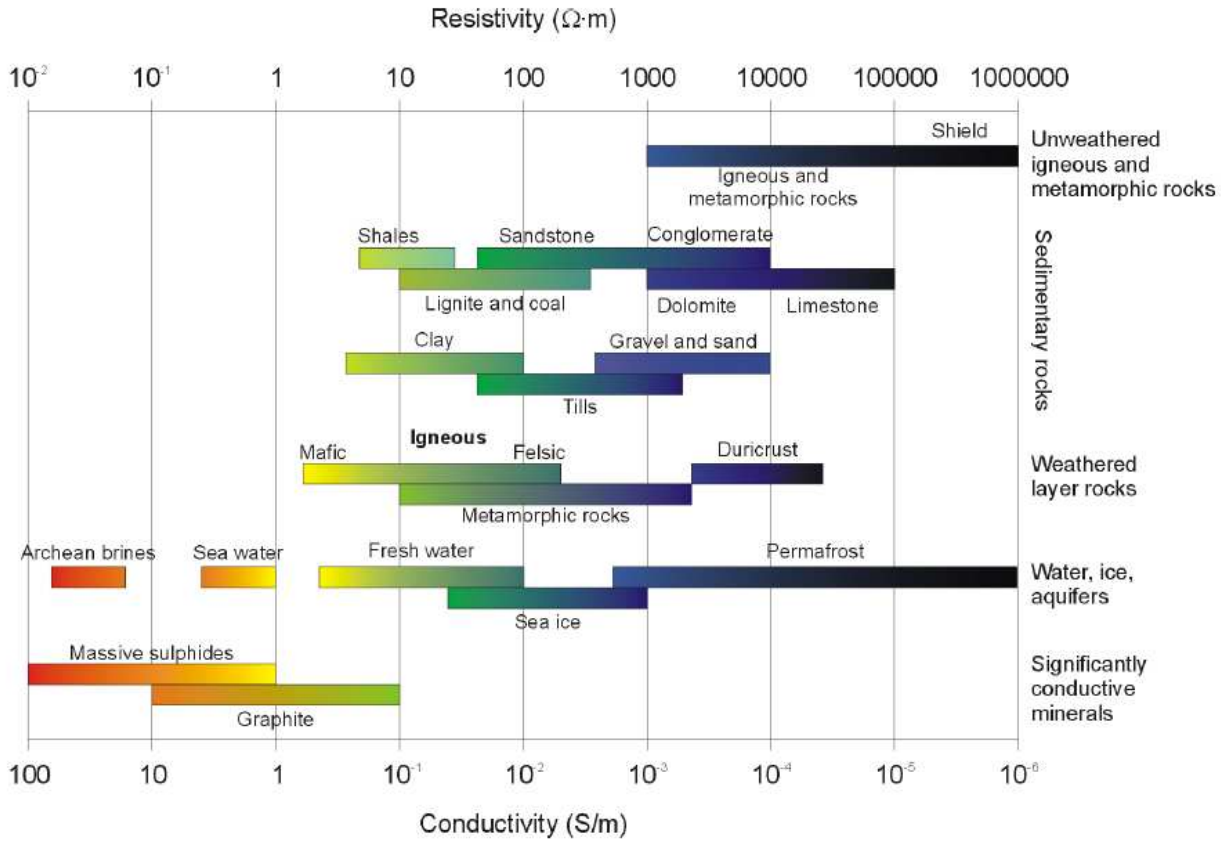

Figure 2-1: *Ranges in electrical conductivity of some common Earth materials. Taken from Marti (2006), modified from Palacky (1987).*

The naturally varying magnetic field induces an electric current (known as a telluric current), which by Faraday's Law, induces an electric field in the Earth. This induced electric field produces a secondary magnetic field. The strength of the electric field is dependant on the conductivity of the medium (Jones, 1999). Through the simultaneous recording of the time variations in the magnetic and electric fields, and the calculation of their ratios at varying frequencies, it is possible to derive the conductivity distribution with depth and

distance (Jones, 1999). The variations in conductivity with depth can then be used to gain information about the electrical structure of the lithosphere. There are a number of factors responsible for variations in conductivity: different rock types and compositions have conductivities which vary over orders of magnitude (figure 2-1), a wet environment will likely be more conductive than a dry environment, strongly interconnected conductive minerals will enhance conductivity compared with poor interconnection, and an increase in temperature will decrease resistivity. These are just some of the possible factors that may be responsible for an observed resistivity structure. They will be discussed in more detail in later sections.

2.2 The physics of the MT method

Maxwell's equations are a set of four equations that were published by Maxwell in his two volume textbook in 1873: A Treatise on Electricity and Magnetism (Maxwell, 1873a,b). The equations describe the behaviour of both electric and magnetic fields and their interaction with matter, and are therefore the fundamental physics upon which the MT method is built. They are described in differential and integral (in square brackets) form, and in words corresponding to the integral form (Feynman *et al.*, 1964) below:

$$\nabla \cdot \underline{E} = \frac{q}{\epsilon_0} \qquad \left[\oint_S \underline{E} \cdot \underline{n} ds = \frac{q}{\epsilon_0} \right] \tag{2.1}$$

This first equation (2.1) is essentially Gauss' Law for an electric field, and can be described as:

$$(flux\ of\ E\ through\ a\ closed\ surface) = (Charge\ inside)\ /\ \epsilon_0.$$

$$\nabla \times \underline{E} = -\frac{\partial \underline{B}}{\partial t} \qquad \left[\oint_c \underline{E} \cdot d\underline{l} = -\frac{\partial}{\partial t} \int_S \underline{B} \cdot \underline{n} ds \right] \tag{2.2}$$

The second of Maxwell's equations (2.2) is Faraday's Law of induction, and can be described as:

$$(line\ integral\ of\ E\ around\ a\ loop) = -\ (the\ time\ rate\ of\ change\ of\ the\ flux\ of\ B\ through\ the\ loop).$$

$$\nabla \cdot \underline{B} = 0 \qquad \left[\oint_S \underline{B} \cdot \underline{n} ds = 0 \right] \tag{2.3}$$

Equation 2.3 is Gauss' Law for a magnetic field, and can be described as:

$$(flux\ of\ B\ through\ a\ closed\ surface) = 0.$$

$$\nabla \times \underline{H} = \underline{J} + \frac{\partial \underline{D}}{\partial t} \qquad \left[\oint_c \underline{H} \cdot d\underline{l} = \underline{I} + \frac{\partial}{\partial t}\int_S \underline{D} \cdot \underline{n} ds\right] \tag{2.4}$$

This fourth equation (2.4), commonly known as the Ampere-Maxwell Law, is Ampere's Law with Maxwell's term ($\frac{\partial \underline{D}}{\partial t}$) added to it, and can be described as:

$$(The\ integral\ of\ H\ around\ a\ loop) = (Current\ through\ the\ loop) + (the\ time\ rate\ of\ change\ of\ the\ flux\ of\ D\ through\ the\ loop).$$

where $\underline{E}$, and $\underline{B}$ are the measured electric (Vm^{-1}) and magnetic (Teslas [T]) fields respectively, q is the electric charge density (coulombs per unit volume), ϵ_0 is the electric permittivity in free-space (Fm^{-1}), and t is time. $\underline{n}$ is a unit vector normal to the area element ds of the surface S and $d\underline{l}$ is a vector element of length along the contour. $\underline{I}$ in equation 2.4 is defined as $\underline{I} = \int_S \underline{J} \cdot \underline{n} ds$. $\underline{J}$, the total electric current density (Am^{-2}) is related to $\underline{E}$ by equation 2.5 (where σ is conductivity (Sm^{-1})), which is Ohm's Law and has implications for the accumulation of charge at a conductivity discontinuity. $\underline{D}$ is electric displacement (Cm^{-2}), and is related by equation 2.6, where ϵ is the permittivity of the material. $\underline{H}$ is the magnetic intensity (Am^{-1}) and is related to $\underline{B}$ by equation 2.7, where μ is the magnetic permeability (Hm^{-1}) of the substance.
The constitutive equations relating these are:

$$\underline{J} = \sigma \underline{E}, \tag{2.5}$$

$$\underline{D} = \epsilon \underline{E}, \tag{2.6}$$

$$\underline{B} = \mu \underline{H}. \tag{2.7}$$

In the MT method, it is assumed (see assumption viii of the MT method (page 18)) that bulk rock conductivity variations far outweigh the effects of variations in electrical permittivities and magnetic permeabilities. Therefore free-space values for electrical permittivities ($\epsilon_0 = 8.85 \times 10^{-12}\ Fm^{-1}$) and magnetic permeabilities ($\mu_0 = 1.2566 \times 10^{-6}\ Hm^{-1}$) are assumed.

The penetration of an electromagnetic wave in a conductor (e.g. rock for induction in the Earth) depends on the oscillation frequency. The relation is known as the electromagnetic skin depth phenomenon and is the reason for MT measurements being made over a range of

frequencies. Each frequency of measurement is essentially also a measurement at a certain length, which is depth in a 1D Earth. The electromagnetic skin depth phenomenon is described by

$$\delta(\omega) = \sqrt{\frac{2}{\mu_0 \sigma \omega}} \approx 500\sqrt{\rho T}, \tag{2.8}$$

where δ is the penetration of an electric field (in metres) with an angular frequency ω into a half-space of uniform or average conductivity σ. Thus, penetration is assured at any depth and depends only on the period (T) of measurement, and resistivity (ρ) of the subsurface. In theory, all we would need to do to probe deeper into the Earth, is to measure at longer and longer periods.

2.3 Assumptions of the MT method

There are a number of simplifying assumptions that are utilised when considering electromagnetic induction in the Earth. These have been discussed by a number of authors (e.g., Cagniard, 1953; Wait, 1954; Price, 1962, 1973; Simpson & Bahr, 2005) and are summarised below, modified from Simpson & Bahr (2005). It is important that these assumptions be born in mind and one should realise when they are being violated.

i *Maxwell's equations (equations: 2.1, 2.2, 2.3, 2.4) are obeyed.*

ii *The Earth does not generate electromagnetic energy, it only absorbs or dissipates it.*

iii *All fields can be regarded as conservative and analytic (has a first derivative at all points) away from their sources.*

iv *The electromagnetic source fields utilised by the MT method may be treated as being uniform, plane-polarised electromagnetic waves, with near-vertical incidence to the Earth's surface.* This is commonly known as the *plane-wave assumption* and may be violated when the source field is too near, or in polar and equatorial regions.

v *No accumulation of free charges is sustained in a layered Earth.* However, in a 2D or 3D Earth, charges are accumulated and dissipated (on a cycle given by the frequency of interest) along conductivity discontinuities, producing the non-inductive static shift effect.

vi *The Earth behaves as an ohmic conductor, and charge is conserved. i.e.,* $\underline{J} = \sigma \underline{E}$, and $\nabla \cdot \underline{J} = -\frac{\partial \rho}{\partial t}$.

vii *The Quasi-stationary approximation: Time-varying displacement currents ($\frac{\partial \underline{D}}{\partial t}$, Maxwell's term in equation 2.4) are small compared with time-varying conduction currents ($\underline{J}$, in equation 2.4) for the period range* 10^{-5} *s to* 10^{5} *s.* Even at high frequencies and in very resistive environments, the displacement currents are likely to be about one order of magnitude smaller. This allows us to treat induction in the Earth as a diffusion process, further allowing us to gain responses that are volumetric averages of Earth conductivities. Strictly, this condition applies only in the sub-surface

viii *Variations in electrical permittivities and magnetic permeabilities of rocks are negligible compared with variations in bulk rock conductivity.* Within the Earth, the dielectric permittivity can vary from $\epsilon_0 = 8.85 \times 10^{-12}\ Fm^{-1}$ (in a vacume and air) up to $80 \times \epsilon_0$ (in water). In the presence of a highly magnetised layer, the magnetic permeability may be many times greater than $\mu_0 = 1.2566 \times 10^{-6}\ Hm^{-1}$. If μ_0 is assumed, the resulting magnetised layer would be misinterpreted to be more resistive than it actually is (Kao & Orr, 1982). Thus, it is clear that this assumption could be inappropriate in highly magnetic or very wet environments.

Electromagnetic fields in the earth must not only obey Maxwell's equations, but also the appropriate conditions to be applied at boundaries between the homogeneous regions involved in the problem. Thus in order to fully specify the assumptions of the MT method, we state the boundary conditions below, given two regions, medium 1 and medium 2 (from Ward & Hohmann, 1987).

The normal component of $\underline{B}$, B_n, is continuous across an interface separating medium 1 and medium 2, i.e.,

$$B_{n1} = B_{n2}. \tag{2.9}$$

The normal component of $\underline{D}$, D_n, is discontinuous across an interface separating medium 1 and medium 2 due to the accumulation of a surface-charge density ρ_s, i.e.,

$$D_{n2} - D_{n1} = \rho_s. \tag{2.10}$$

The tangential component of $\underline{E}$, E_t, is continuous across an interface separating medium 1 and medium 2, i.e.,

$$E_{t1} = E_{t2}. \tag{2.11}$$

The tangential component of $\underline{H}$, H_t, is continuous across an interface separating medium 1 and medium 2 if there is no surface current, i.e.,

$$H_{t1} = H_{t2}. \tag{2.12}$$

The normal component of current density $\underline{J}$, J_n, is continuous across an interface separating medium 1 and medium 2, i.e.,

$$J_{n1} = J_{n2}. \tag{2.13}$$

The scalar potentials, appropriate to static fields, V and U defined by: $\underline{E} = -\nabla V$, and $\underline{H} = -\nabla U$, are continuous across an interface, i.e.,

$$V_1 = V_2 \text{ and } U_1 = U_2. \tag{2.14}$$

The modified Maxwell's equations, taking the assumptions above into account, may be transformed into the frequency domain:

$$-\frac{\partial \underline{B}(t)}{\partial t} = -i\omega \underline{B}(\omega) \tag{2.15}$$

$\nabla\cdot(\nabla \times \underline{A}) = 0$ for any vector field $\underline{A}$. We can take the divergence of equation 2.4.

$$\mu_0 \nabla\cdot(\sigma \underline{E}) = \mu_0(\sigma \nabla\cdot \underline{E} + \underline{E}\cdot \nabla\sigma) = 0 \tag{2.16}$$

it then follows from equation 2.1 that

$$\frac{q}{\epsilon_0} = -\underline{E}\frac{\nabla\sigma}{\sigma} \Rightarrow \frac{q}{\epsilon_0} = -\underline{E}\nabla \ln\sigma \tag{2.17}$$

resulting in the modified Maxwell's equations in the frequency domain:

$$\nabla \times \underline{E} = -i\omega \underline{B} \tag{2.18}$$

$$\nabla \times \underline{B} = \mu_0 \sigma \underline{E} \tag{2.19}$$

$$\nabla\cdot \underline{E} = -\underline{E}\nabla \ln\sigma \tag{2.20}$$

$$\nabla\cdot \underline{B} = 0 \tag{2.21}$$

using the proven vector field identity (where $\underline{F}$ is any vector)

$$\nabla \times (\nabla \times \underline{F}) = (\nabla\cdot \nabla\cdot \underline{F}) - \nabla^2 \underline{F} \tag{2.22}$$

We can then take the curl of equations 2.18 and 2.19 respectively, yielding

$$\nabla^2 \underline{B} = i\omega\mu_0\sigma \underline{B} + \mu_0 \underline{E} \times \nabla\sigma \tag{2.23}$$

$$\nabla^2 \underline{E} = i\omega\mu_0\sigma \underline{E} - \nabla(\underline{E}\nabla \ln\sigma) \tag{2.24}$$

In a homogeneous halfspace, the conductivity is constant, ($\nabla\sigma = \underline{0}$), and therefore equations 2.23 and 2.24 simplify to diffusion equations

$$\nabla^2 \underline{B} = i\omega\mu_0\sigma \underline{B} \tag{2.25}$$

$$\nabla^2 \underline{E} = i\omega\mu_0\sigma\underline{E} \tag{2.26}$$

These diffusion equations have solutions of the form

$$\underline{B} = \underline{B_1}e^{i\omega t - qz} + \underline{B_2}e^{i\omega t + qz} \tag{2.27}$$

$$\underline{E} = \underline{E_1}e^{i\omega t - qz} + \underline{E_2}e^{i\omega t + qz} \tag{2.28}$$

with complex wave number, q,

$$q = \sqrt{i\mu_0\sigma\omega} = \sqrt{\frac{\mu_0\sigma\omega}{2}} + i\sqrt{\frac{\mu_0\sigma\omega}{2}} \tag{2.29}$$

The real part of q governs the attenuation, and the inverse of the real part, is the skin depth (equation 2.8). However, assuming the earth does not generate electromagnetic energy (assumption ii), $\underline{B_2} = \underline{0}$ and $\underline{E_2} = \underline{0}$.

Inserting these solutions into equation 2.18, and assuming $E_y = 0$, produces

$$\nabla \times \underline{E} = \frac{\partial E_x}{\partial z} = -\sqrt{i\omega\mu_0\sigma}E_x \tag{2.30}$$

$$= -i\omega B_y, \tag{2.31}$$

from which can be derived what is known as the *Schmucker-Weidelt transfer function* (Weidelt, 1972; Schmucker, 1973)

$$C = \frac{1}{q} = \frac{1}{\sqrt{i\mu_0\sigma\omega}} = \frac{E_x}{i\omega B_y} = -\frac{E_y}{i\omega B_x} \tag{2.32}$$

Combining equation 2.32 with q yields,

$$\rho = \frac{1}{\sigma} = \frac{1}{|q|^2}\mu_0\omega = |C|^2\mu_0\omega, \tag{2.33}$$

and if $\underline{\underline{C}} = \frac{\underline{\underline{M}}}{i\omega}$,

$$\rho_{a,ij}(\omega) = \frac{\mu_0}{\omega}|M_{ij}(\omega)|^2 = \frac{1}{\mu_0\omega}|Z_{ij}(\omega)|^2 \tag{2.34}$$

Equation 2.34 provides us with what is known as the apparent resistivity, ρ_a (Ωm). It is termed the apparent resistivity because, except in a half-space, it is not the true resistivity, but an average resistivity for the volume being sensed at a given period. The impedance phase is the phase lead of the electric over the magnetic field and may be calculated using equation 2.35.

$$\phi_{ij}(\omega) = \tan^{-1}\left(\frac{\mathrm{Im}\{Z_{ij}(\omega)\}}{\mathrm{Re}\{Z_{ij}(\omega)\}}\right) \tag{2.35}$$

Equations 2.34 and 2.35 are not independent of each other. The apparent resistivity function (ρ_a) can in fact be predicted from the phase (ϕ) function, except for a scaling coefficient (Weidelt, 1972). MT data are most often presented as a plot of apparent resistivity and phase as a function of increasing period (T), such as is displayed in figure 2-2.

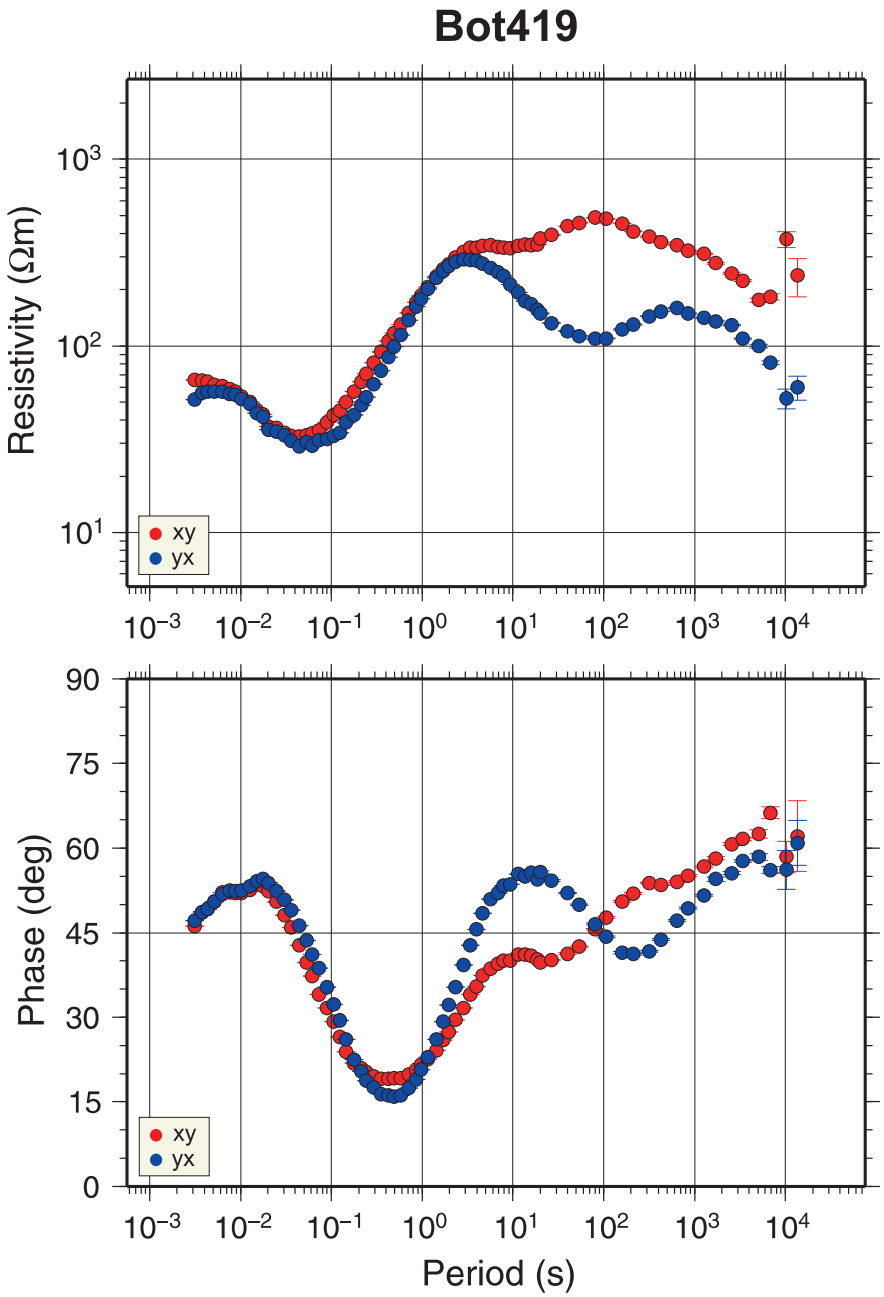

Figure 2-2: *An example of typical MT data (site: Bot419) as it is most commonly displayed; apparent resistivities and phases as functions of increasing period (a proxy for increasing depth) for the two off-diagonal elements (xy and yx).*

2.4 The impedance tensor

A magnetotelluric transfer function is, by definition, a function that relates the measured electromagnetic fields at given frequencies, and depends only on the electrical properties of the material and not the nature of the source. MT transfer functions are represented by impedance or magnetotelluric tensors.

The impedance tensor relates, for each frequency, the orthogonal horizontal electric (E_x, E_y) and magnetic (H_x, H_y, or equivalently: B_x/μ_0, and B_y/μ_0) fields. The impedance tensor, $\underline{\underline{Z}}(\omega)$, is thus a complex second-rank tensor, described by equation 2.36.

$$\begin{pmatrix} E_x(\omega) \\ E_y(\omega) \end{pmatrix} = \begin{pmatrix} Z_{xx} & Z_{xy} \\ Z_{yx} & Z_{yy} \end{pmatrix} \begin{pmatrix} B_x(\omega)/\mu_0 \\ B_y(\omega)/\mu_0 \end{pmatrix} \qquad or \quad \underline{E} = \underline{\underline{Z}}\ \underline{B}/\mu_0 \tag{2.36}$$

The magnetotelluric tensor, $\underline{\underline{M}}$ described by Weaver *et al.* (2000) is identical, except that it uses the $\underline{B}$ instead of the $\underline{H}$ fields to describe the relationship (equation 2.37).

$$\begin{pmatrix} E_x(\omega) \\ E_y(\omega) \end{pmatrix} = \begin{pmatrix} M_{xx} & M_{xy} \\ M_{yx} & M_{yy} \end{pmatrix} \begin{pmatrix} B_x(\omega) \\ B_y(\omega) \end{pmatrix} \qquad or \quad \underline{E} = \underline{\underline{M}}\ \underline{B} \tag{2.37}$$

$\underline{\underline{M}}$ and $\underline{\underline{Z}}$ are complex, and thus each component (M_{ij} and Z_{ij}) contain real and imaginary parts, i.e. they not only have a magnitude, but also a phase.

2.4.1 The tipper vector

The tipper vector, also known as the geomagnetic transfer function, is a dimensionless quantity, which is the representation of the ratio of the vertical to horizontal magnetic field components (equation 2.38).

$$H_z(\omega) = (T_x(\omega), T_y(\omega)) \begin{pmatrix} B_x/\mu_0 \\ B_y/\mu_0 \end{pmatrix} \tag{2.38}$$

The tipper vector is normally represented as induction vectors (more commonly described as induction arrows), the concept of which was first formulated by Parkinson (1959, 1962), and Wiese (1962). Induction arrows are essentially two real, dimensionless vectors, which represent the real and imaginary parts of the tipper vector on the xy plane (equations 2.39, and 2.40).

$$\underline{T}_{\mathrm{Re}}(\omega) = (\mathrm{Re}(T_x), \mathrm{Re}(T_y)) \tag{2.39}$$

$$\underline{T}_{\mathrm{Im}}(\omega) = (\mathrm{Im}(T_x), \mathrm{Im}(T_y)) \tag{2.40}$$

Lateral conductivity variations generate vertical magnetic fields, which means that induction arrows can be used to infer the presence or absence of lateral variations in conductivity (Jones & Price, 1970; Jones, 1986; Simpson & Bahr, 2005). The *Parkinson convention* (Parkinson, 1959), as opposed to the *Wiese convention* (Wiese, 1962), is the convention used by most practitioners, where the induction arrows point *towards* the anomalous current concentrations rather than *away* from them (Jones, 1986; Simpson & Bahr, 2005).

2.5 Possible cases of the impedance tensor

2.5.1 The 1D Earth

For a one-dimensional Earth (i.e. the conductivity changes only with depth), the diagonal components (Z_{xx} *and* Z_{yy}) of $\underline{\underline{Z}}$, which relate the parallel electric and magnetic fields, are zero. The off-diagonal terms (Z_{xy} *and* Z_{yx}) are the same since there are no lateral variations in conductivity, but are of different sign in order to preserve the right-hand rule. Thus, for the case of a 1D Earth, $\underline{\underline{Z}}$ can be represented by equation 2.41,

$$\underline{\underline{Z}}_{\mathrm{1D}}(\omega) = \begin{pmatrix} Z_{xx}(\omega) & Z_{xy}(\omega) \\ Z_{yx}(\omega) & Z_{yy}(\omega) \end{pmatrix} = \begin{pmatrix} 0 & Z_{xy}(\omega) \\ -Z_{xy}(\omega) & 0 \end{pmatrix}. \tag{2.41}$$

It is clear from equation 2.29 that the real and imaginary parts of Z_{ij} will have the same magnitudes for a homogeneous half-space (1D Earth). Additionally, $Z_{xy} = -Z_{yx}$, and the apparent resistivity is equal to the actual resistivity:

$$\rho_{a,ij(\omega)} = \frac{1}{\mu_0 \omega} \left| Z_{ij}(\omega) \right|^2 = \rho_{1D}, \tag{2.42}$$

Since the real and imaginary parts of the impedance have the same magnitude, and are the same for both of the off-diagonal terms, the impedance phase is equal to 45° for all ω for a half-space.

$$\phi_{1D}(\omega) = \tan^{-1}\left(\frac{\mathrm{Im}\{Z_{ij}(\omega)\}}{\mathrm{Re}\{Z_{ij}(\omega)\}}\right) = 45\,\mathrm{deg}, \tag{2.43}$$

$$\phi_{yx}(\omega) = \phi_{xy}(\omega) - \pi \tag{2.44}$$

It is worth noting that in the 1D case, given error-free MT data at all frequencies, there is a unique model that will fit the data (Tikhonov, 1965; Bailey, 1970; Weidelt, 1972; Parker, 1983).

2.5.2 The 2D Earth, and the fault model

For an Earth model where the conductivity varies with both depth and lateral extent, either a 2D or 3D interpretation is required. The conditions under which a body may be treated as 2D are explored by Jones (1983b). It is found that it depends largely on the length extent of the body (L) and the skin depth of the host rock (δ_h). If the the ratio $\frac{L}{\delta_h}$ is far greater than 1 for the frequency of interest, then a 2D interpretation of the structure should give approximately the correct conductivity structure. If the body is too short (small L) or the frequency too low (large δ_h), resulting in the ratio being smaller than 1, then a full 2D interpretation using both modes will not be valid and a 3D interpretation is necessary. A real world situation where a 2D model is appropriate could be for example, a crustal interpretation of a transect across a long (>200 km in length) fault structure that is in a fairly conductive environment (δ_h <100 km).

The 2D case is obviously more complex than the 1D case. Where there is a conductivity discontinuity, there will be a build up of charge. This build up of charge at a boundary, is a direct consequence of Ohm's law (equation 2.5, page 16) and the boundary condition, which requires the electric current density, $\underline{J}$, to be continuous across the boundary. It can be seen from equation 2.5 that if $\underline{J}$ must be continuous across the boundary, and σ is discontinuous (it has different values (σ_1 and σ_2) on either side of the boundary), then the electric field $\underline{E}$ across the boundary must be discontinuous, and have different amplitudes on either side of the boundary. This is achieved through the buildup of charge on the boundary surface. These charges then deflect or refract the electric field at the boundary. The amount of charge built up in shallower regions is larger than in deeper regions since the impinging current is more intense in shallower regions due to the skin depth effect. The boundary effect on electric current is well described by figure 2-3; note also that the current flows nearer to the surface on the more conductive side (σ_1) of the region. A current vortex is formed in the conductive side of the model (figure 2-3), and there are two vortices of opposite senses formed during each complete oscillation (Jones & Price, 1970). All components of $\underline{H}$ and the tangential components of $\underline{E}$ are continuous across a boundary (Jones & Price, 1970).

In the 2D case (figure 2-4), there is one lateral direction (defined as x) along which there are no field variations. The x direction in this case would represent what is known as the *geoelectric strike* or *strike* direction. For the ideal 2D case, electric and magnetic fields are mutually orthogonal, with electric fields parallel to the strike direction inducing magnetic fields only perpendicular to strike in the vertical plane, and magnetic fields parallel to the

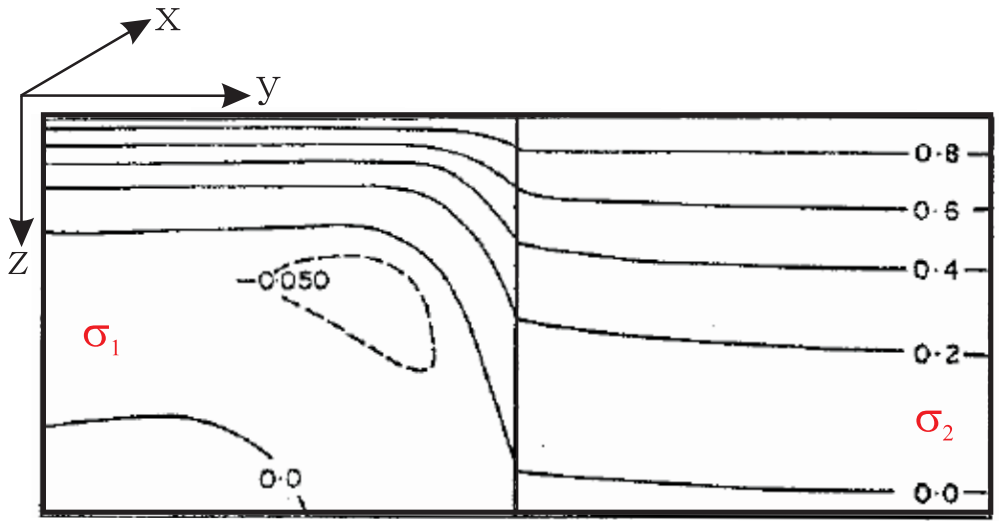

Figure 2-3: *Lines of E_y current flow (equivalent to contours of equal H_x) for the TM mode at a vertical conductivity boundary, for one instant in the oscillation period (1 second). $\sigma_1 = 10\sigma_2$. Modified from the numerical solution of Jones & Price (1970).*

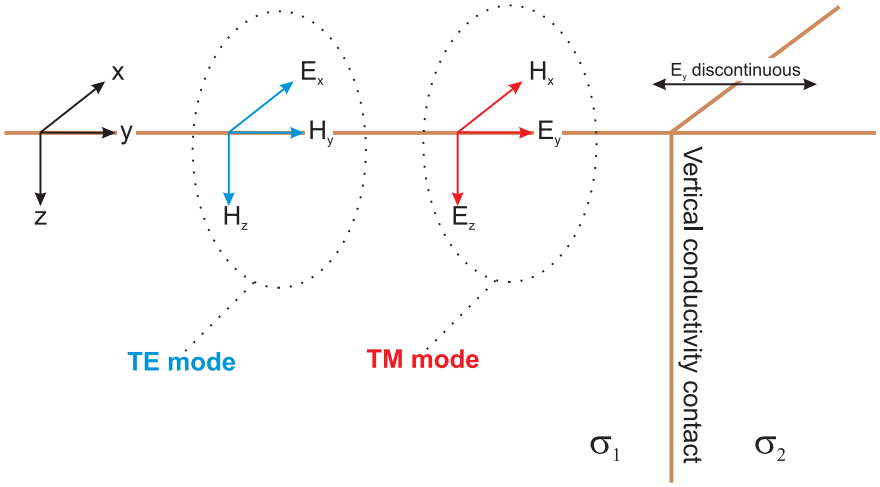

Figure 2-4: *A graphical description of a simple 2 quarter-space model, with different apparent resistivities meeting to form a vertical conductivity boundary. Due to the conservation of current across a boundary, E_y is discontinuous. In this idealised 2D case, the electromagnetic fields can be decoupled into what are known as the TE and TM modes. Redrawn and modified from Simpson & Bahr (2005)*

strike direction inducing electric fields only in the vertical plane perpendicular to strike. Under these circumstances, Maxwell's equations can be expanded, and decoupled into two modes, each mode relating 3 parts of the electric and magnetic field. One mode, known as the Transverse Electric (TE) mode or **E**-polarisation, is composed of E_x, B_y, B_z, and de-

scribes electric currents flowing parallel to the geoelectric strike (x in figure 2-4). The other mode known as the Transverse Magnetic (TM) mode or **B**-polarisation, is composed of B_x, E_y, E_z, and describes magnetic fields parallel to the geoelectric strike and electric currents flowing perpendicular to the geoelectric strike. The two polarisations may be described by:

$$\left.\begin{aligned} \frac{\partial E_x}{\partial y} &= \frac{\partial B_z}{\partial t} = \mathrm{i}\omega B_z, \\ \frac{\partial E_x}{\partial z} &= \frac{\partial B_y}{\partial t} = -\mathrm{i}\omega B_y, \\ \frac{\partial B_z}{\partial y} &- \frac{\partial B_y}{\partial z} = \mu_0 \sigma E_x, \end{aligned}\right\} \textit{TE mode.} \tag{2.45}$$

$$\left.\begin{aligned} \frac{\partial B_x}{\partial y} &= \mu_0 \sigma E_z, \\ \frac{-\partial B_x}{\partial z} &= \mu_0 \sigma E_y, \\ \frac{\partial E_z}{\partial y} &- \frac{\partial E_y}{\partial z} = -\mathrm{i}\omega B_x, \end{aligned}\right\} \textit{TM mode.} \tag{2.46}$$

The colour in equations 2.45 and 2.46 correspond to the colours used in the description of the two modes in figure 2-4. In the ideal 2D case, in strike coordinates, the impedance tensor can be described by equation 2.47.

$$\underline{\underline{Z}}_{\mathrm{2D}}(\omega) = \begin{pmatrix} 0 & Z_{xy}(\omega) \\ Z_{yx}(\omega) & 0 \end{pmatrix} = \begin{pmatrix} 0 & Z_{TE}(\omega) \\ Z_{TM}(\omega) & 0 \end{pmatrix}. \tag{2.47}$$

The diagonal elements are zero since the electric components are related to orthogonal magnetic components only. The off-diagonal elements (Z_{xy} and Z_{yx}) represent essentially the TE and TM modes respectively. They are normally different in magnitude, and have opposite sign. The opposite sign results in the xy and yx phases being in different quadrants (1st and 3rd). Note that the tipper vector (equations 2.38, 2.39, and 2.40) is only associated with the TE mode.

In the 2D case when the impedance tensor is not in strike coordinates, as is generally the case for recorded data, the diagonal components will not be zero, and the modes will be mixed up in the impedance tensor. However, it is possible to rotate the impedance tensor through an angle θ around a vertical axis using a Cartesian rotation matrix $\underline{\underline{R}}_\theta$ (equation 2.48) until the diagonal components of $\underline{\underline{Z}}$ are zero and the impedance tensor is in strike

coordinates, $\underline{\underline{Z}}_{2D}$ (equation 2.49).

$$\underline{\underline{R}}_{\theta} = \begin{pmatrix} \cos\theta & \sin\theta \\ -\sin\theta & \cos\theta \end{pmatrix} \text{, and } \quad \underline{\underline{R}}_{\theta}^{T} = \begin{pmatrix} \cos\theta & -\sin\theta \\ \sin\theta & \cos\theta \end{pmatrix}, \tag{2.48}$$

$$\underline{\underline{Z}}_{2D} = \underline{\underline{R}}_{\theta}\, \underline{\underline{Z}}_{obs}\, \underline{\underline{R}}_{\theta}^{T}. \tag{2.49}$$

$\underline{\underline{R}}_{\theta}^{T}$ is the transpose of the rotation matrix $\underline{\underline{R}}_{\theta}$, $\underline{\underline{Z}}_{obs}$ is the impedance tensor in the observational reference frame, and $\underline{\underline{Z}}_{2D}$ is the impedance tensor rotated through an angle θ to strike coordinates.

2.5.3 The 3D Earth

If the conductivity distribution varies in all three directions, no matter what the rotation angle, there will be no angle that results in the diagonal elements vanishing. It is also no longer possible to separate Maxwell's equations into two modes. The 3D Earth requires the determination of the four elements of the full impedance/MT tensor.

2.6 Electrical anisotropy

A substance that is electrically anisotropic has a variation of an electrical property depending on the direction in which it is measured (Sheriff, 1999). It is possible for Earth materials to have such properties for a number of reasons and in a number of circumstances which will be discussed in more detail in a later section. A rock could therefore have a resistivity structure such that the resistivity measured in the three orthogonal directions of a Cartesian coordinate system is different in all three directions. This may be represented by a resistivity matrix, $\rho(x, y, z)$,

$$\rho(x, y, z) = \begin{pmatrix} \rho_{xx} & \rho_{xy} & \rho_{xz} \\ \rho_{yx} & \rho_{yy} & \rho_{yz} \\ \rho_{zx} & \rho_{zy} & \rho_{zz} \end{pmatrix}. \tag{2.50}$$

which is symmetric and positive-definite (Pek & Verner, 1997). The symmetric and positive-definite conditions allow the matrix to be written as a diagonal matrix of three principal resistivities (ρ_1, ρ_2, and ρ_3, all positive) and three angles, which relate the orientation of the tensors principal axes to the reference frame used (e.g. (x', y', z') *to* (x, y, z)) (Heise

et al., 2006b). Pek & Verner (1997) use three angles in the Cartesian coordinate system (α_S, α_D, and α_L) known as the *strike*, *dip* and *slant* angles of the anisotropy respectively.

$$\rho(x,y,z) = \underline{\underline{R}}_z^T(\alpha_S)\underline{\underline{R}}_x^T(\alpha_D)\underline{\underline{R}}_{z'}^T(\alpha_L) \begin{pmatrix} \rho_1 & 0 & 0 \\ 0 & \rho_2 & 0 \\ 0 & 0 & \rho_3 \end{pmatrix} \underline{\underline{R}}_{z'}(\alpha_L)\underline{\underline{R}}_x(\alpha_D)\underline{\underline{R}}_z(\alpha_S), \tag{2.51}$$

$\underline{\underline{R}}$ is the Cartesian rotation matrix, $\underline{\underline{R}}^T$ is its transpose, and the subscript represents the axis about which the rotation occurs. The rotation angles are applied in the order α_S, α_D, then α_L around the z-axis for α_S, the x-axis for α_D, and then around the latest z-axis (z') for α_L.

Under the plane-wave assumption (assumption iv, page 17), there is no vertical magnetic field for induction in a 1D Earth. Horizontally varying magnetic fields diffusing downwards in the Earth will induce horizontal electric fields at right angles, which in turn drive the telluric currents. Therefore the primary current induced in a 1D Earth has only horizontal components. For this reason it is generally not possible to determine the full electrical anisotropy of a halfspace, and using the MT method it is only possible to measure the anisotropy of the principal resistivity matrix components projected onto the horizontal plane (Earth's surface). This means that we are unable to distinguish between horizontal anisotropy, and anisotropy that has a dip angle, but produces the same lateral anisotropy when projected onto the horizontal plane (Heise *et al.*, 2006b). It is important to note that using the MT method we are measuring a bulk resistivity, and therefore at great depth it is impossible to resolve the scale of the anisotropic structure (microscopic or macroscopic) (Wannamaker, 2005). Typically, and in a similar manner to the seismic anisotropy approach, electrical anisotropy is represented by the direction of maximum conductivity, ϕ_E, which is either parallel or perpendicular to the geoelectric strike direction. The magnitude is often represented by the phase difference, $\delta\theta$, between the two off-diagonal elements of the impedance tensor. A small phase difference indicates a 1D environment, while a larger phase difference would indicate 2D or 3D regional structures or anisotropy. Electrical anisotropy measurements, for a given site, for a given frequency or depth, are therefore commonly represented as a vector, aligned in the conductive direction, and scaled by the phase difference between the off-diagonal elements of the phase tensor.

It is worth mentioning here the recent study by Heise *et al.* (2006b). They demonstrate through modelling that MT phase split is a result of the vertical resistivity contrast in a 1D situation, and that given an anisotropic half-space there will be no phase split, with the

only information that there is an anisotropic region present contained in the amplitude of the MT response. It is for this reason that taking the maximum phase split when doing our calculations (discussed later) is more robust.

2.7 Distortion: the problem

Small-scale or near-surface conductivity inhomogeneities distort the magnetotelluric impedance tensor in three ways (Groom & Bahr, 1992):

1. They produce the well-known static shift effects sometimes observed on sounding curves.

2. If the underlying conductivity structure is 2D, then the two regional impedance's are mixed in an arbitrary coordinate system. This results in a change in shape and level of the sounding curve and distortion of the phase curves.

3. At sufficiently high frequencies (short periods) for the size of the distorting body, the inhomogeneity generates, through induction, anomalous magnetic fields that, in turn, alter the background phases.

These small-scale, or near-surface, inhomogeneities are either not of interest to the MT practitioner, who is more concerned with the larger-scale, deeper structures, or the inhomogeneities are too spatially undersampled to allow interpretation. The small-scale inhomogeneities are necessarily near the surface; otherwise they would merely contribute to the effective bulk response.

Distortion effects can be viewed as inductive and galvanic, although these effects are not entirely separate. If the time-varying magnetic field induces currents that flow in a closed loop, a secondary magnetic field is induced, which adds to the primary magnetic field. This secondary magnetic field is the inductive distortion effect, which decreases in proportion to the regional inductive response with increasing period (point three above) (Groom & Bahr, 1992). Due to flux of the regional currents through small-scale conductivity heterogeneities, surface charges build up at the boundaries, which produce an electrostatic field (similar to what was described in the previous section "The 2D Earth and the fault model"), resulting in the channelling or distorting of the regional currents. This is the galvanic distortion component (points one and two above), which may persist to the longest periods (Jones, 1988), and may also be a result of topographic effects (Jiracek, 1990). The problem of current channelling, as this distortion is often referred to, can therefore be associated with the

existence of charge distributions on conductivity discontinuities (Jones, 1983b), of which the magnetic effects can be ignored at sufficiently long periods (Chave & Jones, 1997) due to their magnitude, but the electric field effects are comparable with the other electromotive forces present. Price (1973) called these charges the *villains of the piece*. The currents are most strongly perturbed when the gradient of the electrostatic potential (scalar, not vector) is of the same order of magnitude as the normal electric field (Jones, 1983b).

As is well demonstrated by Chave & Smith (1994), magnetic field distortion can be important in a decomposition analysis, particularly at higher frequencies (shorter periods). Magnetic distortion decays with increasing period, hence declining in importance as period increases. Chave & Smith (1994) demonstrate, using an example of data collected in Canada, that the electric galvanic distortion decomposition does not sufficiently describe the distortion model at higher frequencies, and that it is necessary to incorporate both the electric and magnetic field galvanic distortion into the model to adequately describe the distortion affecting the response. This is especially important in the decomposition of seafloor MT data.

The distortion effect of the electric field can mathematically be represented by a real, frequency-independent 2×2 matrix, $\underline{\underline{C}}$.

$$\underline{\underline{C}} = \begin{pmatrix} C_{xx} & C_{xy} \\ C_{yx} & C_{yy} \end{pmatrix}. \tag{2.52}$$

Where the inductive distortion effects, and those due to the magnetic effects of the charges, may be neglected, the measured impedance tensor may then be described by equation 2.53.

$$\underline{\underline{Z}}_{obs} = \underline{\underline{R}}_{\theta}\, \underline{\underline{C}}\, \underline{\underline{Z}}_{2D}\, \underline{\underline{R}}_{\theta}^{T}. \tag{2.53}$$

where $\underline{\underline{Z}}_{obs}$ is the measured/observed impedance tensor in acquisition coordinates, $\underline{\underline{Z}}_{2D}$ is the regional impedance tensor in strike coordinates, $\underline{\underline{C}}$ is the telluric distortion tensor, and $\underline{\underline{R}}_{\theta}$ is the rotation tensor.

The problem of distortion of the impedance tensor is exactly that, a problem. It is a problem caused by our inability to model the Earth at all scales, from electrode separation scale (tens of meters) to hundreds of kilometers. There have been many concerted efforts to counter, characterise, and identify the problem of distortion and its effects in 1D, 2D, and 3D, some of which will be described in a later section. The techniques have included

mathematically, statistically, and physically based ideas; however, none have proved ideal and this remains a significant challenge for the MT practitioner, particularly for the 3D problem.

2.8 Data acquisition

The collection of MT data involves the recording of fluctuations in the natural horizontal electric and ideally both horizontal and vertical magnetic fields. There are a number of types of instrumentation available to make these measurements. In the SAMTEX experiment we used Phoenix Geophysics' broadband MTU5 and MTU5A instruments, which use coil magnetometers. At some sites we also used instruments known as LIMS, borrowed from the Geological Survey of Canada (GSC). The LIMS recorded for longer and use fluxgate magnetometers that are sensitive to longer periods, aiding us in gaining very long period data at some of the sites. The electrodes that were used for both of these systems were non-polarising lead, lead-chloride (Pb-$PbCl$) electrodes.

Once permission from the landowner to install the MT site has been attained, a suitable location is sought. An ideal site would be far from human interference, far from electrical noise (e.g., DC train lines and electric fences), and in an area with minimal topography and soil that is easy to excavate (for the sake of a happy field crew). Figure 2-5 (page 32) is a compilation of photographs taken during the field work in South Africa and Botswana, which portray the instrumentation and practicalities of field work. There are two common layout possibilities for an MT site (in an L or + design). In this project the instrumentation has been installed in a layout described schematically in figure 2-6 (page 33). Four of the electrodes are oriented geographically north-south and east-west, and buried typically 50 metres from the ground electrode. They are all buried in a hole, in mud made with salt water to gain a low contact resistance with the ground. The magnetometers are also orientated north-south and east-west, and levelled. The three magnetometers (north-south, east-west, and vertical) are all then buried to keep them stable and to help reduce temperature effects on the readings. Any remaining cable from the electrodes or magnetometers is laid out uncoiled to avoid inductive coupling.

The station is then left to recorded the time varying electric and magnetic fields, an example of which is given in figure 2-7 (page 34). Due to the difficulty in digging holes at this site, the vertical magnetic field sensor could not be buried, and so only the horizontal

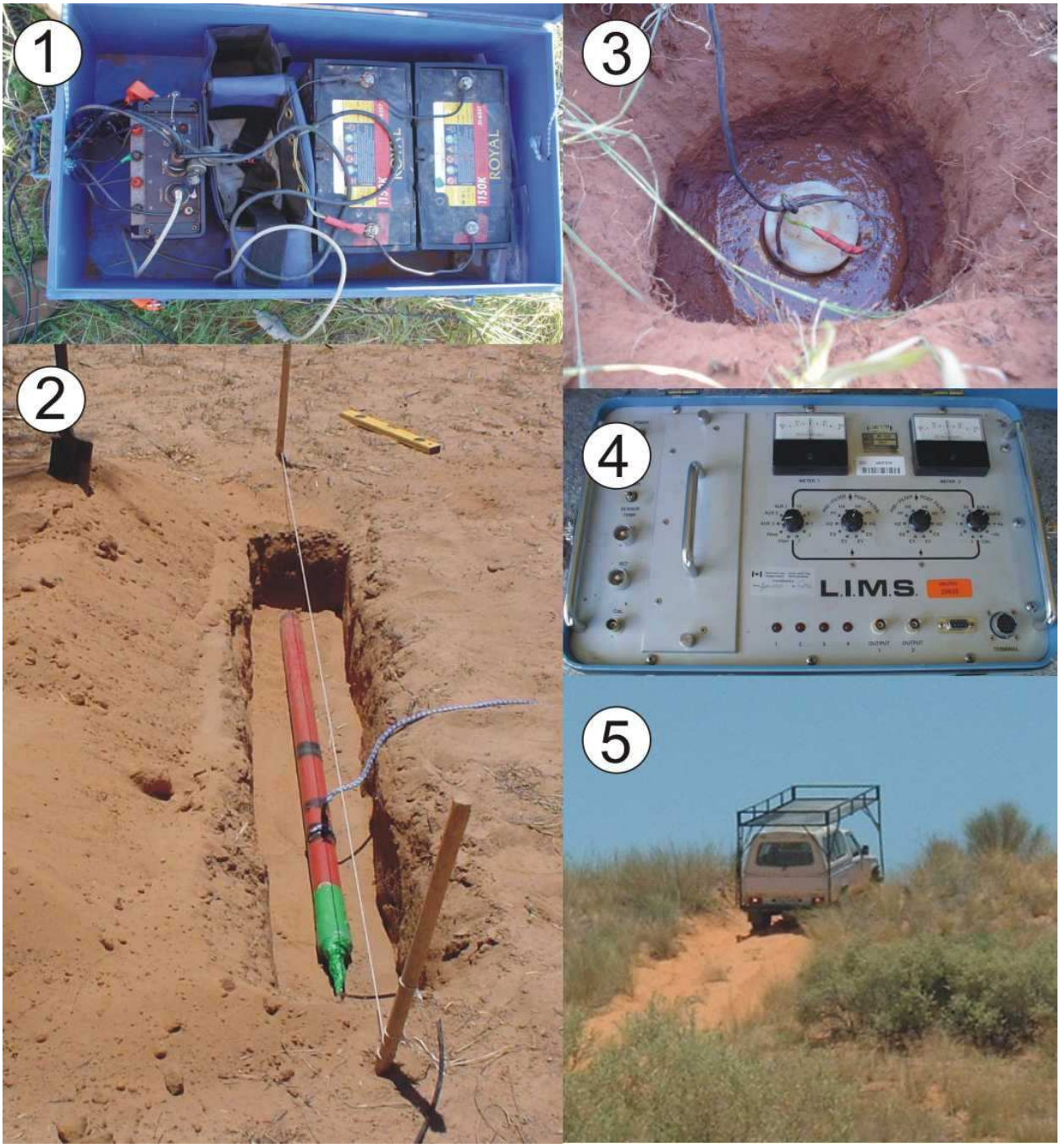

Figure 2-5: *Typical instruments and field work. 1: A Phoenix MTU5A recording unit, with batteries. 2: A broadband coil (magnetometer) levelled, orientated, and ready to be buried. 3: A lead-lead chloride non-polarising electrode in mud, and ready to be buried. 4: A LIMS recording unit. 5: A lot of rather interesting driving.*

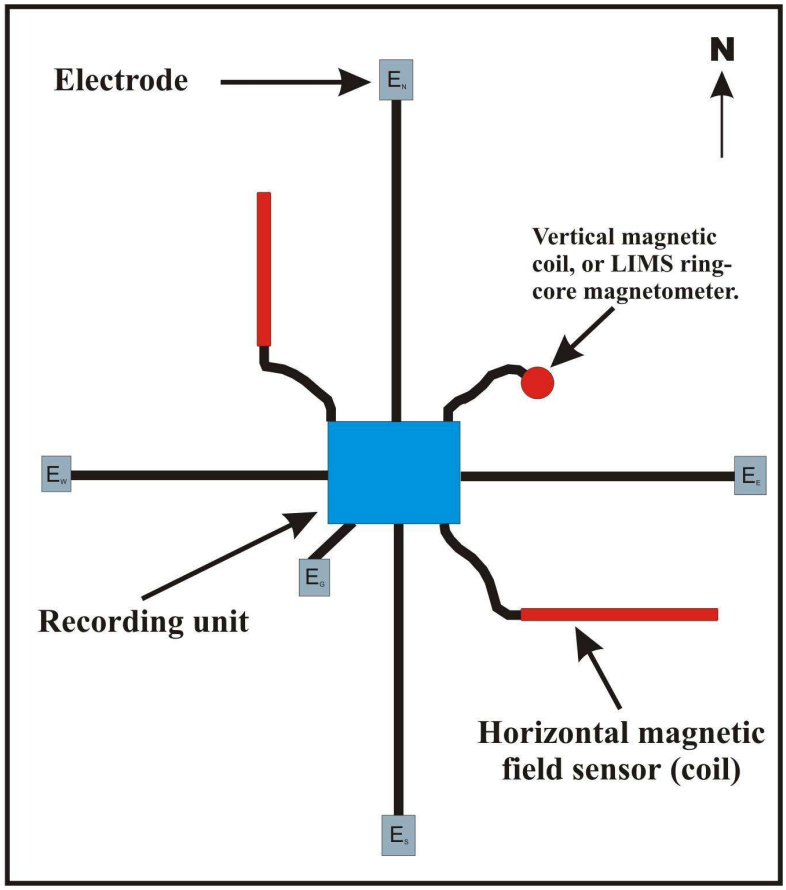

Figure 2-6: *A schematic plan view of a typical Broadband MT station layout, with 2 photos on the left of Samtex fieldwork*

magnetic fields were measured. Broadband MT stations were left to record for 2 to 3 days, while the long period systems were left recording for approximately 4 to 6 weeks.

2.9 Data processing

The electrical and magnetic field fluctuations that are measured are now routinely processed using robust processing techniques (e.g., Jones *et al.*, 1989; Egbert, 1997; Chave & Thomson, 2004) in order to gain what is known as a MT response function that is in the form of an impedance tensor. It is in this area of the MT method, along with inversion, that the largest strides have been made in recent years due largely to progress in the computing power available to practitioners. Robust processing codes are termed as such because they aim through statistical means to be unbiased toward the noise and non-plane-wave components contained in the recorded signal. The source of noise (a common problem in MT data) depends on the environment where the study is taking place; however, common examples of

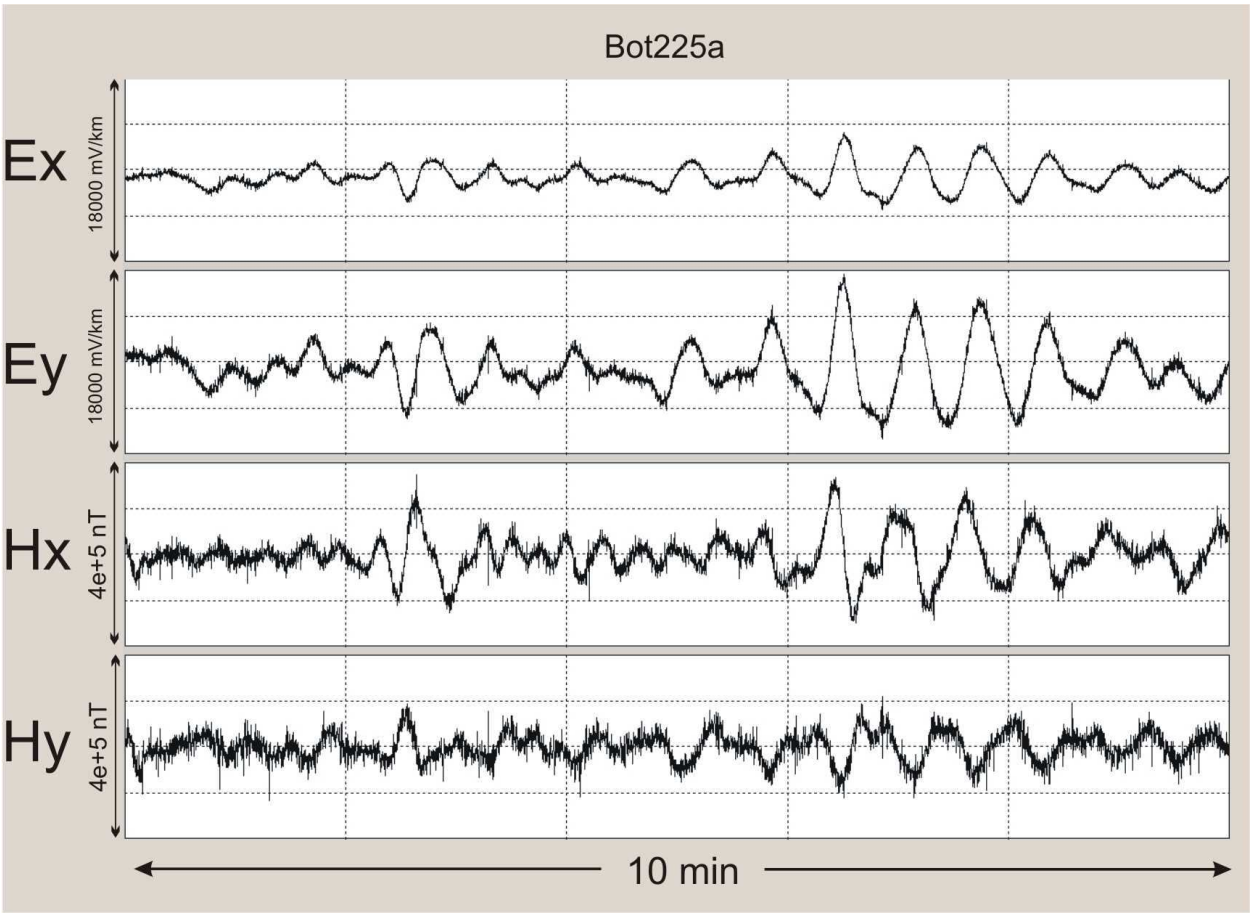

Figure 2-7: *Typical recorded time series for an MT site. 10 minutes recording of Ex, Ey, Hx, and Hy. Hz was not recorded for this site.*

noise sources include DC train lines, generators, mining activity, and the like. Jones *et al.* (1989) demonstrate the importance of using robust processing techniques as well as the use of a remote reference field. The general steps for the processing of MT data are outlined below.

2.9.1 Pre-conditioning

The first step in the processing of MT data is the transform of the data from the time domain to the frequency domain. In order to achieve this, it is necessary to pre-condition the data to reduce the effect of trends, remove severe noise (spikes), and to reduce the effects caused by having data of finite length. The pre-conditioning splits the time series into segments, the size of which depends on the period band being calculated. The more segments there are, the better the statistical results will be later in the processing sequence. Pre-conditioning is

normally done with a windowing function such as a Hanning or Hamming window.

2.9.2 Conversion to the frequency domain

Once pre-conditioned, the windowed data are converted to the frequency domain, normally using either a Fourier Transform (either Fast Fourier Transform or Discrete Fourier Transform), or a wavelet transform. Each field component of the recorded data must be calibrated with respect to the particular instrument's sensitivity. Some instrument calibrations (e.g., induction coil sensor) are frequency-dependent, and therefore the calibrations need to be applied as such, while others (e.g., the fluxgate magnetometer) are frequency-independent. Ideally six to ten frequencies per decade are evaluated; more are unnecessary because the dispersion relation of Weidelt (1972) predicts similar results for neighbouring frequencies, however fewer could result in aliasing in the frequency domain (Simpson & Bahr, 2005).

Once in the frequency domain, we have a raw power spectrum for each time segment for each channel (E_x, E_y, B_x, B_y, and B_z), from which the 6-10 evaluation frequencies per decade are chosen. The auto and cross spectra for each time segment, which are essentially the products of the field components and their complex conjugates (e.g., $B_x(\omega) \cdot B_x^*(\omega)$, $B_y(\omega) \cdot B_x^*(\omega)$, $B_z(\omega) \cdot B_x^*(\omega)$, $E_x(\omega) \cdot B_x^*(\omega)$, $E_y(\omega) \cdot B_x^*(\omega)$, etc.), for each evaluation frequency (ω) are then calculated (Marti, 2006). These spectra are stored in what is termed a *spectral matrix* (e.g., equation 2.54), for each evaluation frequency. For the same evaluation frequency, there will be a number of spectral matrices, resulting from each time segment that is processed. These spectral matrices are stacked for each evaluation frequency, and may be selected by hand (where noise-free time windows are observed) or weighted using statistical techniques.

$$
\begin{array}{ccccc|c}
B_x & B_y & B_z & E_x & E_y & \\
\hline
B_x \cdot B_x^* & B_x \cdot B_x^* & B_x \cdot B_x^* & E_x \cdot B_x^* & E_y \cdot B_x^* & B_x \\
 & B_y \cdot B_y^* & B_z \cdot B_y^* & E_x \cdot B_y^* & E_y \cdot B_y^* & B_y \\
 & & B_z \cdot B_z^* & & & B_z \\
 & & & E_x \cdot E_x^* & E_y \cdot E_x^* & E_x \\
 & & & & E_y \cdot E_y^* & E_y
\end{array}
\tag{2.54}
$$

2.9.3 Estimation of Transfer Functions

Transfer functions, also known as earth response functions, are calculated to remove noise and to provide us with intuitively meaningful output, such as an impedance tensor (a type of transfer function). Equations 2.36 and 2.38 can be expanded to:

$$E_x(\omega) = Z_{xx}(\omega) \cdot H_x(\omega) + Z_{xy}(\omega) \cdot H_y(\omega), \tag{2.55}$$

$$E_y(\omega) = Z_{yx}(\omega) \cdot H_x(\omega) + Z_{yy}(\omega) \cdot H_y(\omega), \tag{2.56}$$

$$H_z(\omega) = T_x(\omega) \cdot H_x(\omega) + T_y(\omega) \cdot H_y(\omega). \tag{2.57}$$

In order to solve these equations for the impedance tensor and tipper vector, they are multiplied by their complex conjugates. If the remote reference processing method (first introduced by Gamble *et al.* (1979)) is being utilised, whereby there are simultaneous measurements made at a distance from the recorded site, it is possible to remove uncorrelated noise between the stations. In order to do this, the remote horizontal magnetic field complex conjugates are used instead of the locally recorded ones. The magnetic rather than the electric fields are normally used because the horizontal magnetic fields are more homogeneous and usually less affected by noise. Of course correlated noise will remain. Equations 2.55, 2.56, and 2.57 can be solved using the following equations whose parameters are elements of the spectral matrix calculated in the previous step.

$$Z_{xx} = \frac{\langle E_x R_x^* \rangle \langle H_y R_y^* \rangle - \langle E_x R_y^* \rangle \langle H_y R_x^* \rangle}{DET}, \tag{2.58}$$

$$Z_{xy} = \frac{\langle E_x R_y^* \rangle \langle H_x R_x^* \rangle - \langle E_x R_x^* \rangle \langle H_x R_y^* \rangle}{DET}, \tag{2.59}$$

$$Z_{yx} = \frac{\langle E_y R_x^* \rangle \langle H_y R_y^* \rangle - \langle E_y R_y^* \rangle \langle H_y R_x^* \rangle}{DET}, \tag{2.60}$$

$$Z_{yy} = \frac{\langle E_y R_y^* \rangle \langle H_x R_x^* \rangle - \langle E_y R_x^* \rangle \langle H_x R_y^* \rangle}{DET}, \tag{2.61}$$

and for the induction vector elements,

$$T_x = \frac{\langle H_z R_x^* \rangle \langle H_y R_y^* \rangle - \langle H_z R_y^* \rangle \langle H_y R_x^* \rangle}{DET}, \tag{2.62}$$

$$T_y = \frac{\langle H_z R_y^* \rangle \langle H_x R_x^* \rangle - \langle H_z R_x^* \rangle \langle H_x R_y^* \rangle}{DET}, \tag{2.63}$$

where

$$DET = \langle H_x R_x^* \rangle \langle H_y R_y^* \rangle - \langle H_x R_y^* \rangle \langle H_y R_x^* \rangle,$$

and R_x^*, and R_y^* are either local or remote complex conjugate magnetic fields.

It should be noted that since there are four possible series that relate the horizontal magnetic and electric fields, any two of which may be used to form the auto-spectra and cross-spectra, there are six possible estimates for each of the four impedance tensor elements, although two are unstable in the 1D case (Sims *et al.*, 1971). Since generally the electric fields are far noisier than the magnetic fields, the estimate for each element provided above is usually the least biased, and statistically the best. It is worth noting that if there is noise in H, then DET will be large, resulting in impedance estimates being under-estimated.

There are a number of processing codes available, both commercial and free (e.g., Egbert & Booker, 1986; Egbert, 1997; Chave & Thomson, 2004), that will perform differently depending on the nature and quantity of the noise contained within the recorded signal. If the noise contamination is coherent between the local and remote station, then remote reference processing will not remove this. If the noise contamination (signal to noise ratio) is poor enough, it is possible that robust processing codes could regard the signal as noise, since there is less of it, and merely enhance the noise by rejecting signal. It is often a worthwhile exercise to apply more than one processing code to MT data, or to portions of data for a given site as some times during recording may be quieter (less noise) that others. Additionally, there are a number of parameters in the different codes that may be adjusted and altered (coherence thresholds, etc.) to suit and characterise the nature of the noise contamination in the signal. Processing of MT data is a time consuming task, that is as much detective work and trial-and-error as it is an art.

2.10 Distortion analysis and removal

The problem of distortion was discussed in a previous section. In order to remove distortion effects, and to gain a better understanding of the geoelectric dimensionality and directionality inherent in the data, the data are analysed with what is commonly described as distortion analysis. There are a number of different methods for this analysis and consequently there are a number of reviews on the subject, and how the problem may be tackled (e.g., Jiracek, 1990; Groom & Bahr, 1992; Groom *et al.*, 1993; McNeice & Jones, 2001). The basic ele-

ments obtained from the various approaches, although in different forms, generally represent a regional strike estimation, a measure of the anisotropy, a measure and description of the galvanic distortion that effects the measurement, and an estimation of the distortion free impedance tensor. However, some methods, such as the Phase tensor (Caldwell *et al.*, 2004), do not produce these elements, but are useful for characterising the dimensionality and distortion inherent in the impedance tensor.

In the following two subsections, the Groom-Bailey (Groom & Bailey, 1989) decomposition (referred to as GB decomposition from here on) and the phase tensor analysis (Caldwell *et al.*, 2004) are described. The GB decomposition is one of the most commonly used decomposition techniques, whereas the phase tensor, although not a decomposition technique, is a recently developed diagnostic and characterisation technique. These are by no means the only techniques available; others include Swift (1967), Weaver *et al.* (2000), and Bahr (1988), and there are constant efforts being made to improve these existing techniques, as well as to solve the problem of distortion removal in a 3D environment (e.g. Utada & Munekane, 2000; Garcia & Jones, 2001).

2.10.1 Groom-Bailey decomposition

Proposed by Bailey & Groom (1987), the GB decomposition technique requires the distortion to be real and frequency independent, with electric distortion considered to be of greatest significance rather than magnetic distortion. GB aims to separate the local 3D distortion from the regional 1D or 2D response by factorising the measured impedance tensor into a rotation matrix, $\underline{\underline{R}}_\theta$, a distortion tensor, $\underline{\underline{C}}$, and the regional 2D impedance tensor, $\underline{\underline{Z}}_{2D}$, as described by equation 2.53.

This method of distortion analysis is often preferred by practitioners not only because it gives physically-based meaning to the parametrisation (a few other methods do too), but also because the parametrisation is in terms of determinable and indeterminable parts. No other method separates the determinable from indeterminable parameters. The distortion tensor is itself factorised into a product of three tensors: *twist*, $\underline{\underline{T}}$, *shear*, $\underline{\underline{S}}$, *local anisotropy*, $\underline{\underline{A}}$, and a scaling or *gain* factor, g (equation 2.64).

$$\underline{\underline{C}} = g\,\underline{\underline{T}}\,\underline{\underline{S}}\,\underline{\underline{A}}. \tag{2.64}$$

The *twist*, *shear*, and *anisotropy* may be represented by equations 2.65, 2.66, and 2.67 respectively, where t, e, and s are real values. In general decomposition, there are nine

unknown parameters (regional strike, the four components of the distortion tensor, and the two complex regional impedance's), and we only have eight data (the four complex values of the impedance tensor). *Twist* and *shear* are the determinable parts of the distortion, while *anisotropy* and the *gain* factor, g, are, in the GB factorisation, indeterminable,

$$\underline{\underline{T}} = \frac{1}{\sqrt{1+t^2}} \begin{pmatrix} 1 & -t \\ t & 1 \end{pmatrix}, \tag{2.65}$$

$$\underline{\underline{S}} = \frac{1}{\sqrt{1+e^2}} \begin{pmatrix} 1 & e \\ e & 1 \end{pmatrix}, \tag{2.66}$$

$$\underline{\underline{A}} = \frac{1}{\sqrt{1+s^2}} \begin{pmatrix} 1+s & 0 \\ 0 & 1-s \end{pmatrix}. \tag{2.67}$$

As can be seen from equation 2.65 the effect of the *twist* tensor is to rotate the electric field vectors through a clockwise twist angle $\phi_{twist} = \tan^{-1} t$. The *shear* tensor develops anisotropy on axes that bisect the principal axes of the regional induction, thereby "shearing" the fields. The magnitude of *shear* is normally characterised by a shear angle $\phi_{shear} = \tan^{-1} e$ which, if we consider intuitively the effect of the shear operator (equation 2.66), would not be meaningful for angles greater than 45°. Thus, it is reasonably required that $|e| \leq 1$, and therefore ϕ_{shear} cannot exceed 45°. The *anisotropy* tensor, also known as the *splitting* tensor, simply stretches the two field components by different factors. These effects are shown graphically in figure 2-8.

With nine unknowns and only eight knowns, the problem is underdetermined. However, the gain and anisotropy factors are indeterminable, and are absorbed into the regional impedance response, reducing the number of unknown parameters and allowing for a unique solution, albeit with a scaled regional impedance. The parameters of the distortion model are solved for simultaneously. The absorption of g and $\underline{\underline{A}}$ into $\underline{\underline{Z}}_{2D}$ results in a regional impedance tensor, in which the apparent resistivity curves are shifted by an unknown scaling factor. The shapes of the apparent resistivity and impedance phase curves are unchanged. A least-square fitting procedure is used to try to fit the measured data with a model. The accuracy of fit of the model to the data is measured by the χ^2 misfit term (Groom & Bailey, 1989), which is a misfit parameter calculated from the data, the data errors, and the data modelled by the decomposition.

McNeice & Jones (2001) extended GB decomposition. In their extension, a global minimum is sought to determine an appropriate geoelectric strike direction and distortion pa-

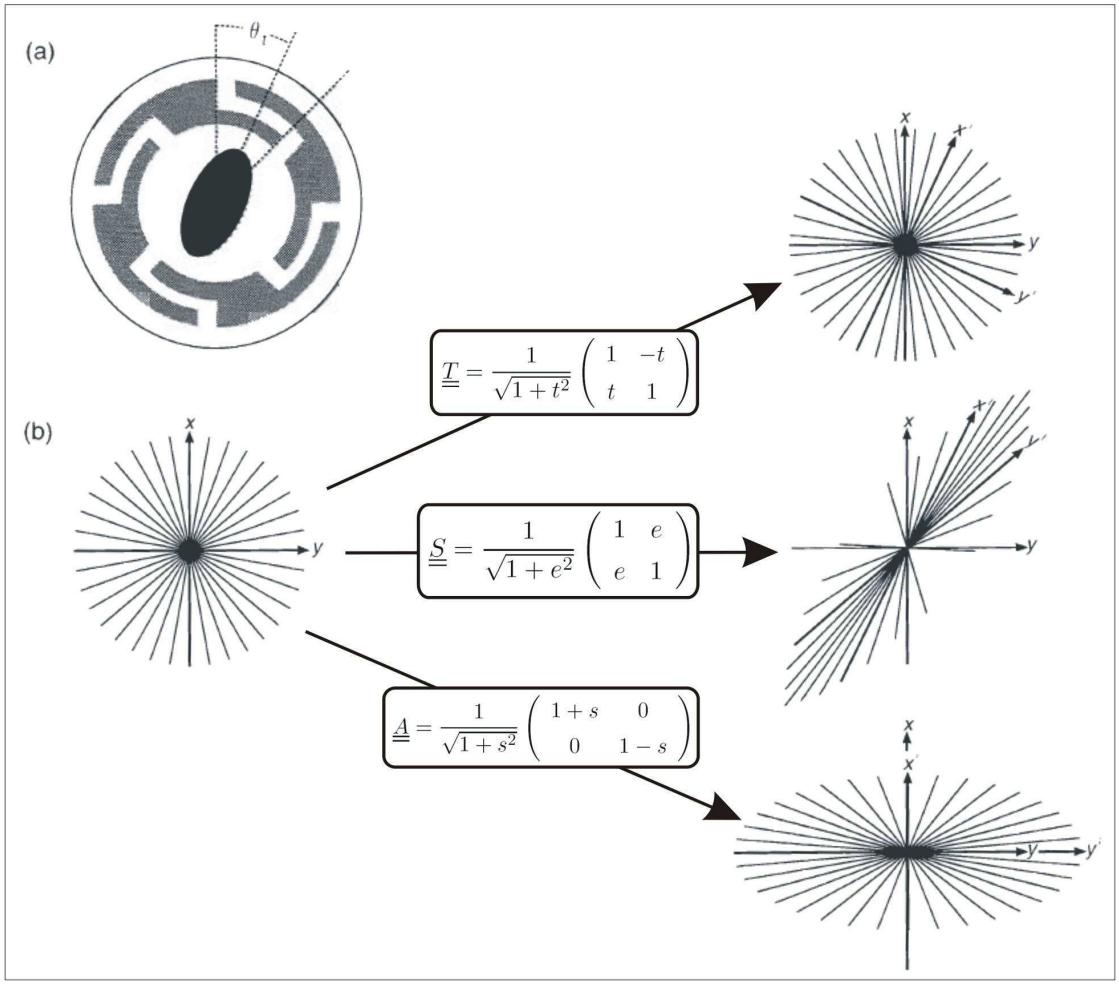

Figure 2-8: *(a) A contrived example of distortion. Conductive overburden (grey), on an insulating substratum (white). Inside the circular region of overburden is an elliptical and highly conducting region (black), such as a swamp. Measurements are made at the centre of the swamp. The swamp first twists the telluric currents through an angle θ_t, its local strike. The anomalous environment then imposes shear and anisotropy effects on the data. (b) A group of unit vectors (left) which have had the twist, shear, and anisotropy tensors (equations 2.65, 2.66, and 2.67 respectively) applied to them (right). Modified from Simpson & Bahr (2005), originally from Groom & Bailey (1989).*

rameters for a range of frequencies and a set of sites. This is useful when trying to find an appropriate strike direction for a profile to be modelled in 2D. The method has been written as a computer program called *Strike* and is freely available (McNeice & Jones, 2001).

The resulting output of the GB decomposition is a geoelectric strike direction (although this has 90°ambiguity) and a regional impedance tensor that may be used for modelling,

although a further correction is necessary due to the scaling of the apparent resistivity curves.

2.10.2 The MT Phase Tensor

Caldwell *et al.* (2004) give the first published description of the MT phase tensor method. The main advantage of this method is that there are no assumptions about the dimensionality of the regional structure; it is valid even where both the distorting heterogeneity and regional structure are 3D. The biggest disadvantage of the method is that it does not help the MT practitioner to recover an undistorted impedance tensor. However, recently efforts have been made instead to model the phase tensor estimates themselves (Heise *et al.*, 2006a).

It can be shown that the phase relationships in the impedance tensor are a second-rank tensor. The phase tensor expresses how the phase relationships change with polarisation. Unlike the impedance tensor, in the presence of purely electric effects of galvanic distortion, it preserves the regional phase information, even when the impedance tensor from which it is calculated is affected by galvanic distortion.

Assuming $\underline{\underline{X}}$ is the real part of the impedance tensor, and $\underline{\underline{Y}}$ is the imaginary part of the impedance tensor, the impedance tensor can be written $\underline{\underline{Z}} = \underline{\underline{X}} + i\ \underline{\underline{Y}}$. If the regional impedance tensor is $\underline{\underline{Z}}_R = \underline{\underline{X}}_R + i\ \underline{\underline{Y}}_R$, then the distorted real part may be written $\underline{\underline{X}} = \underline{\underline{C}}\ \underline{\underline{X}}_R$, and the distorted imaginary part may be written $\underline{\underline{Y}} = \underline{\underline{C}}\ \underline{\underline{Y}}_R$. Equation 2.68 demonstrates that the observed and regional phase tensors are identical and independent of the galvanic distortion tensor, $\underline{\underline{C}}$, viz.,

$$\begin{aligned}
\underline{\underline{\Phi}} &= \underline{\underline{X}}^{-1}\ \underline{\underline{Y}}, \\
&= (\underline{\underline{C}}\ \underline{\underline{X}}_R)^{-1}\ (\underline{\underline{C}}\ \underline{\underline{Y}}_R), \\
&= \underline{\underline{X}}_R^{-1}\ \underline{\underline{C}}^{-1}\ \underline{\underline{C}}\ \underline{\underline{Y}}_R, \\
&= \underline{\underline{X}}_R^{-1}\ \underline{\underline{Y}}_R, \\
&= \underline{\underline{\Phi}}_R.
\end{aligned} \tag{2.68}$$

The phase tensor may be written in the Cartesian coordinate system in terms of real and imaginary parts of $\underline{\underline{Z}}$ (equation 2.69)

$$\begin{bmatrix} \Phi_{11} & \Phi_{12} \\ \Phi_{21} & \Phi_{22} \end{bmatrix} = \frac{1}{\det(X)} \begin{bmatrix} X_{22}Y_{11} - X_{12}Y_{21} & X_{22}Y_{12} - X_{12}Y_{22} \\ X_{11}Y_{21} - X_{21}Y_{11} & X_{11}Y_{22} - X_{21}Y_{12} \end{bmatrix}, \tag{2.69}$$

where $\det(X) = X_{11}X_{22} - X_{21}X_{12}$ is the determinant of $\underline{\underline{X}}$. Through singular or principal value decomposition, the phase tensor may be represented as the product of three matrices (equation 2.70) (Caldwell *et al.*, 2004),

$$\underline{\underline{\Phi}} = \underline{\underline{R}}^T(\alpha - \beta) \begin{bmatrix} \Phi_{max} & 0 \\ 0 & \Phi_{min} \end{bmatrix} \underline{\underline{R}}(\alpha + \beta), \tag{2.70}$$

where $\underline{\underline{R}}(\alpha + \beta)$ is a rotation matrix (equation 2.71), and $\underline{\underline{R}}^T$ is its transpose or inverse,

$$\underline{\underline{R}}(\alpha + \beta) = \begin{bmatrix} \cos(\alpha + \beta) & \sin(\alpha + \beta) \\ -\sin(\alpha + \beta) & \cos(\alpha + \beta) \end{bmatrix}. \tag{2.71}$$

The expressions for α and β (also known as the skew angle) are represented by equations 2.72 and 2.73 respectively.

$$\alpha = \frac{1}{2}\tan^{-1}\left(\frac{\Phi_{12} + \Phi_{21}}{\Phi_{11} - \Phi_{22}}\right), \tag{2.72}$$

$$\beta = \frac{1}{2}\tan^{-1}\left(\frac{\Phi_{12} - \Phi_{21}}{\Phi_{11} + \Phi_{22}}\right). \tag{2.73}$$

The phase tensor may be characterised by three coordinate invariants (three independent scalar quantities that are independent of the coordinate system used to express the tensor). The phase tensor coordinate invariants used by Caldwell *et al.* (2004) are β, Φ_{max}, and Φ_{min}. The coordinate invariants Φ_{max} and Φ_{min} may be characterised by equations 2.74 and 2.75 respectively. The skew angle, β, is a measure of the tensor's asymmetry in the regional MT response. The angle α expresses the tensor's dependence on the coordinate system. The expression α, along with β, Φ_{max}, and Φ_{min} (the three coordinate invariants), completely define the tensor,

$$\Phi_{max} = (\Phi_1^2 + \Phi_3^2)^{1/2} + (\Phi_1^2 + \Phi_3^2 - \Phi_2^2)^{1/2}, \tag{2.74}$$

$$\Phi_{min} = (\Phi_1^2 + \Phi_3^2)^{1/2} - (\Phi_1^2 + \Phi_3^2 - \Phi_2^2)^{1/2}, \tag{2.75}$$

where $\Phi_1 = (\Phi_{11} + \Phi_{22})/2$, $\Phi_2 = [\det(\Phi)]^{1/2}$, and $\Phi_3 = (\Phi_{12} - \Phi_{21})/2$.

The phase tensor may be plotted graphically as an ellipse, as is shown in figure 2-9, for each frequency of each site. The direction of the major axis of the ellipse is given by the angle $\alpha - \beta$, which defines the relationship of the tensor to the observer's reference frame

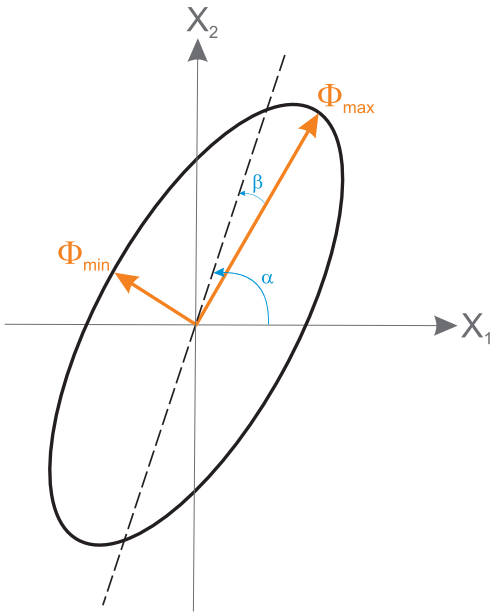

Figure 2-9: *The graphical representation of the phase tensor, redrawn from Caldwell* et al. *(2004). The ellipse may be described by the three coordinate invariants* Φ_{max}, Φ_{min}, β *(should it be non-symmetric), and the angle* α.

(X_1, X_2) (Caldwell *et al.*, 2004).

In the 1D case, $\Phi_{max} - \Phi_{min}$ should be zero, and the phase tensor ellipse will be represented by a circle. In the 2D case, $\Phi_{max} - \Phi_{min}$ will not be zero, and the phase tensor will be represented by an ellipse. However, in 2D the phase tensor is symmetric, and therefore the skew angle (β) will be zero. In 3D, the phase tensor is not symmetric, and accordingly, β will be non-zero. Hence, in an analysis, a large value for β will indicate that the conductivity structure of the subsurface is 3D. Caldwell *et al.* (2004) found that a small value of β does not necessarily mean the regional structure is not 3D, and it is necessary to also look at the variation in direction of the major axis of the tensor ellipse with period and location. If this direction is constant, it likely indicates a 2D conductivity structure; however if it is variable, it may indicate the region is 3D.

In summary, the principal axes of the phase tensor ellipse (Φ_{max}, Φ_{min}) indicate the horizontal directions of the maximum and minimum induction current, which reflects lateral variations in the conductivity structure (Caldwell *et al.*, 2004). The phase tensor skew angle (β), and the variations in the directions of the major axis of the tensor ellipse give an indication of whether the case is 3D or 2D.

2.11 Modelling and Inversion of MT data

The ultimate aim of acquiring MT data is to gain a better understanding of the conductivity structure of the subsurface in order to relate this to geology and Earth processes. The most common and visual means of gaining an idea of the conductivity structure of the subsurface is through modelling and inversion of MT response estimates. Once distortion has been removed from the data, and the dimensionality inherent in the data has been analysed (using methods such as GB decomposition and Phase tensor analysis), the next step is to apply a modelling and inversion technique suitable for the particular dataset.

The aim is therefore to find a 1D, 2D, or 3D model where conductivity variations with depth and lateral extent (in 2D and 3D) would produce, through the propagation of electromagnetic fields in the model in accordance with Maxwell's equations, model responses at the surface of the model, such that they are consistent with the observed MT responses. These model responses are normally in the form of apparent resistivities and phases, and a misfit between the observed and model responses are normally presented as an RMS misfit.

There are two methods for creating this model: forward modelling and inversion. Forward modelling is now routine, and may be readily calculated for any of 1D, 2D, or 3D conductivity structures, using a variety of codes such as: Wannamaker *et al.* (1987), finite elements method; Mackie *et al.* (1993), finite-difference method, some of which even allow for the calculation of the responses over a model with electrically anisotropic regions (e.g., Pek & Verner, 1997) also a finite-difference method.

The problem of trying to fit measured data with forward modelled data manually is that finding a model that fits your data can be an incredibly time consuming trial-and-error task, particularly for 3D models. Many inversion techniques try to do this task automatically, through a combination of forward modelling and minimisation of the misfit between the observed responses and the forward model responses. The forward model is adjusted until a minimum misfit is found between the observed and modelled responses.

Inversion of MT data is common, although almost exclusively for 1D and 2D problems. Three-dimensional inversion, although huge strides have been made in recent years, remains very much in the development stages. There are a number of 2D inversion codes available, which are commonly used among MT practitioners (e.g. REBOCC, Siripunvaraporn & Egbert (2000), ABIC, Uchida & Ogawa (1993), RLM2DI, Rodi & Mackie (2001), also imple-

mented in the software WinGlink, produced by Geosystem srl.). Normally, in the 2D case, MT responses that have had distortion removed are all rotated to the regional geoelectric strike coordinate system and 2D inversion is performed on the data for a selected profile. It has been generally observed (SAMTEX, 2005) that, for a given dataset, the larger features remain consistent in the inversion, regardless of the inversion technique used, although there are smaller features that may differ.

The technique of 3D inversion of MT data is still in its infancy. It is being largely restricted by computing power available, and testing with synthetic data is still an important part of the development. A major step in its development occurred with the release to the public (i.e. open-source code) of 3D MT inversion code by Siripunvaraporn *et al.* (2005). Prior to this, most 3D inversion code has been developed and tested by a select few, or was only commercially available. Surely the release of this code to the public can only aid in the progression of techniques of 3D inversion. However, we are still by no means near a stage where we are able to invert for large datasets of experimental MT data, and for the time being, the majority of MT practitioners will be restricted to creating interpretive models using 2D inversion software, and 3D forward models.

3

Seismic anisotropy theory

3.1 What is seismic anisotropy?

Seismic body waves (P-waves and S-waves) travel through the interior of the Earth. Propagation velocity of P-waves, V_P,

$$V_P = \sqrt{\frac{K + \frac{4}{3}\mu}{\varrho}} \tag{3.1}$$

and S-waves, V_S,

$$V_S = \sqrt{\frac{\mu}{\varrho}} \tag{3.2}$$

depends on density, ϱ, and the elastic moduli of a material. The bulk modulus, K, is defined as the pressure increase needed to produce a given relative decrease in volume, while the shear modulus, μ, is defined as the ratio of the shear stress to the shear strain. P-waves (compressional waves) are sensitive to both the bulk modulus (incompressibility), and shear modulus (rigidity), whereas S-waves (transverse waves) are sensitive to the shear modulus only.

Seismic velocity anisotropy is the property of a material that causes seismic wavefields to propagate at different velocities in different directions. In an anisotropic medium, wave

propagation is more complicated. There are three plane waves that propagate with different speeds and perpendicular polarisations. These polarisations are no longer strictly parallel or perpendicular to the direction of energy propagation, which leads to the three waves often being referred to as the quasi-P and quasi-S waves (Savage, 1999). Seismic velocity anisotropy may be broadly separated into two categories. *Azimuthal anisotropy*, which effects both compressional and shear waves, refers to velocity variations with azimuth around a measurement location (station). Wave speeds measured at such a station would have a variation dependent on the backazimuth[1]. *Polarisation anisotropy* refers to the property that causes shear and surface wave speeds to differ for different polarisations of the wave travelling along the same path or direction.

There are five seismic methods that yield information on anisotropy in the Earth. These include: looking at relative arrival/delay times (generally compressional P-waves, but also S-waves); receiver functions (RF's); Pn anisotropy; surface waves; and shear wave splitting (SWS). Each of these techniques has had varying amounts of usage; some are still in the development stages, whereas others, such as shear wave splitting, are well studied. Fouch & Rondenay (2006) give a concise summary of these different techniques and their relative strengths and weaknesses, summarised in table 3.1, with their sampling regions portrayed schematically in figure 3-1. In this study however, we are concerned only with shear wave splitting anisotropy from teleseismic events.

3.1.1 What are SKS and shear waves?

When looking at shear wave splitting of phases such as SKS, SKKS, or PKS, we are looking at teleseismic shear waves that have passed through the Earth's core, along paths described in figure 3.2(a). An SKS wave travels from its source to the Earth's liquid outer core as a S-wave, where it would be converted to a P-wave as it travels through the outer core (by convention an outer core P-wave is called a K phase). S-waves cannot travel through the core since it is liquid, and the shear modulus is equal to zero in a liquid. When the SK wavefront emerges at the other side of the core, part of it is converted back to an S-wave that travels to the Earth's surface, which is what would be observed as an SKS wavefront at a seismic observation station. SKKS waves travel a similar path, but have an additional internal reflection as a P-wave off the core-mantle boundary (CMB). When they are observed at stations on the Earth's surface, SKS and SKKS waves have near-vertical incidence (figure

[1]The direction from the seismic station towards a seismic source, clock-wise from north

Table 3.1: *A brief summary of the various advantages and disadvantages of techniques used for calculating continental seismic anisotropy. The techniques are: shear wave splitting (SWS); receiver functions (RF's); surface waves; looking at relative arrival/delay times (arrival times); and Pn anisotropy.*

Property	**SWS**	**RF's**	**Surface waves**	**Arrival times**	**Pn anisotropy**
Horizontal resolution	very good	very good	poor	good	poor
Vertical resolution	very poor	The best of these techniques.	Good to 300 km		Good, but only samples just beneath the crust-mantle boundary.
Other advantages	Given adequate coverage, dipping and multiple layers of anisotropy may be extracted.			Can gain some constraints on dipping axes of anisotropy. Simple to compute.	Direct estimate of uppermost mantle with limited uncertainty as to depth location.
Other disadvantages	Sufficient data coverage requires lengthy recording periods	It is a non-linear and underdetermined problem, requiring simplifying assumptions.	First-order phase velocity signal can be explained by either lateral isotropic variations, or by anisotropic parameters.	Stringent data coverage requirement	

3-1). Although SKS, SKKS, and PKS are the most commonly used phases for shear wave splitting analysis, there are other phases which may be used. Generally the phases that are used are limited to those that fall within the *shear wave window* (those waves with angles of incidence less than 35°) to avoid complications due to nonlinear particle motion. Additionally, epicentral distances, such that the relevant phases are either the first arrival, or arrive such that they are not contaminated by other phases arriving at the same time, are necessary. Figure 3.2(a) is a graphical representation of the paths taken by these and other teleseismic waves. Their predicted traveltimes as a function of epicentral distance is displayed in figure 3-3, which is based on the IASP91 standard Earth velocity model of Kennett & Engdahl (1991). The epicentral distance is the angle subtended at the centre of the Earth between the source epicenter and seismic recording station positions. There are many other phases that are not shown in the figure for clarity, but which may also interfere with these arrivals.

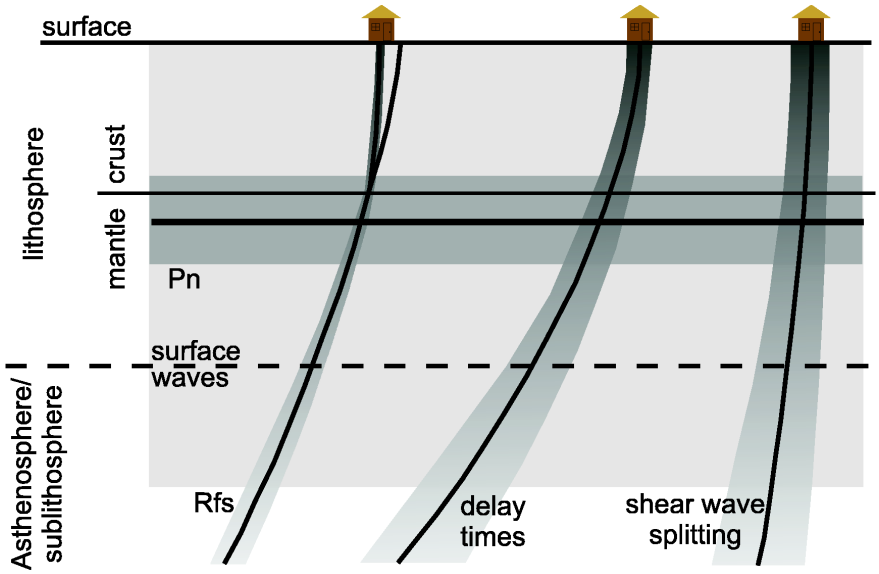

Figure 3-1: *A schematic portrayal of raypaths and their sampling regions for the seismic anisotropy analyses described in table 3.1. Shaded areas represent sampling areas, including relative Fresnel zone volumes (not to scale). From Fouch & Rondenay (2006)*

3.2 Seismic SKS shear wave splitting

Early work on shear wave splitting of long period converted waves was undertaken by Vinnik *et al.* (1984) and Kind *et al.* (1985), and further advanced by Silver & Chan (1988) and Vinnik *et al.* (1988) (unfortunately Vinnik *et al.* (1984) and Vinnik *et al.* (1988) are not easily accessible, as they are written in Russian). The SKS shear wave splitting method relies on the birefringence properties of near-vertical incidence shear waves. The incident S-wave, upon entering the anisotropic medium is split into two orthogonally polarised S-waves, with different velocities (described schematically in figure 3.2(b) for the more complex 2-layer case). The amount of birefringence is the fractional difference between these two velocities (Sheriff, 1999).

Birefringent splitting, also called *double refraction*, that occurs in seismic waves may be described in much the same manner as that of optical anisotropy. Light entering an anisotropic medium (e.g., a crystal of calcite) is split into two refracted light rays polarised at right angles to one another. Each polarisation encounters a different refractive index (i.e., travels at a different velocity), which results in the phenomenon of double refraction. The classic example of this would be the double image that is produced when a piece of the mineral calcite is placed over an image. This property of optical anisotropy is used in optical

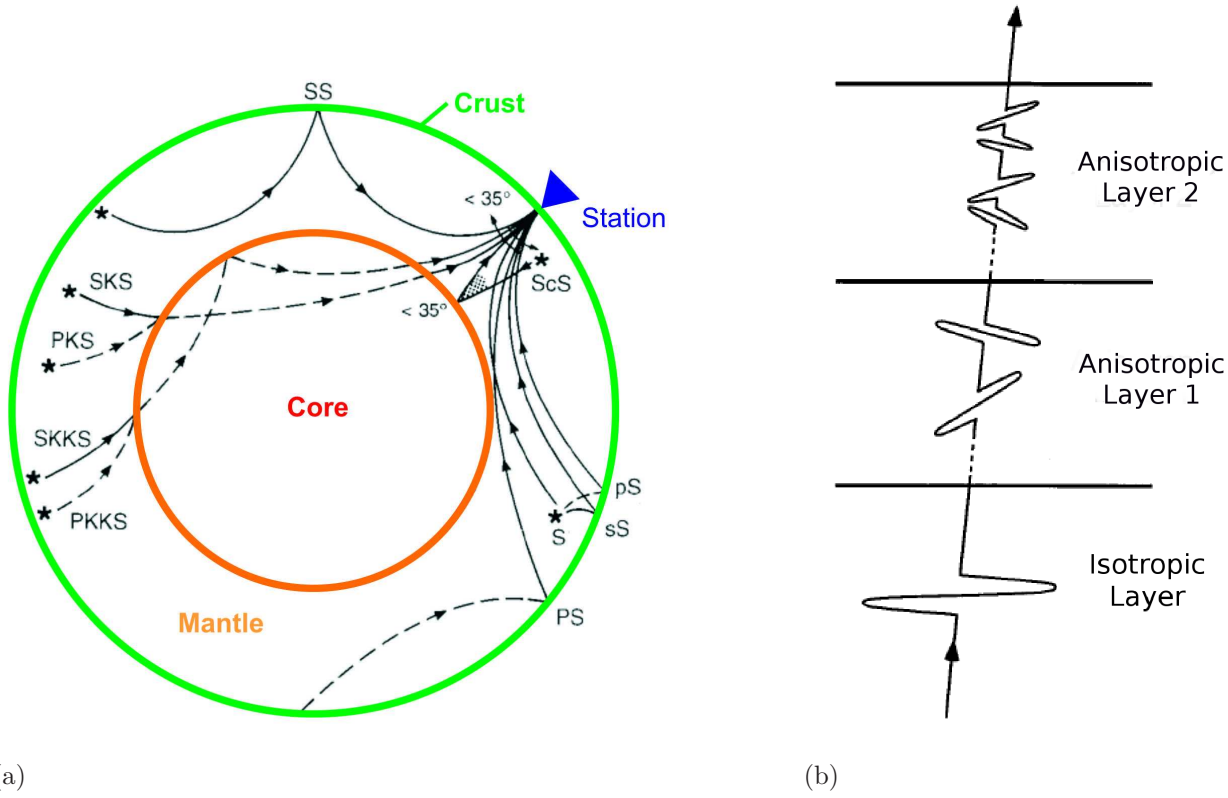

(a) (b)

Figure 3-2: *(a) Figure describing seismic wave paths through the Earth that have been used for shear wave splitting studies. Solid lines represent S path segments, while dotted lines represent P path segments. Modified from Savage (1999). (b) Schematic diagram of shear wave splitting in the case of two anisotropic layers. From Yardley & Crampin (1991).*

mineralogy in conjunction with a polariser for mineral identification.

In its most simple form, the time delay (δt) between the fast and slow polarised seismic waves passing through an anisotropic medium may be defined as:

$$\delta t = L(\frac{1}{V_{S1}} - \frac{1}{V_{S2}}), \tag{3.3}$$

where L is the length of the anisotropic path that is traversed by the wave, and V_{S1} and V_{S2} are the propagation velocities for the fast and slow polarisations respectively for the direction of propagation through the medium. Thus, it is these three factors (L, V_{S1} and V_{S2}) that determine the amount of splitting observed between the fast and slow shear waves at a station. This may also be represented as an anisotropy percentage (A_S):

$$A_s = 200(V_{S1} - V_{S2})/(V_{S1} + V_{S2}), \tag{3.4}$$

Seismic shear wave anisotropy is generally characterised by the the measured values of a

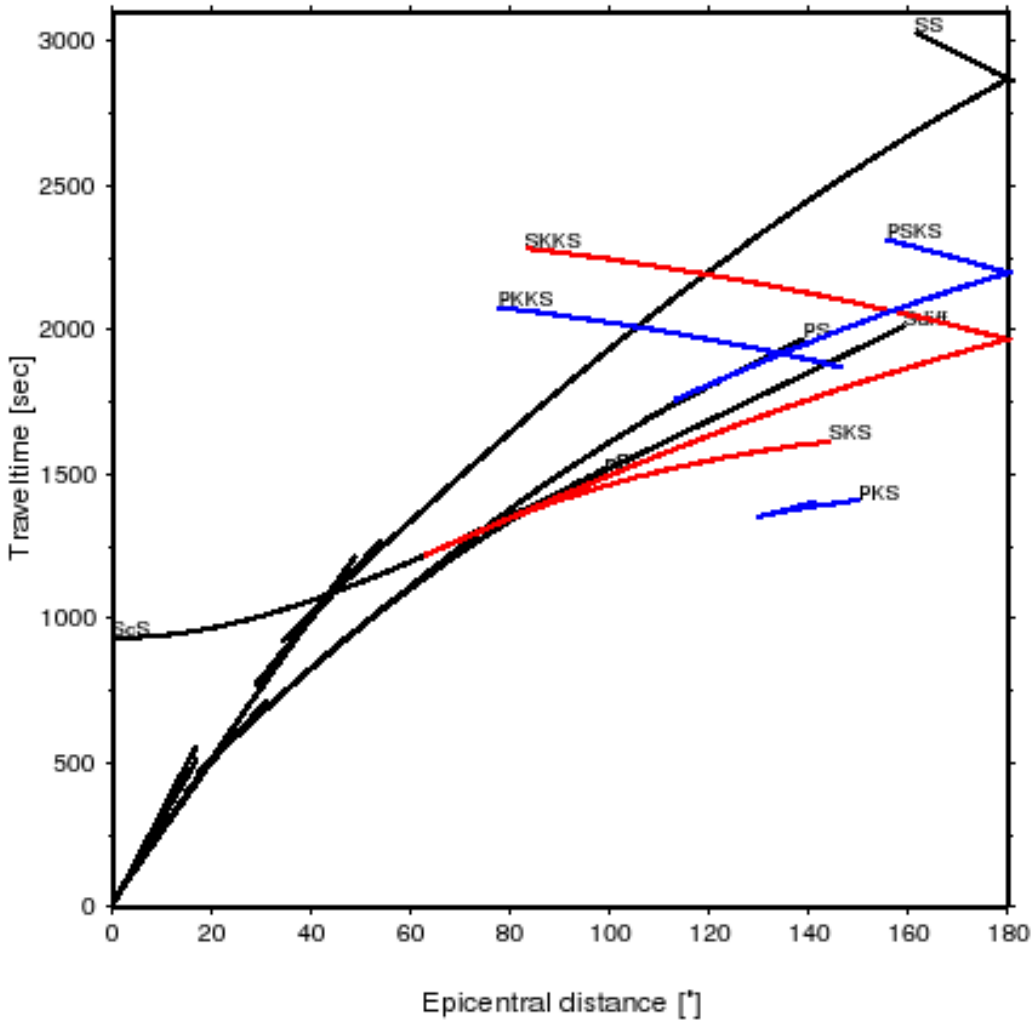

Figure 3-3: *Predicted traveltimes plotted versus epicentral distance, for the IASP91 standard Earth velocity model (Kennett & Engdahl, 1991), for the phases described in figure 3.2(a). Taken from Do (2006).*

fast-axis direction ϕ_a (same direction as V_{S1}) and either a delay time δt_a or anisotropy percentage A_s. In some cases a shear wave may be visually observed to have been split into two polarisations. This occurs when the wavelength of the split shear waves are smaller than the delay time δt (more common in higher frequency local S waves), and/or the anisotropic layer has a very high anisotropy magnitude. In such cases the horizontal components of the observed seismograms may be rotated around an azimuth until the fast or slow azimuth is attained, where the fast shear wave is seen only on the fast component and the slow shear wave is seen entirely on the slow component. Thus, the fast-axis and delay time between the two shear waves are easily quantified. In cases where this is not the case and the two

waves are not distinct, more sophisticated techniques are necessary for the splitting analysis (discussed later). It should be noted that for an incident shear wave polarised in the same direction as the fast or slow polarisation direction of an anisotropic layer, no splitting would be observed since only the fast or slow shear wave occurs. These measurements, where there is no splitting, are usually termed *null* measurements.

Thus, the technique appears very simple at first; however, there are many complicating factors. If the symmetry system is one of transverse anisotropy with a horizontal symmetry axis and one layer, then the observations would be relatively straightforward. Given a different symmetry system, e.g., one with a dipping symmetry axis, or a situation with multiple layers or lateral variations, observations become far more complicated and more difficult to unravel.

Given multiple layers of anisotropy, the shear wave would be split twice, once by the first (lower) layer, into 2 shear waves, then again by the second (upper) layer, which would split each of the S-waves from layer one again, resulting in four individual waves being observed at the receiver (figure 3.2(b)). However, these four individual arrivals are often unresolvable, and a single apparent fast axis direction, ϕ_a, and a single apparent delay time, δt_a, would be observed (Silver & Savage, 1994). In a two layer anisotropic system such as this, measured under the assumption of a single layer, the apparent fast axis direction and the apparent delay time would produce, as a function of backazimuth, systematic variations with a $\pi/2$ periodicity (figure 3-4).

Figure 3-4 displays the $\pi/2$ periodicity observed in the splitting parameters as a function of backazimuth for two cases of two-layer anisotropy. These are synthetic results calculated using the method of Silver & Savage (1994), and illustrate the need for excellent backazimuthal coverage in order to distinguish between single layer and two layer anisotropy, as well as the need for even better coverage to be able to determine which layer is on top. Given very good coverage however, Silver & Savage (1994) demonstrate that properties of observed splitting parameters measured under the assumption of one layer of anisotropy, when there are in fact two layers, can still have meaning, and be related in a straightforward manner to the splitting parameters of two layers.

Rümpker & Silver (1998) show, through modelling, the complexity of backazimuthal variations in splitting parameters. While the models they test still show the 90° periodicity shown by Silver & Savage (1994), Rümpker & Silver (1998) show that in using different initial

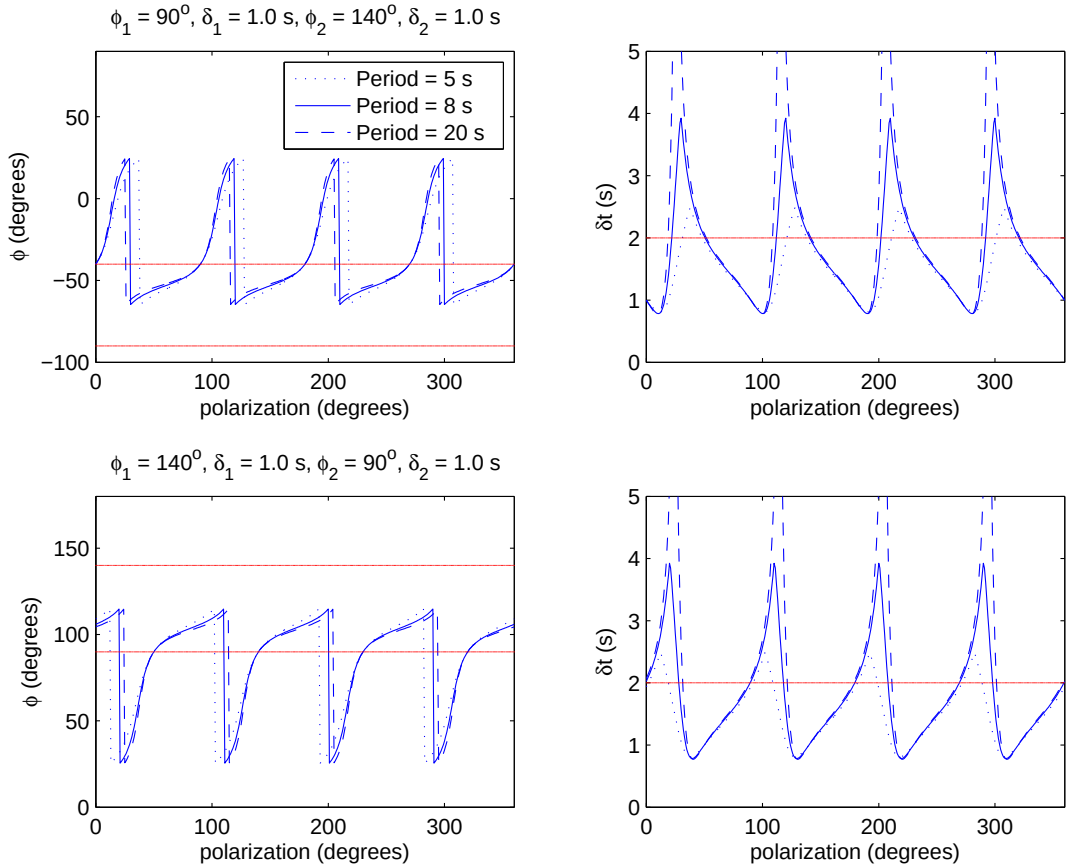

Figure 3-4: *Curves for predicted apparent splitting parameters (ϕ_a, δt_a) as a function of incoming polarisation direction. The first case (top two graphs) has ϕ_1=90°(-90°) (bottom layer) and ϕ_2=140°(-40°) (top layer), $\delta t_1 = \delta t_2 = 1.0$ s. The second case (bottom two graphs) is the same as the first, except that ϕ_1 and ϕ_2 are reversed: ϕ_1=140°(-40°) (bottom layer) and ϕ_2=90°(-90°) (top layer). Straight lines are ϕ_1 and ϕ_2, while curved lines are the analytic results at periods of 5 s, 8 s, and 20 s (Silver & Savage, 1994). Example taken from Silver & Savage (1994), recalculated and replotted.*

polarisations, multiple anisotropic layers, and smoothly varying fast axis directions within an anisotropic layer, the backazimuthal patterns are quite variable. Additionally, they note that the difference in splitting parameters recovered between a two layer model and a single layer model with a smoothly varying fast axis direction can be virtually indistinguishable. However, at higher frequencies they may be distinguishable since a two layer model would produce four distinct arrivals, whereas the smoothly varying model would only produce two distinct arrivals. Finite-difference modelling of laterally varying anisotropy by Rümpker & Ryberg (2000) demonstrate that lateral variations produce a 180° periodicity in splitting parameters as a function of backazimuth, which also occurs at near-vertical incidence for

anisotropic layers with an inclined symmetry axis (Rümpker & Ryberg, 2000).

A caution worth raising is that in order to obtain an adequate backazimuthal coverage, the general consensus is that on average about 5 years of recorded data are necessary, depending also on the region. It is however also clear that even with excellent azimuthal coverage, it can still be difficult to distinguish between different model cases, and often further constraints from the deformation history of the study region may be required to resolve ambiguity.

3.3 Where along the path does the anisotropy occur?

One of the biggest drawbacks of the SKS shear wave splitting technique is that there is no inherent depth information to place a constraint on the depth of the anisotropic layer or layers. If using direct S-waves, the anisotropy could reside anywhere between the source and the receiver. Using core-refracted waves, the anisotropy may reside anywhere between the core-mantle boundary and the surface of the Earth. This is because when the core-refracted phase is travelling through the liquid outer-core, it is propagating as a P-wave, and when it exits the core some of it is converted back to an S-wave, which is radially polarised and not split. The liquid outer-core essentially "*resets*" the S-wave, removing any splitting that occurred between the focus (source) and the core.

The only way to gain an idea of the depth at which the anisotropy occurs is through inferences and by using other geophysical results. Commonly, in order to gain information on the extent of the anisotropy, practitioners will assume an anisotropic symmetry system and orientation (usually the simplest: transverse anisotropy with a horizontal symmetry axis), assume the anisotropy has occurred in the upper mantle, assume an average value for the degree of anisotropy (often $\approx 4^{\circ}$, as a consequence of laboratory and theoretical results), and then use δt to calculate possible path lengths in the anisotropic layer. This would provide information on the thickness of the layer, but still does not provide much information on the depth location. The alternate approach is to assume a thickness, and a percentage anisotropy can be calculated (Savage, 1999). Similarly, this gives information on the anisotropic layer, but still not much information on its depth extent.

A means of gaining information on the depth distribution of the anisotropic data is to compare splitting with other measures of seismic anisotropy such as Pn or surface waves, among others, which have better control on the depth distribution of anisotropy. Although

not as well localised as for MT, the surface wave technique provides a constraint on the depth of anisotropy in a somewhat similar manner. Another common argument used to gauge the depth of the anisotropic region is the Fresnel zone argument. A seismic ray is normally considered to be a tube, the diameter of which is defined as the first Fresnel zone. The size of the Fresnel zone is dependent on period and traveltime. If one station measures different anisotropic parameters for events with opposite backazimuths, it suggests that the source of anisotropy is located beneath the bottom-most point where the Fresnel zones intersect. If two nearby stations measure different splitting parameters for the same event, it suggests that the anisotropy resides above the top-most point where the Fresnel zones intersect (figure 3.5(a)). This means that for a closely spaced seismic array, with good splitting events, it is possible to use this argument to place approximate bounds on the top and bottom of the anisotropic layer. The Fresnel zone argument is however an inference, rather than a constraint, since it involves assumptions as to the true sensitivity functions.

There are other comparisons that can be made, such as comparing splitting from local or teleseismic direct S and ScS (c indicates a reflection at the core-mantle boundary), with that from SKS events. However one of the problems with all this evidence for depth distribution of anisotropy is that it is often conflicting (Savage, 1999). Figure 3.5(b) is a summary of the depth extent of shear wave anisotropy that has been inferred and determined from various studies.

3.4 Data preparation and analysis methodology

Before analysing shear wave splitting data there is a lot of data preparation that is necessary. This ranges from selecting appropriate events and time windows to looking at the data to see if it is useable or not.

3.4.1 Data Preparation and selection

Converted shear wave phases, such as SKS, SKKS, and PKS, will only be observed at certain times and locations after an event, such as an earthquake or nuclear explosion. The ideal criteria for observing these phases, and therefore for shear wave splitting analysis of such phases is described in this section. Typically, a database of suitable events is compiled from a number of criteria prior to any analysis.

The first of the criteria that needs to be satisfied is for the event-station pair to have

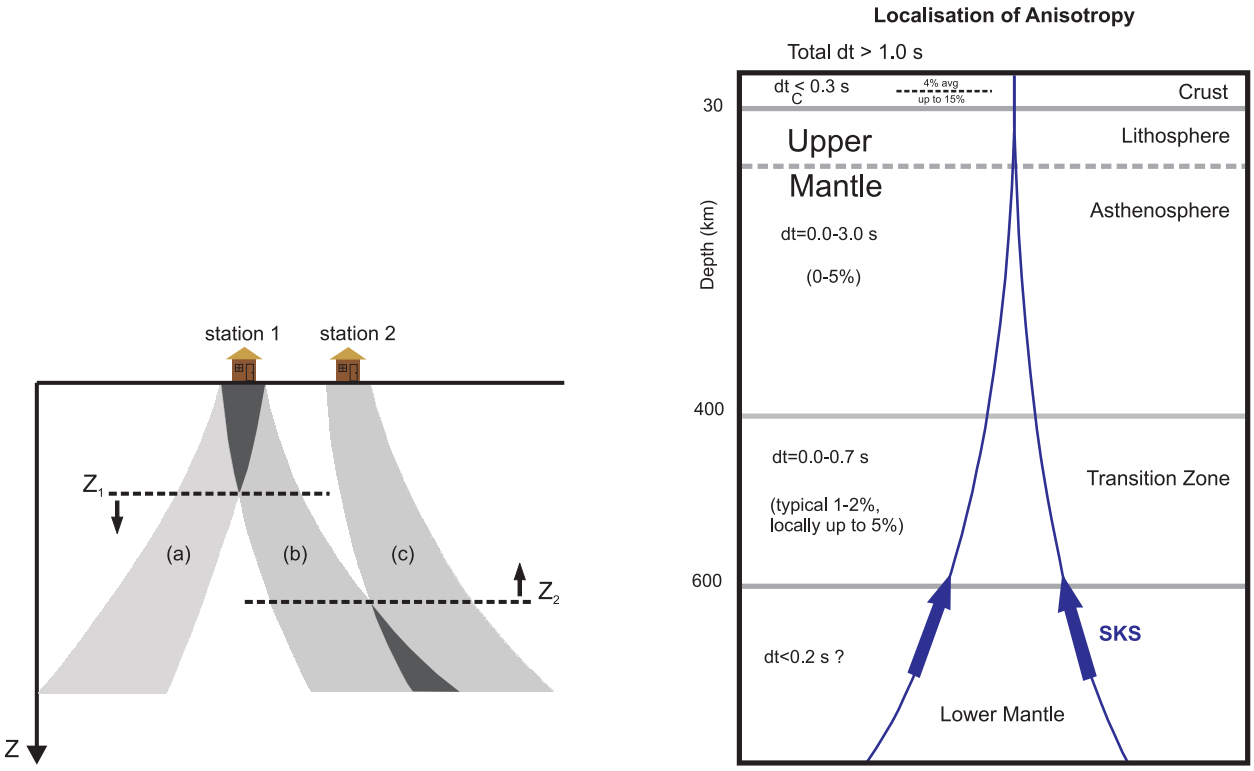

(a) (b)

Figure 3-5: *(a) A schematic representation of the Fresnel zone as a function of depth, Z, for SKS phases arriving nearly vertically at two neighbouring seismic stations. Fresnel zones for paths b and c have the same backazimuth, whereas path a has a backazimuth from an opposite direction. Overlapping paths would produce similar splitting parameters, thus if station 1 produces different splitting parameters for event paths a and b, it indicates that the anisotropy must lie below the depth where they overlap (i.e., below Z_1). While if station 1 and 2 produce different splitting parameters for paths a and c, which have a similar backazimuth, it indicates that the anisotropy must lie above the depth where they overlap (i.e., above Z_2). Redrawn from Alsina & Snieder (1995). (b) A summary of the depth extent of shear wave anisotropy determined by various studies. Redrawn from Savage (1999)*

an appropriate ***epicentral distance***, Δ, in order to observe the sought after phase. The angle must be great enough such that the seismic wave can travel through, and be converted at, the core. Additionally, it is necessary to observe at an epicentral distance where the arrival in question is isolated and distinct from interference with other phases. Figures such as figure 3-3, which is based on the IASP91 standard Earth velocity model (Kennett & Engdahl, 1991), give an indication of the epicentral distance that would correspond to locations where good shear wave observations could be expected. The figure shows that all events with a distance over 90° are suitable for splitting analysis and that at these distances, core

converted phases start to become isolated from other phases. High quality SKS phases will most often be observed from events with distances of 90°-110°, whereas high quality SKKS phases are most often observed from events with epicentral distances 110°-130°.

The second criteria for event selection is the event ***magnitude***. A higher magnitude event generally produces a seismogram with a better signal to noise ratio, but can have a far more complicated wave train. In seismically quiet environments, smaller magnitude earthquakes may be used, whereas in noisy environments (e.g. isolated island locations), larger magnitude events may be required. In general though, events greater than about 5.5 can be used.

The third criteria is the ***hypocentral depth*** of the event. Deeper earthquakes generally produce better core converted shear waves with lower frequencies. However, deep earthquakes are not only limited to particular regions (subduction zones) but are also less frequent than shallower events. Thus it is not practical for most studies to have a limit on the shallowest hypocentral depth, as one could be left with very few events, and these events would likely not have a well distributed back azimuthal range.

There are a number of searchable online earthquake catalogues (e.g., Advanced National Seismic System catalog, ANSS[2]) from which lists of appropriate events can be compiled given the criteria above, and information on the duration of recording of each station. From these event lists, it is possible to calculate the predicted arrival times of body waves at a specific epicentral distance using a given Earth model (e.g., iasp91 of Kennett & Engdahl, 1991). There are programs available online[3] that can be used for this calculation. Once the predicted body wave travel times have been calculated, appropriate time windows may be extracted from the seismogram recordings. Once seismic data have been recorded, it is normally stored and archived by consortiums such as the Incorporated Research Institute for Seismology, IRIS[4], in standard data formats such as *sac* or *seed*. From data centres like IRIS, seismographic data are publically available for the scientific community to freely download and use for data analysis. Finally, these downloaded seismograms of appropriate time windows are then ready for whichever analysis technique they are intended.

[2]http://www.ncedc.org/anss/catalog-search.html
[3]http://www-gpi.physik.uni-karlsruhe.de/pub/widmer/IASP91/iasp91.html
[4]http://www.iris.edu/

3.4.2 Analysis techniques

Where split shear waves are not completely separated, and analysis is not possible visually, other techniques are necessary for the analysis of shear wave splitting. Vinnik *et al.* (1989) and Silver & Chan (1991) describe two popular techniques have been developed in order to do this. Both techniques, which are very nearly equivalent, seek the fast axis direction and delay time through a global grid search, with the aim of reproducing or removing the effect of the anisotropy on the observed horizontal seismogram components of the shear waves.

The observed seismograms are normally recorded on three components, orientated north-south (the N component), east-west (the E component), and vertically (the Z component). In the analysis, the horizontal components (N and E), are rotated into the backazimuths, thereby resolving the radial (SV phase) and transverse (SH phase) components. The first step in the data analysis is to visually inspect the selected data window to see if there is a good shear wave arrival, with a suitable signal to noise ratio for a meaningful analysis. If there is not any anisotropy, the shear wave is not split, and core refracted waves which are radially polarised will have all the energy from the shear wave on the radial component. If, however, there is anisotropy, and the shear wave is split, then there will be energy on the transverse component, the waveform of which approximates the time derivative of the radial component if the splitting is small compared to the period (Vinnik *et al.*, 1989; Silver & Chan, 1991). The particle motion is usually displayed in a *polarisation diagram* or *hodogram*, and is a plot of the components of motion against each other. Each point on a polarisation diagram represents a moment in time, and the amplitudes of two components of a seismogram at that time. A split shear wave will typically have a cruciform shape for completely split fast and slow shear waves, or an elliptical particle motion for longer wavelengths or smaller splits where the two split waves are only separated by a fraction of a period. A converted shear wave that is not split will simply have a linear particle motion.

The Vinnik *et al.* (1989) shear wave splitting analysis technique synthesises the transverse component from the observed radial component of the phase being analysed. This is done over a range of values for different δt and ϕ pairs, with the aim of minimising the difference between the synthesised and observed transverse components, using cross-correlation methods. It is difficult to quantify the accuracy of the resulting values of δt and ϕ since the noise present in the seismic records is not known.

The Silver & Chan (1991) method is a related approach that searches for the best pairs of

values of δt and ϕ that will remove the energy from the transverse component. This is done by searching for the values that reverse the geometrical operations on the split waveform, i.e. find the inverse operator that returns the split waveform to the waveform as it would be prior to splitting. This may also be done by finding the value pairs that minimise the eigenvalues of the covariance matrix of the two rotated seismograms. The method produces the corrected radial and transverse seismograms, as well as a formal error estimate (Silver & Chan, 1991).

Figure 3-6 from Savage (1999) (originally from a study by Marson-Pidgeon & Savage, 1997) demonstrates a good shear wave splitting measurement using the method of Silver & Chan (1991). An important feature to note in figure 3-6 is that there is very little energy on the "corrected" transverse seismogram (figure 3-6 (b)), indicating that the splitting parameters used have "removed" the anisotropy effect adequately. This is also verified by figure 3-6 (c) where the particle motion has changed from elliptical to linear after correction.

The Vinnik *et al.* (1989) and Wolfe & Silver (1998) methods invert observations simultaneously for many different locations, angles of incidence, and back azimuth, to produce a single apparent fast axis and delay time for a station. Whilst this may be more robust, since it increases the signal to noise ratio, the validity of the averages depends on the variability of the parameters for the symmetry system. Single observation methods are better to determine if azimuthal variations are caused by dipping symmetry axes, or by heterogeneous anisotropic properties (Savage, 1999). It is therefore a worthwhile exercise to look first at single event splitting analysis for multiple events at a site, prior to the use of these techniques.

The methods of Vinnik *et al.* (1989) and Silver & Chan (1991) will measure the apparent splitting parameters for any symmetry system, so long as the S arrivals are mainly in the horizontal plane (Savage, 1999). This restriction is removed when extended to three components (e.g. Sileny & Plomerova, 1996; Aster *et al.*, 1990), although for nearly vertical incidence waves (such as SKS and SKKS), the difference between the methods is small.

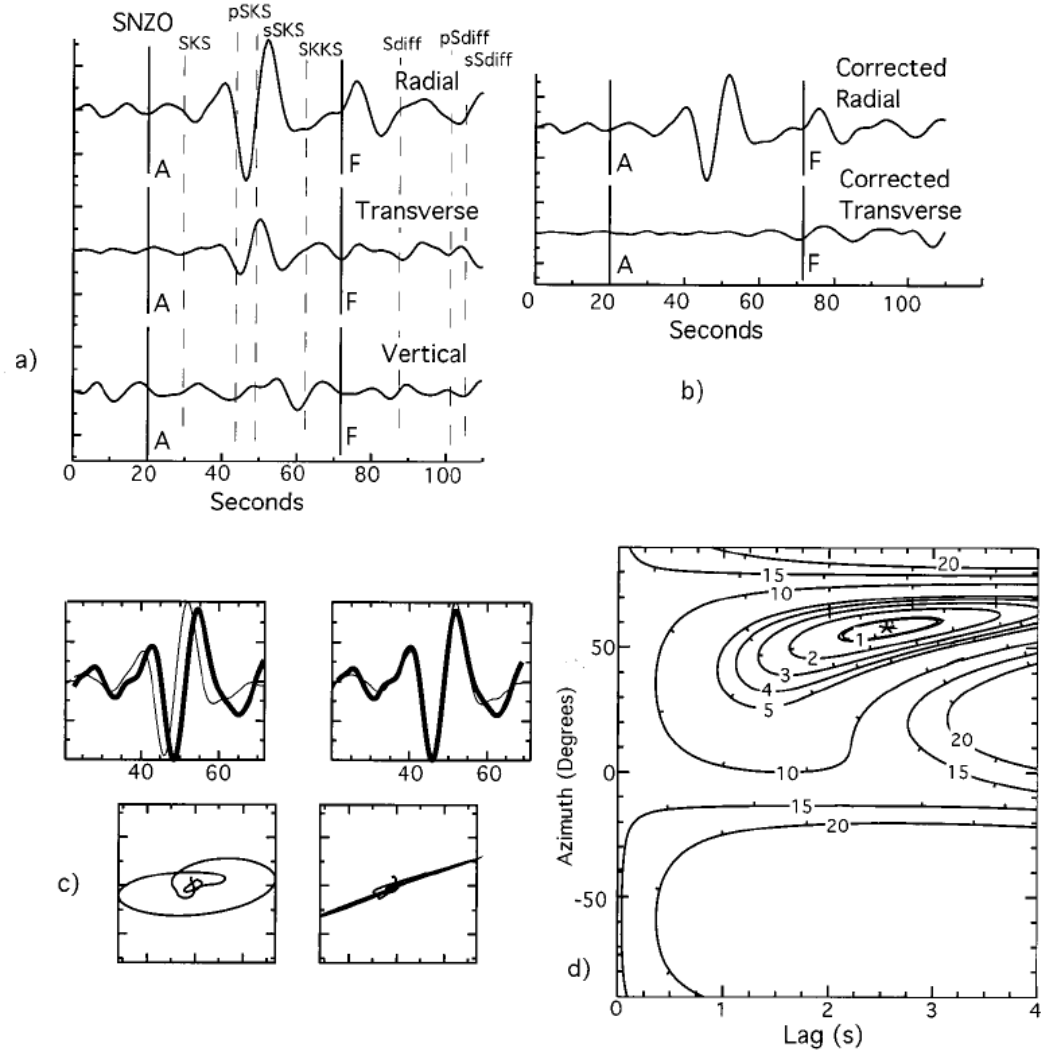

Figure 3-6: *An example of a good shear wave splitting measurement made using the method of Silver & Chan (1991) from a station in New Zealand.* **(a)** *The original radial, transverse, and vertical seismograms, with the predicted phase arrival times. The window that was analysed is between the two vertical lines, A and F. Vertical scale set by radial component amplitude.* **(b)** *The corrected radial and transverse components.* **(c)** *The top two plots show the uncorrected (left) and corrected (right) superposition of the fast (thin black line) and slow (bold line) components. Note the similar pulse shapes. The bottom two plots show the uncorrected (left) and corrected (right) particle motion. Note the change in shape from elliptical to linear of the particle motion after correction.* **(d)** *A plot of the energy on the transverse component after correction with different δt and ϕ parameters. The $\star$ represents the minimum value, surrounded by the 95% confidence region (double contour), and multiples of that contout interval. Taken from Savage (1999).*

4

The relationship between MT and Seismic anisotropy

4.1 Why are seismic and MT results complementary?

It will always be possible to garner more information about the subsurface of the Earth from multiple geophysical methods rather than one since the various techniques and methods each have their strong points as well as their pitfalls. Through using more than one technique we have the potential to minimise the effects of these pitfalls, and maximise our understanding of the Earth. Davis *et al.* (2003) provide an example of how the combination of different geoscientific datasets provide a better understanding of the Slave craton (Canada) than would be possible by using the datasets individually.

Seismic and MT data are analysed using different techniques, producing results that may be compared with varying degrees of appropriateness and success. Propagating seismic wave fields respond to the density, bulk modulus (incompressibility), and shear modulus (rigidity) of the medium through which they propagate (generally bulk rock properties), while electromagnetic fields respond to the conductivity variations of the medium produced for example

by: rock type, fluids present, or melt present (generally minor constituents of the rock). These are very obviously different physical properties, although it is clear that something such as a region of partially molten rock, would be observed in both the conductivity and seismic response of a region due to a change in conductivity as well as a change in the elastic properties (bulk and shear moduli) of the medium. However, if a seismic effect were observed due to a density contrast, it will not necessarily contribute to an observable electromagnetic response. Similarly, the conductivity of a region may be significantly affected by the interconnection of very minor constituents in the rock, which may not have any detectable effect on the seismic response. Thus, by combining these two geophysical methods, it may be possible to improve the interpretation of a given region.

One of the most problematic areas for seismic shear wave splitting analysis of teleseismic phases is vertical resolution, caused by the use of seismic waves with near-vertical ray paths and long wavelengths. The advantage of using this method to gain information on seismic anisotropy in the Earth is that, even though there is no inherent depth information in the technique, the horizontal resolution can be exceptionally good for a closely spaced array. However, conversely, the MT method has intrinsic vertical dependency due to the skin depth phenomenon, which assures penetration at any depth depending on the period and the resistivity of the subsurface. It is therefore quite clear that if electrical and seismic anisotropy are due to the same causative effect (discussed later), then these two techniques should be quite exquisitely complementary for the characterisation of the anisotropic layer or body.

4.2 Why would we expect a correlation?

The last statement of the previous paragraph is only true if the cause of anisotropy is the same for both techniques. In this section we explore the important question of what causes anisotropy, firstly looking at the likely causes of anisotropy separately for each technique, followed by a comparison of the probable combined effects.

4.2.1 Causes of electrical anisotropy

A number of different causes have been suggested for electrical anisotropy. Unfortunately, from MT measurements alone it is very difficult to distinguish one cause from another and normally the type of geological environment as well as other geoscientific data, such as petrological or geochemical data, are required to identify the cause with confidence. In the near-surface or upper crustal regions, electrical anisotropy may be caused by the preferential

orientation of a mineral fabric in a rock, such as interconnected graphite in a shear zone (Ji *et al.*, 1996), although this is also a possibility at greater depths (Jones *et al.*, 2001). However, one of the requisites for a mineral phase giving rise to electrical anisotropy anywhere in the subsurface is that it be interconnected, or at least partially interconnected in a significant manner over distances of the order of the inductive scale length (Everett, 2005). It has been observed that mineral phases such as graphite can form along grain boundaries and therefore along foliations and lineations, referred to as shape-preferred orientation (Mareschal *et al.*, 1995; Jones, 1992). Interconnected saline fluid-filled cracks are another possible explanation for electrical anisotropy, however this would only be a likely cause in the crustal environment and importantly would contribute to both seismic and electrical anisotropy.

Anisotropic hydrogen diffusion in olivine has been proposed as a mechanism for reducing electrical resistivity of mantle materials (Karato, 1990; Hirth *et al.*, 2000) and it is a suggestion that has gained a lot of interest due largely to recent laboratory experiments (Wang *et al.*, 2006; Yoshino *et al.*, 2006), although there remains a great deal of controversy even in some of these recent results (Hirth, 2006). Poe *et al.* (2005) suggests that concentrations of a few hundred ppm water is sufficient to raise the conductivity of olivine by several orders of magnitude compared with dry olivine. Olivine, the most abundant mineral in the upper mantle, is electrically anisotropic, with the [100] axis (also known as the a-axis) having the highest rate of hydrogen diffusion, thereby being the most conductive direction (Schock *et al.*, 1989; Mackwell & Kohlstedt, 1990). The olivine crystal aligns preferentially when under strain and therefore many crystals with similar alignment would contribute to an overall anisotropic effect. Initial concerns with respect to this mechanism creating electrical anisotropy in the upper mantle were that it was thought that the amount of electrical anisotropy that could be produced was insufficient to account for the magnitudes observed. Random resistor network modelling by Simpson & Tommasi (2005) suggested that it could only account for, at most, one third of the average measured values. However, more recently, Gatzemeier & Tommasi (2006) showed, using finite-element modelling, that this is likely a lower bound on estimations of mantle electrical anisotropy and that factors of up to 10 in electrical anisotropy may be achieved from hydrogen diffusion in olivine. Gatzemeier & Tommasi (2006) found that factors even greater than 15 were possible in highly deformed mantle rocks (most likely produced by dislocation creep) where not only strong crystal preferred orientation, but also shape preferred orientations are produced. Recent work by Beran & Liboitzky (2006) and Grant *et al.* (2007) note that for lithospheric rocks, the water content in olivine is low compared to that of pyroxenes, and Wang *et al.* (2006)

infer that the water content in the continental upper mantle is $<10^{-3}$ wt%. Higher contents are observed in clinopyroxene (≈400 ppm) and orthopyroxene (≈200 ppm) compared with olivine (<55 ppm). This work suggests that using hydrogen diffusion in olivine as an explanation for electrical anisotropy for the continental lithosphere (olivine dominated) may be incorrect (Jones *et al.*, 2007). Interestingly, the values of Grant *et al.* (2007) also suggest that the water content is independent of lithospheric age.

If lattice preferred orientation (LPO) of olive is used as an explanation, one of the requisites is that there is a consistent and widespread crystal alignment in the electrically anisotropic region. Unfortunately, to date there have been no electrical anisotropy measurements made on mantle rocks to corroborate models such as those of Simpson & Tommasi (2005) and Gatzemeier & Tommasi (2006). This is due largely to the difficulty involved in making the measurement, and also because laboratory measurements have tended to focus on physical property measurements other than electrical anisotropy.

It is of course likely that not only does the cause of electrical anisotropy differ slightly from one geological region to the next, but also that the anisotropy is not only due to one single factor, but is rather a combination of several factors that may only be valid for certain depths. It is also important to remember that MT measurements are only measuring horizontal contributions to electrical anisotropy, and that in some regions, it may have a greater value, but have a reduced response to the MT measurement if it also has a dip angle. However, it should also be noted that in non-layered structures, or in the presence large-scale heterogeneity, the TM mode component of current flow will sense conductivity with currents that include a vertical component.

4.2.2 Causes of seismic anisotropy

Similarly to electrical anisotropy, there are a number of suggested causes for seismic anisotropy, which vary from one geological environment to another. There are generally thought to be three main causes of seismic anisotropy. Firstly, there is what is known as *effective anisotropy*. Effective anisotropy depends strongly on wavelength and can be produced by thin isotropic layers with different elastic properties (Savage, 1999). To seismic waves with wavelengths longer than the thickness of the layer, these layers will appear anisotropic. If they were horizontal layers, this would produce radial anisotropy with a vertical slow axis.

The second main type of seismic anisotropy is thought to be produced by cracks or fractures, and is known as *crack-induced anisotropy*. At higher frequencies, and in near-surface or crustal scale studies, oriented fracture cracks and fluid-filled fractures have been suggested as a major cause of anisotropy (Crampin, 1987; Kaneshima *et al.*, 1988; Crampin & Chastin, 2003). The cracks may be filled with gas, liquid, or solid. Vertical parallel fractures would cause a vertically propagating shear wave to be split into a fast and slow polarisation, with the fast polarisation direction being parallel to the strike of the cracks as well as parallel to the maximum horizontal stress direction (figure 4-1 (a)) (Crampin & Chastin, 2003).

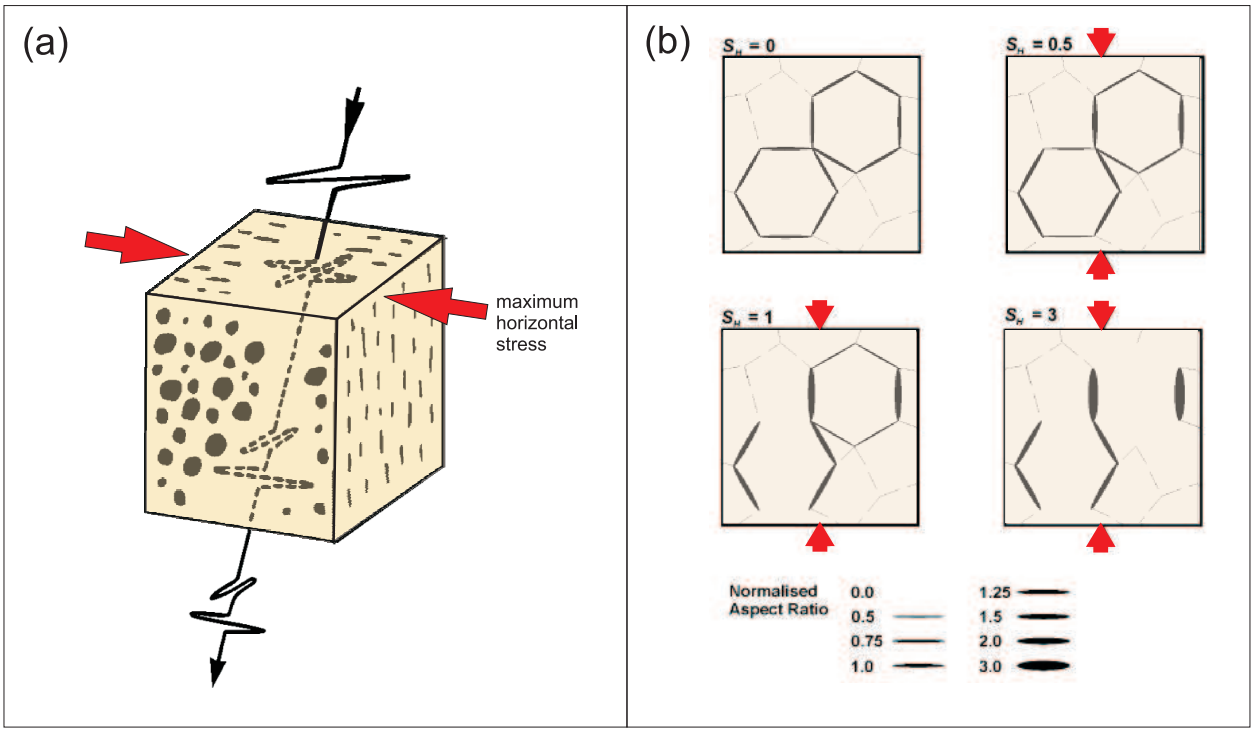

Figure 4-1: *(a) The effect of parallel vertically aligned fluid-filled cracks on a near-vertically, downward propagating shear wave. The shear wave is split into a fast polarisation (parallel to cracks and the direction of maximum horizontal stress) and a slow polarisation. It is likely that if these were saline fluid-filled cracks, and they have interconnection, that the fast polarisation would also be the more conductive direction. (b) Plan view schematic illustration of the evolution of aligned cracks. S_H represents values of horizontal differential stress, normalised to the critical value at which cracks first begin to close. Both figures modified from Crampin & Chastin (2003), figure (b) originally from Crampin & Zatsepin (1995).*

The third main cause suggested for seismic anisotropy is due to the alignment of anisotropic mineral crystals, often referred to as anisotropy resulting from *LPO*, or as *intrinsic anisotropy*.

Anisotropic minerals are present in both the crust and mantle. If these anisotropic crystals become preferentially aligned, then the bulk effect is one of an anisotropic medium. In the crust, rocks that are anisotropic due to LPO of minerals include; gneisses, schists, sedimentary rocks, and amphibolites, among others. Seismically anisotropic minerals occurring in the crust that cause these rocks to be anisotropic, and have an orientation that is strain dependent include amphibole, biotite, and other phyllosilicate minerals (Valcke *et al.*, 2006). Seismic anisotropy in the mantle is predominantly attributed to LPO anisotropy, and is an important branch of research in the field of mineral physics. Olivine and pyroxene are both abundant in the upper mantle and are both seismically anisotropic (though olivine is more abundant) however, pyroxene is smaller in anisotropic magnitude and also likely to be less strongly orientated (Mainprice & Silver, 1993). Thus, upper mantle seismic anisotropy from LPO is commonly attributed to the preferential alignment of olivine and has been for a long time (e.g. Hess, 1964). It has been suggested that there is seismic anisotropy as deep as the transition zone, between the 410 km and 660 km discontinuities (Montagner & Kennett, 1996; Vinnik & Montagner, 1996), and that this might be due to LPO of anisotropic minerals such as β spinel (Fouch & Fischer, 1996), which is a high pressure polymorph of olivine. There was originally little support for seismic anisotropy between the transition zone and the D" layer, as it is thought that the general trend is that anisotropy decreases with increasing temperature and pressure (i.e. depth) however, recent work suggests that although this may be generally true it is not always the case (Do *et al.*, 2006). Mainprice *et al.* (2000) present a summary of the major physical and chemical variations in the Earth's mantle that control seismic anisotropy (figure 4-2).

4.2.3 How are stress and strain related to anisotropy?

Not only is it important to be able to ascertain the cause of anisotropy, be it electrical or seismic, but it is important to know how the "cause" formed. Without knowledge of how anisotropy is related to Earth processes, the measurement of electrical and seismic anisotropy would be meaningless. However, if we are able to relate the anisotropy to past or present strain, and the resulting stress or deformation, this provides a useful constraint for understanding the formation and dynamics of a given geological environment.

Smaller scale near-surface anisotropy has been more thoroughly investigated largely because the environments under which the stress and strain occur (relatively low pressure and temperature) are easily reproduced or modelled and contain less unknowns. Additionally, the results may be readily and directly compared to what is found. Crack formation in

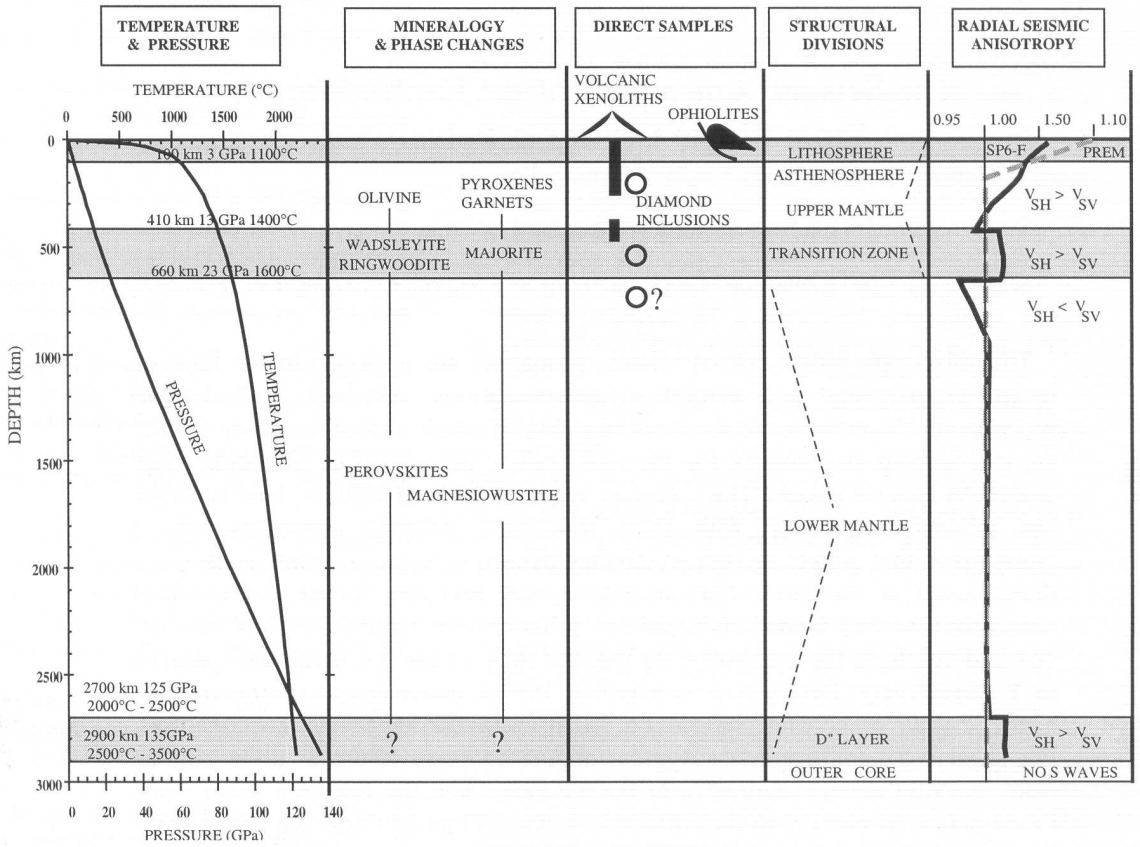

Figure 4-2: *A summary of the major physical and chemical variations in the Earth's mantle, which control seismic anisotropy. Taken from Mainprice* et al. *(2000). The seismic model SP6-F comes from Montagner & Kennett (1996) and the PREM model comes from Dziewonski & Anderson (1981)*

relation to strain, and therefore anisotropy, has be extensively observed and studied (e.g. Crampin, 1987; Kaneshima *et al.*, 1988; Crampin & Chastin, 2003). Crampin & Chastin (2003) and Crampin & Peacock (2005) provide reviews of work done on the modelling of the formation of strain-induced fluid-filled cracks and its relation to stress. Figure 4-1 (b), originally from Crampin & Zatsepin (1995) demonstrates through modelling how these cracks evolve, becoming preferentially aligned with the direction of maximum horizontal differential stress. Vertical cracks (figure 4-1 (a)) produced in this manner will only occur below a *critical depth* where the vertical stress becomes greater than the minimum horizontal stress (usually between 500 and 1000 m) (Crampin & Peacock, 2005), although laboratory measurements (Hrouda *et al.*, 1993) suggest that at depths of 10-15 km, these cracks close, and therefore anisotropy below these depths must be due to other phenomena (Savage, 1999).

As discussed earlier, LPO, also known as Crystal Preferred Orientation (CPO) may develop in a rock producing a bulk rock anisotropy. The mechanism and environment of deformation, as well as the type and extent of strain, will control the development of LPO. The LPO of olivine is one of the preferred theories for lithospheric and sublithospheric seismic and sometimes electrical anisotropy, and therefore the way in which this relates to stress is an important and currently very active field of study. In upper mantle conditions there are two important types of deformation, namely; *diffusion creep* and *dislocation creep*.

Deformation through diffusion creep occurs at either relatively low stress or small grain size, or both. This solid-state diffusive mass transport between grain boundaries or across a crystal lattice has a strain rate that increases linearly with stress, and decreases significantly with grain size (Karato & Wu, 1993). Under the diffusion creep regime, no preferred orientation is developed, and the deformed material is isotropic attaining no LPO.

Contrastingly, deformation through dislocation creep occurs at high stress levels, large grain size, or both. Dislocation creep is deformation resulting through the motion of crystalline dislocations within grains. The strain rate increases nonlinearly with stress, but is insensitive to grain size (Karato & Wu, 1993; Savage, 1999). Deformation through the dislocation creep mechanism will produce a preferred orientation and therefore result in a rock that has a bulk anisotropy, with the strength of anisotropy (i.e. the strength of preferred orientation) dependent on the magnitude of strain. Strain rates developed by both mechanisms are sensitive to temperature and pressure, though the magnitude of the temperature and pressure effects are different for each. Thus, for a given temperature and pressure, the mechanism that has the higher strain rate becomes the dominant creep mechanism. This allows the dominating creep deformation mechanism to vary with depth and with regional temperature deviations (Karato & Wu, 1993). The symmetry of LPO is dependent on the history of deformation, which may be extremely complex. As an example, symmetrical LPO with respect to foliation and lineation results from a coaxial deformation history, whereas asymmetrical LPO results from non-coaxial deformation histories (Do, 2006). Theoretical and experimental studies suggest that preferred orientation in the mantle forms in aggregates due to the alignment of slip planes and directions with the shear plane direction (Savage, 1999).

There are two main arguments for LPO anisotropy below continental lithosphere. The first is that anisotropy correlates with absolute plate velocity directions or mantle flow, being

formed by the relative motion between the plates and the upper mantle below, resulting in the fast direction of seismic anisotropy in the upper mantle being parallel to the relative motion (Vinnik *et al.*, 1992, 1995, 1996). The diametrically opposed counter-hypothesis suggests that anisotropy below older continental regions is dominantly a response to fossil, or frozen-in, crystal alignment created at the time of primary lithospheric formation (Silver & Chan, 1991; Silver, 1996) (described schematically in figure 4-3). The hypothesis of Silver & Chan (1991) is supported by fast axis directions which align with surface structural features, suggesting that the surface features and the features at depth were formed at the same time. This argument supports the *tectosphere* idea proposed by Jordan (1978). However, in some regions, such as much of North America and southern Africa, the dominant geological structure is also largely parallel to current plate motion and thus asthenospheric flow cannot be ruled out as a contributing factor simply by the correlation of geologic structure with splitting. These two hypotheses have been discussed by a number of authors (e.g. Silver, 1996; Park & Levin, 2002; Fouch & Rondenay, 2006), and remains a contentious issue.

There are further complexities to these arguments, although some may not be applicable to the continental craton environment. Jung & Karato (2001) show that the addition of large amounts of water to olivine (e.g. in subduction zones) can change the relation between flow geometry and seismic anisotropy by changing the type of fabric that is produced. Jung & Karato (2001) define three types of fabric (A-type, B-type, and C-type), each of which would produce different anisotropy results. This theoretical work has been supported by observations in a subduction-type metamorphic belt by Mizukami *et al.* (2004). Additionally, Holtzman *et al.* (2003) demonstrate that the presence of melt weakens the alignment of the olivine *a* axis ([100] axis), and where the melt segregates to form networks of shear zones it may even cause the alignment to be at 90° to the shear direction. Neither of these mechanisms are expected to be currently operative in Archean or Proterozoic aged lithosphere. However, if the Silver & Chan (1991) hypothesis is valid, perhaps these effects could remain frozen into the lithosphere during the formation of the region?

Although the general consensus among geophysicists is that seismic anisotropy in the upper mantle is due to LPO, it has also been suggested by Crampin & Peacock (2005) that in the upper 400 km of the mantle, shear wave splitting is in fact caused by films of liquid melt aligned parallel to the direction of maximum stress, exactly analogous to the fluid-saturated grain boundary cracks in the crust. Crampin & Peacock (2005) contest that melting in the mantle would first occur along grain boundaries (Daines & Kohlstedt, 1997), and, given

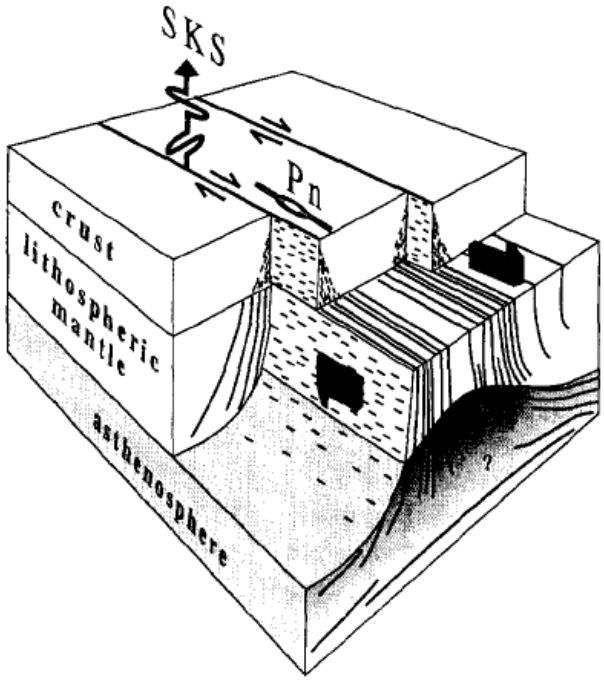

Figure 4-3: *Schematic representation of a lithospheric-scale shear zone. In this idealised situation, foliation planes are near-vertical, and a-axis orientation would be horizontal and parallel to the strike slip motion. The fast axis split direction (and the Pn fast propagation direction) would be parallel to the trend of the shear zone. It would also be expected that any interconnected mineral phase would be most likely to be interconnected in the direction parallel to the trend of the shear zone, producing a situation where the most conductive direction and fast axis direction are near parallel. From Vauchez* et al. *(2000).*

triaxial stress, the melt would appear as thin films of liquid melt along grain boundaries. Such films of melt, similarly to the crustal fluid-filled cracks, would be aligned parallel to the direction of maximum stress, which would infer that the mantle is pushed by spreading centres rather than pulled by subduction. Although not discussed by Crampin & Peacock (2005), substantial connectivity of this melt would significantly lower resistivities, and depending on the nature of the connectivity, it might produce significant electrical anisotropy.

In brief, the concept that the olivine *a*-axis orientates subparallel to horizontal flow direction, or to the extension direction in the upper mantle, and that for simple shear and large strains the maximum extension is approximately parallel to shear seems to be valid for many, but far from all, cases (Savage, 1999). There are many complexities as we move from one strain and geological environment to another, a factor one should be cognizant of when

making an interpretation or inference.

4.2.4 Which causes will produce a correlation?

The previous sections discussed some of the causes of electrical and seismic anisotropy separately, and how they might form. However, the effect may be different for each, it may enhance or diminish the correlation between the fast axis direction of shear wave splitting and the most conductive direction of MT anisotropy. Table 4.1 is an attempt to summarise the effects of some of the proposed causes, as well as whether there would be an overall correlation increase or decrease between the two.

From table 4.1, we see that LPO, fluid-filled cracks, and cracks of partial melt (should they exist) would likely cause azimuthal correlation between electrical and seismic anisotropy. An interconnected mineral phase would likely only affect the electrical anisotropy. Interconnected partial melt could certainly affect electrical anisotropy, although its effect on seismic anisotropy would likely depend on the nature of the interconnected melt (amount, size, and shape). The last effect mentioned on the table is 2D heterogeneity, such as a 2D fault or shear zone, or a terrane boundary. If this structure comprises a conductivity contrast such as between two geological terranes of differing conductivity, then it will have an effect on the electrically more conductive direction, although this is not an anisotropic effect (discussed in more detail later). The structure will also likely have an effect on the seismic anisotropy, although probably only if the structure is of sufficient size.

4.3 Past studies of MT and teleseismic anisotropy

It is always prudent to inspect past studies that are similar in nature to gain ideas, different perspectives, and an understanding of the work that has already been carried out. The work done in this thesis was partly inspired by the work of Ji *et al.* (1996) and Eaton *et al.* (2004). More recently there has been concurrent similar work to the research done here by Frederiksen *et al.* (2006) and Padilha *et al.* (2006). The four studies mentioned are described briefly below and, although they are not the only studies of this nature, they are representative of the type of work that is being done in this field of study. A brief description of each study along with the main points and conclusions is presented.

The first study looking closely at the correlation between teleseismic shear wave splitting

Cause	*Effect on SKS splitting*	*Effect on MT anisotropy*	*Combined Effect*
Fluid-filled cracks	✓	✓ strong	✓
LPO	✓	✓ weak	✓
Interconnected mineral phase	✘	✓ strong	?
Interconnected partial melt	?	✓ strong	?
"cracks" of partial melt	✓	✓ strong	✓
2D heterogeneity	?	✓ strong	?

Table 4.1: *A summary of the different causes of anisotropy and the resulting effect on the fast axis direction and magnitude of SKS shear wave splitting and the electrical most conductive direction. The last column indicates whether the combined effect would result in an enhancement or reduction in the correlation between the two.* ✓ *implies an increase or improvement;* ✘ *implies that there is likely no effect; and* ? *implies that the effect may be dependent on the geological situation.*

and the geoelectric strike directions of MT data was that of Ji *et al.* (1996), who undertook a study of previously collected and analysed data (Senechal *et al.*, 1996; Mareschal *et al.*, 1995) across the Grenville front, between the Archean craton and Proterozoic Grenville province in Canada (figure 4-4). With 10 teleseismic stations and 12 MT stations (some nearly co-located) along the profile, Ji *et al.* (1996) noted that the MT showed strong anisotropic behaviour for a given frequency range, with the most conductive directions at an oblique angle to the fast axis directions determined from teleseismic SKS and SKKS shear wave splitting. The seismic anisotropy is most easily explained to be due to LPO of upper mantle minerals, while the electrical anisotropy was thought to arise from the preferred interconnection of a conducting mineral phase since it was thought to be too strong to be due to LPO, and if it were due to LPO one would expect that the seismic fast axis and electrically more conductive direction would correlate without any obliquity. The suggestion that the electrical anisotropy is due to a conducting mineral phase is supported by kimberlite xenolith information from a kimberlite near station 2 on the profile. Given these two likely causes, Ji *et al.* (1996) conclude that the obliquity between the two sets of measurements is a result of fabric symmetry with respect to the structural framework. The fast-axis direction due to LPO is parallel to the bulk shear direction at large strains, whereas the MT most

conductive direction is parallel to the foliation and lineation. Ji *et al.* (1996) further use this obliquity to infer a dextral shear sense of movement across this boundary, consistant with surface geology, and providing a possibly useful means of gaining an understanding of the geodynamics of a region by using these two techniques in conjunction.

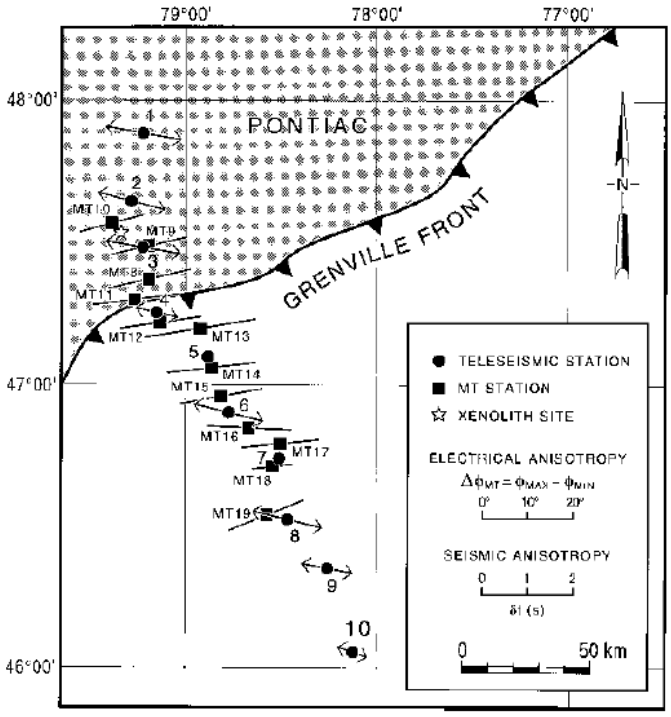

Figure 4-4: *Amplitudes and azimuths of shear wave splitting and electrical anisotropy over the Grenville front in Canada. MT azimuths are the most conductive direction scaled by phase difference, while the teleseismic azimuths are the fast axis directions, scaled by delay time. From Ji* et al. *(1996).*

The work by Ji *et al.* (1996) was followed up by Eaton *et al.* (2004), with the aim of testing this hypothesis across the Great Slave Lake (GSL) shear zone in northern Canada (figure 4-5). Eaton *et al.* (2004) use nearly collocated seismic and MT stations (data results also published separately in Wu *et al.* (2002) and Eaton & Hope (2003)) and find a strong correlation between the seismic fast axis direction and the MT most conductive direction, and do not observe any systematic obliquity between the two data sets as was observed by Ji *et al.* (1996). They use the close correlation to place depth constraints on the seismically anisotropic region, and suggest that the systematic obliquity observed by Ji *et al.* (1996) is absent for one of two reasons. Either both the seismic and electrical anisotropy are a result of LPO, which would produce aligned anisotropy such as that observed in Fennoscandia (Bahr

& Simpson, 2002) and Australia (Debayle & Kennett, 2000; Simpson, 2001), although the latter study consisted of only three MT stations, or, the severity of shearing in the GSL shear zone has resulted in the LPO and foliation and lineation planes becoming parallel, analogous to the classical schistosite-cisaillement (S-C) fabrics under conditions of high strain. The work by Ji *et al.* (1996) and Eaton *et al.* (2004) is not too dissimilar to the idealised situation portrayed in figure 4-3.

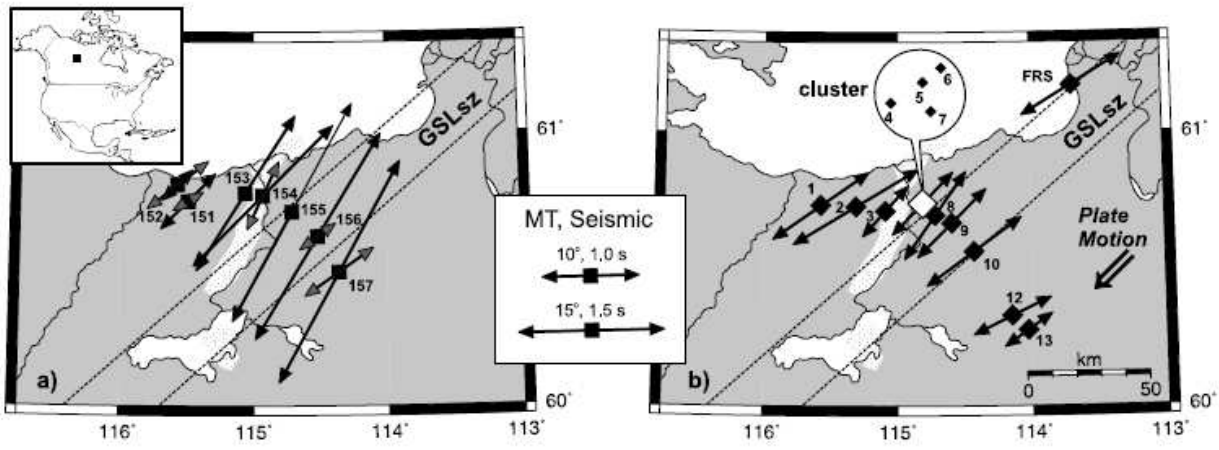

Figure 4-5: *Locations of stations from an MT (Wu* et al.*, 2002) (left) and teleseismic (right) (Eaton & Hope, 2003) experiment across the Great Slave Lake shear zone, northern Canada. MT black and grey vectors (left figure) represent geoelectric strike vectors for 0.1-20s (crustal) and 20-1000s (lithospheric mantle) period bands respectively. Seismic fast-axis directions (right figure) are single layer averages. From Eaton* et al. *(2004).*

In more recent work, Frederiksen *et al.* (2006) compare MT geoelectric strike with teleseismic SKS shear wave splitting in eastern Ontario and southwestern Quebéc, Canada (figure 4-6). The geoelectric strike directions plotted by Frederiksen *et al.* (2006) are not the most conductive directions, but rather the directions are plotted as the direction that plots closest to the mean shear wave split fast axis direction. The correlation of mantle with crustal MT geoelectric strike data (and observed geologic structure) suggest that large parts of the upper mantle have remained in place since the Neoarchean, while at many sites in the Grenville province there is a high angle between these strike directions, suggesting that the mantle below this region has undergone significant deformation since the Grenvillian orogeny. The region explored by Frederiksen *et al.* (2006) includes the area studied by Ji *et al.* (1996). The systematic obliquity between the seismic fast direction and the electrically most conductive directions observed by Ji *et al.* (1996) at the Grenville front is restricted to that

region. Although there does seem to be some clear consistency in some regions between the fast split and geoelectric strike directions, there is clearly more complexity, particularly in the Grenville province, than has been observed in some previous studies. Frederiksen *et al.* (2006) note that this is likely due to larger scale structure, but that the ≈50 km MT station spacing does not allow this question to be fully examined.

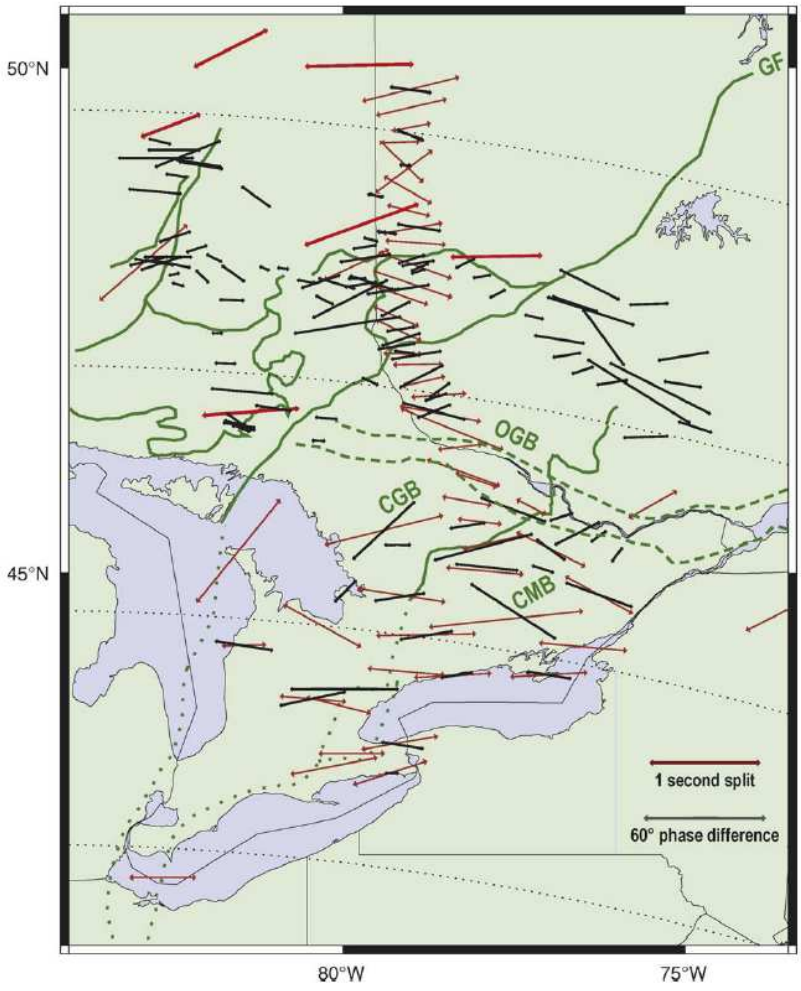

Figure 4-6: *Figure from Frederiksen* et al. *(2006) comparing SKS fast axis directions with the geoelectric strike directions across the Grenville Front in Canada. Note that the geoelectric strike direction is not necessarily the most conductive direction. The MT geoelectric strikes are for the period range 1-1000 s. The MT strike direction arrows are scaled by phase difference, and the SKS fast direction arrows are scaled by delay time.*

Padilha *et al.* (2006) report another recent study from south central Brazil (figure 4-7). They find a strong correlation between the MT most conductive direction and the fast axis

of shear wave splitting. The correlation shows no consistent obliquity, and appears to be consistent from the crust to asthenospheric depths; however, the directions are not consistent with present day apparent plate motion. Padilha *et al.* (2006) suggest that this could be due to coherent deformation in the lithosphere, with no deformation between the lithosphere-asthenosphere boundary either because there is no significant lateral mantle flow, or because the rigid lithosphere is much thicker than expected. Additionally, it is suspected that the most conductive direction and the fast axis split direction are both due to the LPO of upper mantle minerals such as olivine.

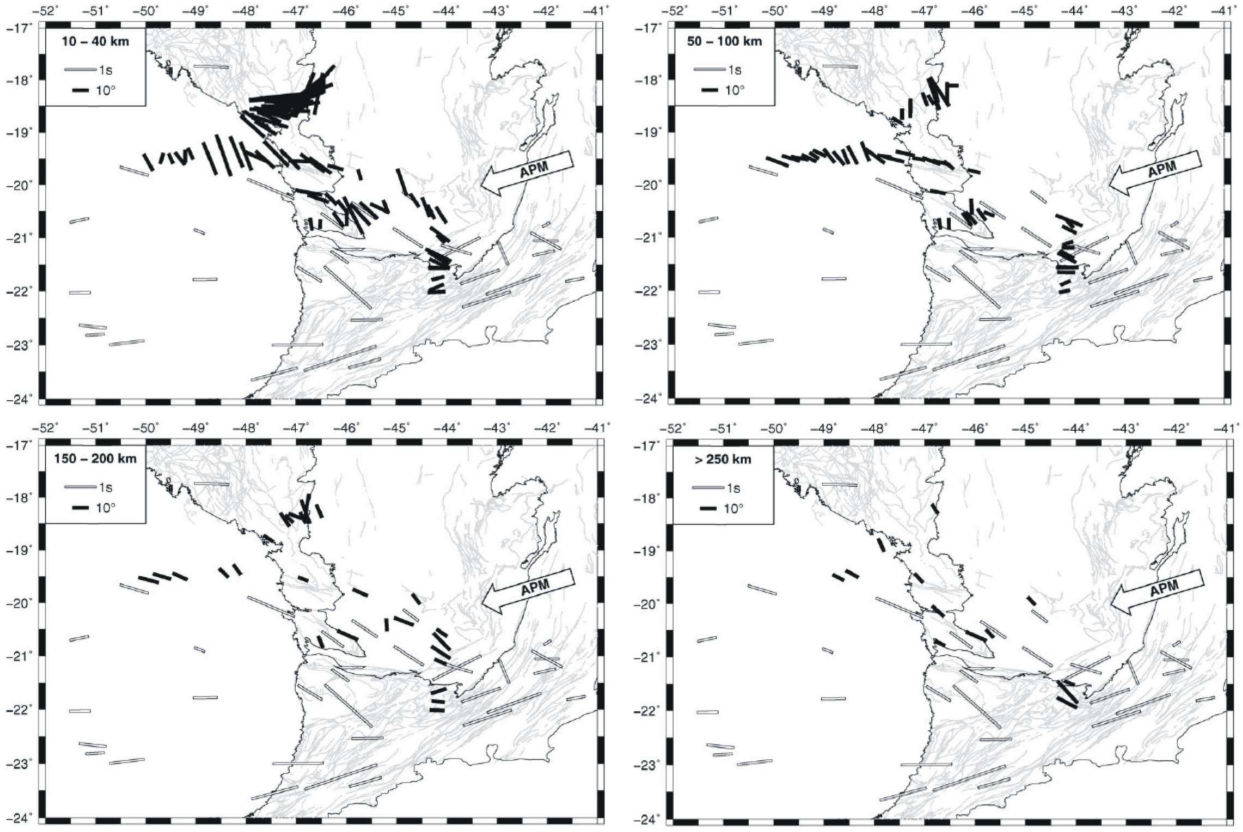

Figure 4-7: *Azimuths and magnitudes of shear wave splitting (open bars) and geoelectric anisotropy (solid bars) in south central Brazil for four different depth ranges from Padilha* et al. *(2006). The figures are: 10-40km (top left); 50-100km (top right); 150-200km (bottom left); and >250km (bottom right).*

It is clear from the brief recount of these studies that there is potential for gaining information on the past and present geodynamics of a region using these two techniques, more so than would be obtained separately. Additionally, there is also the opportunity to

add constraints and counteract pitfalls of each of the methods (e.g. add depth constraints to the seismic anisotropy). However, it is also clear that there is variability between different geological environments, and so one should be careful when interpreting such results.

5

Teleseismic shear-wave splitting in southern Africa

5.1 Introduction

This study involves the comparison between electrical and seismic anisotropy. Although there is no reason to suspect that the results of the teleseismic shear wave splitting study undertaken by Silver *et al.* (2001) were incorrect, it was decided to re-analyse some of the data. Firstly, the study of Silver *et al.* (2001) was published in a very short article considering the amount of data analysed. With mainly the results, and very little of the data, being published one does not get to grips fully with the characteristics of the data. Secondly, a preliminary analysis of some of the MT data from the first field season suggested there may be two layers of anisotropy, and so one of the aims of reprocessing the seismic data was to explore the possibility that there may be two layers of seismic anisotropy, or other subtleties that may have been overlooked in the original analysis. Additionally, since we are using the results of these data, it is prudent to have a good understanding of how the results were obtained and of any special features of the data, something that can best be achieved by doing at least some of the re-processing oneself.

5.2 Southern African Seismic Experiment

The Southern African Seismic Experiment (SASE), as part of the Kaapvaal Craton Project (Carlson *et al.*, 1996, 2000), was conducted over the southern African region from 1997 to 1999, with the aim of investigating the seismic structure of the region. Broadband seismic stations covered the Kaapvaal craton, part of the Zimbabwe craton, and some of the surrounding mobile belts, and were known as the Kaapvaal Seismic Array (figure 5-1). In total, 82 stations were occupied during the experiment, with some recording for approximately a year, and others recording for the full duration of the experiment (≈2 years).

The results of the experiment have been widely reported (e.g. Carlson *et al.*, 2000; James *et al.*, 2001; James & Fouch, 2002; Silver *et al.*, 2001, 2004) although work on these data continues. Some of the results are briefly described here: The crustal thickness was inferred over the different geological terranes (Nguuri *et al.*, 2001; Stankiewicz *et al.*, 2002; James *et al.*, 2003) showing sharp receiver function responses over cratonic regions. There is a low velocity zone beneath the Bushveld complex (James *et al.*, 2001) that Shirey *et al.* (2002) suggest corresponds to different diamond and diamond inclusion compositions. Seismic anisotropy inferred from shear-wave splitting analysis, reported by Silver *et al.* (2001, 2004), shows clear differences in splitting parameters over the various cratons and terranes, and in their interpretation they suggest that it provides support that mantle deformation is preserved from as far back as the formation of the Earth's earliest continents. High-quality seismic data from 31 stations have also been obtained from a dense broadband array near Kimberley (the Kimberley Telemetered Array) as part of the SASE experiment. These data have helped to provide well-resolved constraints on the structure and composition of the lowermost crust and Moho (James *et al.*, 2003). James & Fouch (2002) give an excellent review of some of the results of the SASE as well as geochemical studies and interpret the significance of the results for craton formation and evolution.

5.3 SASE shear wave splitting results

One aspect of the results from the SASE experiment is the seismic anisotropy inferred from shear-wave splitting measurements reported by Silver *et al.* (2001, 2004) (figure 5-2). There was also an additional study done on the Kimberley Telemetered Array by Fouch *et al.* (2004b), although the data from this study have not been reprocessed, and are not discussed in depth here.

The seismic results as reported by Silver *et al.* (2001, 2004) are presented in figure 5-2.

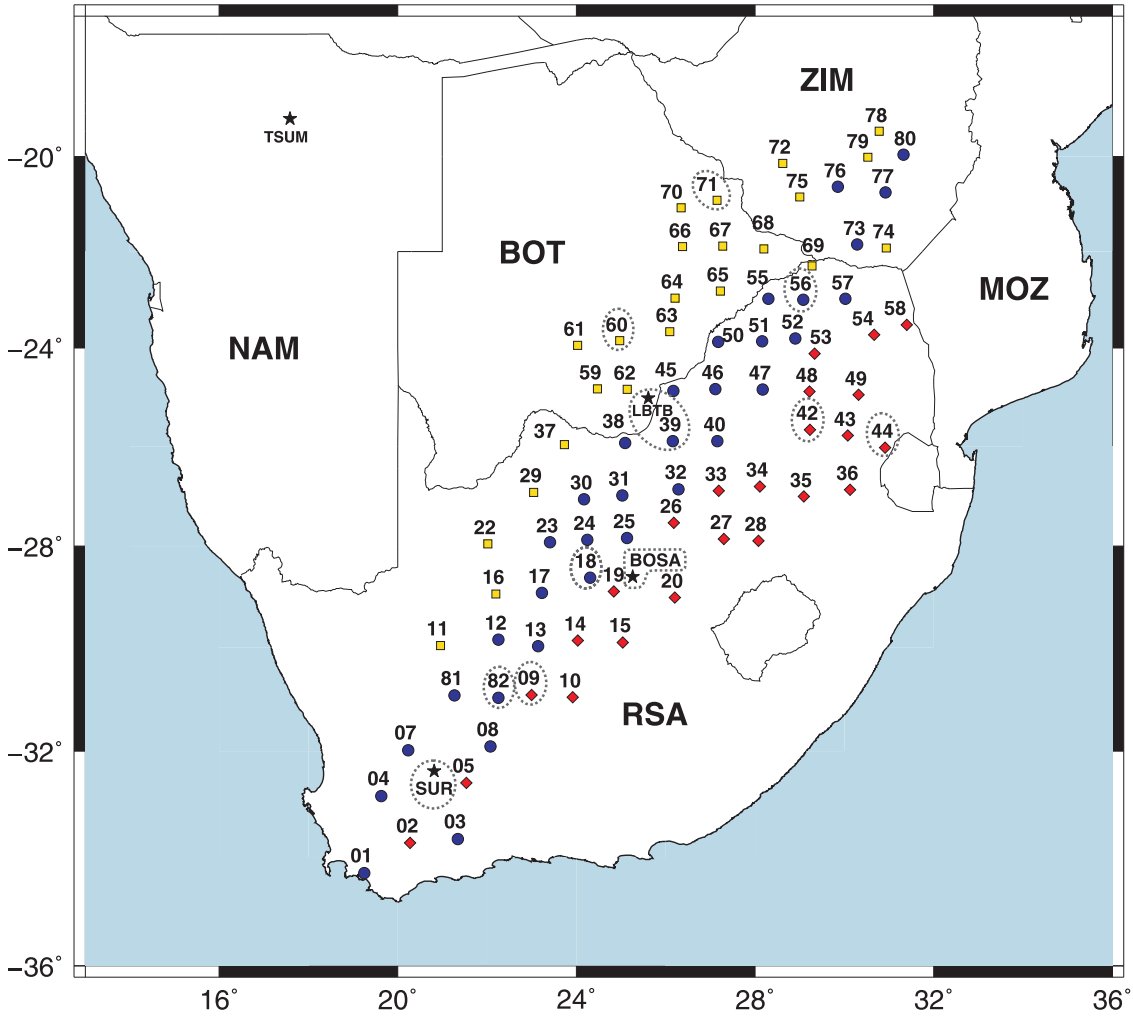

Figure 5-1: *Location map for the southern African seismic array stations, with political boundaries, and stations that have been re-analysed circled. Yellow squares denote stations deployed during the first year of the experiment (April 1997). These stations were redeployed in April 1998 to station locations denoted by red diamonds. Stations represented by blue dots were deployed for the full two years of the experiment. The stations were named by the numbers next to the symbols, with the prefix "SA". Additionally, the locations of four permanent stations: SUR, BOSA, LBTB, and TSUM are indicated. In total 82 stations were occupied during the experiment. NAM: Namibia, BOT: Botswana, ZIM: Zimbabwe, MOZ: Mozambique, RSA: Republic of South Africa.*

They make mention of three interesting and striking observations in their results: 1) an arc of values from the southwestern Kaapvaal craton up to the Limpopo, where the fast axis direction is parallel to the trend of the arc; 2) fast axis values are parallel to the Great Dyke in Zimbabwe; 3) the contrast between the relatively weak anisotropy on the eastern

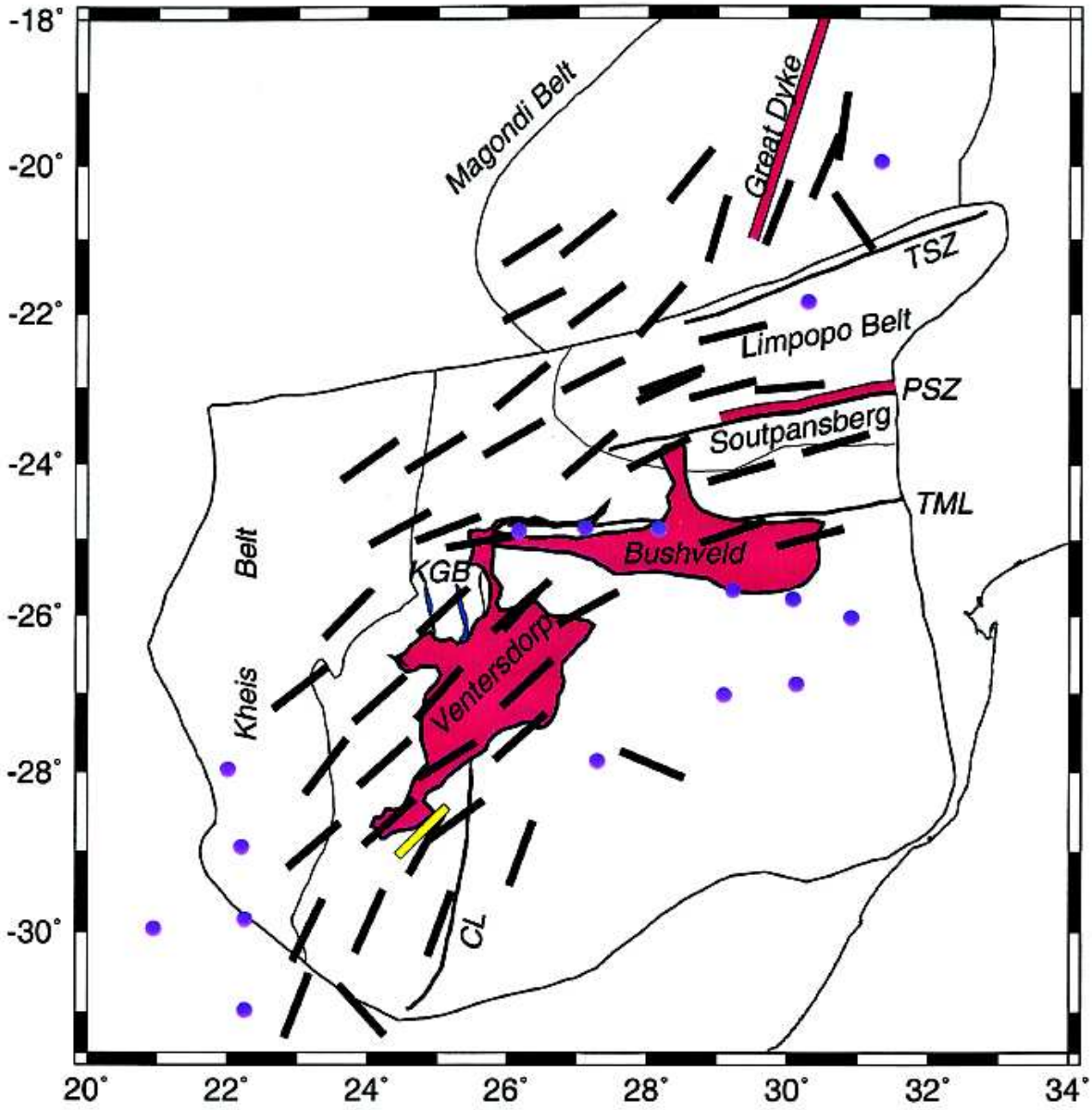

Figure 5-2: *Results of shear wave splitting study reported in Silver* et al. *(2004). Map shows the orientation of the fast polarisation direction from the Kaapvaal Seismic Array (black bars), and the average from the Kimberley Telemetered Array (yellow bar), overlain on relevant geological features. Only the highest-quality measurements are shown here. Purple dots represent near-zero splitting delay times. Abbreviations: TML: Thabazimbi Murchison Lineament, CL: Colesberg Lineament, KGB: Kraaipan Greenstone Belts, SZ: Shear zone. Major rift systems with basaltic magmatism: Great Dyke, Ventersdorp (surface exposures), Bushveld and Soutpansberg, shown in red.*

Kaapvaal Craton, with the stronger anisotropy in surrounding areas to the north and west (not presented in figure 5-2 from Silver *et al.* (2004)). Silver *et al.* (2001, 2004) suggest that seismic anisotropy is dominated by deformational events in the Archean, located within the lithosphere, rather than by present-day processes in the sublithospheric mantle. Figures 5.3(a) and 5.3(b) were used to support this argument, in addition to a qualitative look at the results in figure 5-2, which shows clear regional variations in the splitting parameters within cratonic southern Africa. Figure 5.3(a) compares the splitting results of the study with two models of absolute plate motion (APM) directions from Gripp & Gordon (1990, 2002). There is no clear trend between the splitting results and the trend of either of the APM models. Conversely, when the splitting results are plotted with primary surface geological trends (figure 5.3(b)), there does tend to be a better correlation in many, but by no means all, areas. Additionally, the results from the smaller array ($\approx 60\times40$ km) surrounding the Kimberley region (Fouch *et al.*, 2004b) show a systematic variation in splitting delay time across the array, decreasing from about 0.8 to 0.2 seconds over only 60 km. The small aperture of the array suggests that these differences are a result of variations in lithospheric mantle fabric, and not deeper.

Silver *et al.* (2001, 2004) suggest that the results of the Kaapvaal shear-wave splitting study represent Archean-aged deformational structures and are not due to absolute plate motion, after the hypothesis suggested by Vinnik *et al.* (1992, 1995). It is difficult to gain accurate depth constraints on shear-wave splitting results however, Silver *et al.* (2001) infer that the causative anisotropic layer resides at upper mantle depths, within the lithosphere. It was inferred to be at these depths for a number of reasons. Firstly, crustal splitting was measured using P-to-S converted phases at the Moho. The splitting delay time calculated for the crust was found to be approximately 0.15 s. The fast axis direction of the anisotropy in the crust is not well constrained due to the small delay times, although the delay times were thought to be a more robust value. Secondly, using Fresnel-zone arguments (Rümpker & Ryberg, 2000), the abrupt changes is splitting parameters at nearby stations constrains the *top* of the anisotropic layer to be no deeper than 50 - 100 km. Lastly, the surface wave study of Freybourger *et al.* (2001) places the anisotropy within the lithosphere.

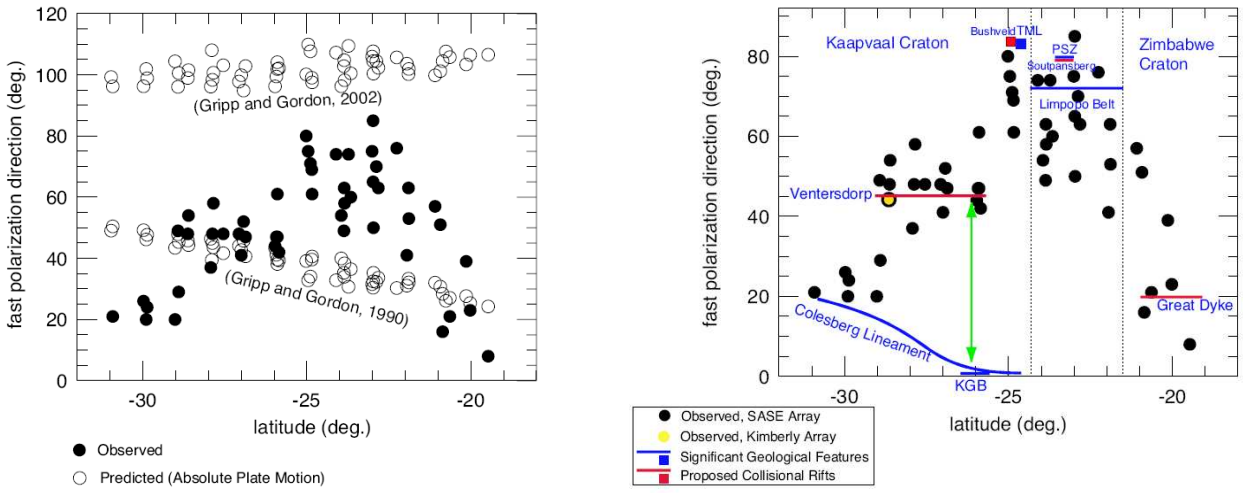

(a) (b)

Figure 5-3: *The results of the shear wave splitting study reported in Silver* et al. *(2004) are thought to be due largely to fabric that has been frozen-in to the lithosphere during the deformational history of the region. The arguments for this are drawn largely from these two plots. (a) A comparison of the shear wave splitting results with two models of absolute plate motion (APM) (Gripp & Gordon, 1990, 2002). (b) A comparison of the shear wave splitting results with primary surface geological features. The two vertical dashed lines give the approximate latitude range of the Limpopo belt.*

5.4 Re-analysis of SASE shear wave splitting

For reasons relating to resources and expertise, the splitting re-analysis was conducted using the method of Silver & Chan (1991), utilising code written by Professor David W.S. Eaton[1], with helpfull additional code and advice from Dr. Mark D. Behn[2]. It was necessary to decide this early on in the study, as it has consequences, such as to which data format was going to be downloaded.

5.4.1 Event selection

The first step in the shear wave splitting re-analysis of some of the SASE data was to select the events that were going to be analysed. In order to reduce the vast amount of data that are available for download from the IRIS[3] data centre, there are a number of criteria that

[1]University of Western Ontario, Canada. Now at the University of Calgary, Canada.
[2]Woods Hole Oceanographic Institution, MA, U.S.A.
[3]http://www.iris.edu/

may be used to select certain events that will be more likely than others to contain SKS, SKKS, and PKS splitting (discussed in Chapter 3). The Advanced National Seismic System catalogue, ANSS[4], was used to select this list of events. The criteria used to do this initial selection were: start and end date when the recordings were being made, a minimum magnitude of 6.0, and epicentral distance criterion. The final list of events to be inspected for shear wave splitting may be characterised by the histograms in figure 5-4. Figure 5.4(a) is a histogram of the magnitudes of the events selected; all are above 6.0 (as selected), but magnitude decreases in number with increasing magnitude as would be expected since larger magnitude earthquakes occur less frequently. Figure 5.4(b) is a histogram showing the epicentral distances of the selected events which fall within the window where SKS, SKKS, and PKS arrivals would be expected. The hypocentral depths (figure 5.4(c)) show more events at shallower depths, as would also be expected since deep earthquakes are restricted to regions where there are subducting slabs, and are thus less frequent, less well distributed, and at the "wrong" epicentral distances. Even though there is a relatively short period of recording, there does appear to be a fairly good backazimuthal coverage (figures 5.4(d), 5-5) with respect to the approximate array centre; however, it should also be noted that this will be different for each station since there is a slight positional difference as well as recording time period for each. These data were downloaded in compressed sac binary format, for each site that recorded these events. Data included three components (BHN, BHE, BHZ), with a time window of 2 minutes before the first P arrival, to 40 minutes after the first P arrival.

Once the first set of criteria has been satisfied, and we have a preliminary list of events that may be useful for splitting analysis, the next step is to plot the corresponding seismogram for a given event at all the stations, to see if the event has resulted in data that may be useful in a splitting analysis. This is the first look at the actual data, and is where obviously poor events (e.g. figure 5-6), with low signal to noise ratios and no clear shear wave arrival, may be removed from the list for further analysis, while high quality events (e.g. figure 5-7) are retained for the splitting analysis. This process is only done for one horizontal component of the seismogram, and if an event shows no clear shear wave arrival, it is necessary to check the other horizontal component seismogram before discarding. This is necessary because if it happens that the seismic anisotropy in the region is, for example, predominantly east-west, and the backazimuth of the event is east or west of the station, it is likely that most of the shear wave energy may be on the E component seismogram. If we were to look only at the N component seismogram in this process, we would likely throw this

[4]http://www.ncedc.org/anss/catalog-search.html

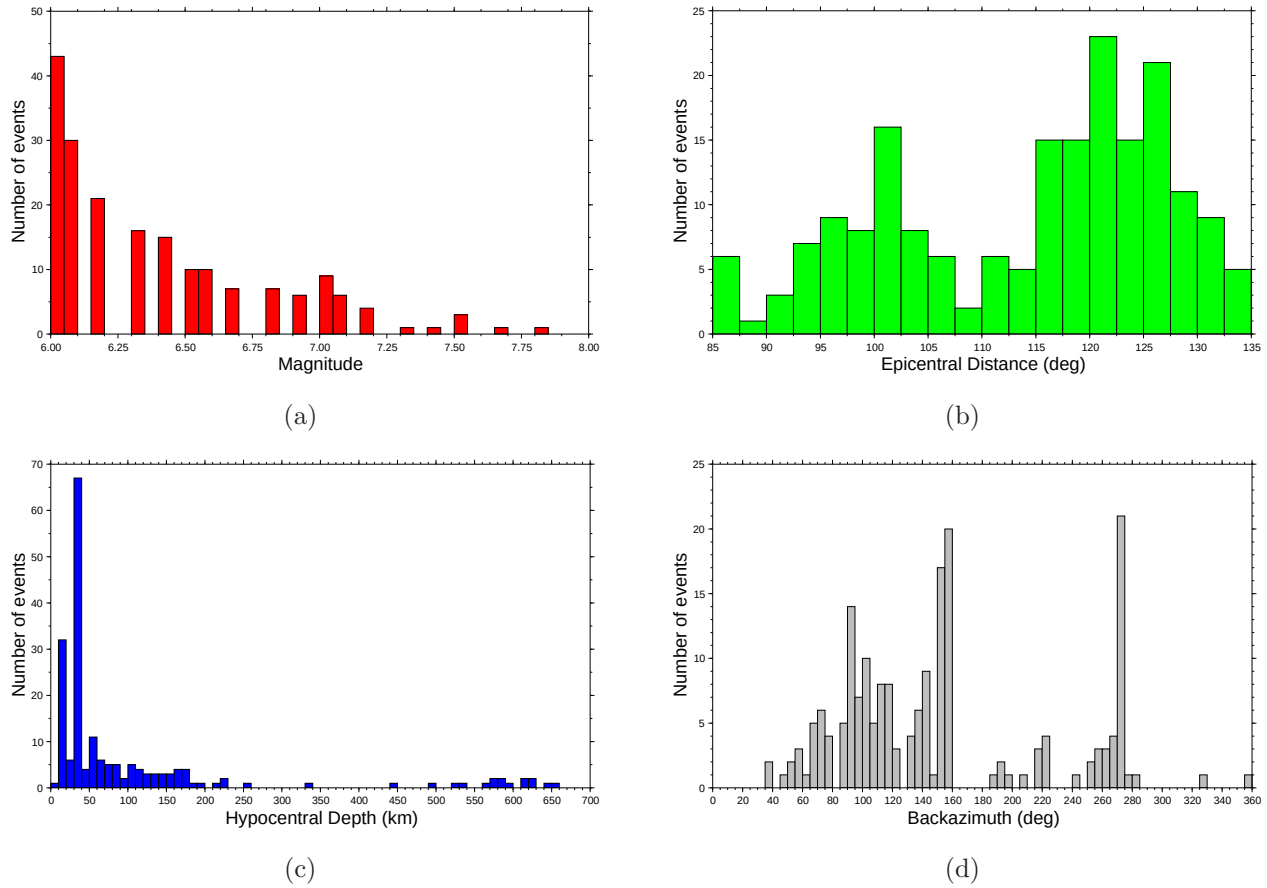

Figure 5-4: *Histograms describing the nature of all the events originally selected for shear wave splitting re-analysis of the SASE array data. (a) The magnitudes selected are all 6.0 or greater, as these generally provide better signal to noise ratios. (b) The epicentral distances of the events selected are in the range 85°to 135°, which encompasses the range where SKS, SKKS, and PKS are expected. (c) The hypocentral depth of the events. (d) Backazimuthal coverage of events.*

event away, when, in actual fact, it provides very useful information. An event such as this would be recorded as a null event, with the E component (the radial component) having the majority of the shear wave energy.

5.4.2 Station selection

The next step in the re-analysis was to select the stations that were to be re-analysed. The first criteria for this was to, where possible, select stations that had recorded for longer periods of time and would therefore be likely to have more splitting data (blue stations in figure

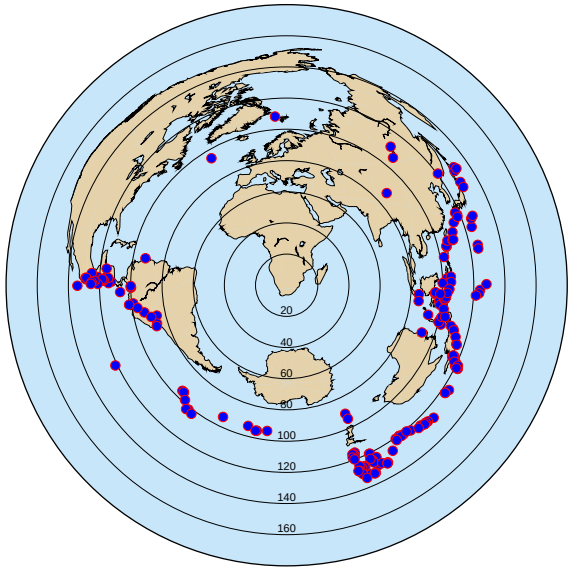

Figure 5-5: *Event locations for the preliminary list of events to be used in the splitting analysis of the SASE stations (Appendix 3).*

5-1). Additionally, it was decided that it would be best to select sites that were representative of the different geological regions (on craton, off craton, etc.), as well as sites with different splitting results (nulls and good splits). Using these criteria, the sites that were originally selected for reprocessing were sites: SA18, SA39, SA56, SA82, SA09, SA60, SA71, SA42, and SA44 (figure 5-1, table 5.1). Although the last five only recorded for one year, they were selected because they were representative of different splitting parameters and different regions. Subsequent to the original re-analysis, other stations that were re-analysed in order to try to gain further information, include the three permanent stations: SUR, LBTB, and BOSA (figure 5-1) (Appendix 4).

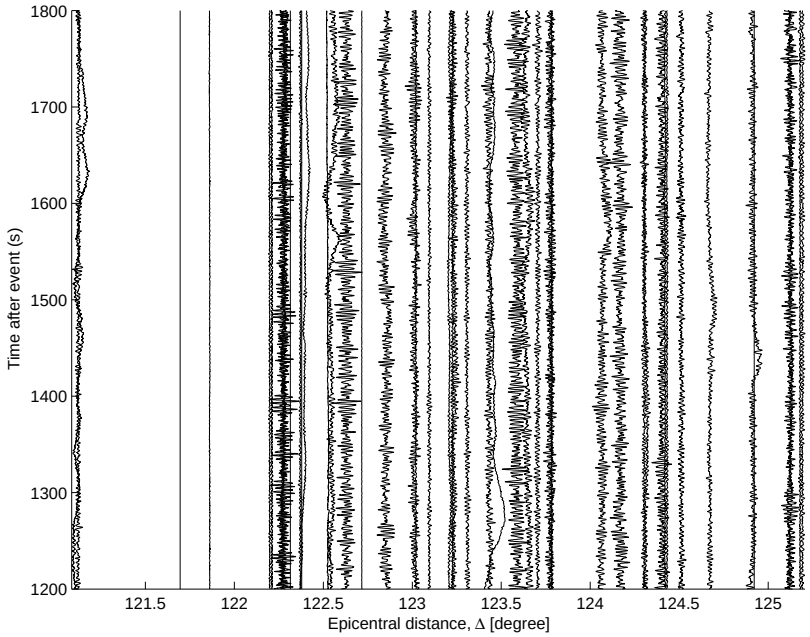

Figure 5-6: *Plot of the seismogram of the N component for each site as a function of epicentral distance, for the range where an SKS split would be expected. This plot is for a magnitude 6.0 event at a depth of ≈139 km, located near Fiji occurring on 14/12/1998 at 19:35:27. There is no clear shear wave arrival at any of the stations for the N component seismogram. This was repeated for the E component seismogram, which provided a similar result. This event was therefore discarded, and was not used for the splitting analysis.*

Station	Fast axis	Delay time	Location	Record time
SA18	48˚	0.75 s	western Kaapvaal craton	2 years
SA39	47˚	0.80 s	western Kaapvaal craton	2 years
SA56	75˚	0.60 s	Limpopo belt	2 years
SA82	null	0.00 s	Namaqua-Natal mobile belt	2 years
SA09	21˚	0.50 s	Namaqua-Natal mobile belt	1 year
SA60	58˚	0.85 s	western Kaapvaal craton/Kheis belt	1 year
SA71	51˚	0.75 s	Zimbabwe craton	1 year
SA42	null	0.00 s	eastern Kaapvaal craton	1 year
SA44	null	0.00 s	eastern Kaapvaal craton	1 year

Table 5.1: *Table with seismic stations selected for shear wave splitting reanalysis. Splitting parameters are those of Silver* et al. *(2001).*

5.4.3 Preparation for splitting analysis

Data from each of these stations were then analysed for SKS, SKKS, and PKS splitting for each of the events on the list of good potential splits. This was done by plotting the radial and

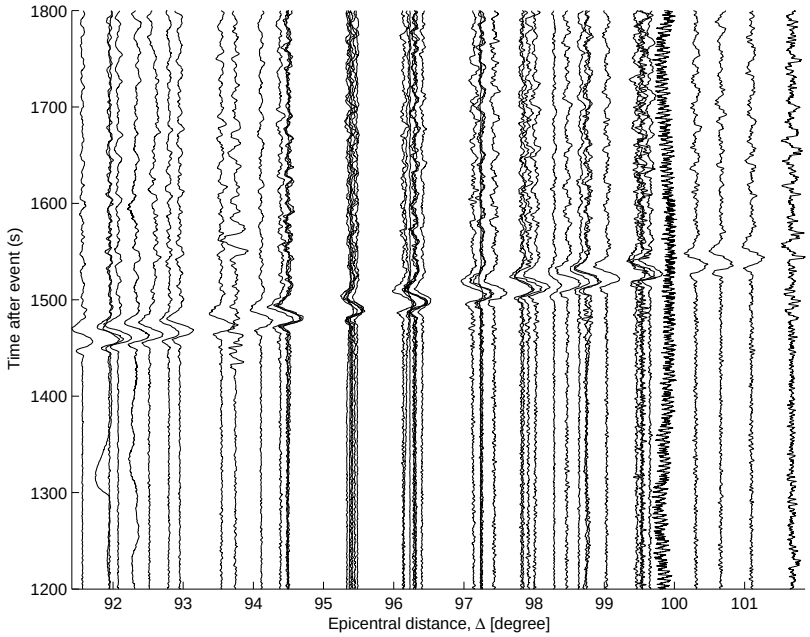

Figure 5-7: *A plot of the seismogram of the N component for each site as a function of epicentral distance, for the range where an SKS split would be expected. This plot is for a magnitude 7.0 event at a depth of ≈24 km, located near Indonesia occurring on 25/11/1997 at 12:14:34. There is a very clear shear wave arrival at most of the stations for the N component seismogram. This event might produce a good splitting result at some of the stations, and was therefore retained for the splitting analysis.*

transverse traces for each event over a time interval that encompasses the predicted travel time using the IASP91 model (vertical red line in figure 5-8) for each phase for the given event-station pair. The recording in figure 5-8 is a good example of a null, since visually all the energy is on the radial component. From this analysis, a time window is selected around the split phase, defining the time segment to be used later in the splitting analysis. If necessary this time window may be changed slightly at a later stage in the analysis in order to get a complete ellipse of the particle motion.

5.4.4 Splitting analysis

Once the time window for each possible splitting at a station had been selected for the list of events, the windowed data segments were analysed using the method of Silver & Chan (1991). The quality of the splitting analysis, or the splitting itself, can then be seen quite clearly. Examples of various quality splits are displayed in the analysis results in figures 5-9, 5-10, and 5-11. Figure 5-9 displays the results from a good split. Importantly, the particle

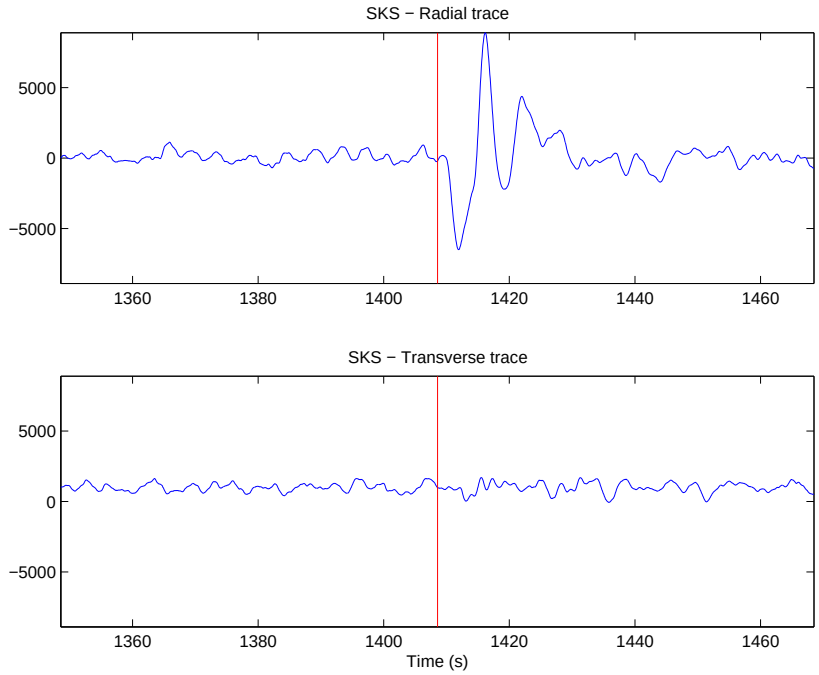

Figure 5-8: *A radial and transverse trace of an event on the 08/04/1999, recorded at station SA44. Vertical axis is the scaled magnitude, scaled by the maximum amplitude of both traces. The red line is the predicted arrival time of the SKS phase from the IASP91 model. This is a good example of a null result, with all the energy on the radial trace.*

motion (portrayed in the hodogram) has changed from elliptical, prior to the analysis (red line), to near linear after splitting has been removed (blue line). This indicates that the splitting parameters obtained in the analysis are appropriate. Additionally, the error map shows a fairly well constrained region of lowest error (dark blue).

In contrast to figure 5-9, figure 5-10 is a medium quality split, and figure 5-11 is a poor split. In figure 5-11 there is poor signal-to-noise ratio in the seismograms (visible in the plot of the unrotated waveforms). Additionally, not only is the particle motion, after splitting has been removed, still not linear, but the error surface in the error map is not very tightly constrained (there is a large region of dark blue, where the splitting parameters may fall). Another situation where the parameters are not normally well constrained is when there is a null splitting result (figure 5.12(a)). A null response is characterised by having nearly all the energy on one component, producing a particle motion that is already near linear. This constrains a possible splitting direction to $\pm$ 90°, although the delay time is not well constrained. Quite often the data windows for the analysis need to be edited slightly to obtain a window containing only the split shear wave of interest, although from experience

this seldom alters significantly the results of the splitting analysis.

Once these analyses have been completed, we are able to plot splitting parameters as a function of backazimuth. This provides a means with which to infer whether there is a more complex anisotropy system than a single horizontal layer (the simplest), as was discussed in chapter 3. Figure 5-13 is a an example of this from one of the reanalysed sites (SA71). Of the sites that were analysed, this is the site with the most high-quality splitting results, and with probably the best backazimuthal coverage. Figure 5.12(b) is a plot of the backazimuth directions (black lines) of null splitting results from SA82. Of the sites analysed, this has the most null values. Since a null result has 90° ambiguity for a possible fast axis direction, we also plot the backazimuth+90° (blue lines). It is then possible for us to take these single event splitting results for each station, and stack the events using the method of Wolfe & Silver (1998). This assumes that there is a single layer of anisotropy with a horizontal symmetry system. The results of this multi-event stacking procedure is an error map of the fast axis and delay time over the searched parameters, the minimum of which corresponds to the single fast axis direction and delay time value appropriate for a single horizontal layer of seismic anisotropy. These results are described later in table 5.2, with an example of the error map produced in this analysis displayed for site SA71 in figure 5-13.

5.5 Results of splitting re-analysis

One of the aims of this part of the study was to become more familiar with the SASE seismic data and to see if there were any peculiarities in the data that might have been overlooked in the Silver *et al.* (2001) study. In order to asses if there may be anything unusual, we plot the splitting parameters as a function of backazimuth (as discussed earlier). The upper two plots in figure 5-13 display this for station SA71, which has the best backazimuthal variation and good splits of all of the re-analysed sites. It is clear that although this is one of the better sites the backazimuthal coverage is still relatively poor. A model for a single horizontal layer of anisotropy would correspond to two horizontal lines in these plots, and could, for the most part, fit our data (figure 5-13). This is the case for most of the sites re-analysed. However, there is one data point in the fast-axis vs. backazimuth plot in figure 5-13 that has a fast axis direction of 85° and appears to contradict this simple model, since all the other fast axis directions are around 45°. However it is only one data point, and unfortunately the splitting analysis for this station-event pair is not well constrained (lower left in figure 5-13), having a low signal-to-noise ratio and a fairly poorly constrained error map.

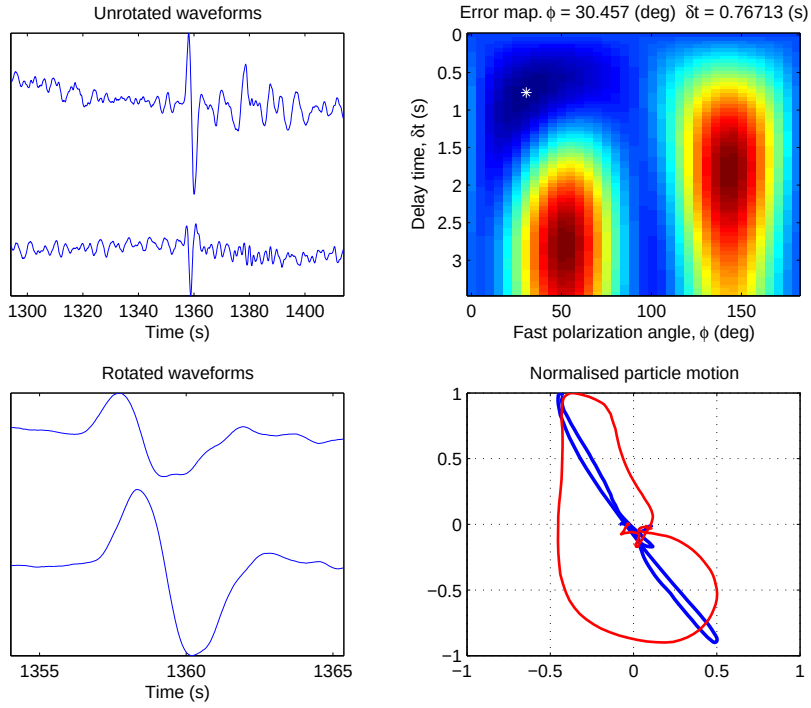

Figure 5-9: *An example of a good splitting result at station SA39 for a single event at 07h50 on the 22/05/1997. Top left: Radial (top) and transverse (bottom) seismograms in window around split phase. Top right: Error map of delay time and fast axis direction over searched parameters. Minimum value marked with white star. Bottom Left: Rotated fast (top) and slow (bottom) seismograms over the time window analysed. Bottom right: Normalised particle motion diagram (hodogram) of original (red) and corrected (blue) seismograms.*

It was the result obtained for station SA71 that was the motivation behind the reanalysis of the permanent stations BOSA, LBTB, and SUR. It was thought that, since there was a longer period of recording at these stations, they may provide splitting results with better backazimuthal coverage, and therefore a better indication as to whether the unusual data point observed at station SA71 is likely to indicate more complex anisotropy or if it is merely a poor splitting result. After careful event selection, the analysis did not provide the significantly better backazimuthal coverage that was hoped for. The three permanent stations have clearly had some operational difficulties, however, this situation does seem to be better for more recent events. Station SUR is a null station (as was observed by Silver *et al.* (2001)). Stations BOSA and LBTB provide fair splitting results, although they are generally not of high quality. Both stations LBTB and BOSA do each have a single event analysis (different events) that would contradict a single layer model. Both of these unusual

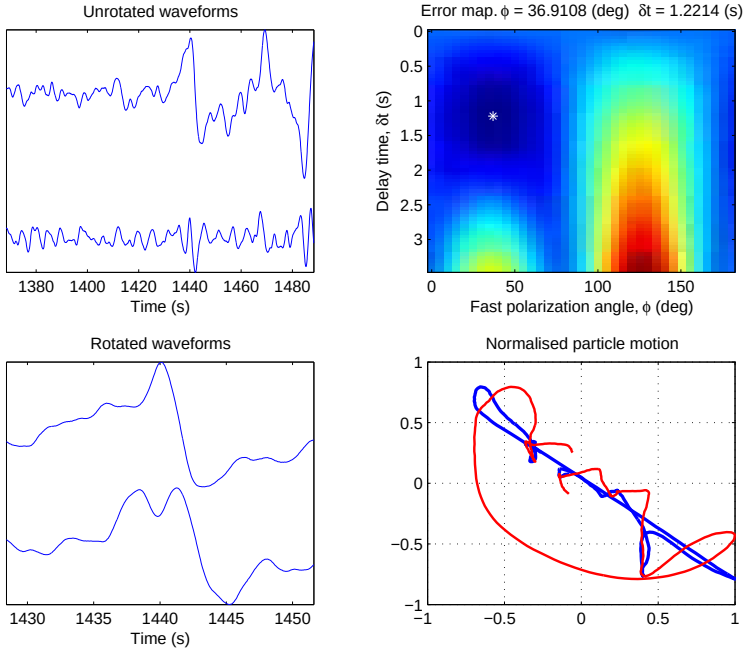

Figure 5-10: *An example of a medium quality splitting result at station SA18 for a single event at 06h15 on the 28/10/1997. Explanation as in figure 5-9.*

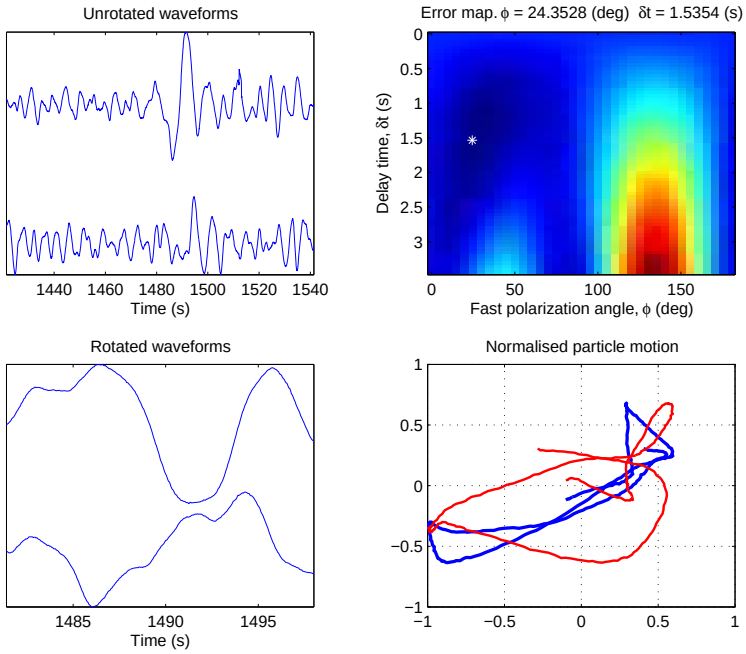

Figure 5-11: *An example of a poor quality splitting result at station SA71 for a single event at 16h33 on the 21/03/1998. Explanation as in figure 5-9.*

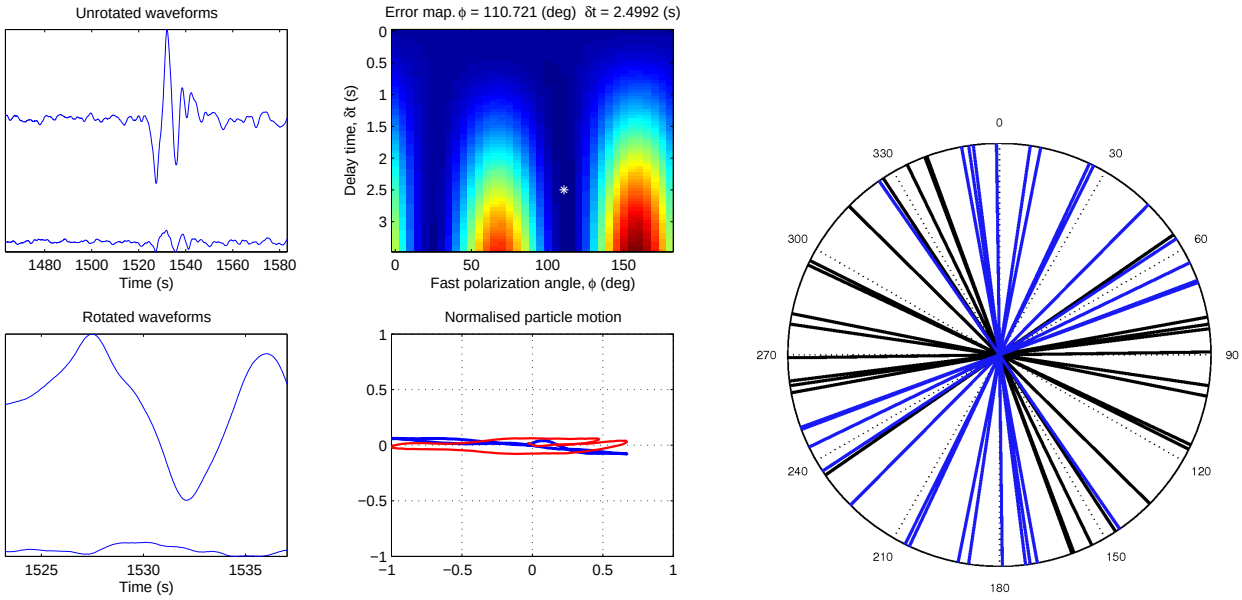

(a) (b)

Figure 5-12: *(a) An example of a null splitting result at station SA82 for a single event at 11h08 on the 05/04/1999. Explanation as in figure 5-9. (b) The null results as a function of backazimuth (compass plot) for station SA82. Black lines are the actual backazimuth directions, while the blue lines are 90° to the backazimuth.*

splits are of medium/poor quality, and occur at backazimuths both different to that observed in SA71. Unfortunately, after systematically searching and analysing events for each of these stations with backazimuths around the same values as the unusual splitting results, there was no other split that could be found to support, or to contradict, this result. Since the unusual results are singular at each station, medium/poor in quality, and cannot be supported by other splitting analysis at a nearby backazimuth, we cannot make any further deductions from these data with any confidence. Of course, with the backazimuthal coverage we obtain, it would likely be possible to fit a huge number of models to these data by simply using a forward model, such as that of Silver & Savage (1994) (figure 3-4), and thus we are unable to exclude, with confidence, the existence of more complex anisotropy.

The waveform inversion method of Özalaybey & Savage (1994) was used on four sites with good splitting results to try to estimate splitting parameters assuming two horizontal anisotropic layers. This inversion method is very similar to the multi-event averaging technique of Wolfe & Silver (1998), except that the effects of double, rather than single, layer splitting are modelled. Unfortunately, the results of this analysis did not provide any

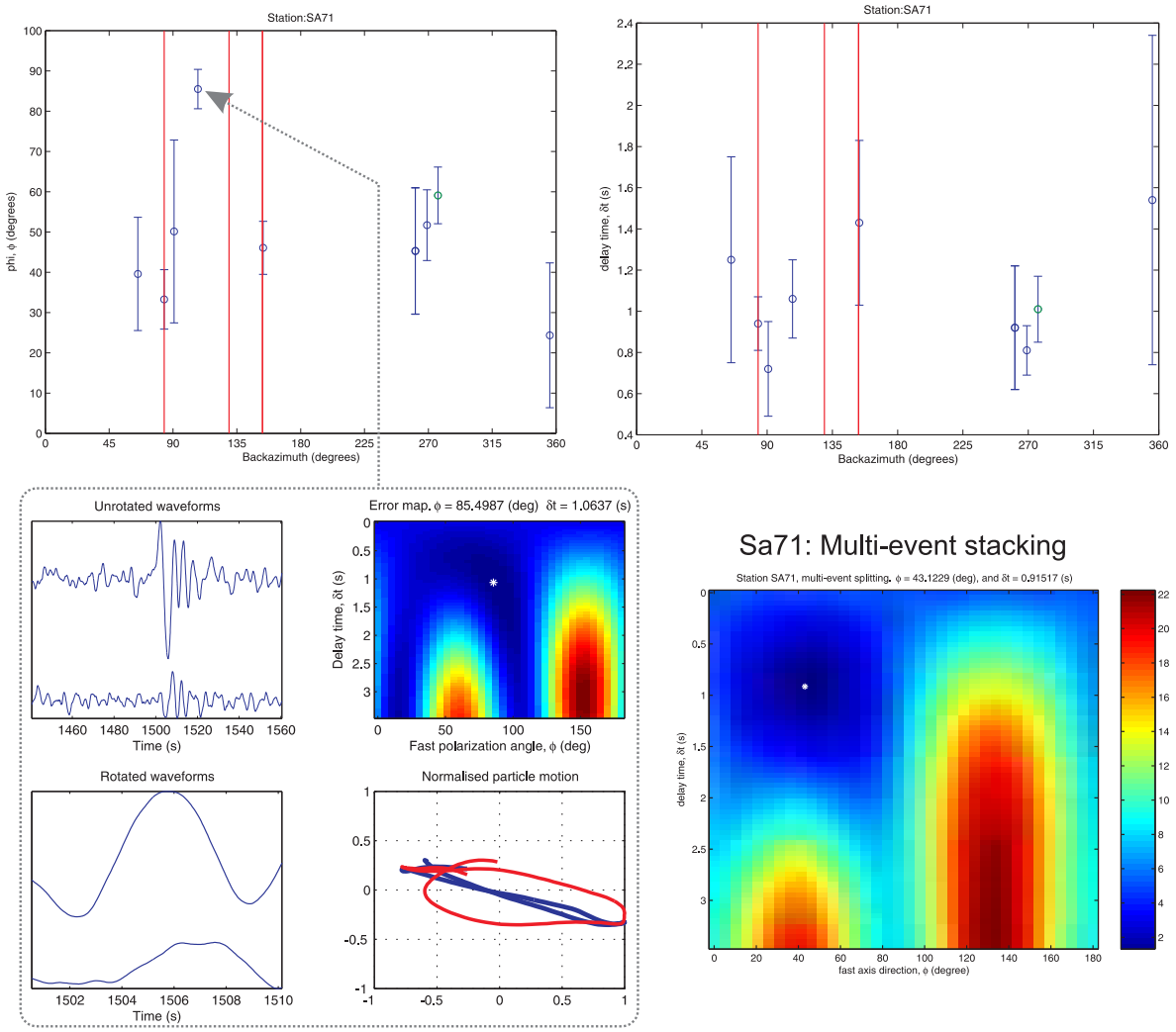

Figure 5-13: *Splitting results from station SA71 as a function of backazimuth. Top left: Fast axis direction versus backazimuth. Top right: Delay time versus backazimuth. Red vertical lines are null measurements. Bottom left: Single event splitting analysis from a magnitude 7.2 event in eastern New Guinea on 22/12/1997 at 02h05. Bottom right: Results of multi-event stacking for station SA71.*

conclusive constraints on two-layer anisotropy for any of the four stations that were used for this analysis.

Table 5.2 is a summary table of the multi-event stacking results obtained in this study compared with the results from the Silver *et al.* (2001) study. Note that the number of events used in this study (last column in table 5.2) is counted multiple times if multiple split phases (e.g. SKS and PKS) are used from the same event. We were unable to obtain from Silver

et al. (2001) a list of the events and phases that they used for their analysis, so differences may be due to choice of events. As can be seen in the table below, apart from LBTB and possibly SA18, there are no statistically significant differences between the results of Silver *et al.* (2001) and this study. The null stations that were observed by Silver *et al.* (2001) are all observed as nulls in this study (SA82, SA42, SA44, SUR). Taking errors into account, sites SA39, SA56, SA09, SA60, and SA71 are statistically the same, although stations SA09 and SA60 have large errors due to the low number of splitting events found in the analysis (1 and 2 respectively). Again, taking errors into account, station SA18 is only different in the two studies by one degree for the fast axis direction, with the delay times calculated being statistically the same. However, assuming normal distributions of 10000 samples (simply a rough reference value of samples), the null hypothesis that the mean fast axis directions (37° and 48°) are equal at the 0.05 significance level can be rejected. Station BOSA has exactly the same fast axis direction in the two studies, although the delay times are not within error of each other by 0.08 s. Station LBTB has different fast axis directions, but delay times that correspond between the two studies, only because the error on the delay time is large for this study. Our results for BOSA and LBTB are however far more consistent with, and are statistically the same as, the analysis done by Barruol & Ben Ismail (2001) on permanent stations in the region. A feature that is consistant throughout the results of our study is that the errors that we derive are consistently larger than those of Silver *et al.* (2001). Since we might be using different events for our analysis, it is unlikely that we would get exactly the same results, and it was thought that it may be due to this study using less events. Although, from discussion with these authors (Gao, S.S. Personal communication, September 2007), other possibilities that were suggested which may contribute to the discrepancy in errors is the use of different filtering parameters, as well as using different beginning and end times of the seismogram section for the splitting measurements (window times).

It is pleasing that the measured parameters of Silver *et al.* (2001) and this study are very similar, indicating that the results are robust, and that our analysis techniques and programs are sound. What is not so satisfying about the measurements is the lack of quality splitting results for a broad backazimuth, which would allow us to have more certainty on the nature of the anisotropy. However, this was to be expected due to the relatively short recording time of the array.

Table 5.2: *A comparison of the splitting parameters obtained by Silver* et al. *(2001), with the parameters obtained in this study, for the reprocessed sites. Parameters include: fast axis direction and error (ϕ, and σ_ϕ), delay time and error (δt, and $\sigma_{\delta t}$), as well as the number of events actually used in this study for each station. First number is split events, number in brackets includes null events. The last column indicates if results are in agreement, Y; marginally different, M; or completely different, N. Y(B) indicates agreement with the study by Barruol & Ben Ismail (2001).*

	Silver *et al.* (2001)				**This study**					Agreement
Station	ϕ	σ_ϕ	δt	$\sigma_{\delta t}$	ϕ	σ_ϕ	δt	$\sigma_{\delta t}$	# events	Y/M/N
SA18	48°	4°	0.75 s	0.08 s	37°	6°	0.97 s	0.14 s	7 (22)	N
SA39	47°	3°	0.80 s	0.10 s	40°	5°	0.78 s	0.10 s	5 (12)	Y
SA56	75°	2°	0.60 s	0.12 s	68°	14°	0.76 s	0.20 s	2 (26)	Y
SA82	null	-	0.00 s	-	null	-	0.00 s	-	0 (20)	Y
SA09	21°	8°	0.50 s	0.12 s	32°	31°	0.52 s	0.80 s	1 (5)	Y
SA60	58°	4°	0.85 s	0.12 s	45°	22°	0.77 s	0.32 s	2 (8)	Y
SA71	51°	4°	0.75 s	0.07 s	43°	8°	0.90 s	0.16 s	10 (14)	Y
SA42	null	-	0.00 s	-	null	-	0.00 s	-	0 (9)	Y
SA44	null	-	0.00 s	-	null	-	0.00 s	-	0 (15)	Y
SUR	null	-	0.00 s	-	null	-	0.00 s	-	0 (6)	Y / Y(B)
LBTB	80°	5°	0.45 s	0.18 s	47°	15°	0.69 s	0.41 s	5 (15)	N / Y(B)
BOSA	54°	4°	0.45 s	0.08 s	54°	11°	0.92 s	0.31 s	5 (13)	M / Y(B)

5.6 Comparison with plate motion and mantle flow

LPO from asthenospheric flow, or the resulting present-day deformation within the asthenosphere that is a result of the motion of the tectonic plate over the deeper mantle, is a commonly invoked explanation for teleseismic shear wave splitting. It is therefore necessary to compare the fast axis direction of the splitting results with models of flow and plate motion in order to observe if there is a correlation, and whether this may be the cause of shear wave splitting in a region. This was considered by Silver *et al.* (2001) but we take a closer look at it here.

There are many different models that have been proposed and created for both plate motion as well as mantle flow. The two plate motion models that are plotted in figure 5.3(a) are HS2-NUVEL1A (Gripp & Gordon, 1990) and HS3-NUVEL1A (Gripp & Gordon, 2002), both of which are models that represent motion relative to a fixed hotspot reference

frame. The HS3-NUVEL1A model is newer, with smaller uncertainties, being averaged over a shorter and more uniform time interval. However, Gripp & Gordon (2002) suggest that the movement of the African plate in the HS3-NUVEL1A model may be subject to small systematic errors. If the asthenospheric mantle is assumed to be fixed in a hotspot reference frame, then these model plate motion directions would likely represent the fast axis splitting directions if the anisotropy is due to shear at the base of the lithosphere. It will be noted that there appears to be a very strong difference between the two models for the motion of the African plate (figure 5.3(a)). This is likely because the absolute velocity of Africa is not well constrained, since plate velocities are small.

The earlier HS2-NUVEL1A model of Gripp & Gordon (1990) does tend to fit GPS data for the region far better than the HS3-NUVEL1A model, even although the GPS data are sparse (figure 5-14). We have used GPS data analysed by the Jet Propulsion Laboratory, California Institute of Technology[5], with the ITRF2005[6] reference frame. The plate motion models of Gripp & Gordon (1990, 2002), which are referenced to the fixed "hotspot" frame were calculated using the calculator provided by UNAVCO[7].

5.6.1 Seismic anisotropy from mantle flow models

Mantle flow modelling is a very active field of research, with models continually adding more constraints from various geoscientific techniques (e.g., geochemistry, petrology, etc.). It is possible to predict the seismic anisotropy direction from mantle flow models. Simple shear flow is a flow pattern expected to prevail throughout most of the asthenosphere, as the differential motion between the lithosphere and upper mantle is accommodated within the low-viscosity asthenosphere (Conrad *et al.*, 2007). Although unusual fabrics may occur in certain regions which are high stress and/or water-rich (Jung & Karato, 2001; Mizukami *et al.*, 2004; Kneller *et al.*, 2005) such as subduction zones, the a-type fabric is expected to be dominant for most regions of the asthenosphere. Therefore for asthenospheric simple shear, with a horizontal shear plane, the horizontal projection of the LPO may be used to predict seismic anisotropy. The assumption here is that the anisotropy forms quickly and does not depend on the deformation history.

[5]http://sideshow.jpl.nasa.gov/mbh/series.html
[6]http://itrf.ensg.ign.fr/ITRF_solutions/2005/ITRF2005.php
[7]http://sps.unavco.org/crustal_motion/dxdt/model/

If the flow is more complex due to spatial and time variations, it is necessary to consider finite strain accumulation. Kaminski & Ribe (2002) introduced the infinite strain axis (ISA) to determine the conditions under which it is necessary to integrate LPO along flow lines (Conrad *et al.*, 2007). The ISA is defined as the asymptotic orientation of the long axis of the finite strain ellipsoid in the time limit of infinite strain (Kaminski & Ribe, 2002). The ISA can be defined for every point and time in a time variable flow field, and since the olivine a-axis aligns with the finite strain ellipsoid for the a-type fabric (Zhang & Karato, 1995), the ISA should approximate the LPO in the upper mantle, assuming that the velocity gradient tensor remains constant for olivine crystals moving along flow lines. Since this is generally not likely to be the case, the ISA direction may change with time, and will only be a good approximation for LPO if the olivine crystals rotate towards the ISA faster than the ISA changes along flow lines (Kaminski & Ribe, 2002). In order to determine if this happens fast enough, Kaminski & Ribe (2002) introduce the grain orientation lag parameter (Π), which is a purely local parameter whose value will in general depend on position and on time if the flow is unsteady. They find that if $\Pi<0.5$, the ISA is a good approximation for LPO. This simplifies the predictions of anisotropy from a given flow field since finite strain calculations are unnecessary.

In this study, we have used the recent mantle flow model constructed by Conrad *et al.* (2007) using finite element modelling, which is driven by combinations of mantle density heterogeneity inferred from seismic tomography (density-driven flow) and surface plate motions (plate driven flow), as undertaken by Behn *et al.* (2004). For the flow fields in their model, they calculate the ISA as well as the Π parameter of Kaminski & Ribe (2002). This means that, from their model, the ISA can be used as an approximation for LPO, and it can be used to test if the approximation is valid by determining if $\Pi<0.5$. Conrad *et al.* (2007) show that Π is small throughout the asthenosphere away from plate boundaries. At plate boundaries, the strain history of flow needs to be considered, and computing strain deformation may involve complex, and often poorly constrained, modelling of the time dependence of the flow field (Kaminski & Ribe, 2001; Becker *et al.*, 2003; Kaminski *et al.*, 2004; Becker *et al.*, 2006). Southern Africa, however, is far from plate boundaries, and so this is not a concern while employing this model in our study. In general, Conrad *et al.* (2007) find that their predictions of LPO (assuming ISA orientation approximates asthenospheric LPO) agree better with shear wave splitting observations below the oceanic regions, while there is a generally poorer fit below continental regions. However, this is not always the case, as they observe in western North America, although lithosphere is known to be thin there. They

conclude that asthenospheric anisotropy is probably present beneath oceanic and continental regions. However, below continents, the lithosphere may retain a fossil fabric that controls the net anisotropy.

5.7 Correlation with plate motion and mantle flow

We take the two plate motion models, HS2-NUVEL1A (Gripp & Gordon, 1990) and HS3-NUVEL1A (Gripp & Gordon, 2002) used by Silver *et al.* (2001), as well as the mantle flow model of Conrad *et al.* (2007) and GPS measurements for comparison with the SASE results. The analysis is done on a map projection so that latitudinal as well as longitudinal variations are visible. These three models are plotted in figure 5-14 together with GPS plate motion directions.

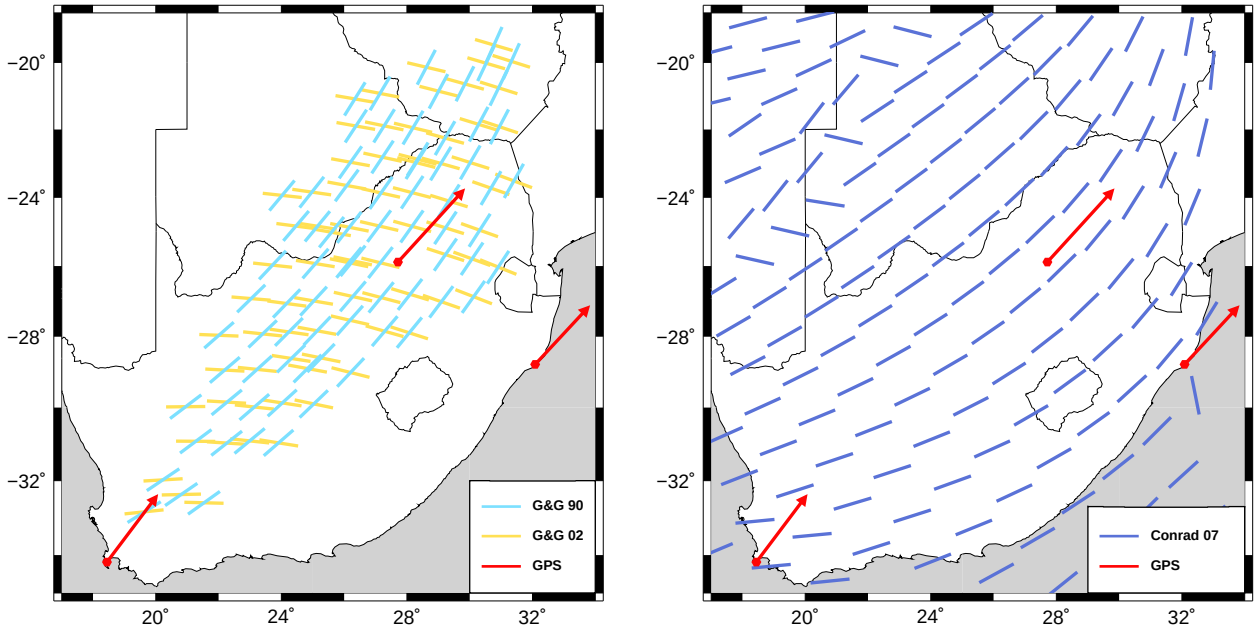

(a) (b)

Figure 5-14: *(a) Plate motion models of Gripp & Gordon (1990) (G&G 90) and Gripp & Gordon (2002) (G&G 02), plotted together with results from GPS measurements. (b) The resulting ISA directions (analogous to splitting fast axis directions) for the flow model of Conrad* et al. *(2007) (Conrad 07) at 225km depth, plotted together with results from GPS measurements.*

It is clear that the model of Gripp & Gordon (2002) is completely different from the other two models as well as the GPS data, which, for the most part, all correlate relatively well with a general northeast-southwest trend. The GPS data, displaying measured plate

velocities in the region of 25 mm/yr, are too sparse to use for a correlation plot with the SASE results (although it is likely to be a linear trend), but they do provide added confidence in the Gripp & Gordon (1990) model. The predicted splitting fast axis direction from the flow model of Conrad *et al.* (2007) is also remarkably similar to the plate motion directions of the Gripp & Gordon (1990) model. There are a few points from the Conrad *et al.* (2007) model over Namibia and one over the Indian Ocean that do not appear to be consistant. It is unclear what has caused these anomalous directions in the model, but since they are away from the SASE array region, and the general trend is consistent with what is presented in the broader global model plot of Conrad *et al.* (2007), these anomalous directions are ignored.

We take the Gripp & Gordon (1990) and Conrad *et al.* (2007) models and subtract the direction of the SASE fast axis splitting directions from the direction predicted by the models in order to gain a measure of the misfit between the observations and model predictions. The SASE splitting directions are then plotted and coloured according to the misfit between the models and the measurements. These results are displayed in figures 5.15(a) and 5.15(b). It should be noted that these results do not take into account the uncertainty in the models, or the errors in the splitting measurements, both of which could improve the correlation and lower the misfit value. This is therefore essentially a "worst case" or "worst fit" scenario.

Since the general trends of the Gripp & Gordon (1990) and Conrad *et al.* (2007) models are very similar, it is not unexpected that figures 5.15(a) and 5.15(b) produce similar results. The western Kaapvaal craton and the Zimbabwe craton are the two regions where there is an excellent fit (blue coloured bars) with the model data. The fit is not as good on the southwestern Kaapvaal craton, and the areas where the fit is worst is in the northeastern Kaapvaal craton and in the Limpopo belt (yellow-orange coloured bars). As noted by Silver *et al.* (2001), the "null" results tend to be clustered on the mobile belts to the southwest, and on the eastern Kaapvaal craton. The implications of these correlation plots are discussed in chapter 7.

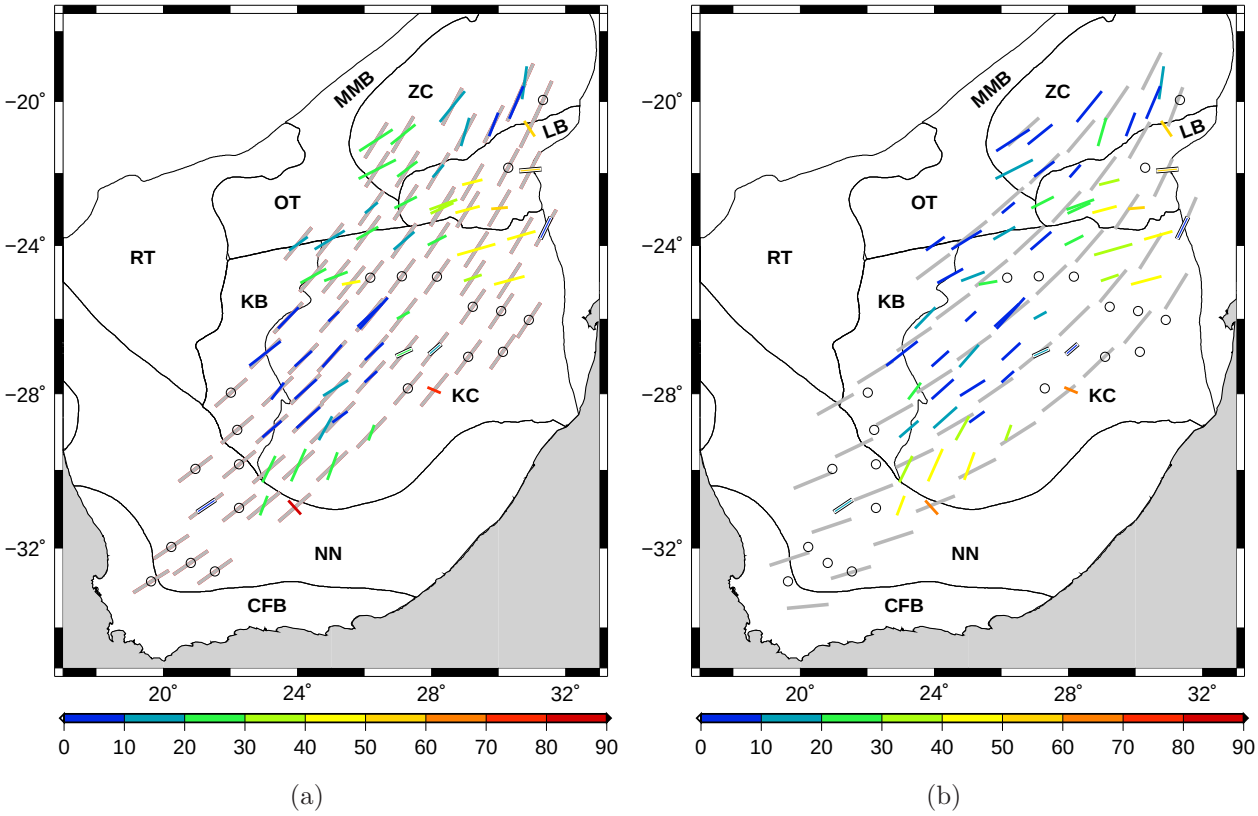

Figure 5-15: *(a) Correlation between the observed SKS fast axis directions, and the plate motion model of Gripp & Gordon (1990). (b) Correlation between the observed SKS fast axis directions, and the ISA directions from the mantle flow model of Conrad* et al. *(2007) at 225 km depth. The misfit in degrees is indicated by the colour of the bar of the SASE results. Null stations are represented by open circles, and poorly constrained splitting results are plotted with a black outline.*

6

MT data analysis

The SAMTEX experiment consists of more than 516 distinct sites located over a huge region in southern Africa (> one million square kilometers). The data have been processed using a variety of processing codes such as those described by Jones *et al.* (1989), Egbert (1997), and Chave & Thomson (2004). Primarily, we have used the commercial processing software of Phoenix Geophysics[1], which is based on Jones *et al.* (1989) method 6, and where data are more contaminated by noise, we generally obtained better results using the code of Egbert (1997). Data are of varying quality with some severely affected by DC train noise and mining related noise, particularly around the Witwatersrand basin where there are many DC train lines and gold mines, and also around the Kimberly region where there are many diamond mines with DC-powered lifts. The poorest data, which are therefore not analysed here, are in the south eastern Kaapvaal craton, where pipelines that carry a DC current to prevent corrosion, together with poor MT signal, have combined to produce very poor quality recorded data. Data collected in Botswana and Namibia are generally of significantly better quality due to the minimal cultural noise in these regions. The resulting output from processing are impedance tensors, from which apparent resistivity and phase curves are derived. The analysis of the impedance tensor and the resulting geoelectric strike directions

[1]http://www.phoenix-geophysics.com

are the focus of this chapter.

6.1 Depth of investigation

In previous studies utilising MT geoelectric strike directions to gain information on the geology of a region, investigators have plotted results for a given period of the data, which corresponds to a certain penetration depth, or depth of investigation. The depth of penetration is determined by the period of the data as well as the subsurface conductivity. Since many of the regions that have been explored have generally been smaller in size, a given period would likely penetrate to an approximately uniform depth over the surveyed region, and thus to plot a map of geoelectric strike directions for a given period is useful. However, it is obvious that simply due to the size of the SAMTEX survey, and the various conductively distinct regions it covers, it is highly unlikely that the electromagnetic penetration will be the same across the entire region. It is therefore necessary to gain information on the penetration depth at each site prior to the analysis.

There are three common methods in use to gain a quantitative approximation of the penetration of an MT response. These are: 1) the Schmucker $\rho^* - z^*$ scheme (Schmucker, 1970, 1973), 2) the Bostick transformation (Bostick, 1977), and 3) the Niblett approximation (Niblett & Sayn-Wittgenstein, 1960). Jones (1983a) showed that the Niblett approximation and the Bostick transformation are in fact exactly equivalent, referred to from here on as Niblett-Bostick depth estimates. The real part of the inductive c-response function ($\rho^* - z^*$) (Schmucker, 1970; Jones, 1980), related to MT impedance by a factor of $\frac{1}{\omega\mu}$, was shown to be the depth of maximum eddy current flow by Weidelt (1972), and is a measure of the depth of investigation. A model across a 2D conductivity heterogeneity (e.g. a terrane boundary or fault) is displayed in figure 6-1, with a resistivity of 500 $\Omega.m$ on the left and 5000 $\Omega.m$ on the right. Niblett-Bostick (NB) depth estimates (equation 6.1)

$$h_{NB} = \sqrt{\frac{\rho_a(T)T}{2\pi\mu_0}} \tag{6.1}$$

were calculated for the model responses using a geometric average (determinant average) of the apparent resistivity for the TE and TM modes. It is clear through looking at the different penetration on either side of the heterogeneity, that they are sensing very different

depths for the same periods. 123 s represents ≈75 km depth on the more conductive (left) side, while the same period is sensing a depth of >200 km on the resistive side (right).

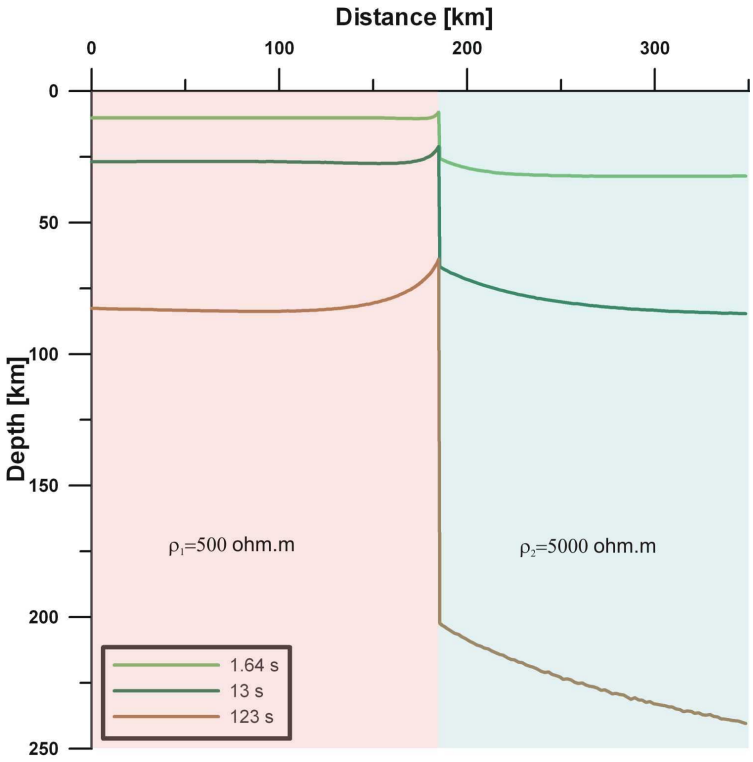

Figure 6-1: *Approximate Niblett-Bostick penetration depths across a 2D fault model for periods of 1.64 s, 13 s, and 123 s. The average of the two modes was used in the penetration calculation.*

Similarly, this can be very nicely demonstrated in our data. Figure 6-2 shows the Niblett-Bostick approximate depth of penetration (for an average of the TE and TM mode resistivity) across the main kap03 profile for the period of 100 s. This plot is worth considering closely. Given a period of 100 s, the depths that are being sensed across the profile vary hugely. Notwithstanding the scatter, there are clear trends visible; in the centre of the resistive craton the penetration is >200 km, whereas over the Bushveld (red bar above Kaapvaal craton) and the Namaqua-Natal metamorphic belt, the penetration depth is only about 10 km. The depth calculations for this plot were done on the original processed data that have not had distortion removed, which would contribute to the scatter in the plot. Static shift effects (not removed by distortion analysis) would also likely influence depth estimates, but by the square root of their value (equation 6.1) (Jones, 1988). Clearly, a map of period dependent results would be meaningless if plotted across this region for one single period value, and a more appropriate means of tackling this problem would be to either split the data into

sections, or to plot results for given depths as opposed to periods. The effect is a direct consequence of the huge variation in the parameter that electromagnetic studies are sensing (figure 2-1), namely electrical resistivity.

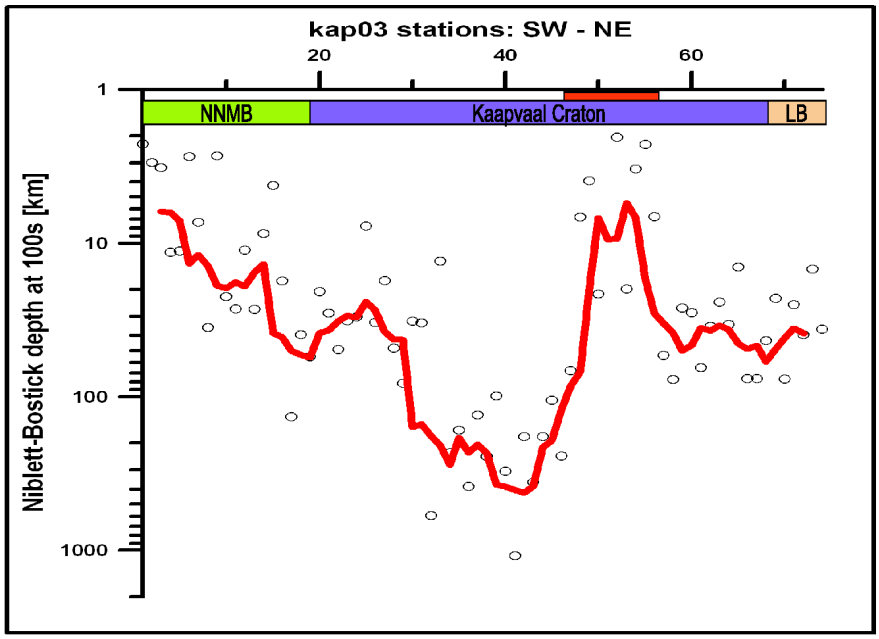

Figure 6-2: *Approximate Niblett-Bostick penetration depths along the kap03 profile (>1500 km in length) at a period of 100 s. The scatter is likely due to local distortion and static shift effects. Red line is a 5-point box car moving average. Note the significant variation in penetration along the profile. NNMB: Namaqua-Natal metamorphic belt. LB: Limpopo Belt. Red bar above the Kaapvaal craton represents the location of the Bushveld Igneous Complex, where there is low penetration.*

A caution which has been raised by Jones (2006) is that the TE and TM modes may penetrate to different depths for a given frequency (where apparent resistivity curves split). This is demonstrated in figure 6-3, where a response from a 2D model is plotted as a function of period, and then as a function of Niblett-Bostick depth. It is clear simply by looking at the marked data points in the plot versus period and their corresponding penetration depths, that there is significantly different penetration for each mode. This is something that should be taken note of. However, there is little that can be done to get around this in current decomposition analysis approaches, and the problematic effect is still present whether plotting versus period or depth. It is, however, still likely to be far more meaningful to plot data for a given average penetration depth in an area than for a given frequency.

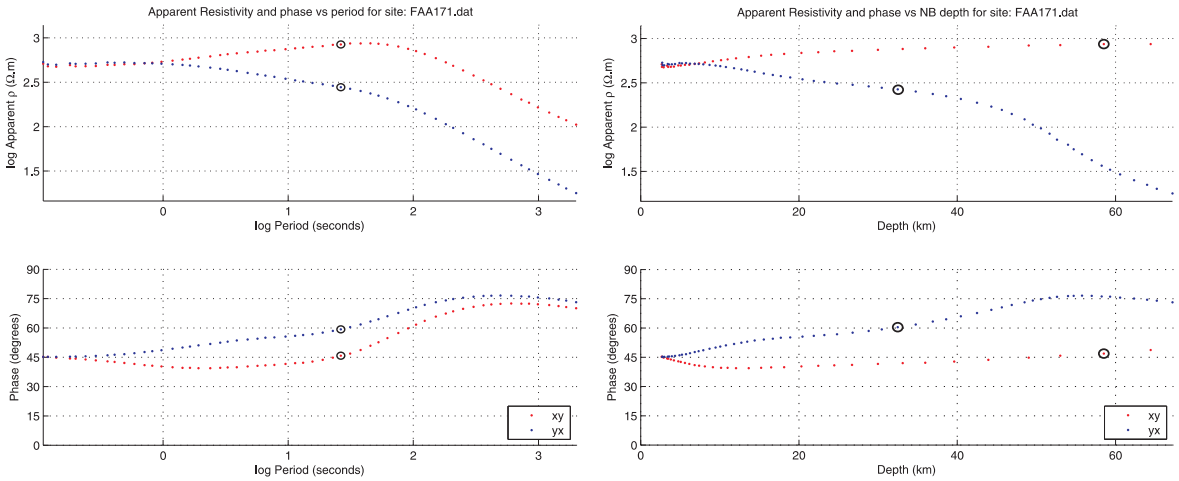

(a) (b)

Figure 6-3: *Model data from a site along a 2D profile such as that in figure 6-1, plotted as a function of period (a), and as a function of Niblett-Bostick depth estimates (b). The circled data points at ≈20 s in (a) are circled in (b), to clearly indicate the different penetration depths for the same period of data.*

It has been observed in other studies (e.g., Eaton *et al.*, 2004) that there is sometimes a different geoelectric strike direction and/or seismic fast axis direction for different depths. One of the aims of this study was to place bounds on the depth of the seismic anisotropy that has been observed in the shear wave splitting results from the SASE project. We therefore wanted to be able to identify variations with depth. For this reason it was decided to find separate representative strike directions at each site, one representative of the crust, and one that was representative of lithospheric mantle, since, if there are different geoelectric strikes at different depths, it is not unreasonable to suspect that the Moho discontinuity may separate them.

Crustal thickness, as defined by the seismic results of the SASE experiment (Nguuri *et al.*, 2001; Stankiewicz *et al.*, 2002; James *et al.*, 2003), varies from ≈35-40 km below the craton, to ≈45-50 km below the Proterozoic regions where the Moho also appears to be more complex. Our aim was therefore to gain a strike direction representative of the crust and a strike direction representative of the upper lithospheric mantle, while avoiding complex structures at the crust-mantle boundary. In order to do this, and at the same time not bias any one site with more or less data, we analyse each profile, as portrayed in figure 6-4. The corresponding periods for Niblett-Bostick depth estimates were calculated for depths of 35 km (open circles) and 45 km (filled circles), which correspond to the approximate crust-

mantle depth. It is the corresponding periods for these depths that is then plotted in this figure. From figure 6-4, a decade-wide band of data was selected above these periods to be analysed for crustal geoelectric strike, and a decade-wide band of data were selected below these points to be analysed for the lithospheric mantle geoelectric strike. The decade-wide bands of data that were selected are quite smoothly varying, and the advantage of doing this for each profile is that we can easily observe any single site that is badly effected by a static shift or instrument calibration error since it will likely be a scattered point along the profile (e.g. site 12 in the OKA profile in figure 6-4). The reason for selecting a decade-wide band for each analysis was to not bias the analysis for any one station with more or less data compared to its neighbours.

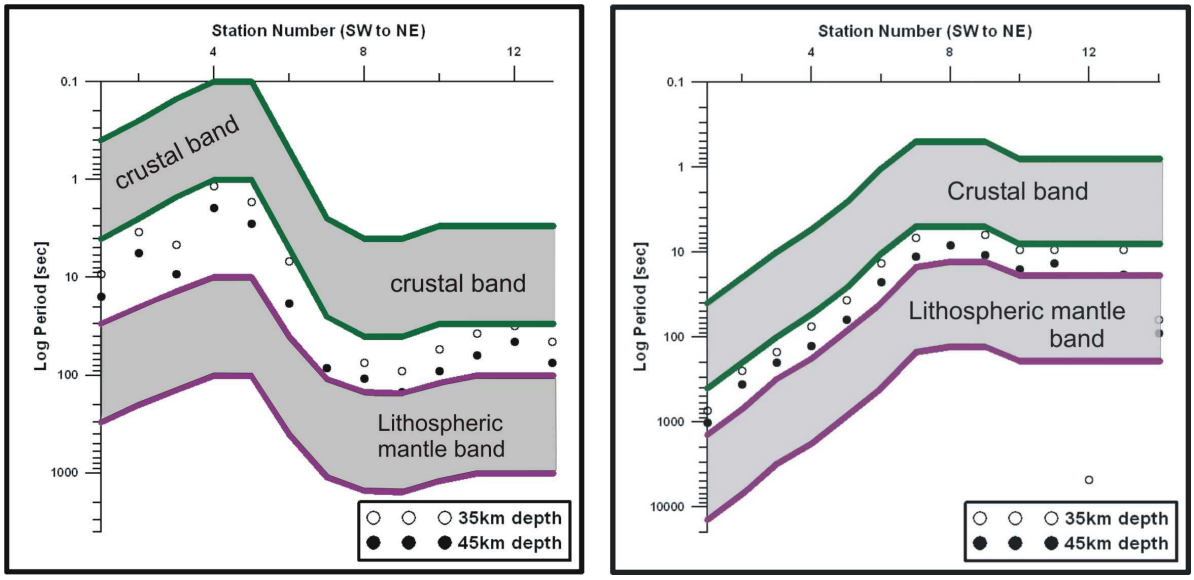

Figure 6-4: *A plot of the corresponding periods for Niblett-Bostick depth estimates of 35 km (open circles) and 45 km (filled circles) depths along the K2G (left) and OKA (right) survey lines (see figure 1-1). Figures such as this were used along each profile (Appendix 1) to then select a corresponding decade-wide band of data representative of the crust (upper grey shaded region) and the lithospheric mantle (lower grey shaded region).*

6.2 GB decomposition analysis

Each site was then analysed twice, separately for each frequency band using the single site Groom-Bailey (GB) approach (Groom & Bailey, 1989) for a range of frequencies, as implemented by McNeice & Jones (2001). The MT phase tensor analysis (Caldwell *et al.*, 2004) was applied to a few of the sites in a preliminary analysis. However; the results were not

strongly different from the GB results at these sites, previous studies had used impedance tensor decomposition techniques, the phase tensor technique was very new at the time of this analysis, and the GB approach is widely accepted, it was decided to conduct the analysis using the GB approach. Our analysis provides us with two (crustal and lithospheric mantle) regional geoelectric strike estimates for each site. The data were analysed using an assumed error floor of 2° for phase, which is equivalent to 7% for apparent resistivity.

The data that are represented below include the majority of, but not all sites. This is because, after the GB analysis, the output data for each site were plotted, visually inspected, and omitted if necessary. Sites were omitted for any of the following reasons: data were very poor, with large scatter and errors; data were insufficient (no penetration to the desired depth); there was a definite crossover between the two modes of the data in the period band of interest, making the task of picking the more conductive direction difficult since it would depend on whether it is taken above or below the crossover point. The conductive direction was taken to be the direction of the mode with the higher phase value, to avoid ambiguities due to static shift (discussed more thoroughly in section 6.3).

The mean RMS values for the one-decade wide GB decomposition for both the crustal and lithospheric mantle results fall below 1.5 for the majority of the sites, with the peak in the values being around 0.5 (figures 6.5(a) and 6.5(b)). This indicates that the data are overfit, and that we could probably reduce the error floor. The histograms in figure 6-5 appear to have a χ^2 distribution, which would be expected if the misfit to the GB model had a normal distribution. Figures 6.5(a) and 6.5(b) therefore provide strong justification for the use of the χ^2 statistic as a means of assessing the validity of the GB model. There is no clear spatial pattern as to certain regions that are well or poorly fit by the decomposition model (figures 6.5(c), 6.5(d)).

The average twist values that are observed from both sets of data fall largely within the range ±15° for the crust and ±25° for the lithospheric mantle band (figures 6.6(a) and 6.6(b) respectively). There are regions (figures 6.6(c), 6.6(d)) that have consistently low twist values, for both the crustal and lithospheric mantle depths (e.g. over the Rehoboth terrane). The low distortion is likely due to the uniform conductive cover in the region, which results in low distortion.

The average shear values fall predominantly in the range ±20° for the crust, while the

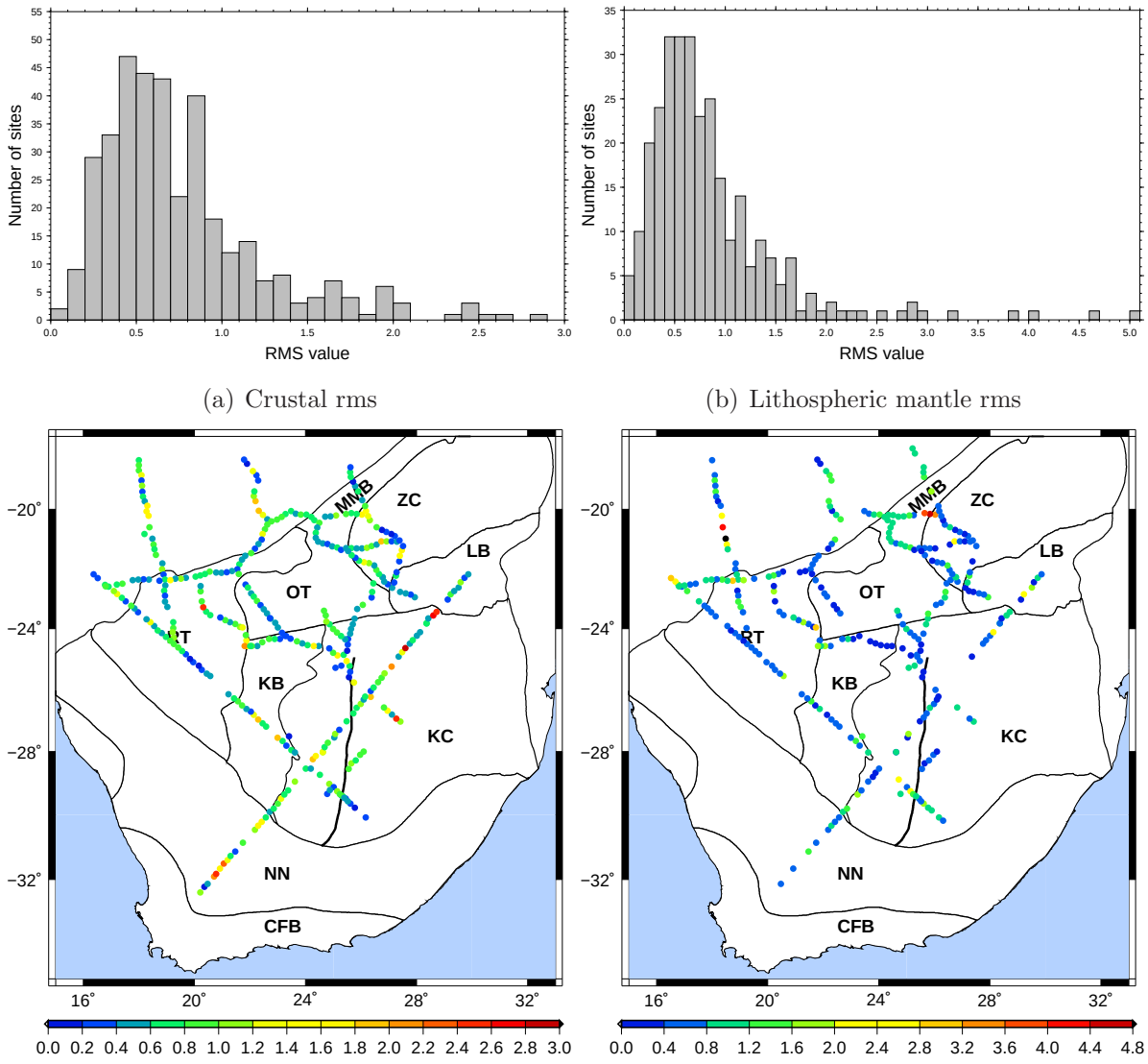

(a) Crustal rms (b) Lithospheric mantle rms

(c) Crustal rms (d) Lithospheric mantle rms

Figure 6-5: *Mean RMS values from the unconstrained GB analysis of crustal (a and c) and lithospheric mantle (b and d) periods. Both the crust and lithospheric mantle analysis result in RMS values that are quite small, with the majority falling below a value of 1, and the mean value being around 0.5.*

lithospheric mantle shear values are far more spread out over the possible ±45° range. Similarly to the twist results, there does appear as though there are regions that have consistently lower shear values (e.g. over the Rehoboth terrane, the Okwa terrane, and the Magondi mobile belt). The observation of spatial variation in the data is important as it gives us an idea as to regions of low distortion. The station responses over the central Rehoboth are high quality and a first look at the apparent resistivity and phase curves indicates that they are generally 1D in nature, so these are consistent and pleasing results. The reason that

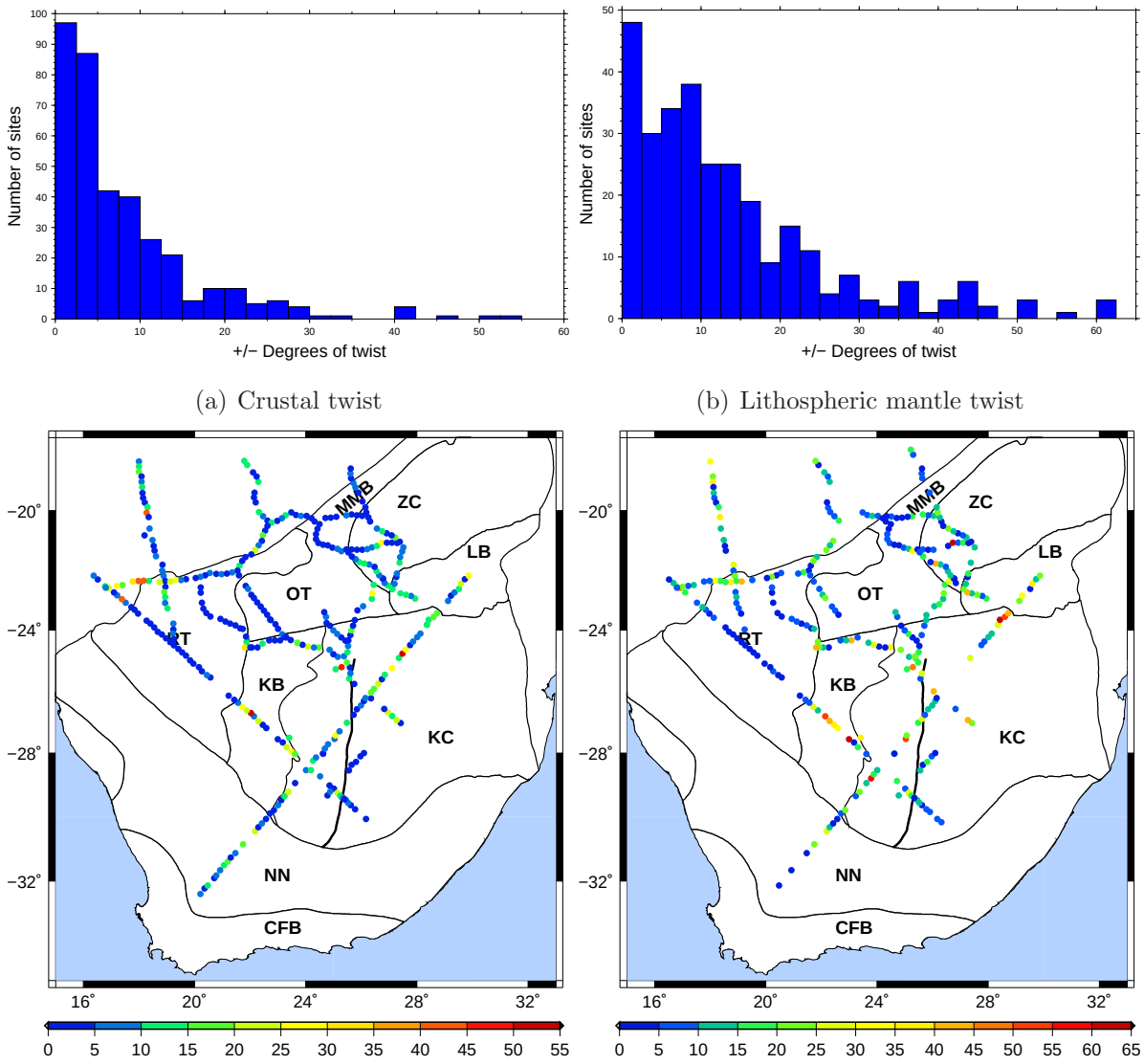

(a) Crustal twist

(b) Lithospheric mantle twist

(c) Crustal twist

(d) Lithospheric mantle twist

Figure 6-6: *Mean twist values (in ± degrees) from the unconstrained GB analysis of crustal (a and c) and lithospheric mantle (b and d) period bands. Both crustal and lithospheric mantle twist values are reasonably small, mostly within the range ±15° for the crust, and ±25° for the lithospheric mantle. Note the regions of low twist values across the Rehoboth terrane (RT) as well as the Okwa terrane (OT) and Magondi orogenic belt (MMB).*

the rms, twist, and shear values are generally slightly larger for the lithospheric mantle than for the crustal analysis, is likely due to the data at longer periods having worse signal to noise ratios and therefore larger scatter and errors. Additionally, at these longer periods, the larger skin depth results in additional and larger-scale crustal features acting as scatterers. Overall, the majority of the data has reasonably low distortion values compared to

what is often observed on shield regions such as the Fennoscandian Shield (Lahti *et al.*, 2005).

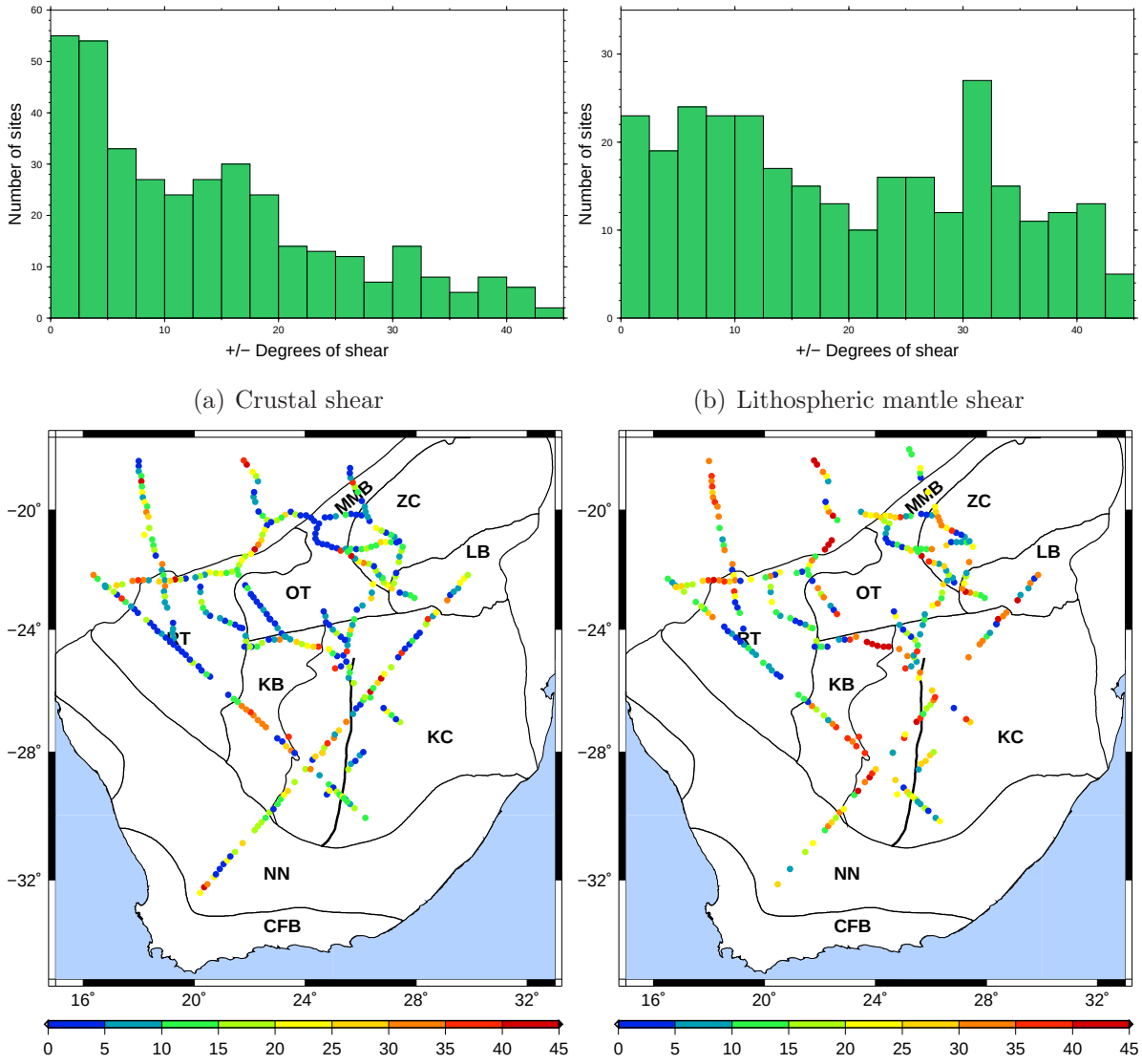

(a) Crustal shear (b) Lithospheric mantle shear

(c) Crustal shear (d) Lithospheric mantle shear

Figure 6-7: *Mean shear values (in ± degrees) from the unconstrained GB analysis of crustal and lithospheric mantle period bands. Maximum values for shear are ±45°. The crustal shear values generally fall within the ±20° range, while the lithospheric mantle values are more uniformly distributed over the ±45° range.*

Further to this analysis, we have found a few regions that are resistive enough, and have sufficiently long periods recorded, such that there is penetration to asthenospheric depths. In these cases there are only a few long period data points corresponding to signals that penetrate to these depths. Additionally these are normally the data with the larger error

bars and scatter. It is therefore impossible to do the same analysis that was done for the crust and lithospheric mantle for the asthenosphere, as there are not enough data to select an entire decade-wide band of data and they are generally of poorer quality. In order to counter this, we have analysed the regions where there is penetration to asthenospheric depths using a multi-site GB decomposition (McNeice & Jones, 2001). Most of the groups use between 4 and 10 sites, with only one group using 2 sites, and one group using 3 sites (Appendix 2). This allows us to compute the best fitting strike direction for all the sites in the group and provides extra constraints to counter that which is lost by using less, and poorer data. This would provide us with less strike directions, but at asthenospheric depths we would expect that MT stations 20 km apart would be sensing the same region, making this analysis both appropriate and satisfactory.

6.3 The electrically more conductive direction

To avoid the 90° ambiguity in the geoelectric strike from the output of the GB analysis, we plot the more conductive direction of the two. This would correspond to the more conductive direction in a region of strong electrical anisotropy and no other structures, thereby providing a measurement of horizontal electrical anisotropy alone. However, it is not only the electrical anisotropy of a region that influences the geoelectric strike direction. Large-scale conductivity heterogeneity, such as that that may be found at a fault or terrane boundary, will also influence the geoelectric strike direction.

6.3.1 The more conductive direction across a fault

The effect on geoelectric strike, plotted as the more conductive direction in the presence of 2D heterogeneity, can most easily be demonstrated with a 2 quarter-space model. This might represent a boundary between two geological regions of differing electrical properties or a large fault. Model responses for a 2 quarter-space fault model, with a conductivity heterogeneity (500 $\Omega.m$ and 5000 $\Omega.m$) were calculated using the code of Pek & Verner (1997). Figure 6-8 was then generated by calculating the appropriate period at each site for an approximate Niblett-Bostick (Niblett & Sayn-Wittgenstein, 1960; Bostick, 1977; Jones, 1983a) penetration depth of 35 km, and then plotting the corresponding apparent resistivities and phases for each of the two modes at that particular period (representative of ≈35 km depth) for each site.

In this paragraph, we discuss three different directional properties; the geoelectric strike

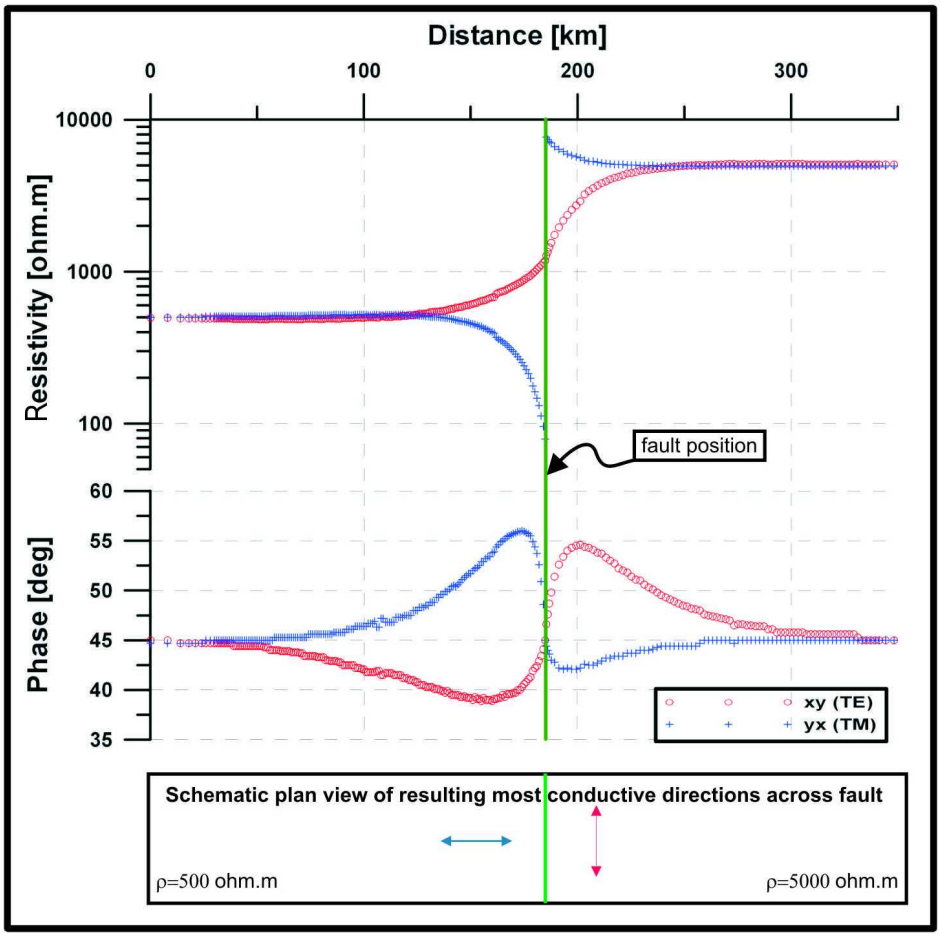

Figure 6-8: *A plot of the variation of apparent resistivity and phase for the xy and yx modes for a Niblett-Bostick depth of ≈35 km along a model profile. The modelled data come from a 2 quarter-space fault model with resistivities of 500 Ω.m on the left of the fault (vertical green line), and 5000 Ω.m on the right of the fault. Data were modelled using finite-difference modelling code after Pek & Verner (1997).*

(which possesses a 90° ambiguity), the geological strike of the model (which in this case coincides with one of the geoelectric strike directions), and the most conductive direction (which in this case also coincides with one of the geoelectric strike directions, and possibly the geological strike direction of the model). If we plot the more conductive direction across the model for the analysis described in the previous paragraph, we would be plotting the TE mode on the right (resistive) side of the structure, which is correctly the geological strike direction of the fault as the TE electric field is parallel to geological strike. Conversely however, the more conductive direction corresponds to the TM mode on the conductive side of the structure, which is perpendicular to the geological strike direction of the fault. Thus, if we plot the geoelectric strike directions as the most conductive directions across a

conductivity boundary (thereby removing the 90° ambiguity is geoelectric strike), we would expect to see a 90° flip in the conductive direction as we move from one side of the fault structure to the other. In order to plot the most conductive direction, one might simply take the mode with the lower resistivity, which would be correct in this idealised, distortion-free 2D model. However, this is liable to be incorrect if one of the modes has a static shift (something not removed by the GB decomposition). Thus, in order to avoid this occurring we choose to plot the mode with the higher phase, since phase is not affected by static shifts, which also corresponds to the more conductive direction. This is clear in figure 6-8, where one can see that regardless of whether we plot the strike direction corresponding to the mode with the lower resistivity or the higher phase, we are plotting the same direction. Importantly, we are not using the more conductive geoelectric strike directions to define the strike direction of structures for 2D interpretation, but we are only concerned with the more conductive direction to remove 90° ambiguity in the correlation with the fast axis direction from seismic anisotropy.

6.4 MT results

The results from the GB analysis of our MT data, using the methodology described above, are presented here, while the discussion of these results is presented in the following chapter. There are essentially three sets of results: The crustal MT results (figure 6-9), the lithospheric mantle MT results (figure 6-10), and the asthenospheric multi-site MT results (figure 6-11). All the MT results are plotted as red bars aligned in the most conductive direction, and are scaled by the maximum phase difference (normalised to a maximum of 30°) between the TE and TM mode in the band analysed, which is a measure of the magnitude of the anisotropy. These values (direction and phase difference) have a somewhat similar manner of describing electrical anisotropy to the fast axis direction and delay time in shear-wave splitting studies. It was decided to use the maximum phase difference in the entire band of data that was analysed, which is likely to be more robust given the study by Heise *et al.* (2006b) who show that the maximum phase split/difference occurs at the vertical resistivity contrast between regions (in 1D), and not in the centre of the region even if it is anisotropic.

The more conductive results for the crust are overlain on the regional magnetic data of southern Africa (figure 6-9). A large portion of the shorter wavelength structure visible in the magnetic data is likely to be related to structures that are confined to the crust, and these data are thus a suitable complimentary background. If these features represent bound-

aries of conductivity heterogeneities, we expect the MT to have some correlation with the structure.

The lithospheric and asthenospheric mantle MT results are plotted over the seismic SKS results of Silver *et al.* (2001), as it is these seismic results, thought to originate from lithospheric mantle depths with which we want to compare our MT data. The shear-wave splitting results are plotted as green bars aligned with the fast axis direction, and scaled by delay time. Light green bars are poorly constrained stations, while blue dots are null stations. Approximate geological terrane boundaries (Nguuri *et al.*, 2001) are plotted on these three sets of results, and are derived largely from potential field data and geological maps. However, large portions of the region, covered by our results are concealed by unconsolidated Kalahari desert sands and are not well known or understood.

The results from our MT analysis are far more complex than has been previously observed in most other studies of this scale (e.g. Ji *et al.*, 1996; Eaton *et al.*, 2004; Frederiksen *et al.*, 2006; Padilha *et al.*, 2006), although this may also be a slightly misleading impression as there is also simply far more data than have been previously analysed for any given study region. While it is possible to gain an overall impression of the results and make a qualitative interpretation as to the meaning of these results, it was decided that a further analysis of these results may prove to be more useful, and to reveal any underlying trends or patterns that may otherwise be overlooked.

6.5 Cluster analysis

In order to try to gain a better understanding of the results and to see if there are any underlying trends that might otherwise be missed, it was decided to use a *cluster analysis* tool on the results. The term *cluster analysis* is a general term for a number of different methods and algorithms that are used to group similar kinds of objects into respective categories or meaningful structures. In science it is generally used to partition a data set into subsets or clusters based on some common characteristic, which is often in the form of a type of *distance measure*. How this common characteristic is described depends on the dataset and what sort of data characteristics one wishes to group or classify. Cluster analysis algorithms fall into two broad categories: *hierarchical algorithms* and *partitional algorithms*. Hierarchical algorithms find successive clusters from previously established clusters, resulting in a "tree structure" type of classification with different levels, while partitional clustering algo-

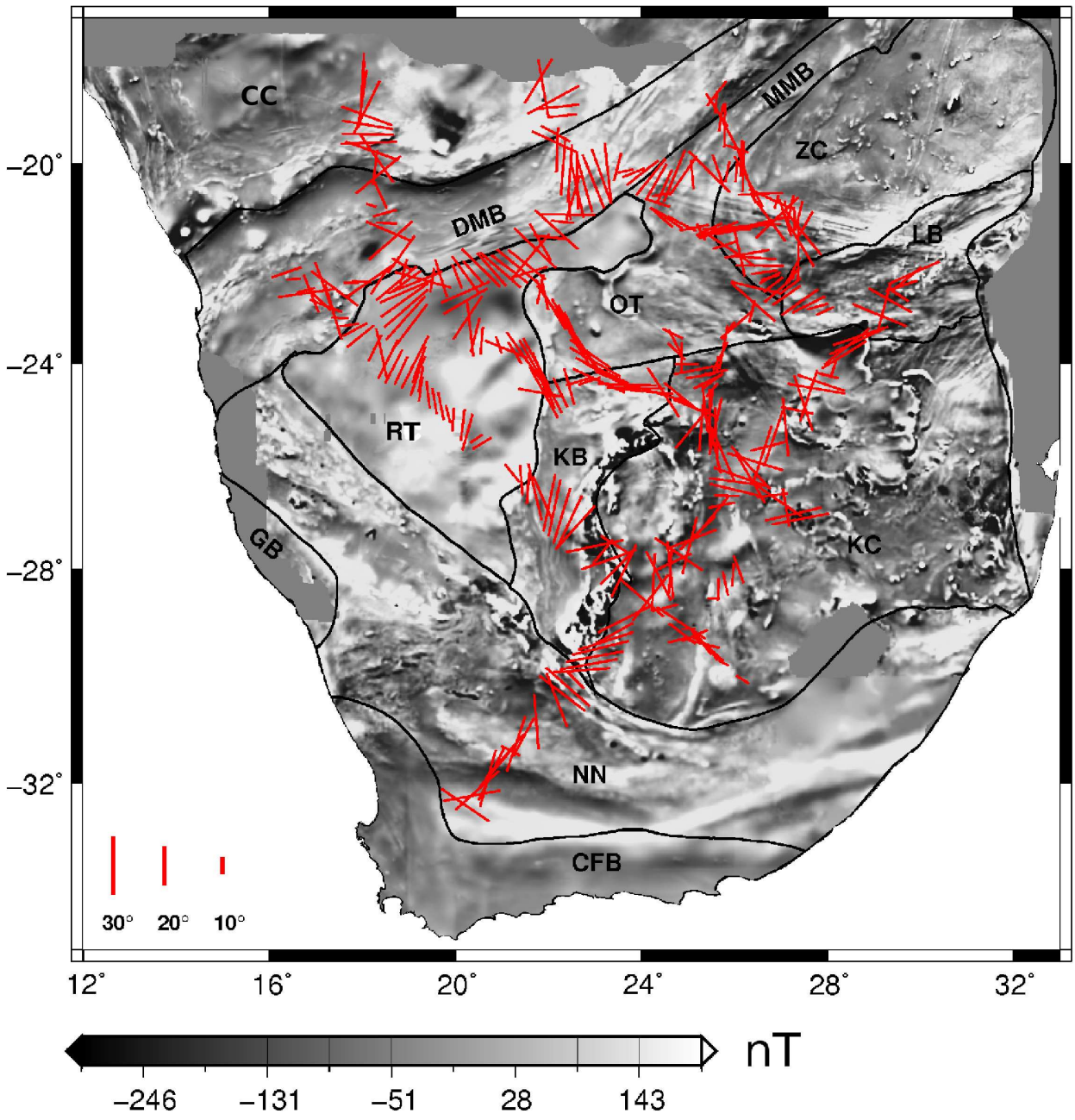

Figure 6-9: *Crustal MT most conductive directions, plotted as red bars, with the length scaled by phase difference, overlain on the regional magnetic data of southern Africa. Geological terrane boundaries are derived largely from regional potential field data (Nguuri* et al., *2001). KC: Kaapvaal craton. LB: Limpopo belt. ZC: Zimbabwe craton. NN: Namaqua-Natal mobile belt. CFB: Cape Fold belt. KB: Kheis Proterozoic fold and thrust belt. MMB: Magondi mobile belt. RT: Rehoboth terrane. GB: Gariep Belt. OT: Okwa Terrane. DMB: Damara mobile belt. CC: Congo craton.*

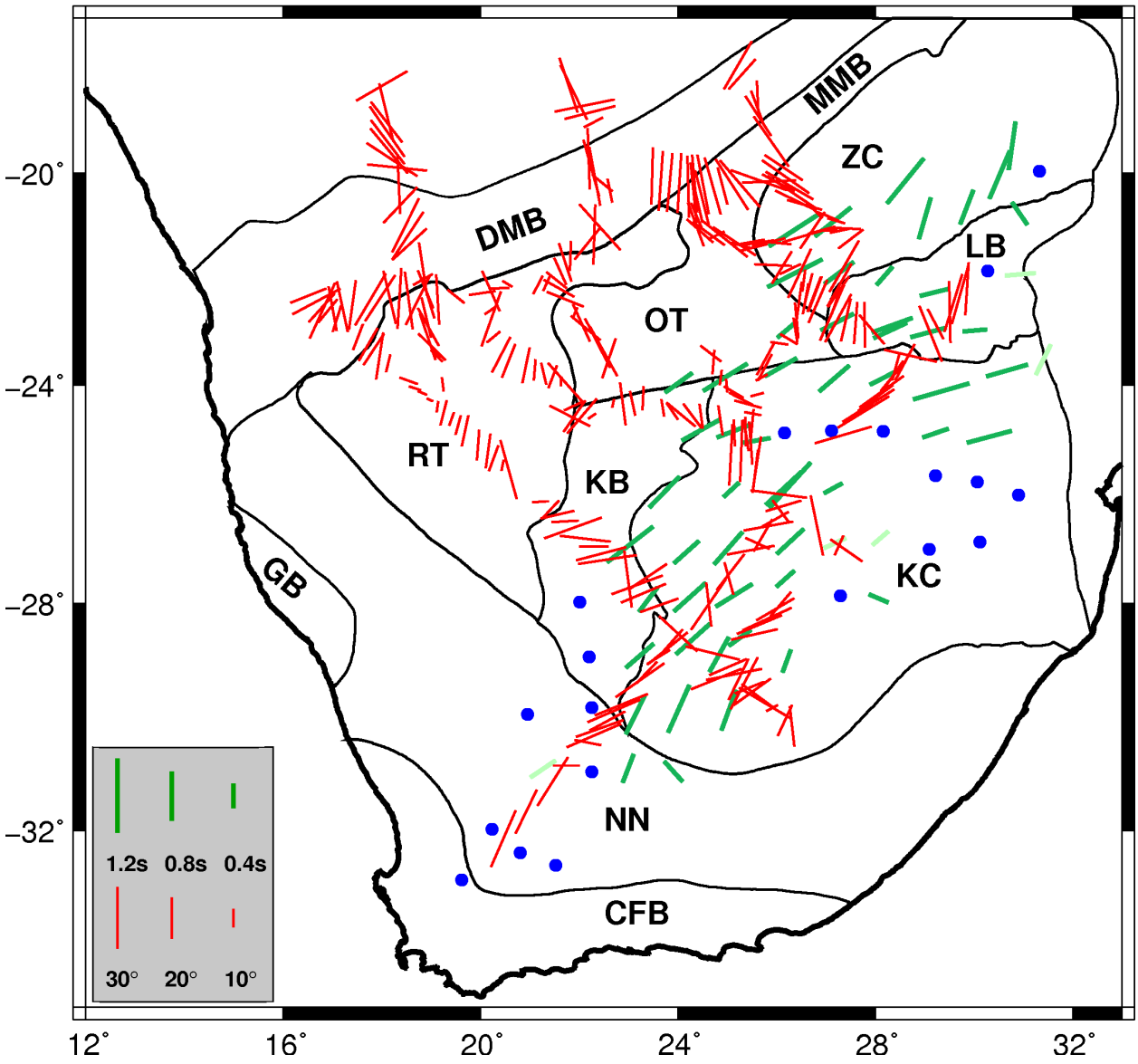

Figure 6-10: *Lithospheric mantle MT most conductive directions, displayed as red bars, with the length scaled by phase difference, overlain on SKS splitting results of Silver* et al. *(2001), plotted as green bars parallel to the fast axis splitting direction, with the length scaled by delay time. Light green bars are poorly constrained splits, and blue dots represent null sites. Geological terrane boundaries are derived largely from regional potential field data (Nguuri* et al., *2001). Terrane names are as in figure 6-9.*

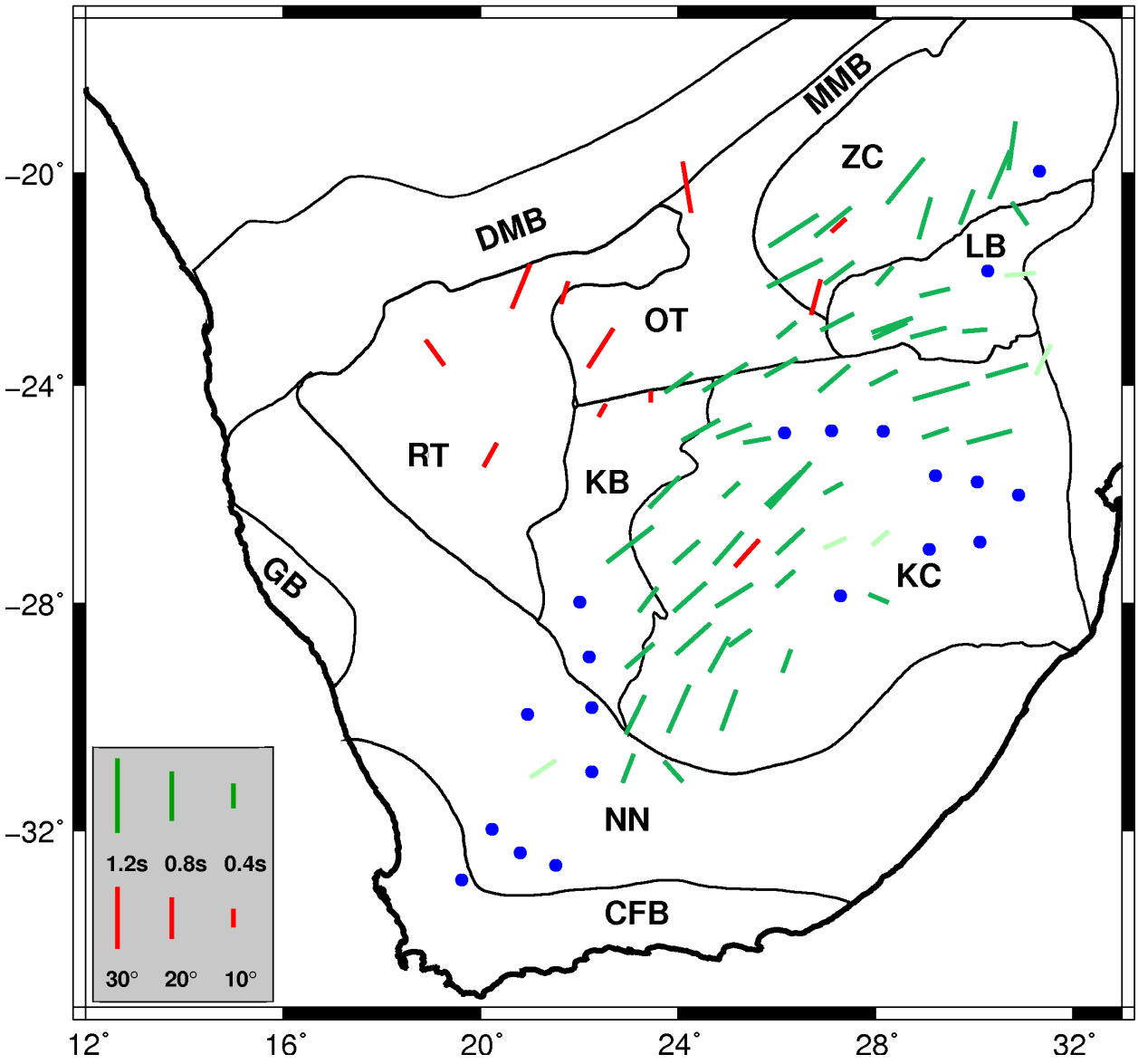

Figure 6-11: *Asthenospheric MT most conductive directions, displayed as red bars with the length scaled by phase difference, overlain on SKS splitting results of Silver* et al. *(2001), plotted as green bars parallel to the fast axis splitting direction, with the length scaled by delay time. Light green bars are poorly constrained splits, and blue dots represent null sites. Geological terrane boundaries are derived largely from regional potential field data (Nguuri* et al., *2001). Terrane names are as in figure 6-9.*

rithms determine all the clusters at the same instance and generally create a single level of clusters.

The hope was that a cluster analysis might prove to be a useful tool for this study, as it may identify trends of regionally distinct areas of geoelectric strike from our MT results. The cluster analysis technique chosen for this analysis is a method known as *k-means* clustering (MacQueen, 1967). This is a partitional clustering technique that is commonly used and is an unsupervised learning algorithm. It involves essentially four steps:

1. Place k random points into the data space that is represented by the objects being clustered. These represent the initial k group centroids.
2. Assign each data point to the group with the closest centroid.
3. When all the data points have been assigned, the positions of the k centroids are recalculated to minimise the variance.
4. Steps (2) and (3) are repeated until the centroid locations no longer move. This produces groups of data that fall into k different groups.

The method seeks to minimise the sum of the within-cluster variances. Conditions of the method include: different clusters may not contain the same data point; no data points are excluded; each cluster contains at least one data point. The initial assignment of cluster means is normally random (but may be predetermined), and can have a significant bearing on the final model performance. It is therefore prudent to re-run the cluster analysis multiple times in order to avoid local minima, and to find the result with minimum variance. An important question is how many clusters we want to group the data into. Obviously there is the upper limit, where the number of clusters is the same as the number of data points, and the lower limit, in which there is only one cluster. There is a tradeoff between having many clusters, with a correspondingly small variance, and having only a few clusters with a higher variance. A common way of deciding on the appropriate number of clusters is using what is termed the *elbow criterion* (known as the L-curve in inverse theory), where the number of clusters versus a measure of the variance is plotted. Figure 6.12(a) is such a plot for our crustal MT results, with the conductive direction being the criteria that we are clustering.

From figures 6.12(a) and 6.12(b) a suitable number of clusters may be selected, where the variance is not too large, while having a small enough number of clusters to make the analysis meaningful. Approximately five clusters appears to be a suitable number for both

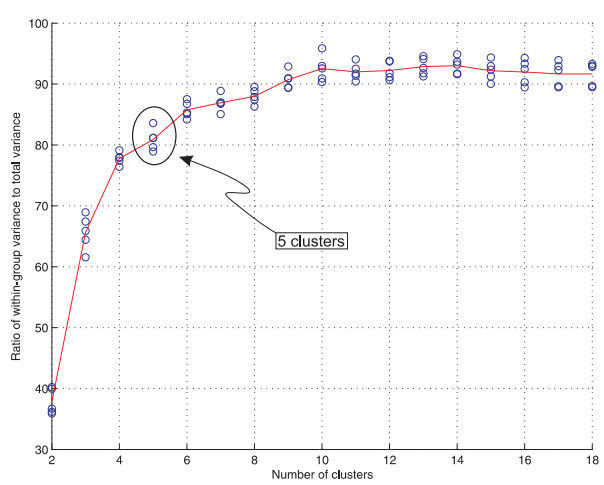

(a) Crustal

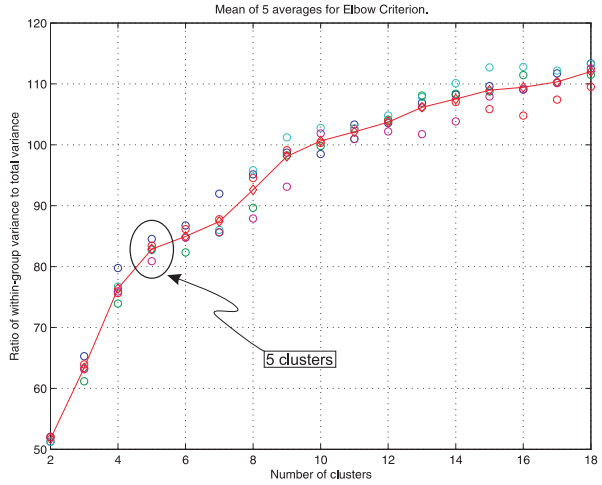

(b) Lithospheric mantle

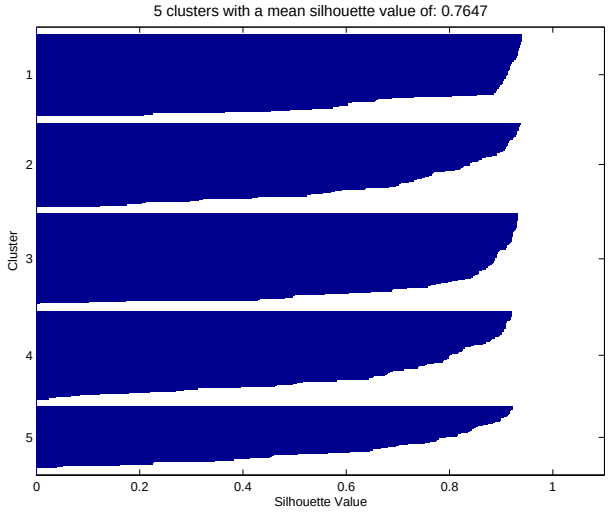

(c) Crustal

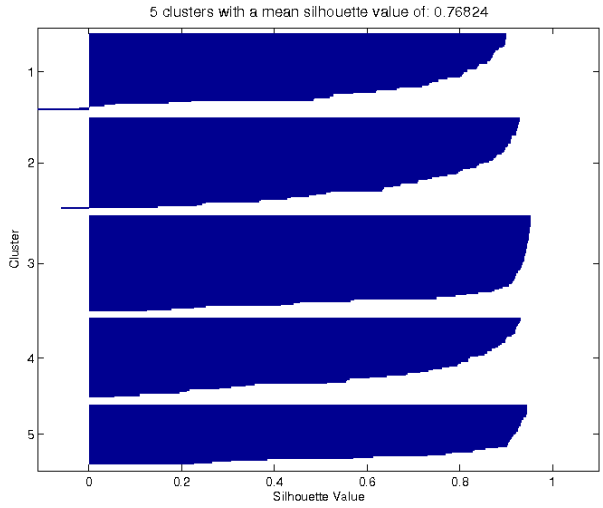

(d) Lithospheric mantle

Figure 6-12: *(a and b) Elbow criterion plot for clustering of the conductive directions of the crustal and lithospheric mantle MT results respectively. The vertical axis is the ratio of within-group variance to total variance, plotted against number of clusters. These are the mean results for well over 500 restarts on each number of clusters. This tradeoff curve shows that we certainly do not gain much using more than 10 clusters in either case, and that the optimal number of clusters is likely around 5, where the gradient of the curve is greatest. (c and d) Silhouette plots for a k-means cluster analysis using 5 clusters, applied to the conductive directions of the crustal and lithospheric mantle MT results respectively.*

crust and lithospheric mantle datasets, although a cluster analysis for 2 to 18 clusters was carried out on both datasets prior to deciding on 5 clusters. A means of visually inspecting

how well separated the resulting clusters are is by creating a *silhouette plot* (e.g. figures 6.12(c) and 6.12(d)). The silhouette plot displays a measure of how close each data point in one cluster is to points in the neighbouring clusters. A value of +1 indicates that the points are very distant, or well-separated, from neighbouring clusters, while 0 indicates that the data points are not distinctly in one cluster or another. A value of -1 indicates that the points are likely assigned to the wrong cluster. For perfectly separated clusters, a silhouette plot would produce essentially a bar graph with values of +1, although this would seldom be the case for real data. Figures 6.12(c) and 6.12(d) are silhouette plots of our crust and lithospheric mantle MT results respectively, clustered by the conductive direction into 5 groups. The results are pleasing, with the majority of the points having a value above 0.8, and an average silhouette value of 0.76 for both data sets. There is no single cluster that is significantly poorer than the others, and minimal points that have negative values.

Finally, after conducting the analysis to decide on the appropriate number of clusters, a k-means clustering analysis of crustal and lithospheric mantle MT results was done for 5 clusters. The initial cluster locations were randomly chosen (within the data space) and this was repeated multiple time ($\gg$500) to avoid local minima in the analysis. The final results used were the ones with the minimum variance from repeated clustering with randomly chosen cluster centroids. The results of the analysis for the crustal and lithospheric mantle conductive directions are displayed in figures 6.13(a) and 6.13(b) respectively. It should be noted that this analysis was done to extract conducting directions that may be related to anisotropy. If it were done primarily in order to extract geoelectric strike directions, we would need to account for 90° ambiguity, and would need to alter this cluster analysis to account for this. The cluster centroid values for the crustal results are: 13.6°, 48.5°, 80.75°, 120.6°, and 158.7°. The cluster centroids for the lithospheric mantle results are: 9.0°, 31.0°, 70.1°, 119.1°, and 164.6°.

This cluster analysis is able to improve the ease with which regions of similar geoelectric strike directions may be visually identified. It is difficult to identify any single direction that is dominant throughout the entire region, or even one general direction/cluster that is prevalent and parallel away from known terrane boundaries. This is something we might expect if the electrical anisotropy was due to the same cause of the seismic anisotropy, which appears to be smoothly varying across the region. Since we felt that 2D structure was having a strong effect on the MT results, particularly the crustal results, we decided that it would be beneficial to analyse major geological features that may be influencing these results to

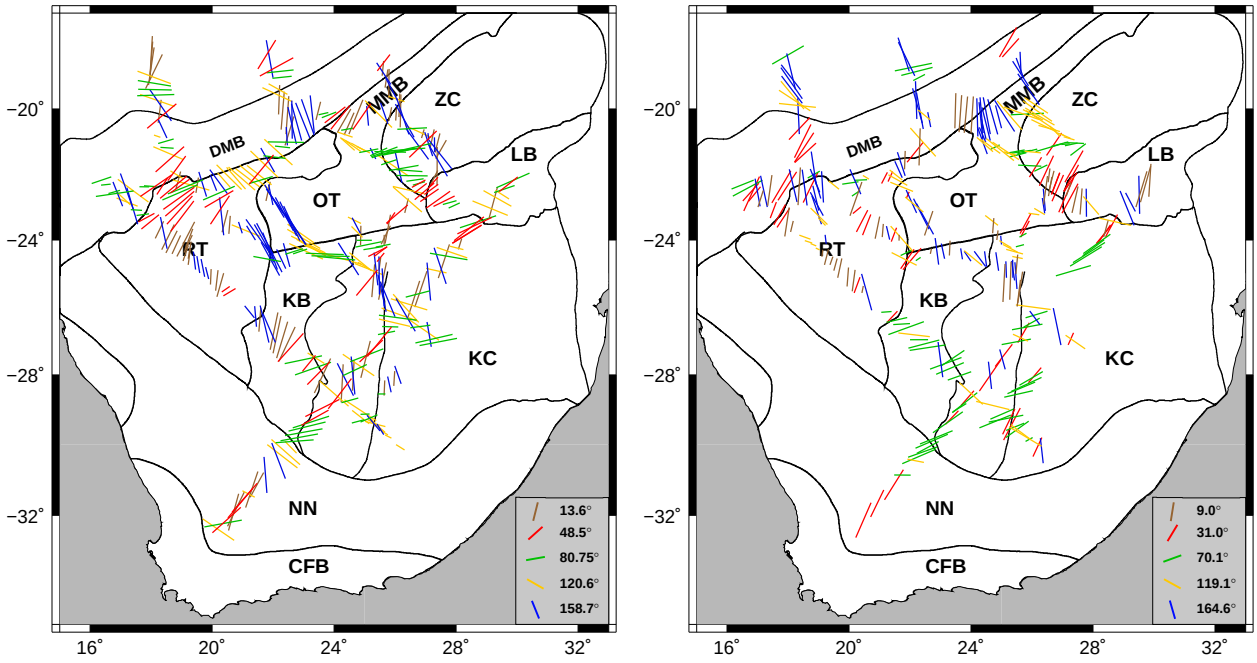

(a) Crustal clusters

(b) Lithospheric mantle clusters

Figure 6-13: *Results of K-means cluster analysis for 5 clusters, on the conductive directions from the crustal (a) and lithospheric mantle (b) MT results. The cluster centroid locations for each are denoted in the key. These plots allow us to more easily see where there are clusters/regions with similar conductive directions. Terrane names are as in figure 6-9.*

see if there is any relationship between the two.

6.6 Correlation of lineaments with MT

A thorough study by Jelsma *et al.* (2004) on major lineaments and their contribution to kimberlite distribution was the starting point for this part in our analysis. Unfortunately we were unable to get the lineament data used in that paper, and so the map was geo-referenced and most of the important lineaments from the map of magnetic lineaments from Jelsma *et al.* (2004) were digitised. Lineaments that were considered "important" were features of substantial length, which are therefore likely to extend to greater depths, and those which appeared to spatially correlate with known terrane boundaries. In total ≈50 major lineaments were digitised (figure 6.14(a)). At this stage we simply plotted each group from our cluster analysis over the lineaments. While this does help to focus on certain data and where they do, and do not, seem to be effected by lineaments, it is also a relatively subjective analysis. There are no given clusters for either the crustal or lithospheric mantle MT results

that appear to be completely related to, or completely unaffected by, the lineaments.

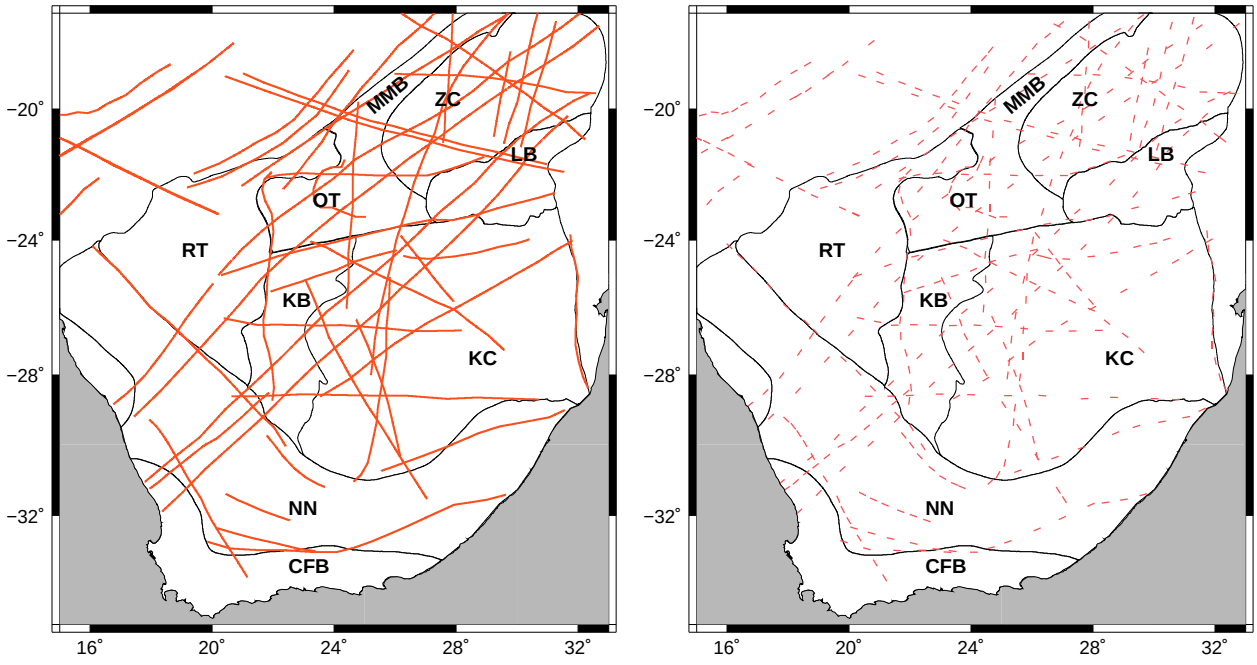

Figure 6-14: *(a) Significant magnetic lineaments across southern Africa, digitised from Jelsma* et al. *(2004). Longer lineaments and lineaments that correspond to known terrane boundaries were digitised as they were considered more significant. (b) The lineaments from (a), converted to points and angles east of north, for subsequent analysis.*

In order to gain a more quantitative description of the lineaments, we convert each lineament to points of latitude and longitude, and to angles east of north as is portrayed in figure 6.14(b). We then correlate these points and angles with our MT conductive directions, calculating a misfit between the MT conductive direction and the nearest lineament. The problem with this approach however, is that in some cases such as where multiple lineaments cross, it may be such that the closest lineament is not necessarily the major lineament, or the lineament which has the greatest effect on conductivity. To simply choose the "better" lineament is too subjective and open to interpretation.

We try to address this issue by using rose diagrams (a histogram for angles) to gain information on any significant correlation. The unfortunate side of this approach is that spatial information is lost. In an attempt to weight more significant features in the lineament data, without simply picking lineaments that appear more important, the data for the

rose diagram are binned, with every 100 km of lineament length corresponding to one angle that has to be binned in the rose diagram. This means that longer, and therefore likely more significant and vertically extensive lineaments, are counted multiple times. Similarly, for the MT more conductive directions, we weight each conductive direction by its phase difference. Each 5° of phase difference corresponds to one occurrence of the angle that is then binned in the rose diagram. This means that conductive directions that show stronger magnitudes (phase difference), are counted multiple times. The results of this analysis are presented in figures 6.15(a), 6.15(b), and 6.15(c) for the lineament data, crustal MT, and lithospheric mantle MT results respectively. These weighting schemes obviously do change the rose diagrams however, the general pattern that is observed is in fact quite similar to the same plots without weighting.

The crustal MT results show a broad azimuthal distribution, with major peaks around 0° and ≈80°. Bearing in mind the physics described for the 2D conductivity heterogeneity model in figure 6-8, we would expect that if the more conductive geoelectric strike direction obtained is purely a result of large 2D heterogeneity, and that the profile extends both sides of the feature, that any peaks observed in the rose diagram due to this would have a corresponding peak ≈90° to it. This is better observed in the unweighted rose diagrams for the MT results (figure 6-16), where peaks that are ≈90° to each other are clearly visible in both the crustal and lithospheric mantle MT results. However, this pattern is not observed for all the peaks in the MT results. The implications of these plots are described in chapter 7.

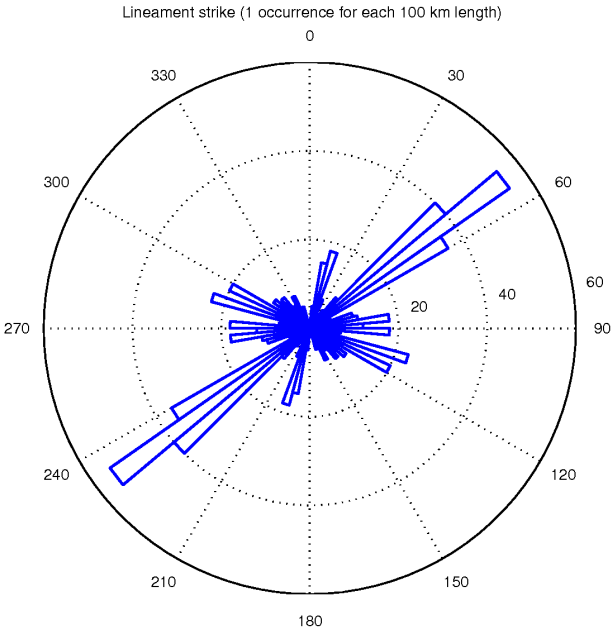

(a) Magnetic lineaments

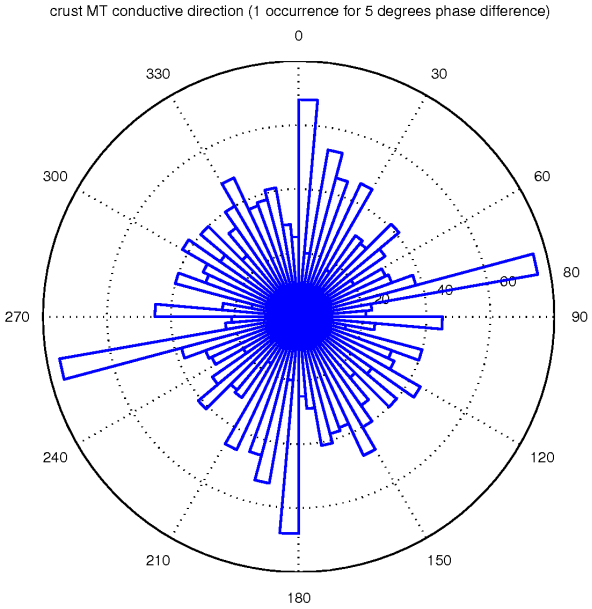

(b) Crustal MT

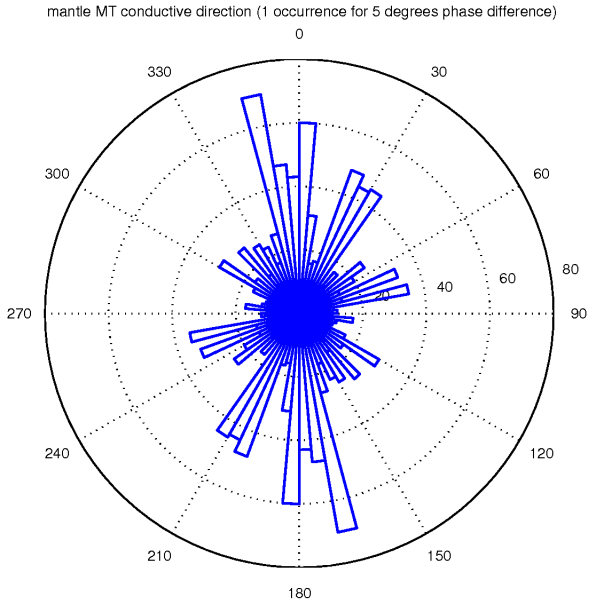

(c) Lithospheric mantle MT

Figure 6-15: *(a) Rose diagram of magnetic lineament angles digitised from Jelsma* et al. *(2004). Each 100 km of lineament length counts as one occurrence for that angle. (b) Rose diagram of crustal MT conductive directions. Each 5° of phase difference counts as an occurrence for that direction/angle. (c) Rose diagram of lithospheric mantle MT directions, also weighted such that each 5° of phase difference counts as an occurrence for that direction/angle.*

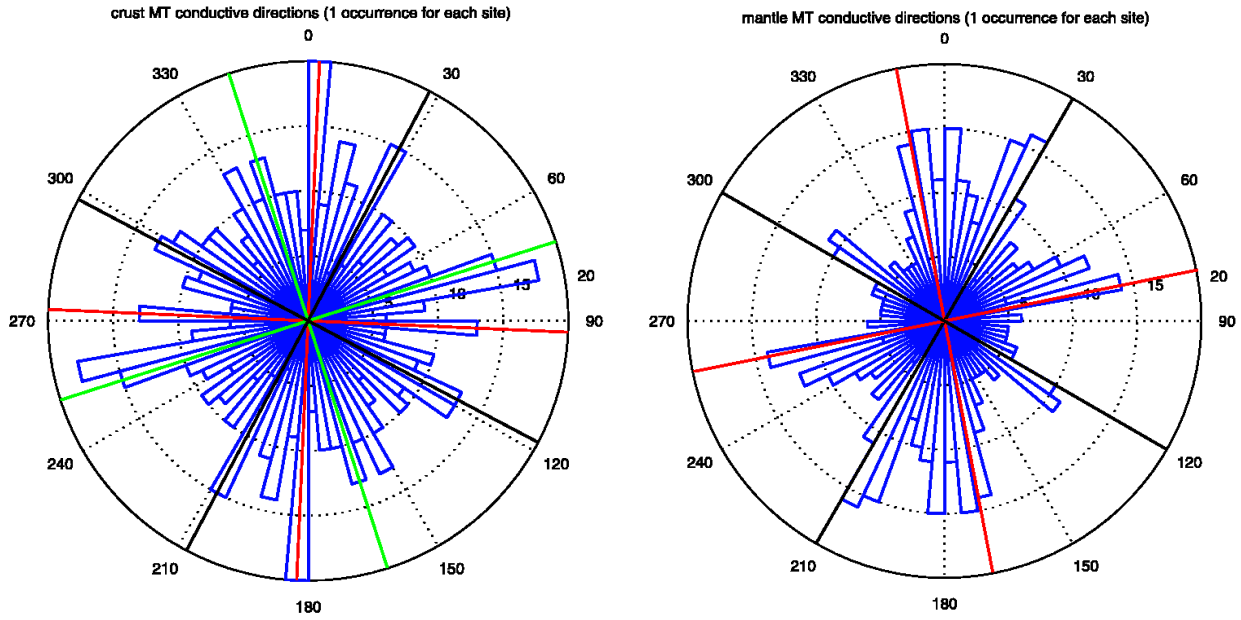

(a) Crustal MT

(b) Lithospheric mantle MT

Figure 6-16: *(a) Rose diagram of crustal MT conductive directions, with one angle for each site. (b) Rose diagram of lithospheric mantle MT directions, with one angle for each site. Red, black, and green lines indicate peaks in conductive directions that have a corresponding peak ≈90° to it.*

7

Discussion of MT and seismic results

7.1 The MT conductive direction results

We are fortunate to have a very large MT data set with extensive coverage to conduct this study. The MT most conductive directions that we observe across the southern African region, both for crustal and lithospheric mantle depths, are generally far more complex in nature than has been observed in previous studies. To facilitate ease of reading and discussion, some of the important figures from previous chapters are repeated in this chapter.

7.1.1 Crustal MT results

The crustal MT results are, for the most part, high quality, as it is generally at the longer periods where data are poorer. The eastern Kaapvaal data are not of adequate quality due to both noise and poor signal during recording and have therefore been excluded. The first impression one gets when viewing the crustal results (figure 7-2) is that they are quite variable and rather complex, although there are some regions that display systematic trends. However, bearing in mind the physics of the model described in figure 6-8, our crustal MT results are quite pleasing. There are clear cases where we observe a near-90° flip in the most conductive direction at known terrane boundaries. It should be remembered however, that

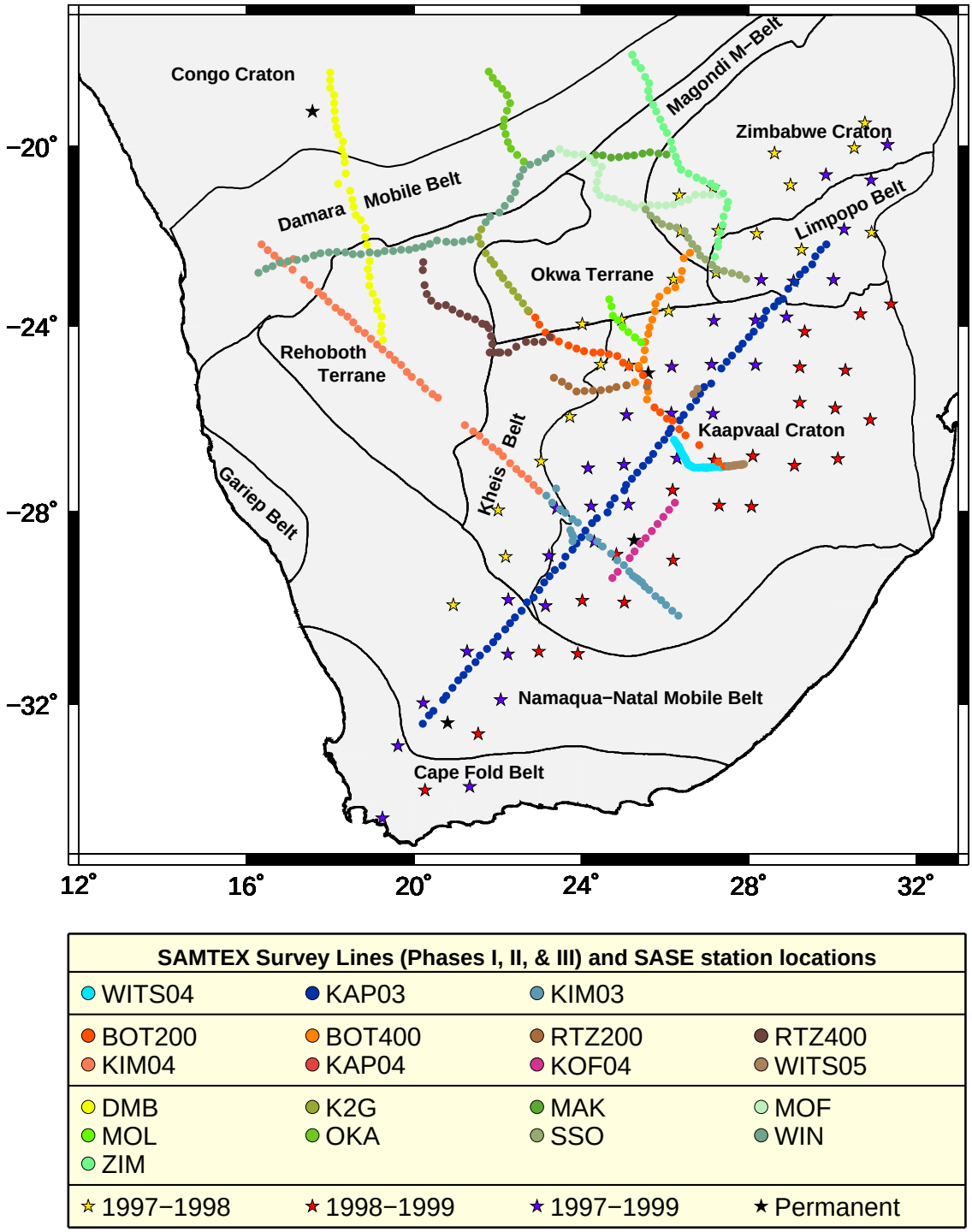

Figure 7-1: *The southern African magnetotelluric experiment (SAMTEX) profile/site locations, and the SASE seismic array station locations, overlain on a map of southern Africa with schematic geological provinces (after Nguuri* et al., *2001).*

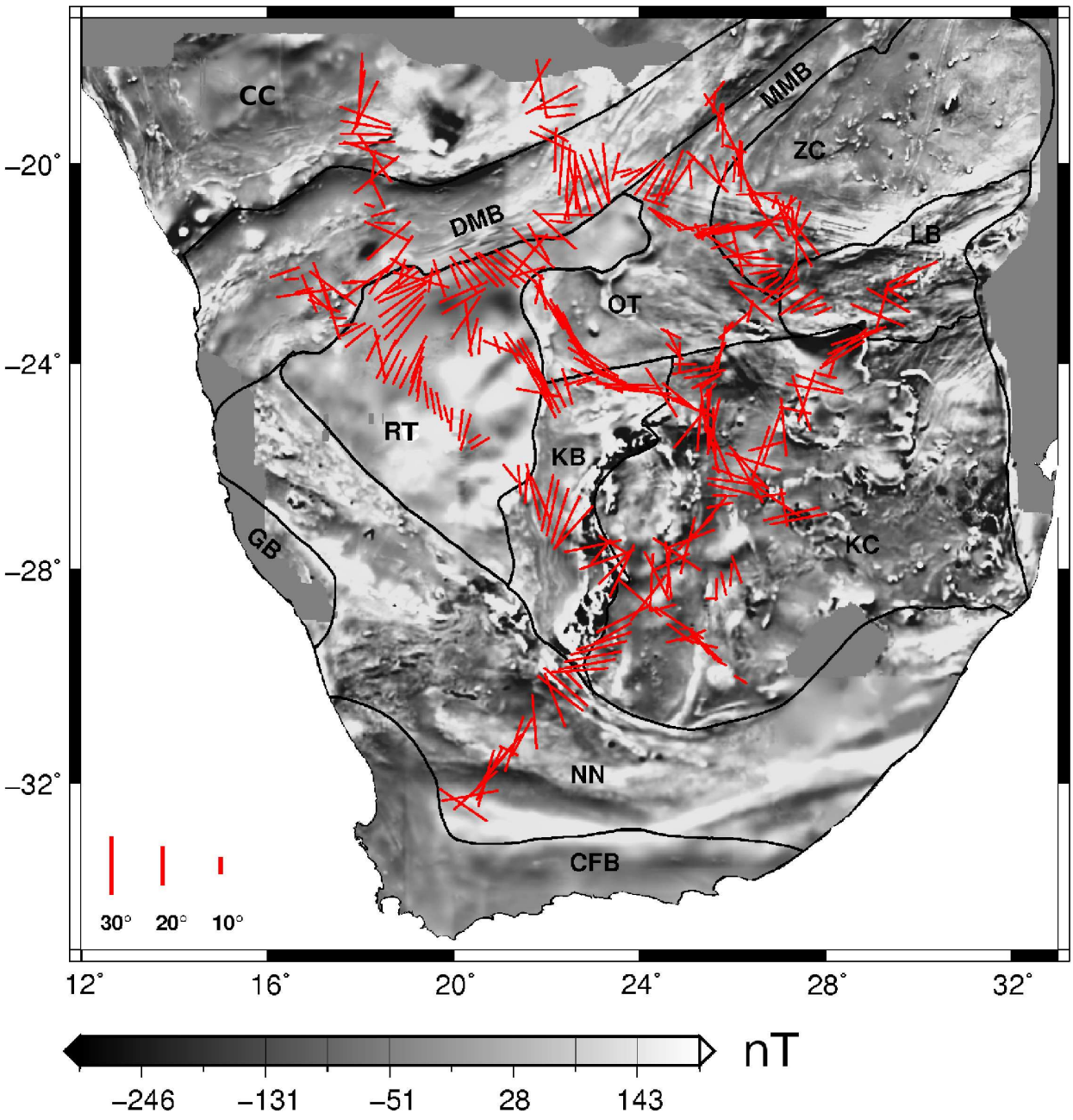

Figure 7-2: *Crustal MT most conductive directions, plotted as red bars, with the length scaled by phase difference, overlain on the regional magnetic data of southern Africa. Geological terrane boundaries are derived largely from regional potential field data (Nguuri* et al., *2001). KC: Kaapvaal craton. LB: Limpopo belt. ZC: Zimbabwe craton. NN: Namaqua-Natal mobile belt. CFB: Cape Fold belt. KB: Kheis Proterozoic fold and thrust belt. MMB: Magondi mobile belt. RT: Rehoboth terrane. GB: Gariep Belt. OT: Okwa Terrane. DMB: Damara mobile belt.*

these need to be boundaries that separate regions of differing conductivity, otherwise this boundary effect will not be observed.

For the purpose of the discussion of our MT results, we will refer to the effect on conductive directions due to boundaries between different conductivities as heterogeneity effects, while electrical anisotropy will refer to anisotropy due to lineaments or cracks, sometimes called macro anisotropy (sketched schematically in figure 7-3). Where discussed, electrical anisotropy due to very small-scale features, such as aligned electrically anisotropic mineral grains, will be termed micro anisotropy. Of course, since MT senses a volume, it is difficult to impossible to distinguish between macro and micro electrical anisotropy.

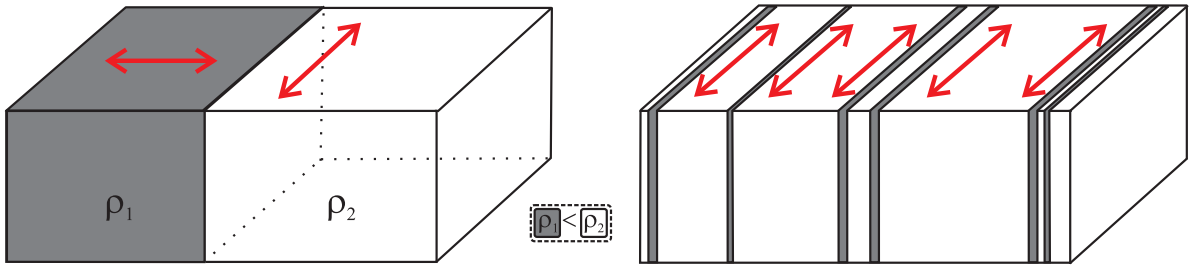

Figure 7-3: *Schematic diagram describing the different effects of conductivity heterogeneity (left) and macro anisotropy due to lineaments or cracks (right) on the electrically conductive directions. It should be noted that for small scale and high frequencies, the right model will produce similar effects at the boundaries to the left model. It is a question of the scale of the inhomogeneity compared with the inductive scale length.*

One of the most clear examples of this 2D heterogeneity effect is on the Kap03 line (figure 7-1, page 128), at the southwestern boundary between the Namaqua-Natal mobile belt and the Kaapvaal craton (figure 7-2). Although slightly more complex than would be observed in the ideal model scenario, we see the more conductive directions change from being parallel to the boundary on the Namaqua-Natal belt, to being nearly perpendicular to the boundary on the Kaapvaal craton (figure 7-2). Another region where we see this effect quite clearly is in the northwest of our survey area on the DMB line (figure 7-1, page 128) as we move from the Damara belt onto the Congo craton; the conductive direction changes from parallel on the northern edge of the Damara belt, to perpendicular to the boundary on the Congo craton (figure 7-2). This has been substantiated by 2D modelling (Spratt *et al.*, 2007), where a conductive crustal feature is imaged on the Damara Belt side of the contact. Other regions where this effect can be observed, though perhaps not quite as clearly, are: on the Kim04 line

as we move from the Kheis Belt onto the Rehoboth terrane, on the Kap03 line as we move across the Colesberg trend, and on the Kap03 line as we move from the Kaapvaal craton onto the Limpopo belt (figures 7-1, 7-2).

It was hoped that the cluster analysis undertaken on the crustal MT data would help to gain a better understanding of the patterns observed in the results. Specifically, we were hoping that this analysis would extract from the complex data set regions that posses a pervasive conductive direction that would more likely be due to electrical anisotropy rather than 2D heterogeneity effects. The results of the analysis (figure 7.4(a)) do serve this purpose to some degree. In the southwestern Okwa terrane, most of the K2G line is classed in one group, with a cluster centroid value of 158°. Another region where there does appear to be a consistent trend is in the central northern Rehoboth terrane, where there is a common north-easterly trend in the data. An additional area with consistent directions is the southwestern Zimbabwe craton and western Limpopo belt, where a northeasterly direction is observed. A direction of around 40° is observed on the Kap03 line in the central Namaqua-Natal belt. These regions, particularly those away from any boundaries such as in the Rehoboth terrane, would provide support for electrical anisotropy as being the predominant cause of conductive direction orientations. However, one feature that was unexpectedly enhanced through the use of the clustering technique is the effect of heterogeneity, discussed above. This is because on either side of the structure, the conductive directions are generally classed into different clusters creating a colour contrast across the boundary to which the eye is drawn. This can be clearly observed in figure 7.4(a) when looking at the regions with boundary effects mentioned at the end of the previous paragraph.

The obvious contribution from heterogeneity to the crustal MT results led us to investigate whether we could find a correlation between major lineaments and boundaries in the region and our MT results. Magnetic lineaments of major extent were digitised from Jelsma *et al.* (2004) and converted to points and angles for the analysis. There were difficulties encountered when trying to spatially correlate these with the MT data orientations because in certain areas there are multiple lineaments and it is impossible to assess in a statistical manner which lineament is the one affecting the MT result, and so it was thought that rose diagrams may be a better means of comparing the results. The lineament data were weighted by length, whereas the MT data were weighted by phase difference; however, the resulting patterns are not too dissimilar to the unweighted versions.

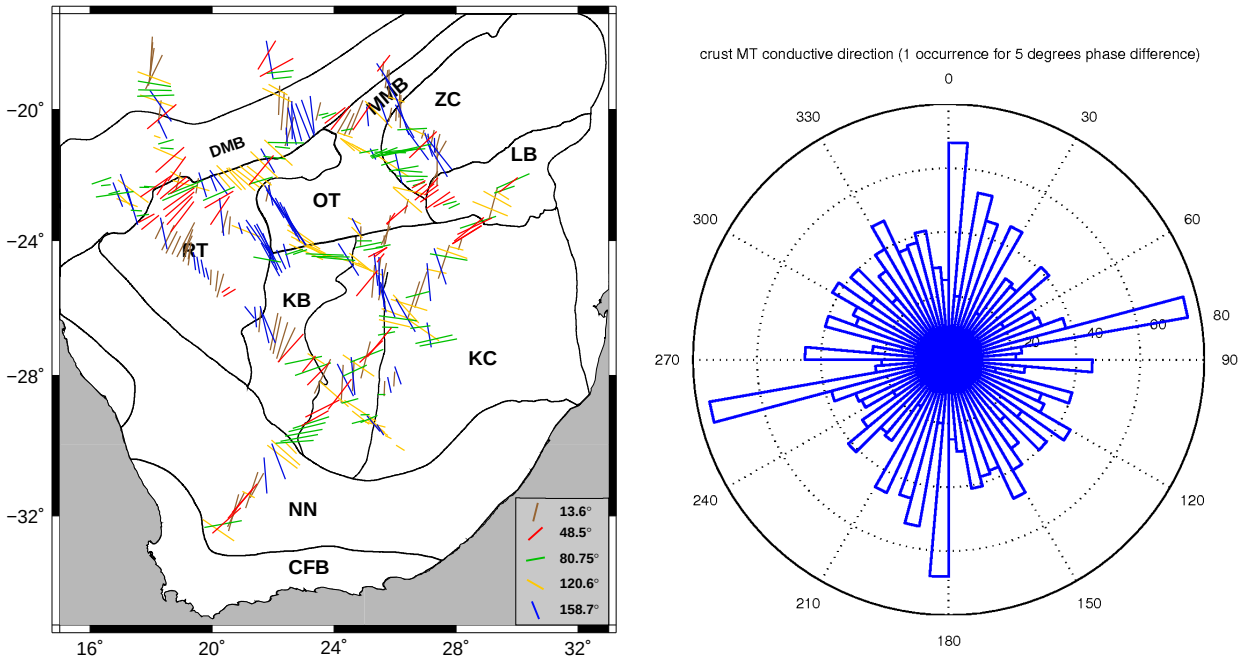

(a) Crustal clusters

(b) Crustal MT

Figure 7-4: *(a) Results of K-means cluster analysis for 5 clusters, on the conductive directions from the crustal MT results. The cluster centroid locations for each are denoted in the key. Terrane names are as in figure 7-2. (b) Rose diagram of crustal MT conductive directions. Each 5° of phase difference counts as an occurrence for that direction/angle.*

The crustal MT results, regardless of whether they are weighted by phase difference (figure 7.4(b)) or unweighted (figure 6.16(a)), show a broad azimuthal distribution. There is no direct correlation that can be made between the major peak in the lineament rose diagram (figure 6.15(a)), and the MT rose diagram for crustal depths, indicating that for the longer magnetic lineaments, which likely correspond to deeper and more substantial structures, there does not seem to be a major conductivity signature associated with them in the crust. This is not to say that there is no direct correlation at all, as some of the smaller peaks in the lineament rose diagram do seem to have a somewhat better correlation with the MT results (e.g. at 90° and 120°). There are two large peaks in the crustal MT rose diagrams at ≈0° and ≈75°. If the MT conductive directions are due to heterogeneity, and the data fall on both sides of a given conductivity heterogeneity, we would expect that, given the physics described in figure 6-8, we would have corresponding peaks in conductive directions approximately 90° to each other. Our crustal MT results are therefore quite pleasing, and indicate one of two things. The two major peaks are not quite 90° to one another because of the complexities of real geological situations, and these are, in fact, the complementary

peaks, indicating that there are some largely north-south and/or east-west features causing these peaks. Alternatively, as indicated in figure 6.16(a), these peaks correlate with other peaks almost exactly 90° apart, but of slightly different size. The difference in size could be explained by the MT data not having equal stations on either side of the heterogeneity, or by having additional (non-heterogeneous/anisotropic) influences in the directions where the peak is larger. If we had done our analysis for given frequencies, the drop-off of the heterogeneity effect will be stronger on the conductive side of a contact compared with the resistive side, which would mean that even for equi-spaced stations there would be a bias towards the resistive side (the direction parallel to the contact). This effect is approximately cancelled by taking approximate depths for the analysis and not a constant frequency for all sites; see figure 6-8, where the constant depth analysis shows a near-equal drop-off on both sides of the fault.

Regardless of which explanation applies, what the rose diagrams do tell us is that there are strong effects due to heterogeneity visible in the crustal MT results that are likely not related to the longer magnetic lineaments with azimuths of ≈50°. The crustal MT results may, however, be related to the lineament peaks at ≈90°, and ≈120°, while there is a peak in the MT results around 75°, which, if not related to the 0° peak, corresponds to heterogeneities with a strike of either ≈75° or ≈165°.

7.1.2 Lithospheric mantle MT results

Since the seismic anisotropy from shear wave splitting analysis had been interpreted to be due to LPO of olivine located in the lithospheric mantle by Silver *et al.* (2001), it was expected that if the seismic anisotropy had an electrical anisotropy signature, we would find a very similar pattern in the lithospheric MT results to those observed in the seismic shear wave splitting analysis. Our analysis shows that this is most certainly not the case, and therefore requires futher analysis and explanation.

Our lithospheric mantle results (figure 6-10) show a stark contrast to the seismic results over which they are plotted, and show a level of complexity comparable to that of the crustal MT results. While in some regions, such as the northeastern and southwestern Kaapvaal craton, there appears to be quite a close correlation between the directions of the MT and seismic fast axis directions, there are also regions where this is certainly not the case, such as on the Limpopo belt where the electrically more conducting directions are near perpendicular to the seismic fast axis direction.

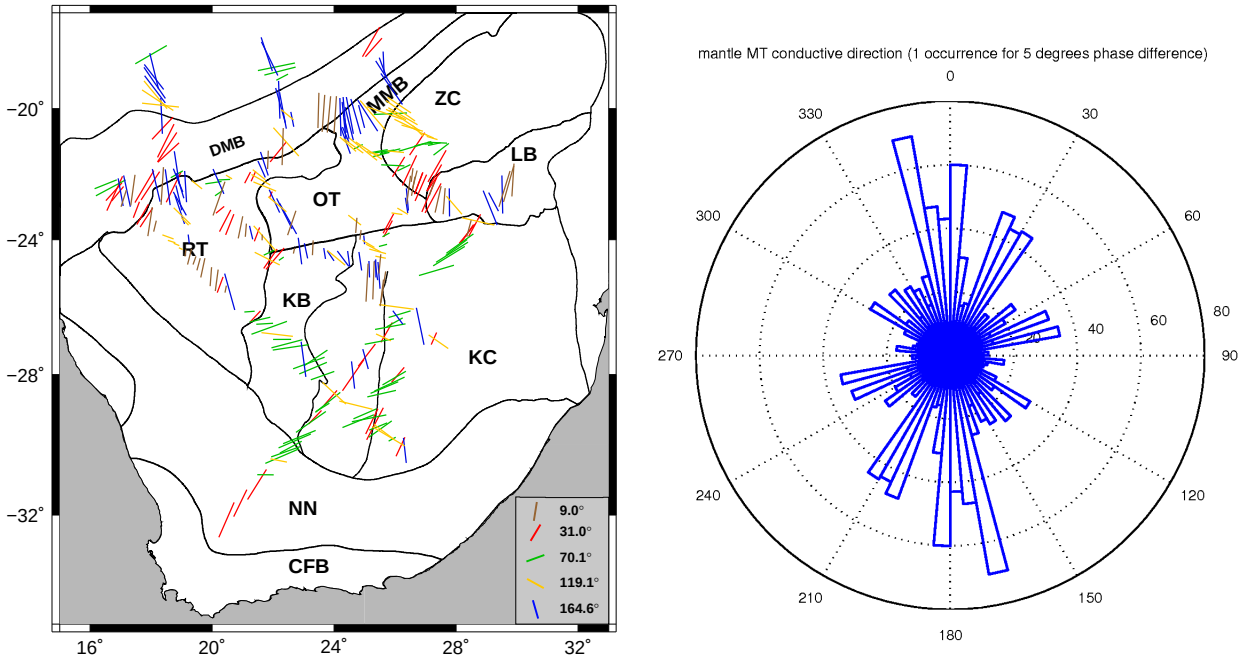

(a) Lithospheric mantle clusters

(b) Lithospheric mantle MT

Figure 7-5: *(a) Results of K-means cluster analysis for 5 clusters, on the conductive directions from the lithospheric mantle MT results. The cluster centroid locations for each are denoted in the key. Terrane names are as in figure 7-2. (b) Rose diagram of lithospheric mantle MT conductive directions. Each 5° of phase difference counts as an occurrence for that direction/angle.*

There are certainly still some areas that seem to be affected by large-scale conductivity structures, such as in the northern part of the OKA line as we move from the Damara belt onto the Congo craton (figures 6-10, 7-1). In order to extract any pervasive directional patterns that may exist in the data, we conducted the same cluster analysis that was undertaken on the crustal MT results, on the lithospheric mantle results, having found five clusters to be appropriate for both sets of data. The results of the cluster analysis (figure 7.5(a)), although still quite complex, do appear to show more uniformity across regions, as one might expect when looking deeper into the Earth due to the spatial averaging nature of EM fields. The southeastern Rehoboth terrane displays a dominantly northeast conductive direction, while the southwestern Kaapvaal craton appears to have a more conductive direction of around 70° (green cluster). Additionally, the northeasterly trend on the Namaqua-Natal belt that was observed in the crustal MT results, appears to be consistent in the lithospheric mantle results. On the southwestern Zimbabwe craton and western Limpopo craton there is a

consistant conductive direction, although it does appear to have a lower angle to the trend observed in the crustal results. These larger regions of consistent conductive direction are likely due to anisotropy rather than heterogeneity effects, as most are away from known large-scale terrane boundaries. Since vertical magnetic fields are generated by lateral conductivity variations and not by anisotropy, the tipper vectors would be an ideal means to confirm our interpretation. However, due to the difficulty of installing vertical magnetometers, there are very little vertical field data in the SAMTEX experiment, particularly over South Africa and the southern regions of Botswana and Namibia.

Similarly to the analysis for the crustal MT, we plot our lithospheric mantle conductive directions on a rose diagram, and compare the results to lineament directions. Again, we see no strong correlation between the major peak at ≈50° in the lineament directions (figure 6.15(a)) and any of the peaks in the conductive directions (figure 7.5(b)). The longer magnetic lineaments likely correspond indirectly to deeper and more substantial structures. The magnetic response of these features would be limited to depths shallower than the Curie depth, although the geological structure may continue deeper. It was therefore expected that, if these longer features do have a conductivity signature, they would be more likely to correspond to our lithospheric mantle, rather than crustal MT results. This provides a strong argument that for the majority of the longer lineaments with ≈50° strike, there is no conductivity signature present. However, we do again note that there are conductive direction peaks that are near-90° apart, albeit of differing sizes, for directions of ≈30° (corresponding peak at ≈120°) and ≈75° (corresponding peak at ≈165°). The directions of both of these peaks correspond well with the crustal results, suggesting that if they are indeed caused by large-scale structure, such as conductivity boundaries, then these boundaries are present at both crustal and lithospheric mantle depths.

This brings us to an important question; where, and by how much, do the crustal and lithospheric mantle results differ? While a qualitative look at the rose diagrams for each depth (figures 7.5(b), 7.4(b)), indicates that although there are some similarities, the results show generally quite different patterns. However, the differences are best presented with more spatial information in figure 7-6, where we plot the lithospheric mantle results scaled by phase difference (as plotted in figure 6-10), but colour the bars by the difference in angle in degrees between the crustal and lithospheric mantle conductive directions. Red bars indicate strong variations between crustal and lithospheric mantle conductive directions, while blue bars highlight areas where there is no significant variation between the crustal and

lithospheric strike directions.

There is a lot of information that may be obtained from figure 7-6. Firstly, we look at the red bars on the Namaqua-Natal belt. In the crustal results there is a strong effect on the conductive directions from the boundary between the Kaapvaal and the Namaqua-Natal, whereas in the deeper lithospheric results, there appears to be far less of an affect. A similar pattern may be observed on the Kim04 line (figure 7-1) at the boundary between the Kheis belt and the Rehoboth terrane. This clear change from our crustal to lithospheric mantle results suggests that these boundaries, at least as far as the conductivity variations are concerned, are located largely in the crust, and do not have the same signature at lithospheric mantle depths.

Conversely to this, we observe that on the central Rehoboth terrane there is a heterogeneity effect in our lithospheric mantle results, which is not apparent in our crustal results (hence the presence of red coloured bars). This is coincident with, or perhaps slightly further northwest of, the approximate position of the Makgadikgadi line (dashed black line in figure 7-6). The Makgadikgadi line, which is not well understood, subdivides the Rehoboth terrane into two subprovinces; the northern Tses Subprovince, which has a weaker magnetic signature than the southern Aroab Subprovince. The change in magnetic signature is thought to reflect a potential transition in the crustal basement across a northeast trending discontinuity (Hoal *et al.*, 1995). However, our results suggest that the conductivity signature of this boundary is, in fact, subcrustal in depth, and perhaps slightly further northwest of the approximate position given by Hoal *et al.* (1995). This places important constraints on a feature, the nature and position of which, are poorly defined (Hoal *et al.*, 1995). Interestingly, the same effect is not clear on the RTZ400 and K2G lines (figure 7-1) further to the northeast (also crossing the black dashed line indicating the approximate position of the Makgadikgadi line in figure 7-6), which, if the lineament is as extensive as it is thought to be, they should be. These interpretations can be further verified with 2D inversions of the MT data along these profiles.

Regions where we see very little variation between the crustal and lithospheric mantle conductive directions are indicated as blue coloured bars in figure 7-6. There are three main regions where this is clearly the case; on the Namaqua-Natal belt (southwest Kap03 line), in the south central Rehoboth terrane (Kim04 line), and in the Okwa terrane (K2G line). This provides an important tectonic constraint on the formation of these regions, regardless of whether the conductive directions are due to structural or anisotropic effects. The impli-

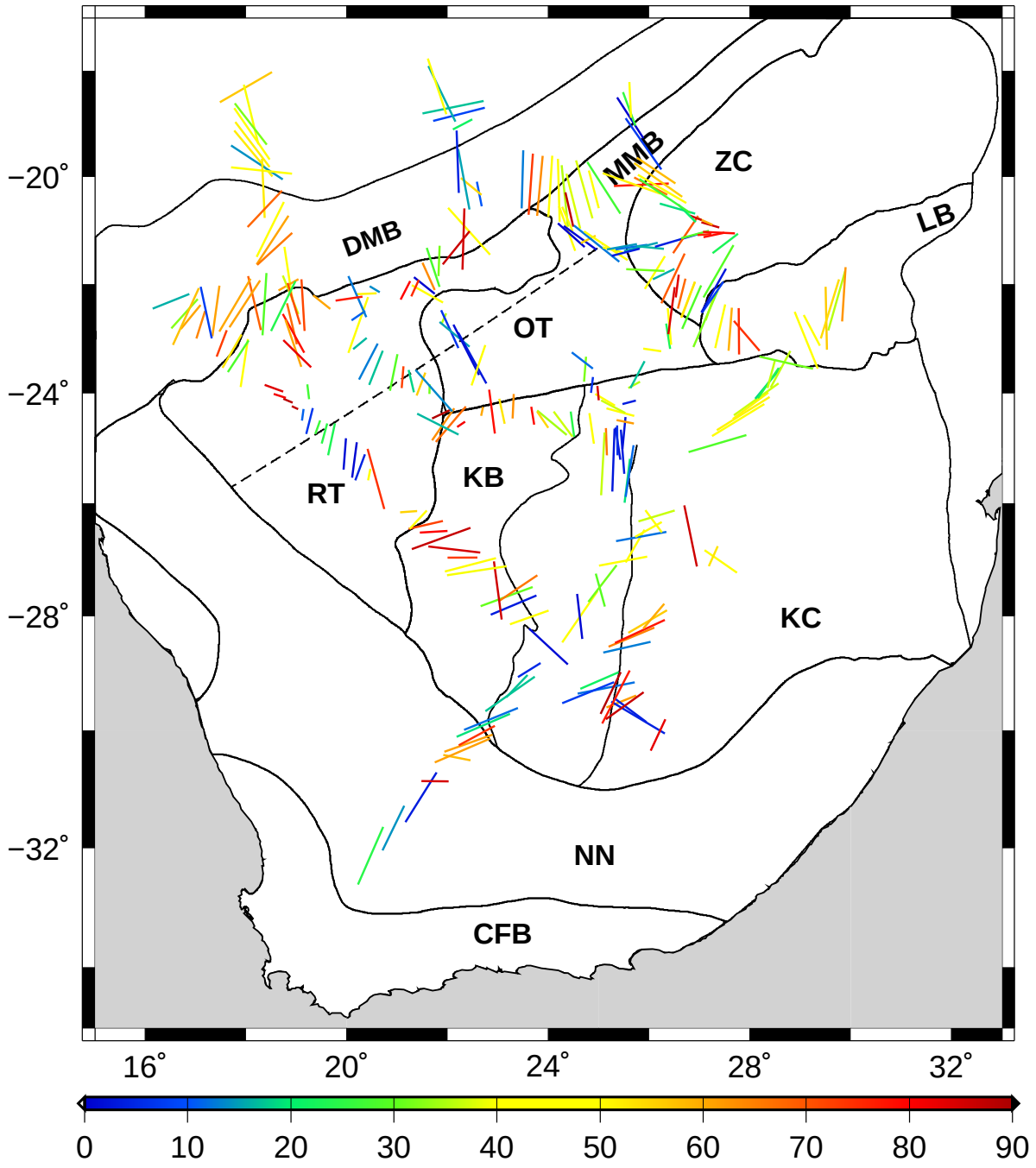

Figure 7-6: *Spatial correlation between the crustal and lithospheric mantle MT most conductive directions. The lithospheric mantle results are plotted with bar lengths scaled by phase difference as before, and with the bars coloured by the difference in degrees between the crustal and lithospheric mantle directions. Red indicates a strong difference, while blue indicates that the two sets of results are similar. Terrane boundaries are as in previous figures, and the dashed black line indicates the approximate position of the Makgadikgadi Line, from Hoal* et al. *(1995).*

cation is that these features are coherent and consistent from crustal through to lithospheric mantle depths, indicating that they likely represent large-scale features that formed through coherent deformation between the crust and lithospheric mantle. In contrast to this, regions with yellow/red bars, indicate either a change in heterogeneity or anisotropy between the crust and lithospheric mantle, perhaps suggesting that deformation has occurred separately, or differently, for the crust and lithospheric mantle.

Although there are substantial heterogeneity effects, both the crust and lithospheric mantle MT results are significantly different from the seismic shear wave splitting results. If the seismic anisotropy has a significant lithospheric component, as is suggested by xenolith studies and the interpretation of Silver *et al.* (2001), then it does not have the same effect on electrical anisotropy. This likely indicates that electrical micro anisotropy due to LPO of olivine is very small, which implies that hydrogen diffusion in olivine is small, and therefore that water content in the southern African continental lithosphere is below 100 ppm in olivine (Poe *et al.*, 2005; Beran & Liboitzky, 2006; Wang *et al.*, 2006; Grant *et al.*, 2007).

7.1.3 Asthenospheric MT results

Our lithospheric mantle results are clearly different to the SASE fast axis directions, which was not what was anticipated from observations in previous studies, although this was perhaps naive to expect considering the complexity of this region. However, this difference hinted that perhaps the lithosphere is not the source of the seismic anisotropy, and is what prompted us to analyse the regions of the MT data that penetrated to asthenospheric depths. The regions where this occurs are sparsly distributed, and also have minimal, and poorer data, which therefore necessitated multi-site analysis to counter these difficulties. Unfortunately the results that we obtain for asthenospheric depths (figures 6-11, 7.7(b)) are not sufficient in number to allow for similar analyses such as those that were conducted on the crustal and lithospheric mantle results.

We compare our asthenospheric MT conductive directions with the plate motion model of Gripp & Gordon (1990) (figure 7.7(a)) and with the shear wave splitting results of Silver *et al.* (2001) (figure 7.7(b)). From figure 7.7(a) we can see that there is, in fact, generally very good agreement between the majority of the asthenospheric MT results and the plate motion model of Gripp & Gordon (1990). If electrical anisotropy does form from aligned olivine (micro anisotropy), in a similar manner to that suggested for seismic anisotropy at the lithosphere-asthenosphere boundary, then this is a very pleasing result. Indeed, the

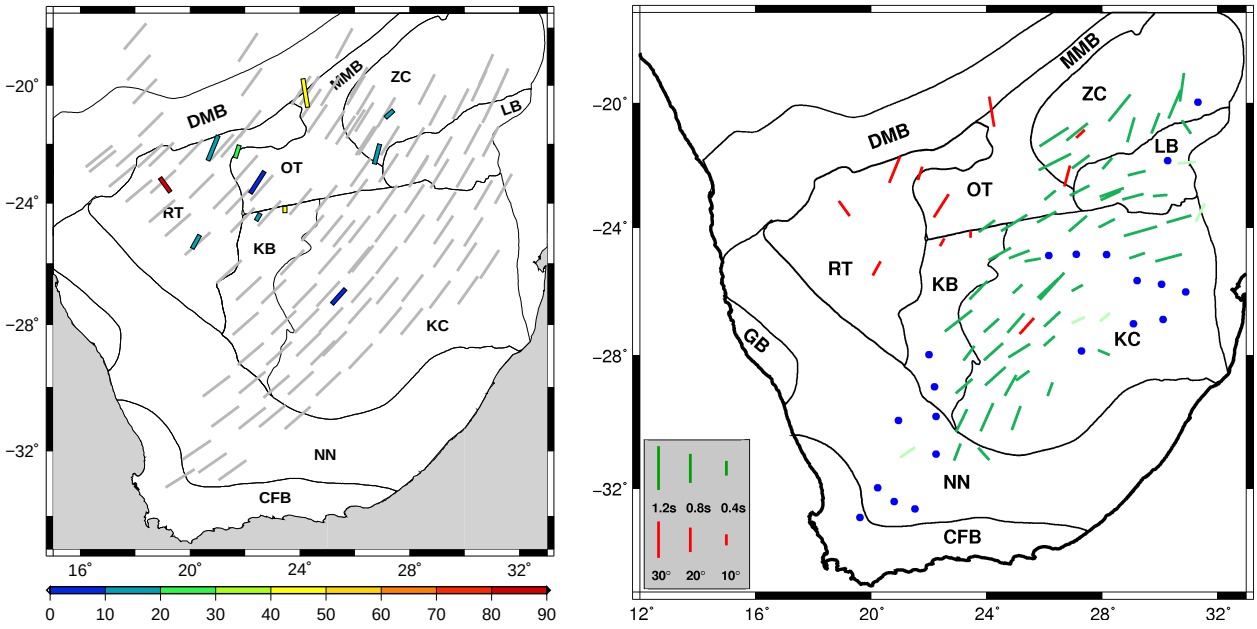

(a) Asthenospheric MT & plate motion

(b) Asthenospheric MT & splitting results

Figure 7-7: *(a) Asthenospheric MT conductive directions compared with the plate motion model of Gripp & Gordon (1990) (grey bars). The MT bars are coloured by misfit (0-90°) between the MT direction and the plate motion direction. (b) Asthenospheric MT conductive directions compared with SASE shear wave splitting results from Silver* et al. *(2001), as in figure 6-11.*

fact that the majority of our results do align well with what is predicted substantiates this suggestion, and adds another constraint for mantle flow and plate motion models in the region. There is only one region where the conductive direction is very different to the plate motion direction, in the northwestern Rehoboth terrane, although there are also two other regions where conductive directions which are also somewhat different (yellow bars). This is possibly due to poor data quality, or very strong lithospheric effects that are masking the asthenospheric response. Additionally, we note that the significantly different direction on the Rehoboth may be related to problems discussed by Jones (2006) where the modes have significantly different penetration, and may result in an analysis of data for the two modes that correspond to different depths. The results observed by plotting the data against NB depths instead of period, such as in figure 7-8, indicates that this latter explanation may be quite plausible. A decomposition analysis conducted on this site for the longest periods, will produce a decomposition result that applies to different depths for each mode, and therefore, depending on the conductivity at those different depths, may result in the erroneous selection of the more conductive direction.

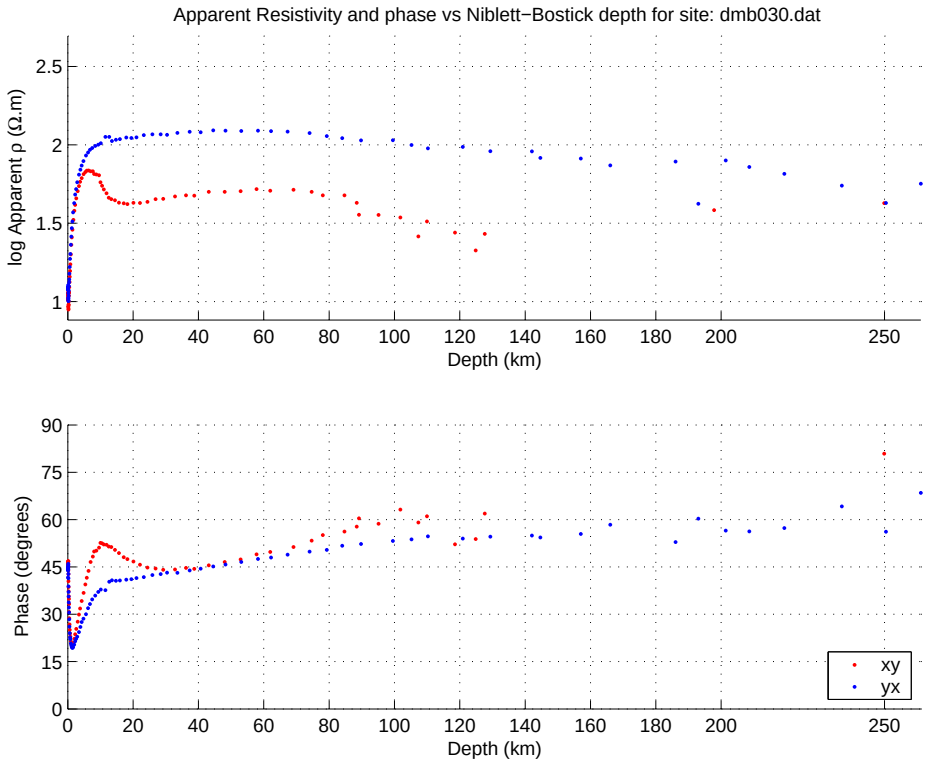

Figure 7-8: *Apparent resistivity and phase for site dmb030 (prior to decomposition) plotted against NB depth as opposed to period, indicating that the two modes have quite different penetration, particularly at the longer periods. The longest periods penetrate to approximately 120 km depth for the xy mode, but these same periods penetrate to approximately 250 km for the yx mode.*

Unfortunately the overlap between the coverage of the SASE experiment and the regions where our MT results penetrate to sub-lithospheric depths is minimal (figure 7.7(b)). There are only three locations where there are deep penetrating MT responses that fall within the SASE array. In two of these three cases the conductive directions are nearly exactly parallel to the fast axis direction of the nearby SASE stations. In the third case, on the southwestern Zimbabwe craton border, the conductive direction is not quite parallel to the fast axis splitting directions that surround it, although it is not completely disparate either (≈35° different). One might be tempted to use these results as evidence that the seismic anisotropy is, in fact, situated at asthenospheric depths, or at least at the lithosphere/asthenosphere boundary, and not within the lithospheric mantle as suggested by Silver *et al.* (2001). However, if we consider the comparative conductive directions obtained for lithospheric mantle depths (figures 6-10, 7-6), we notice that the difference between the conductive directions obtained

for asthenospheric depths and those obtained for the corresponding regions at lithospheric depths are generally not very different. While this prevents us from using these results to localise the depth of the seismic anisotropy to be in the asthenosphere alone (assuming the same causative feature is responsible for both electrical and seismic anisotropy), it does not exclude this possibility, but does allow the possibility that it is located at either or both of lithospheric and asthenospheric depths.

Excluding the two yellow and one red bar from the asthenospheric results plotted against plate motion (figure 7.7(a)), the average phase split observed between the two modes is ≈15°. If this phase split is purely a result of anisotropy, and for arguments sake the lithosphere is electrically isotropic (figure 7-9), modelling using the 2D anisotropic forward modelling code of Pek & Verner (1997) suggests this phase split would require a horizontal anisotropy with a ratio of ≈10:1. If the electrical anisotropy in the asthenosphere is micro anisotropy due to LPO of olivine which seems to be the only plausible cause, then this indicates that the olivine in this region is likely wet and strongly deformed, with well developed LPO (Gatzemeier & Tommasi, 2006) in order to account for these phase split magnitudes.

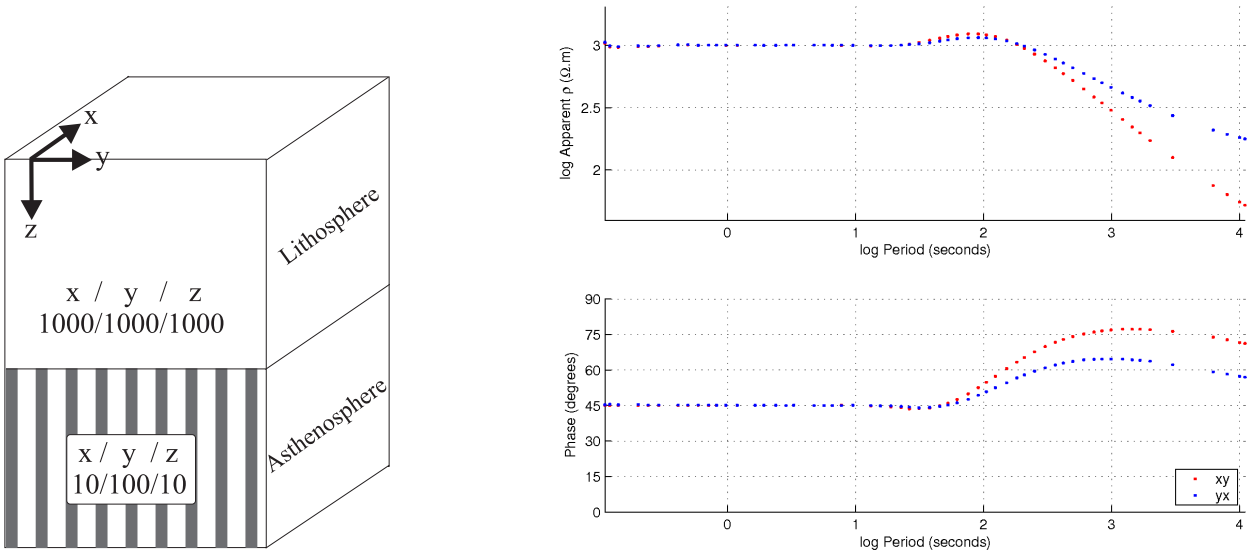

(a) Anisotropic asthenosphere model

(b) Model response

Figure 7-9: *(a) An example of a 2D anisotropic model run using the code of Pek & Verner (1997), with an isotropic 1000 Ω.m lithosphere overlying an anisotropic asthenosphere of vertical conductive sheets of 10 Ω.m (x and z directions) in a 100 Ω.m halfspace (y direction). (b) One of the model responses from (a), which produces a phase split of ≈15°.*

7.2 The SASE shear-wave splitting results

The SASE experiment was conducted from 1997 to 1999, and there have since been three main papers discussing the results of the shear wave splitting analysis. Silver *et al.* (2001) and Silver *et al.* (2004) discuss the analysis and interpretation of the broader SASE stations, while Fouch *et al.* (2004b) describe the results from the smaller array that was deployed for five months around the Kimberly region. Here we discuss briefly what we have learnt from our re-analysis, the key features of the shear wave splitting results, and how and why our interpretation differs from that of Silver *et al.* (2001, 2004).

7.2.1 Shear wave splitting re-analysis. What have we learnt?

One of the main objectives of this part of the study was to become more familiar with the SASE data, and particularly with the shear wave splitting technique itself, something that was certainly worthwhile and successfully accomplished. The multi-event splitting analysis conducted in this study utilised the same technique used by Silver *et al.* (2001), and produced splitting parameters very similar to the results obtained by Silver *et al.* (2001, 2004). As discussed in Chapter 6, in most cases the sites we chose to re-analyse produced results that are statistically identical to those of Silver *et al.* (2001), which is why we decided to use the Silver *et al.* (2001) results for our comparisons with plate motion and flow models, and with our MT results.

Another of the objectives of the re-analysis was to search for any patterns in the single-event splitting analysis as a function of backazimuth that may have been missed, and may indicate that a more complex anisotropy system was present than the single horizontal layer assumed by Silver *et al.* (2001). Although Silver *et al.* (2001) state that they did search for variations in backazimuth, a preliminary study of some of the MT data suggested that there may be two layers of electrical anisotropy, which, as discussed earlier, does appear to be the case in certain areas, and so we considered it prudent to re-examine the seismic data. After careful event selection and systematic backazimuthal searching, including at the three permanent stations, we were unable to confirm that there may be more complex seismic anisotropy. An exercise involving waveform inversion that calculates the splitting parameters assuming two horizontal anisotropic layers was also inconclusive. However, given the poor backazimuthal coverage, we were also unable to discount the possibility that there may be two layers of anisotropy present.

7.2.2 Key features of splitting results

The splitting results are discussed at length by Silver *et al.* (2001) and Silver *et al.* (2004). We will briefly describe the most important features of the results, the key arguments proposed by Silver *et al.* (2001, 2004), as well as constraints from other studies, before adding additional arguments of our own.

The splitting results show significant variation across the array (figure 6-11/7.7(b)). Strong splitting is observed in the central western Kaapvaal craton, on the Limpopo belt, and on the Zimbabwe craton. Small splitting values, and null splitting stations are observed on the eastern Limpopo belt and in the southwestern part of the array, over the Namaqua-Natal and Cape fold belt. The fast axis directions that are observed where there is splitting tend to have a general northeast-southwest splitting direction, except over the northeastern Kaapvaal craton and the Limpopo belt, where the fast axis directions are more east-west in orientation.

Silver *et al.* (2001) constrain the depth of the seismically anisotropic layer, based on four main arguments. First, they measure crustal splitting from P-to-S phases converted at the Moho, and find that the median delay time is small (≈0.15 s), consistant with normally observed crustal splitting values (Savage, 1999). Second, based on Fresnel zone arguments (Rümpker & Ryberg, 2000), abrupt changes in splitting parameters between stations 100 km apart suggest that the top of the anisotropic layer is not deeper than 50-100 km. The third argument is that the surface wave study of Freybourger *et al.* (2001) places the anisotropy within the lithosphere. Lastly, they argue that the splitting is a result of lithospheric anisotropy because the fast axis directions do not align with the predicted directions from plate motion models (figures 5.3(a) and 5.3(b)), but in fact are more consistent with large-scale geologic structures.

Silver *et al.* (2001) note the significant variation in splitting delay time. Splitting observed in this experiment is absent at about 25% of stations, and where splitting does occur, the delay time observed is generally about half the global average of ≈1.0 s (figure 7-10). Silver *et al.* (2001) note that there is a strong correlation between the surface geologic structures of particularly the Limpopo belt and the Great Dyke of Zimbabwe, and suggest that these surface structures posses counterparts in mantle anisotropy indicating a close relationship between surface and mantle deformation.

An important question to address is: how do we explain the stations with null splitting

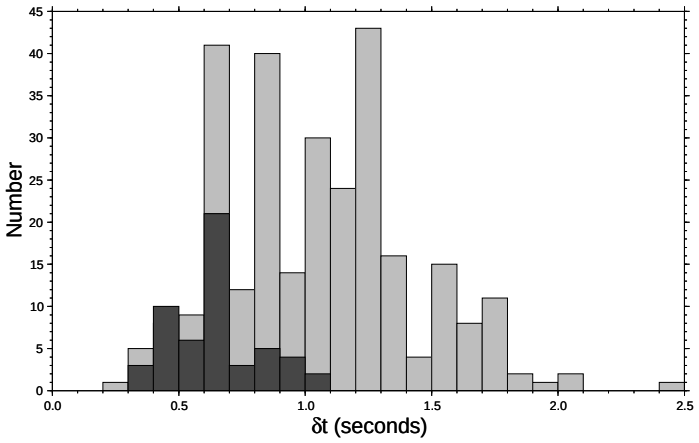

Figure 7-10: *Delay time averages from global studies (compiled from Silver (1996)), with the results of the SASE data overlain in darker grey. Note that splitting delay times (a proxy for anisotropy strength) are significantly less than averages. Null results ignored.*

(taken by Silver *et al.* (2001) to be stations with <0.25 s splitting delay time)? The region may be seismically isotropic, although this is often difficult to invoke as an explanation in geologically complex regions. Silver *et al.* (2001) suggest that since the anisotropy is located within the lithosphere (based on their arguments above), the weak splitting in the off-craton regions is simply due to thinner lithosphere. Silver *et al.* (2001) also state that the eastern Kaapvaal has thicker lithosphere, and therefore the weak anisotropy in this region cannot be simply due to thinner lithosphere, but is likely due to either a difference in vertical coherence of deformation (Rümpker & Silver, 1998; Saltzer *et al.*, 2000) or weaker intrinsic anisotropy (Ben-Ismaïl *et al.*, 2001).

The study by Saltzer *et al.* (2000) used synthetic seismograms to explore how a vertically anisotropic medium affects shear wave splitting measurements. They found that measurements made in typical frequency bands produce an apparent orientation direction that is consistently different to the average of the medium, and is, in fact, weighted towards the upper portions of the model (referred to from here on as the *Saltzer* et al. *(2000) weighted splitting* argument). Additionally, they observed that, for strong heterogeneity, multiple scattering reduces the amplitude of the tangential component seismogram and the associated splitting time, which may result in a null observation when in actual fact there is strong anisotropy present (referred to from here on as the *Saltzer* et al. *(2000) null splitting* argument). Heintz & Kennett (2006) find that from shear wave splitting observations a large part of the Australian region appears isotropic, a result of measurements performed under the assumption of a single layer of anisotropy when two layers with perpendicular fast axis

directions are present (referred to from here on as the *Heintz & Kennett (2006) null splitting* argument). Heintz & Kennett (2006) also caution that for short term deployments data should be analysed and interpreted carefully, as a small amount of data recorded in a highly heterogeneous region may potentially be very misleading.

An examination of mantle xenolith petrofabrics (e.g. Long & Christensen, 2000; Ben-Ismaïl *et al.*, 2001) shows that, at hand sample scale, the rocks of the Kaapvaal Craton lithospheric mantle certainly are seismically anisotropic, although the results reported for the strength of this seismic anisotropy do vary (Ben-Ismaïl *et al.*, 2001; Long & Christensen, 2000; Mainprice & Silver, 1993). Ben-Ismaïl *et al.* (2001) report a mean S-wave anisotropy of 2.64%, while Long & Christensen (2000) and Mainprice & Silver (1993) report maximum S-wave anisotropy values of 4.4% and 3.7% respectively. Mainprice & Silver (1993) indicate that given the ideal orientation of the fabric, it would be possible to observe delay times of over 1 s given the average S-wave anisotropy they calculate.

Silver *et al.* (2001) use the surface wave study of Freybourger *et al.* (2001) as a depth constraint on the seismic anisotropy. The Freybourger *et al.* (2001) study suggests that the anisotropy resides between 40 and 100 km depth. A second look at the surface wave analysis by Saltzer (2002) suggests that the shallowest depths to which the anisotropy can be confined is ≈150 km, but that the data do not confine how deep the anisotropy can extend. Saltzer (2002) suggest that the difference in results between the two studies is due to the improper use of a phaseless filter by Freybourger *et al.* (2001). Additionally, the surface wave study of Saltzer (2002) suggests that shear wave splitting anisotropy should produce ≈2 s of splitting.

An additional study of anisotropy in the region was conducted by Kwadiba *et al.* (2003) on Pn anisotropy from local mining earthquakes on the central Kaapvaal craton. The Pn phase propagates on, or just below, the crust-mantle boundary at upper mantle velocities and may be used to gain information on azimuthal anisotropy. Of course, there is also a tradeoff between apparent anisotropy due to seismic velocity heterogeneity and anisotropy due to aligned fabric. Kwadiba *et al.* (2003) observe a small, but pervasive, azimuthal anisotropy throughout the Kaapvaal craton, with maximum wavespeeds at azimuths of about 15° and 217° in the northern and southern regions of the craton respectively. While the fast wavespeed azimuths are relatively consistent with the shear wave splitting azimuths for the region, Kwadiba *et al.* (2003) do note that they cannot be sure they are measuring azimuthal anisotropy, and the results may in fact be a result of seismic velocity heterogeneity.

7.2.3 Further arguments from this study

Silver *et al.* (2001) discounted the asthenosphere as the main contributor for the SASE results, based largely on the argument generated by figures 5.3(a) and 5.3(b), which show that the observed splitting directions do not follow the plate motion models of Gripp & Gordon (1990, 2002). However, since the inference is being made on a spatially varying data set, this plot is misleading since it is only a plot of the delay time versus latitude, while they should be compared with both latitude and longitude to obtain a better spatial observation of where any correlation exists, or does not exist.

We first plot the shear wave splitting results over the regional magnetic data for southern Africa (figure 7-11) in order to gain a better spatial understanding, compared with figure 5.3(b), of where there is a strong correlation with surface geological trends. Although there certainly does appear to be some strong correlations with large scale features displayed in the magnetic data, such as with the Limpopo Belt structures and the Great Dyke of Zimbabwe, there are also large portions of the region where there is very little correlation. The western Kaapvaal craton in particular, has largely north-south trending geological structures (Corner *et al.*, 1990; de Wit *et al.*, 1992), whereas the fast axis splitting directions over this region are predominantly northeast.

In order to gain a better spatial correlation between plate motion directions and fast axis directions, we plot the fast axis directions of splitting against the plate motion model of Gripp & Gordon (1990) (figure 5.15(a)) and the inferred splitting from the mantle flow model of Conrad *et al.* (2007) (figure 5.15(b)) on maps. The shear wave splitting bars are coloured by the "misfit" angle between the fast axis and plate motion/mantle flow directions. Not surprisingly, since both the plate motion model and mantle flow model have a similar general orientation, these results are quite similar. There is a region of good correlation with the plate motion model in the central-western Kaapvaal craton, and fairly good correlation over the Zimbabwe craton. The region where there is poorest correlation between the fast axis directions and the plate motion or flow model is over the northeastern Kaapvaal craton and Limpopo Belt. We plot these "misfit" results over the S-wave tomography model of southern Africa at 200 km depth from Fouch *et al.* (2004a) (figure 7-12). The tomography model (both in cross-sections and plan view) from Fouch *et al.* (2004a) has clear correlations with geological terrane boundaries and shows strong indications for thick cratonic keels (blue regions) beneath the Kaapvaal and Zimbabwe cratons (Fouch *et al.*, 2004a). Thus, although there are a number of factors to be taken into account, from the observations of Fouch *et al.*

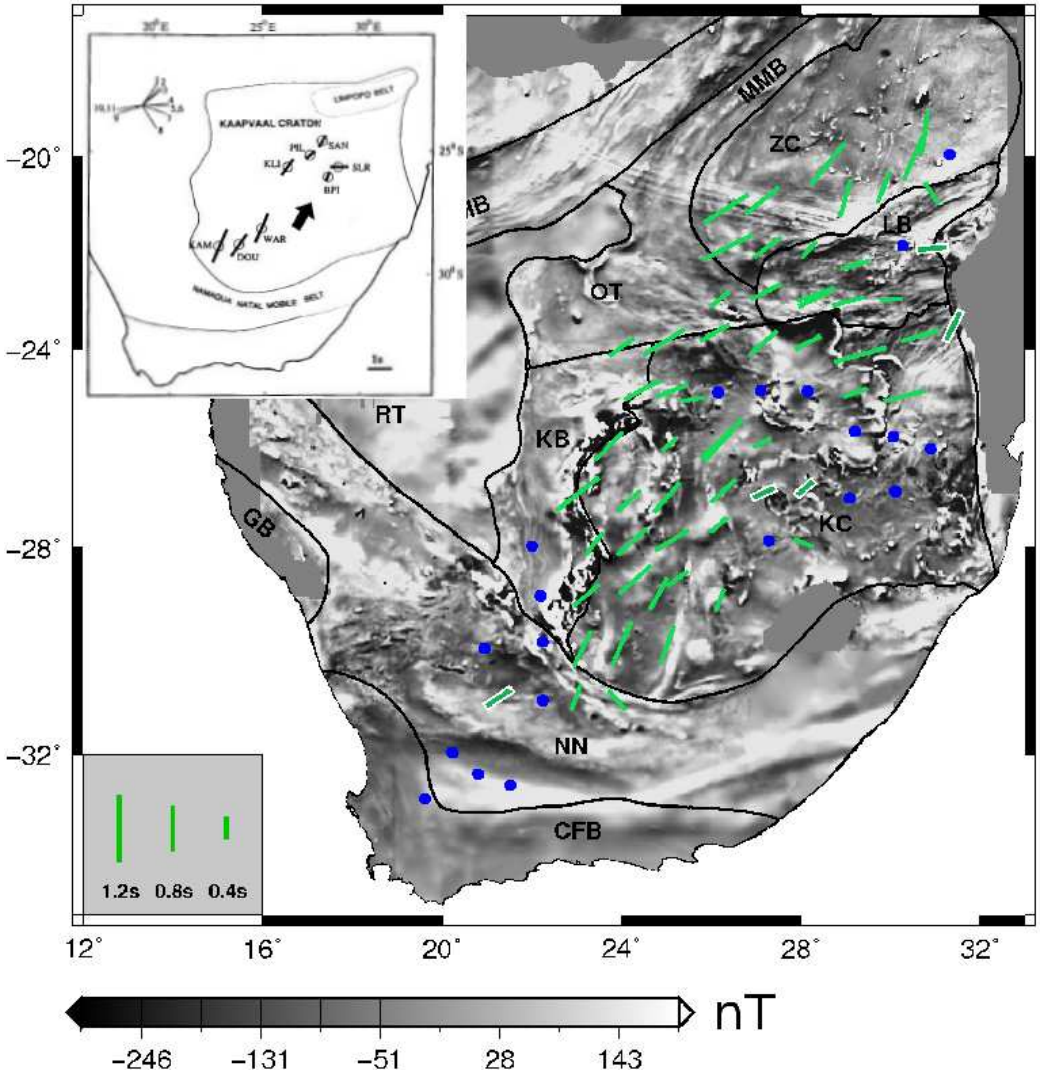

Figure 7-11: *Shear wave splitting results of Silver* et al. *(2001) (fast axis directions, scaled by delay time), overlain on the regional magnetic data of southern Africa. Green bars outlined in white indicate poor quality splitting results. Top left inset presents the results of Vinnik* et al. *(1995).*

(2004a) we use the tomography model at 200 km depth to provide an indication of the lateral extent of regions where the lithosphere appears to be thin and where it appears to be thick. This is done by taking the colours of the tomographic image to be somewhat akin to lithospheric thickness. We observe an intriguing correlation in figure 7-12; we observe a good correlation between the fast axis directions and the plate motion model where there is a thick/cold lithospheric keel (over the central-western Kaapvaal craton, and over the southwestern Zimbabwe craton). Where there is a thinner lithosphere, and no keel visible (Namaqua-Natal belt, Cape fold belt, and possibly the southeastern Kaapvaal craton) we

observe a poor correlation between the fast axis direction and plate motion direction, or null splitting observations. We also note an anomalous region over the Limpopo belt and the very northeastern Kaapvaal craton, where, from the tomography at least, the lithosphere appears to be relatively thick but the correlation between shear wave splitting and plate motion quite poor.

Based on figure 7-12, we assign each of the SASE stations to one of five groups (red, orange/yellow, green, turquoise, blue), corresponding to the tomography model variation percentage. These variations are related, and somewhat akin, to lithospheric thickness, which is how we will refer to them for the purpose of this discussion. However, one should also bear in mind that these anomalies may well be influenced by composition and temperature, as is the suggested cause of the anomaly coinciding with the Bushveld complex (Fouch *et al.*, 2004a). Null splitting stations are assigned a splitting delay time of 0.1 s, and a correlation angle between the fast axis and plate motion directions of 90° (no correlation). From this assignment, we plot the mean delay time against lithospheric thickness (the tomography model variation percentage) (figure 7.13(a)), and the mean correlation/misfit angle against lithospheric thickness (figure 7.13(b)).

If one subscribes to the theory that the seismic anisotropy resides only in the lithospheric mantle, then the difference in splitting magnitude could be explained by simply having less or more anisotropy due to thinner or thicker lithosphere respectively, strongly supported by figure 7.13(a). However, this would not explain why we observe an excellent correlation between plate motion and splitting directions over the majority of regions with a thick lithosphere keel, and a generally poorer correlation over regions with thinner lithosphere (figure 7.13(b)). Silver *et al.* (2001) do acknowledge that thinner lithosphere is correlated with weaker splitting, but do not discuss the observation that splitting on thicker lithosphere correlates well with plate motion. They therefore attribute the difference in splitting to be primarily due to a thinner anisotropic layer (thinner lithosphere) and thicker anisotropic layer (thicker lithosphere).

7.2.4 Possible explanations for SASE splitting

These observations and measurements provide for multiple models that may explain the shear wave splitting results observed across the southern African region. We describe three models that have been previously invoked to explain seismic shear wave splitting anisotropy

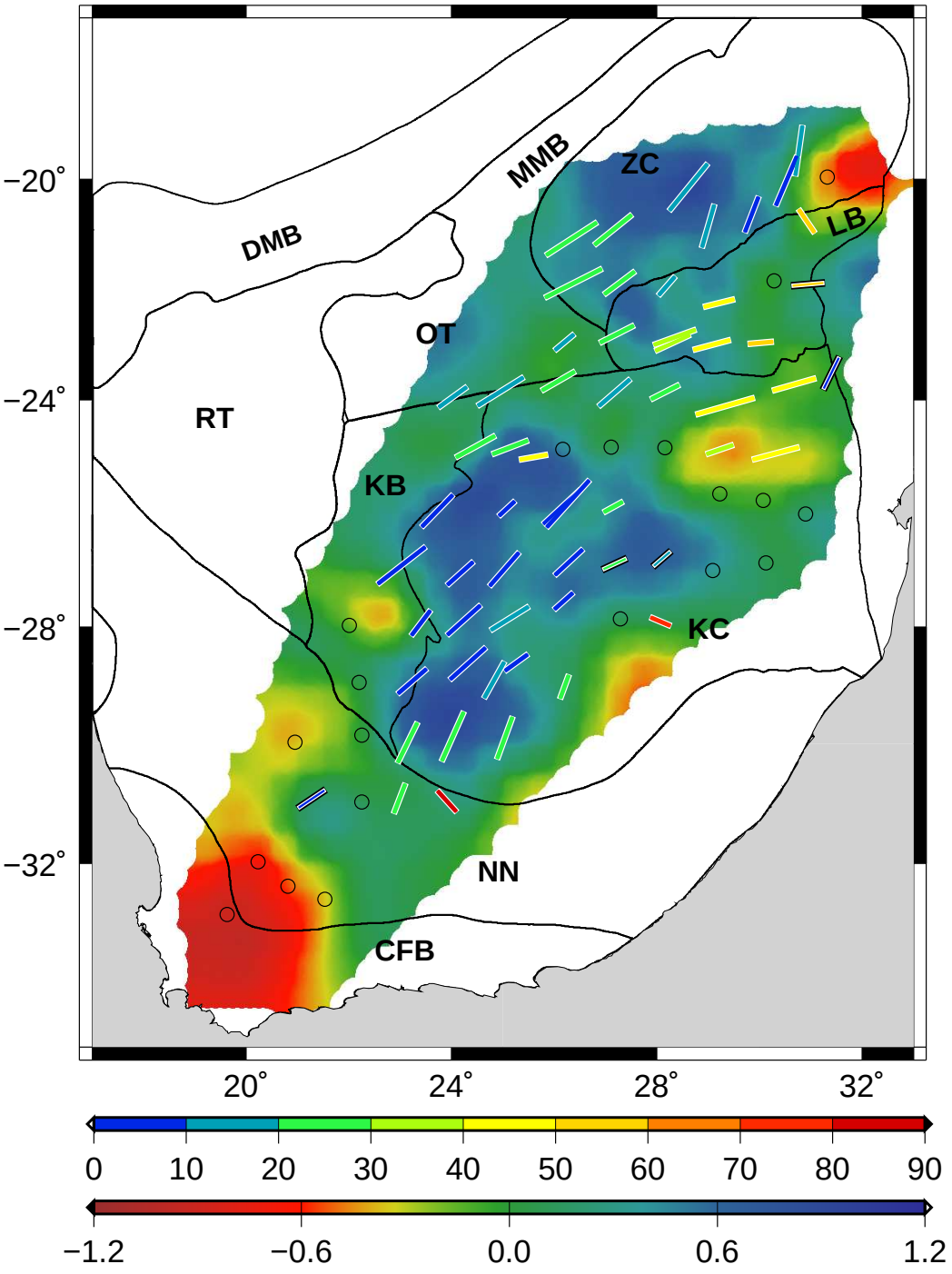

Figure 7-12: *The correlation between the fast axis direction of the SASE splitting results, and the plate motion model of Gripp & Gordon (1990), with the misfit (0°-90°) indicated by the colour of the bar of the SASE results (as in figure 5.15(a)). These results are overlain on the seismic S-wave tomography model of southern Africa at 200 km depth, from Fouch* et al. *(2004a), with percentage variations (-1.2 to 1.2). Null stations are represented by open circles, and poorly constrained splitting results are plotted with a black outline.*

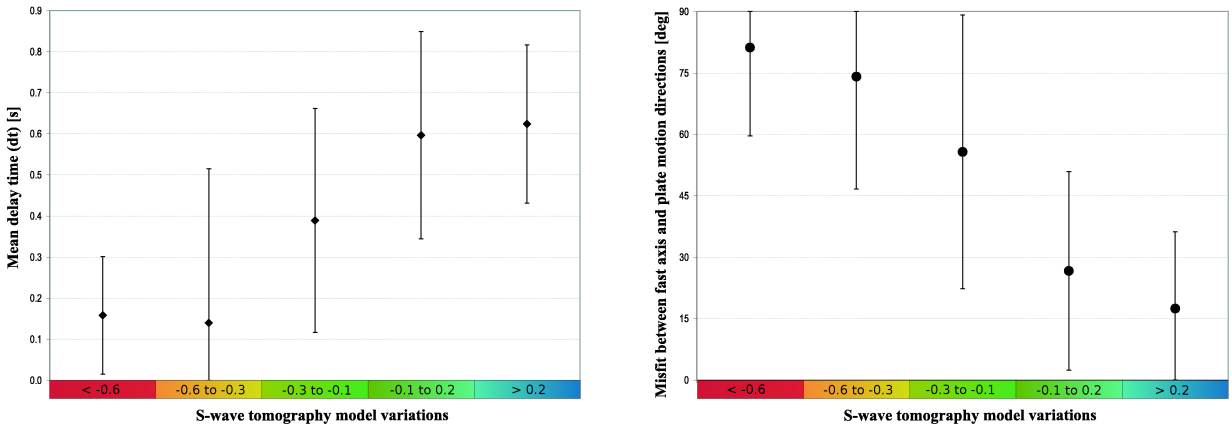

(a) Delay time vs. velocity anomaly

(b) Direction correlation vs. velocity anomaly

Figure 7-13: *(a) Mean shear wave splitting delay times plotted against velocity anomaly (akin to lithospheric thickness) from 200 km depth S-wave tomography model. (b) Mean correlation between fast axis direction and plate motion against velocity anomaly. Stations were assigned to a group/corresponding colour based on figure 7-12 (values on colour bar are approximate velocity percentage variations from figure 7-12), and null splitting stations were assigned a delay time of 0.1 s, and a correlation with the plate motion direction of 90°.*

below continental regions with thick lithospheric keels (Silver & Chan, 1991; Vinnik *et al.*, 1992; Fouch *et al.*, 2000b), and describe how they may and may not be supported by the observations.

The three models (A to C) are shown schematically in figure 7-14, each of which we will consider in turn. The first two models, A and B, depict essentially the two end members of the arguments for shear wave splitting below continental lithosphere. Model A describes the hypothesis of Silver & Chan (1991), who suggest that anisotropy in continental craton regions is dominantly a response to fossil crystal alignment in the lithosphere, with little to no contribution from dislocation creep or mantle flow. This is the model described by Silver *et al.* (2001, 2004) to explain the SASE shear wave splitting observations. The primary supporting observations for this model include (a) the correlation of the splitting with large-scale surface geological features, such as the Limpopo belt, that are not parallel to plate motion, (b) evidence from mantle nodules that the lithosphere is seismically anisotropic (e.g. Ben-Ismaïl *et al.*, 2001), (c) the fact that Fresnel zone arguments suggest that the top of the anisotropic layer is no deeper than about 50-100 km, and (d) the observation that the splitting delay time increases with increasing lithospheric thickness (figure 7.13(a)). The

main argument against this model is the observation of a strong correlation between plate motion and splitting results in the central western Kaapvaal craton, where the surface geological trends do not mimic the splitting directions well at all. In this region, the geological trends are predominantly N-S, whereas the fast axis direction of splitting is NE. In fact, the general northeast direction of splitting across the array is consistent with the plate motion direction. Furthermore, the correlation of the fast axis direction with plate motion increases with lithospheric thickness, whereas one would expect the lithospheric anisotropy directions to dominate the anisotropy where it is thick. Thus, this is completely contrary to what one would expect if the lithosphere was the primary source of anisotropy.

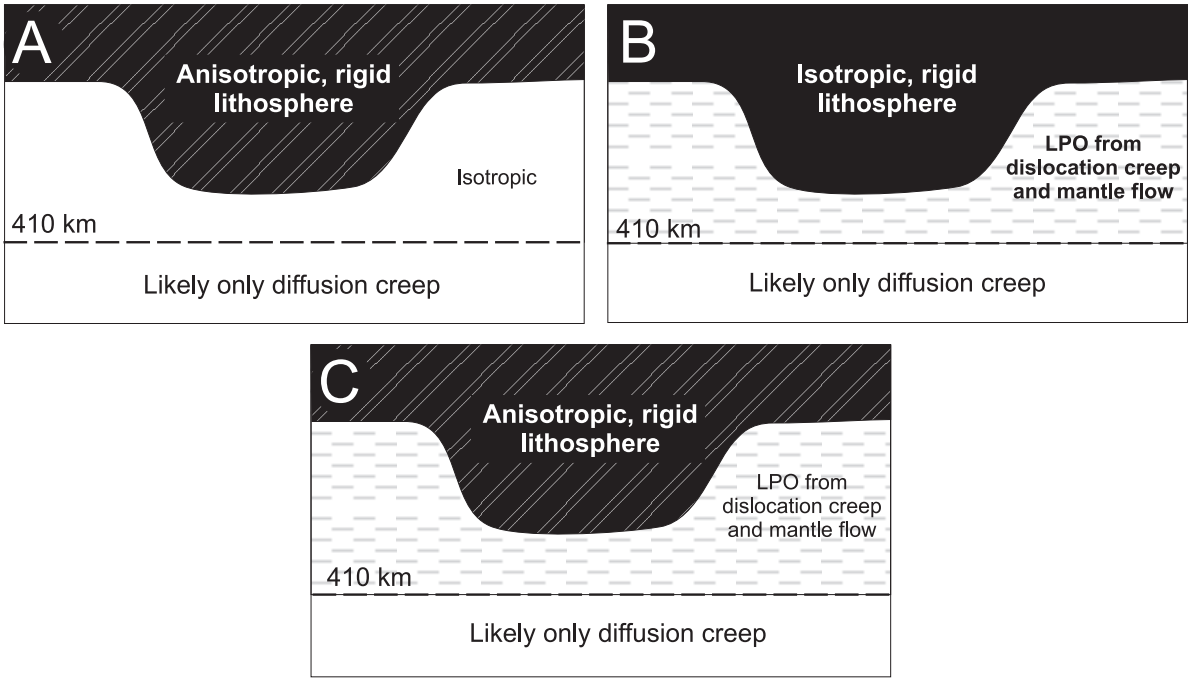

Figure 7-14: *Three cross sectional schematic models (A to C) that have been used to describe shear wave splitting observations in southern Africa (A and B) and elsewhere (C).*

Additionally, it is difficult to reconcile that under oceanic lithosphere, there is splitting interpreted to be induced by asthenospheric flow or dislocation creep, which produces splitting of around 0.8 s (e.g. station SHEL off the west coast of Africa (Behn *et al.*, 2004)), and that this asthenospherically induced contribution disappears below continental lithosphere. An argument that may explain this is that if mantle flow is confined to be between the base of the lithosphere and the 410 km discontinuity, then the flow layer would be greater below thin lithosphere, but possibly negligible below the smaller region between thick lithosphere and the 410 km discontinuity. If this were the case, one might expect to find a systematic

decrease in splitting delay time with lithospheric thickness, an observation not reported in the literature. Substantial arguments may be made for different mantle flow below continent and oceanic lithosphere at active margins, such as an active margin where the oceanic plate is being subducted and is strongly influencing the mantle flow. However the continental-oceanic margins of southern Africa are passive and old, and therefore these arguments do not hold in this region.

Model B essentially describes the hypothesis of Vinnik *et al.* (1992), where anisotropy is believed to form due to the relative motion between the plate and the upper mantle below, and also through mantle flow. It is essentially thought to be of asthenospheric origin, with little to no anisotropy present in the rigid lithospheric mantle. This is the model that is used to explain shear wave splitting results of 8 stations on the Kaapvaal craton region by Vinnik *et al.* (1995) (figure 7-11). Observations favouring this model include the excellent agreement between some splitting directions and the plate motion direction, coupled with the intuition that, certainly under thinner continental lithosphere, there is no reason why flow induced or dislocation creep induced LPO should suddenly cease upon moving from the oceanic to continental lithosphere.

Primary factors that contradict this model include the strong variations in both direction and magnitude between splitting parameters of nearby stations, as well as the presence of null splitting stations. If the splitting was only due to differential flow between the lithosphere and asthenosphere, we would expect to observe more smoothly varying splitting parameters. Also, given asthenospheric anisotropy, an isotropic lithosphere, and fair backazimuthal coverage, there is no reason why null splitting should be observed, particularly over thinner lithosphere, nor why there should be strong variations in the splitting magnitudes.

In neither of the cases presented by models A or B do all the observations support either model completely. We therefore turn to more complex models, which may be supported by all the observations, while still attempting to keep the model as simple as possible (the principle of Occam's razor). Model C represents a combination of both model A and B, with a rigid anisotropic lithosphere from frozen-in past deformation, and an anisotropic asthenosphere due to LPO from mantle flow and dislocation creep. This is very similar to the model proposed by Fouch *et al.* (2000a) for eastern North America. The primary features that support this model include those discussed for models A and B, where there is both correlation between plate motion and splitting directions, as well as a relationship with

geological structure, and the findings of seismic anisotropy measurements on lithospheric mantle nodules. However, there are major contradicting observations in the splitting results for southern Africa to this model. Assuming uniform anisotropy strength in the asthenosphere and the lithosphere, this model would predict the contribution from the asthenosphere to be a maximum in regions where there is thin lithosphere. Additionally, we would expect that over regions of thicker lithosphere, the anisotropy of the lithosphere would dominate, quite contrary to our observations (figures 7-12, 7-13). This model would create 2-layer anisotropy effects, which may be observed in the backazimuthal variations of single splitting measurements. We have searched for this effect in our seismic re-analysis however, our results were inconclusive, and thus we hesitate to use this as a complimenting or contradicting argument to this model. Lastly, the surface wave analysis of Saltzer (2002), contrary to that of Freybourger *et al.* (2001), suggests that there could be splitting of up to 2 s from lithospheric contributions. Thus, if we had this contribution aligned with plate motion/mantle flow contributions we should expect that, at least in some regions where the two are aligned, we observe splitting delay times strong in magnitude, something that is not observed at any of the stations (figure 7-10).

7.2.5 Mantle flow below thick lithosphere

A persistent question, which contradicts all three of the models proposed above, is how we can explain the excellent correlation that we observe between thicker lithosphere and well correlated splitting and plate motion directions. We introduce a strongly anisotropic layer at the base of the lithospheric keel found below old continental regions in an attempt to explain this feature of the observations (similar to a model proposed by Fouch *et al.* (2000a)). In the model for eastern North America, ultimately rejected by Fouch *et al.* (2000b), they suggest that a strong anisotropic layer below the lithospheric keel may be caused by viscosity variations beneath the keel. We suggest that for southern Africa this layer of strong anisotropy is largely a result of increased basal shear below thick lithosphere causing strong LPO from dislocation creep.

If we assume that the flux of mantle material over a vertical column is equal throughout the region, then in order to conserve momentum, it is required that flow be faster below thick lithospheric keels where the flow layer thickness is reduced, similar to the simple mantle flow behaviour modelled by Fouch *et al.* (2000b). Additionally, if this flow is further restricted to be between the base of the lithospheric keel and the 410 km discontinuity as suggested by the

relatively flat 410 km discontinuity observed in the region (Wittlinger & Farra, 2007), relative flow would need to be even faster to conserve momentum. This increased relative flow velocity would likely increase the strain rate and stress levels, resulting in increased strength of LPO due to dislocation creep in this region. Below regions of thinner lithosphere, where the flow layer thickness is greater, and thus the relative flow is slower, the slow moving African plate may not generate stresses and therefore LPO alignment as strongly, resulting in weaker anisotropy below thinner lithosphere. These proposed flow variations are described in the schematic cross section in figure 7-15. Some authors suggest that dislocation creep, causing LPO, is dominant over diffusion creep only down to depths of 250-350 km (Hirth & Kohlstedt, 2003), although seismic studies cannot, at present, put firm constraints on the depth extent of dislocation creep (e.g. Trampert & van Heijst, 2002; Wookey & Kendall, 2004; Do *et al.*, 2006). Dislocation creep is also favoured at lower temperatures, and perhaps lower temperatures may be caused in this region due to cooler keel temperatures?

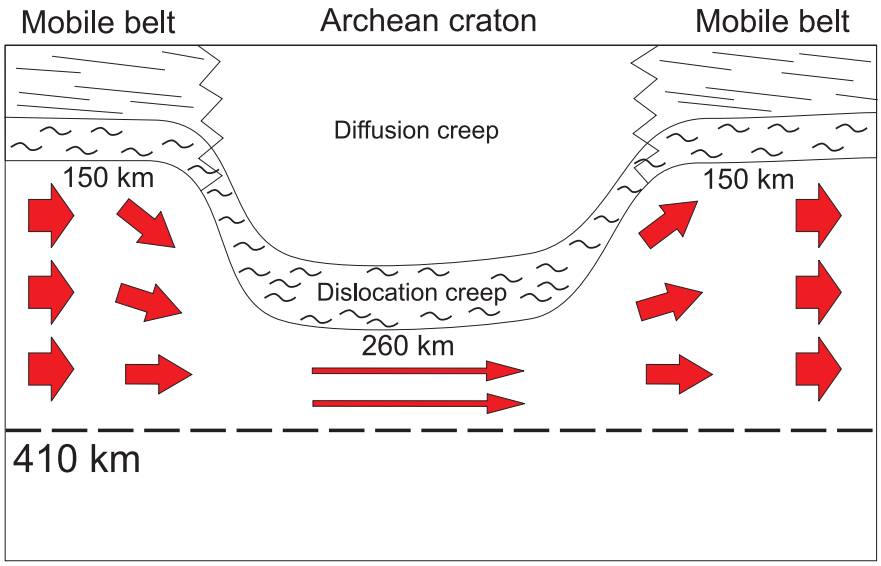

Figure 7-15: *Schematic cross section portraying mantle flow (red arrows) below a lithospheric keel. Longer arrows indicate increased velocity below thicker lithosphere, where there is a smaller flow layer thickness.*

If we were to add this layer of strong anisotropy below thick lithosphere to model B, it would improve the model substantially in that it would account for stronger splitting, better aligned with plate motion directions below the lithospheric mantle. If the contribution from mantle flow and dislocation creep at the lithosphere/asthenosphere boundary is small elsewhere, then this model could very nearly satisfy all of the observations. However, the

major contradicting observation is the splitting that is observed on the Limpopo belt and northeastern Kaapvaal craton, where lithosphere appears relatively thick (assuming the tomography is akin to lithospheric thickness, and excluding the Bushveld complex anomaly), but not as fast/cold as below cratons (figure 7-12), and splitting does not correlate well with plate motion. Additionally, surface wave studies and lithospheric mantle xenolith studies suggest seismic anisotropy in the lithosphere, and our lithospheric mantle MT results give support to having strong heterogeneity in the lithosphere. If we were to add this layer of strong anisotropy below thick lithosphere to model C, it could very nearly explain all the results however, we would still struggle to explain the anisotropy being parallel to plate motion below thick lithosphere. Even with the layer of strong LPO beneath the thicker lithosphere, we would still expect a strong contribution from the lithosphere, which would likely result in splitting fast axis directions that are a combination of both layers, and which display complex backazimuthal variations. While we are unable to verify observations of these backazimuthal variations due to the nature of the recorded data, we are still able to further constrain and explain this model using other observations, such as xenolith studies and our MT results. This leads us to our preferred general model for anisotropy (both electrical and seismic) in southern Africa, discussed below.

7.3 A model for anisotropy in southern Africa

Our proposed model for anisotropy over southern Africa is described schematically in figure 7-16. This model proposes a rigid lithosphere of variable anisotropy and degree of heterogeneity. Over mobile belts, where significant deformation has occurred with a reasonably consistent orientation, we suggest that the degree of heterogeneity is less than in the complex cratonic lithosphere. Underlying the lithosphere is an anisotropic mantle due to LPO from mantle flow and dislocation creep at the lithosphere/asthenosphere boundary. Additionally, we include the strong layer of anisotropy below the thicker lithospheric keel, for the reasons described in the previous section.

Laboratory studies of lithospheric mantle xenoliths provide strong evidence that the lithospheric mantle of southern Africa is seismically anisotropic (Mainprice & Silver, 1993; Long & Christensen, 2000; Ben-Ismaïl *et al.*, 2001). Unfortunately, similar laboratory studies of electrical anisotropy on xenolith samples have yet to be conducted. It should be remembered however, that these samples represent an extremely small region of the subsurface, and the grain size scale of these samples must be compared with the hundreds of metres to kilometres

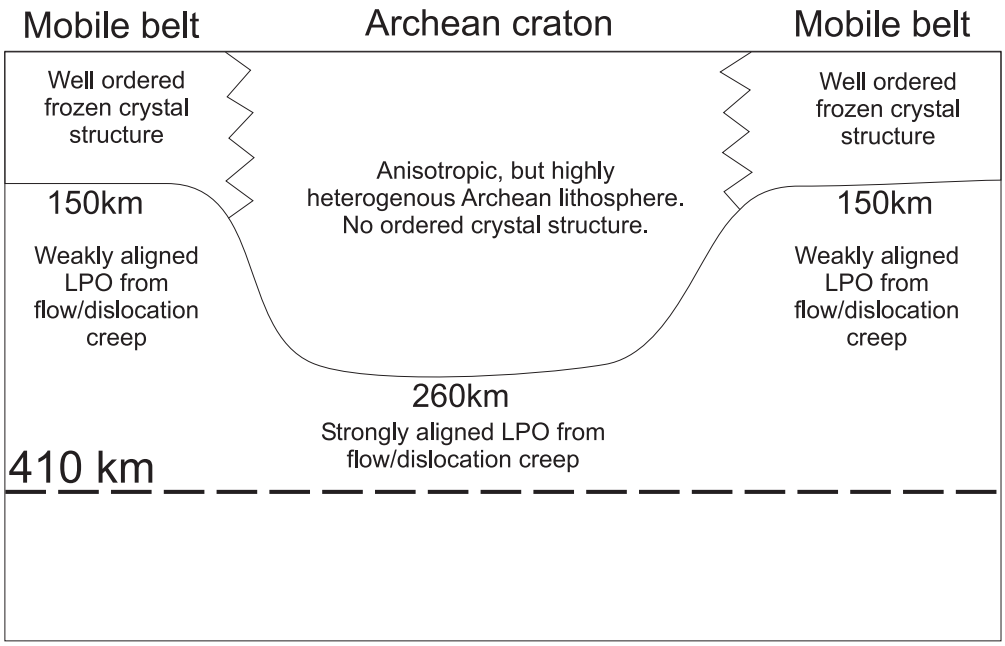

Figure 7-16: *A proposed model for the origin and structure of anisotropy in southern Africa.*

scale of SKS waves. That the lithosphere is anisotropic is also supported by surface wave studies (Saltzer, 2002; Freybourger *et al.*, 2001). However, Saltzer (2002) also suggests that the lower splitting values observed (mean of ≈0.6 s), compared with what is predicted from surface wave results, is due to strong variability in anisotropy as a function of depth. In our proposed model, we have an anisotropic, but heterogeneous, lithosphere over the Archean craton. Certainly, if we consider the complexity of the surface geology of the region (particularly on the cratons), it is likely that there is a significant amount of heterogeneity in the lithospheric mantle.

Heterogeneity in the lithosphere, both laterally and as a function of depth, is strongly supported by our MT results. Figure 7-6 shows that a large proportion of the conductive directions change significantly from crustal to lithospheric mantle depths (yellow and red bars). While some of this can be attributed to effects of heterogeneity, some can surely be attributed to vertical variations in anisotropy. For example, on the central southern Rehoboth, far from any known boundaries, there is a group of conductive directions that cluster around 158° in the crustal results, whereas they fall into a cluster of 10° in the lithospheric mantle, a vertical rotation of about 30° from the crust to the lithospheric mantle. Additionally, and perhaps lending even stronger support to the argument of vertically varying anisotropy and heterogeneity, are the rose diagrams for the crust and lithospheric mantle

conductive directions (figures 6.15(b), 6.15(c)). Whether from heterogeneity, anisotropy, or both, the rose diagrams of the conductive directions for crustal and lithospheric mantle have some similarity, but are generally quite different in pattern, with some major peaks not present in both sets of results, further arguing for vertical variations in the lithosphere.

While our model, and arguments thus far, promote a significant amount of vertical variation in anisotropy and heterogeneity, it should also be noted that there are regions where this vertical variation is far smaller in magnitude. Such areas are likely to be regions where lithospheric deformation has been vertically coherent, such as the regions represented by blue bars in figure 7-6 that indicate that MT conductive directions do not vary as a function of depth, suggesting the heterogeneity or anisotropy is vertically coherent. An example of this is on the Namaqua-Natal belt (away from the boundaries), where crustal and lithospheric mantle conductive directions are consistent. Of course, we should also note that the electrical conductive directions may not always represent the seismic fast axis direction, particularly if the lithosphere is dry. In the case of the Namaqua-Natal belt, the MT conductive directions are in the same general direction as the compressional direction when the belt accreted onto the Kaapvaal craton. It is therefore possible that the MT anisotropy is a result of sparse fractures or cracks that are conductive, whereas LPO alignment of olivine with these stresses may in fact be perpendicular to this direction. This is the proposal of Ji *et al.* (1996), where the seismic direction results from LPO, while the electrical direction results from fabric orientation. If this is the case, it means that the MT is far more sensitive to the fractures or cracks rather than the contribution of olivine LPO, indicating that the lithosphere here is rather dry. Dry olivine has lower hydrogen diffusion, and is less electrically anisotropic.

Over the regions with thicker lithosphere our model proposes a strongly anisotropic layer due to increased differential flow described in the previous section. Given a heterogeneous lithosphere, or a lithosphere that does not contribute a huge amount to the anisotropic signature, we would expect to see a good correlation between the splitting fast axis direction and plate motion; our MT results promote the former explanation.

As noted in the discussion of model A, it is difficult to imagine that there is not any component of anisotropy below continental lithosphere as observed below oceanic lithosphere, due to either mantle flow or dislocation creep. Additionally, our asthenospheric MT results, while perhaps not necessarily requiring a stronger anisotropic layer beneath the thicker lithosphere, are consistent with an asthenospheric component. The few regions where we have MT

results at asthenospheric depths have strong correlations with both the seismic anisotropy and plate motion directions. However, assuming there is a component of anisotropy from the asthenosphere or lithosphere/asthenosphere boundary, in addition to a lithosphere component, there are two questions that need to be answered.

First, why are there not any backazimuthal variations in the splitting parameters? We believe the answer to this is simple - insufficient data. In our analysis, as well as the analysis of Barruol & Ben Ismail (2001), there is insufficient backazimuthal coverage to make a conclusive judgement on this. We therefore cannot use this as an argument against this model, as it may well be present.

Second, given these contributing anisotropic layers, how do we explain the null splitting observations on the Namaqua-Natal mobile belt, and the southeastern Kaapvaal craton? For the null splitting measurements over the Namaqua-Natal mobile belt region, we can appeal to the *Heintz & Kennett (2006) null splitting argument*. We suggested earlier from our MT observations that there is coherent deformation and anisotropy in the lithosphere of this region, and that the trend of the LPO alignment may be NW-SE in orientation (perpendicular to the MT conductive directions) as a result of stresses and strains during accretion. If there is a component of anisotropy from mantle flow or dislocation creep at the lithosphere/asthenosphere boundary, this may lead to a model of two layers of anisotropy with near-perpendicular fast axis directions, analogous to the situation described by Heintz & Kennett (2006) in Australia that produces apparent isotropic measurements. The null splitting measurements observed over the southeastern Kaapvaal craton however, have little constraint from MT on the heterogeneity of the region due to the poor quality of the data recorded in this area. It is unlikely to be isotropic given xenolith studies and the fact that the lithosphere is relatively thick and therefore there is likely a component, possibly even a strong component, of LPO from dislocation creep at the lithosphere/asthenosphere boundary. Surface structural trends in the region are complex, and there is no prevalent NW-SE orientation in orientation of structures, making the *Heintz & Kennett (2006) null splitting argument* an unlikely explanation. We therefore, similarly to Silver *et al.* (2001), turn to the *Saltzer* et al. *(2000) null splitting argument* to explain these results, which suggests that very strong vertical variations in anisotropy results in scattering and apparent null measurements.

A region that requires additional explanation is the northeastern Kaapvaal craton, and the Limpopo belt. The shear wave splitting fast axis directions over the Limpopo belt and

northeastern Kaapvaal craton follow the surface geological trends and do not correlate well with the plate motion direction. According to our MT results, there are vertical variations in conductive directions, although some of this may be attributed to heterogeneity. The seismic tomography indicates that this region also has fairly thick lithosphere, and therefore does not fall in the "mobile belt" end member of our model, but neither in the "Archean craton" end member of our model. It is likely that this region forms a mixture of the two, having a relatively thick lithosphere, but also a relatively well ordered anisotropic lithospheric component. The Limpopo belt and northeastern Kaapvaal regions are known to be strongly deformed, with structures having a dominantly E-W or ENE-WSW alignment (McCourt & Vearncombe, 1992; de Wit *et al.*, 1992; Good & DeWit, 1997). This trend is visible in features such as the prominent Thabazimbi-Murchison Lineament (TML) (Good & DeWit, 1997), the Palala shear zone (PSZ) (Bumby *et al.*, 2001), as well as in the Limpopo belt itself (McCourt & Vearncombe, 1992). This deformation is large-scale, and is likely to produce anisotropy that is perhaps still variable as we move from brittle to ductile deformation as well as moving from lithosphere to asthenosphere, but it is also likely to be more ordered than in other regions due to the consistent orientation of structures and magnitude of deformation. It is somewhat analogous to the schematic diagram of a shear zone (although there is significant compression here too) portrayed in figure 4-3.

The vertical variations in our MT results are around 35° from crust to lithospheric mantle in this region. The MT conductive directions are near-parallel to surface features in the crust, but quite different from these features, or the seismic splitting results, at lithospheric mantle depths. These large-scale structures are highly unlikely to be confined to the crust, and we therefore suggest that the difference between the crust and mantle MT results may be due to the lithospheric MT results being sensitive to another factor, perhaps cracks or fractures formed during compression, which need not be dense in abundance to have a significant effect on the MT. In order to explain the seismic anisotropy in this region, we appeal to the *Saltzer* et al. *(2000) weighted splitting argument* which indicates that given a medium with variable anisotropy, assuming the medium is not too strongly heterogeneous such that scattering results in null observations, the shear wave splitting measurements that are observed are more sensitive to the upper anisotropic portions. The observed seismic anisotropy in this region is likely weighted towards the upper Limpopo belt/TML/PSZ orientation (Saltzer *et al.*, 2000), which is well ordered due to the strength of the deformation that this region has undergone. This may explain why the splitting observations over this area correlate better with large-scale geological structure rather than with the plate motion direction, even

although the lithosphere is thick and there probably is a component of anisotropy linked to plate motion and mantle flow.

Our proposed model and the anisotropy produced, slightly modified from figure 7-16 to include complexities described around the northeastern Kaapvaal craton and Limpopo Belt region (LB), can be summarised in figure 7-17. The Namaqua-Natal region can be explained by the "Mobile belt" part of the model. The majority of the Kaapvaal and Zimbabwe cratons may be explained by the "Archean craton" region of the model, and the northeastern Kaapvaal craton and Limpopo belt may be explained by a blend of these two, described schematically as the "LB" part of the model. Although there is speculation involved in our interpretation, such will always be the case due to the lack of constraints that we have for deep regions. Nevertheless, we believe that this is a reasonable and not unnecessarily complex model, that provides the best explanation for the MT and seismic anisotropy observations of the southern African region.

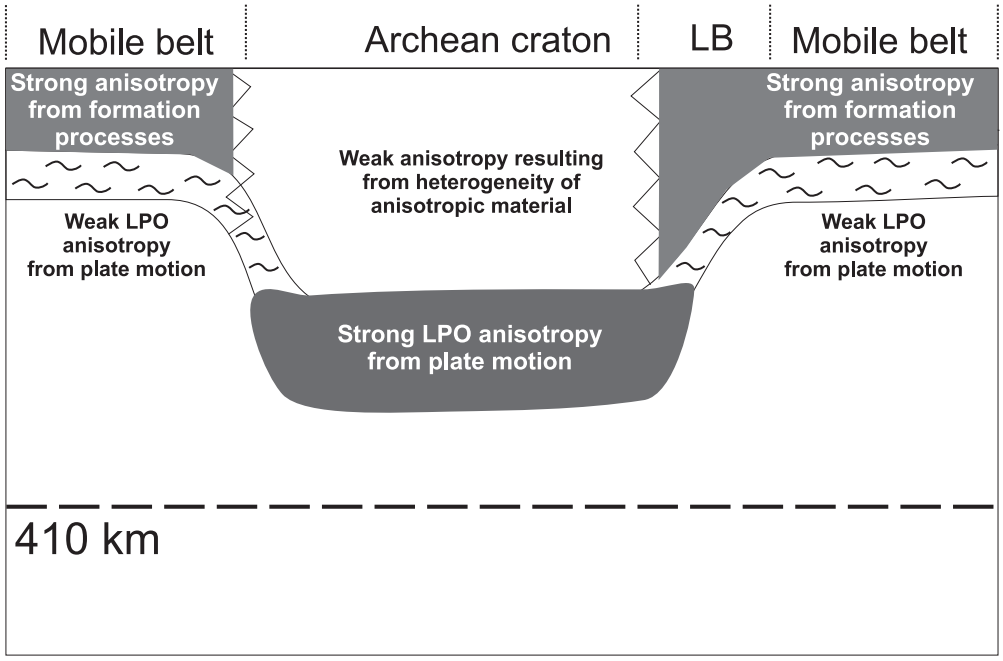

Figure 7-17: *The anisotropy produced by a proposed model for the anisotropy in southern Africa. LB indicates the northeastern Kaapvaal and Limpopo belt region.*

7.4 The correlation between MT and seismic results

At the outset of this study it was hoped that we may find a strong correlation between the SAMTEX MT anisotropy and the SASE seismic anisotropy from shear wave splitting, as had been observed in the earlier studies of Ji *et al.* (1996) and Eaton *et al.* (2004). The hope was that we may be able to use this correlation to place more accurate bounds on the depth and extent of the seismic anisotropy. It is clear from the results of the MT analysis that there is not a ubiquitous correlation for any of the depths analysed (crustal (figure 7-2), lithospheric mantle (figure 6-10), or asthenospheric (figure 6-11)). There does appear to be, at least qualitatively, a significantly better correlation between the MT asthenospheric results and shear wave splitting results; however there are only three regions where we have penetration to asthenospheric depths that are within the SASE seismic array. In these three regions the asthenospheric and lithospheric mantle most conductive directions are not too dissimilar, and thus we are unable to make a definite judgement on whether this tells us that the seismic anisotropy is coming from asthenospheric depths or not. However, from our interpretation of the seismic shear wave splitting data and our MT observations, described by our proposed model for anisotropy (figure 7-16), this does appear to be the case.

MT anisotropy can be due to either or both intrinsic anisotropy and 2D heterogeneity, as described in figure 6-8. Seismic anisotropy from the SKS study was thought to originate in the lithospheric mantle, and generally <0.3 s of delay time can be attributed to crustal shear wave splitting anisotropy (figure 3.5(b)) (Savage, 1999). Thus, the lack of correlation between the seismic shear wave splitting and crustal MT results was expected due to the degree of geological heterogeneity that is present throughout the region and due to the likely small contribution to the seismic anisotropy from the crust.

If the seismic anisotropy observed through the shear wave splitting analysis is located in the lithospheric mantle, as Silver *et al.* (2001) suggest, and it is due to the frozen-in LPO of olivine, then assuming there is no other effect on electrical anisotropy we would expect to see a good correlation between the two sets of results since the fast axis of olivine is also the more conductive direction. The correlation observed (figure 6-10) is not what we would expect given this situation. This may indicate that the source region of the seismic anisotropy is in the asthenosphere, however it may also indicate that the electrical anisotropy is being controlled by other factors, indicating that the lithosphere is dry, and electrical anisotropy of olivine is insignificant. We suggest, as proposed in our model for anisotropy in the region, that it is a combination of large-scale 2D heterogeneity effects as well as anisotropy.

7.4.1 Correlation between seismic and MT parameters

Here we take a closer look at the correlation between the shear wave splitting parameters observed from the SASE data with the results obtained from the GB analysis of the SAMTEX MT data.

We take MT sites that are located within 50 km of a seismic station that displays splitting (i.e. nulls excluded) and plot the fast axis direction versus the conductive direction for both our crustal and lithospheric mantle results (figures 7.18(a) and 7.18(b) respectively). We also plot the seismic delay times against the MT phase difference between the two modes for both crustal (figure 7.19(a)) and lithospheric mantle results (figure 7.19(b)). The scatter between points in these four plots is large, and it is clear that there is weak overall correlation and no significant trend observed between the anisotropy direction and magnitude parameters of the two techniques. Frederiksen *et al.* (2006) note that, in general, one would not expect a full correlation between the delay time and phase difference as, for example, the phase difference of an MT response near a conductivity contrast is a function of both the resistivity contrast as well as the distance from the contact. Additionally, particularly at greater depths, it is likely that the MT response is sensing a horizontally broader region than the region being sensed by the near-vertically propagating shear wave.

We examine whether or not there is any spatial correlation between these splitting and MT parameters by plotting the results on maps (figures 7-18 and 7-19). We take MT stations that lie within 50 km of seismic stations that exhibit splitting, and plot both sets of results on a map of the region for crustal and lithospheric mantle MT results. Where we compare the conductive directions with the fast axis directions, we colour the MT conductive direction bars by the misfit in direction between the two sets of results (figures 7.18(c) and 7.18(d)). Similarly, where we compare the delay time with the phase difference, we colour the MT conductive direction bars (scaled by phase difference) by the misfit between the delay time (0-1 s), and the phase difference (normalised to be from 0 to 1, with 1 representing a maximum phase difference of 30°) (figures 7.19(c) and 7.19(d)). Assuming we are looking at anisotropy and not heterogeneity, where we would need to account for 90° ambiguity, there does not appear as though there are any regions where correlation between azimuths is spatially stronger that other regions. Similarly, the delay times and phase difference, although not hugely different or variable, do not show any specific regions where the correlation is consistently stronger or weaker. This observation tells us that either the MT and seismic data have significantly different responses to the same causative feature, or that they are in

fact responding to different features that may not even be located at the same depth. This, along with the complexity of the MT results, supports our proposed model for anisotropy in southern Africa in figure 7-16 as being a viable model to explain seismic and electrical anisotropy in the region.

7.4.2 Causes of anisotropy

The results of the seismic and MT studies have been described in the first two section of this chapter, where we also look at possible causes of anisotropy. Essentially, in our view seismic anisotropy is interpreted to arise at both lithospheric and asthenospheric depths, with a strongly anisotropic layer observed beneath the centre of the cratons where lithosphere is thicker. Additionally, lithospheric anisotropy, while certainly present, is also likely to be heterogeneous in nature, supported by the crustal and lithospheric mantle MT results, which appear strongly affected by vertical variations and lateral heterogeneity. Taking into account table 4.1 in chapter 4, the causes of anisotropy are likely to be multiple. Certainly, xenolith studies require LPO of olivine to be a cause for seismic anisotropy (lithospheric), which might possibly also have an electrical anisotropy response, although this is less certain and is possibly very weak due to a dry lithosphere. Fluid-filled cracks are not an unlikely possibility, especially for crustal regions where significant deformation has occurred such as in the Limpopo region and Namaqua-Natal belt. While we cannot rule out the contribution to electrical anisotropy from an interconnected mineral phase, such as graphite, particularly in these regions of high deformation, it is not required by our data and if present is likely localised. Our results also provide no reason to believe that cracks of partial melt, or interconnected partial melt, contribute towards either electrical or seismic anisotropy in the southern African region.

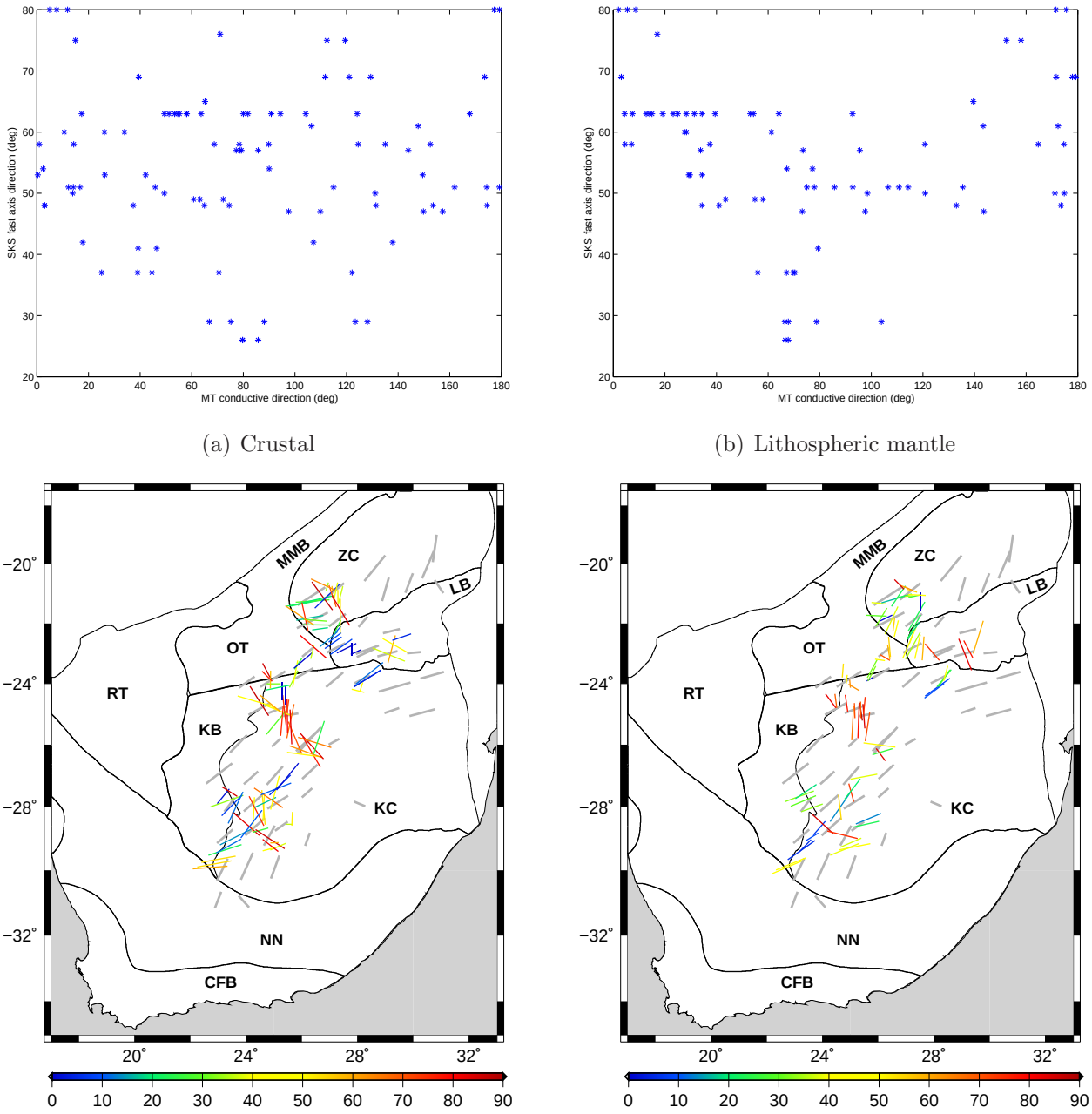

(a) Crustal

(b) Lithospheric mantle

(c) Crustal

(d) Lithospheric mantle

Figure 7-18: *The top two graphs (a and b) are plots of the shear wave splitting fast axis direction versus the MT most conductive direction for the crustal and lithospheric mantle bands respectively, for MT sites within ≈50 km of a seismic station. Poor quality splitting and null seismic stations are ignored. Below are plotted (c and d) the corresponding seismic splitting directions (grey bars) and MT most conductive directions (coloured bars), with the MT results coloured by the misfit in degrees between the fast axis direction and the most conductive direction.*

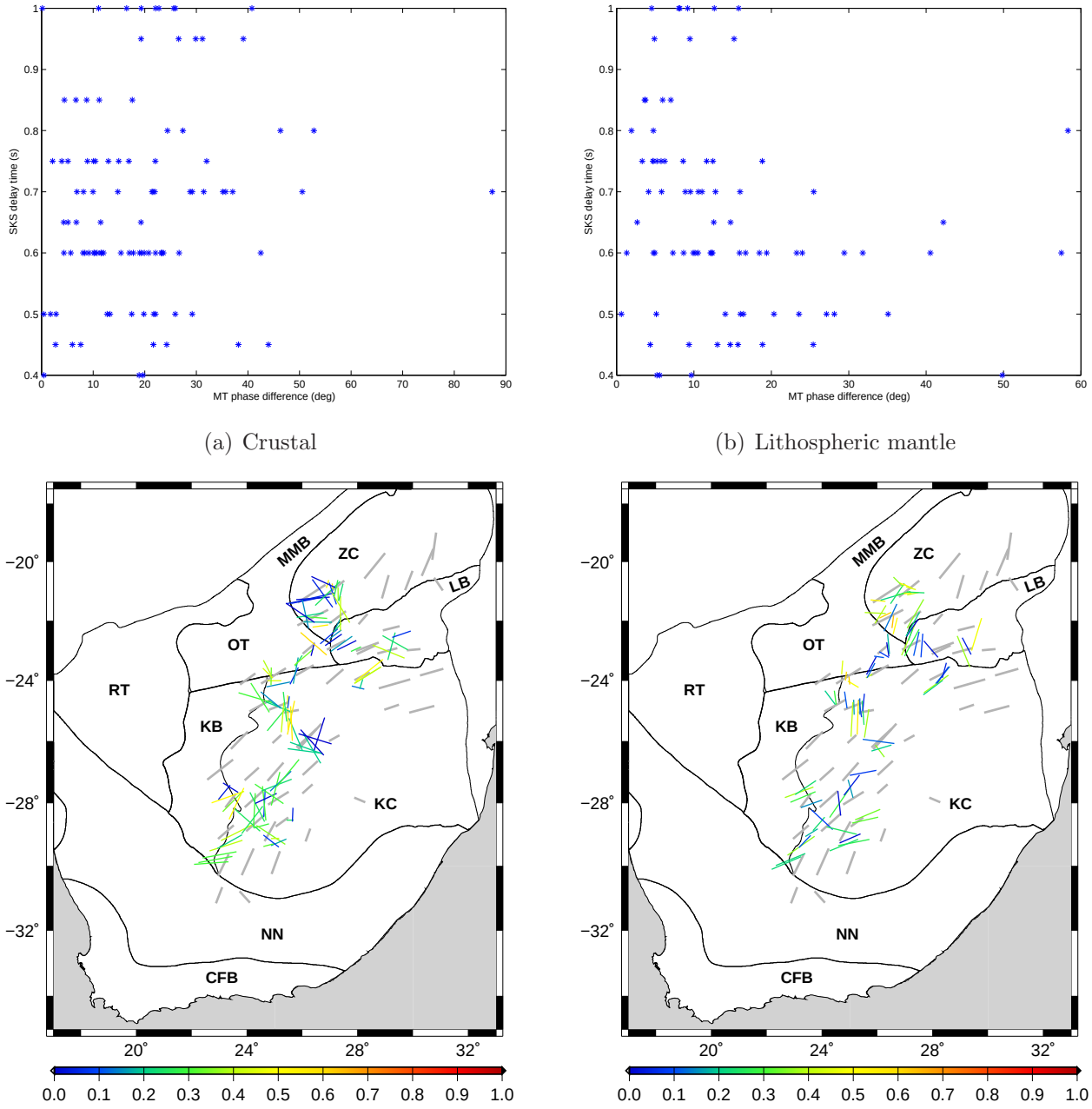

(a) Crustal

(b) Lithospheric mantle

(c) Crustal

(d) Lithospheric mantle

Figure 7-19: *The top two graphs (a and b) are plots of the shear wave splitting delay time versus the MT phase difference for the crustal and lithospheric mantle bands respectively, for MT sites within ≈50 km of a seismic station. Poor quality splitting and null seismic stations are ignored. Below are plotted (c and d) the corresponding seismic (grey bars) and MT results (coloured bars), with the MT results coloured by the misfit between the delay time (0 to 1) and the phase difference (normalised to be from 0 to 1, with 1 representing a maximum phase difference of 30°).*

8

Summary and conclusions

8.1 Summary and main conclusions

This study has utilised extensive MT and seismic data. The SAMTEX MT study, the largest of its kind, has covered broad regions that are largely terra incognita with respect to any deep-probing geophysics, in particular MT. With well over 525 broadband MT sites covering the southern African region and with additional phases of data collection to come, this experiment provides an extensive data set that has, and will continue, to add to our understanding of the geology and tectonics of southern Africa. The seismic data from the SASE experiment was collected prior to this study and has been extensively analysed and reported on using various analysis techniques.

The MT data were processed and analysed using well established methodologies and techniques. However, due to the scale of the survey we have conducted a comprehensive Groom-Bailey type decomposition distortion analysis for various periods that represent the same penetration depths across the region, unlike the traditional approach which is to take one period for a given region that approximates a certain depth for the survey. We have demonstrated the necessity for doing this by demonstrating the variation in penetration

observed with our data. We have explored further the results by using techniques such as cluster analysis and comparing the results with significant lineament features reported in the literature. The main conclusions from the MT results are summarised as follows:

- The crustal MT results suggest that the main cause of variations in the conductive directions is due to large-scale heterogeneity, particularly at terrane boundaries, which are observed as a near-90° flip in the more conductive azimuths.

- Lithospheric mantle MT results are more complex than anticipated, but are marginally less complex than the crustal MT results. There are regions where the effects of heterogeneity observed in the crustal MT results are no longer visible, indicating that these structures are likely only crustal in origin. However, there are regions where the effects of heterogeneity are clearly observed, indicating that the structures contributing to them extend to lithospheric mantle depths.

- The cluster analysis has aided in highlighting regions of consistent strike, as well as strong contrasts, but has failed to identify a ubiquitous conductive direction across the region with similar trends to the shear wave splitting results (≈NE-SW).

- Weak correlations between MT results and major lineaments indicate that, although there certainly are heterogeneity effects in the MT data, they are not likely related to the lineaments of large length extent across the region, though they may be related to lineaments shorter in length. The lineament strike directions do not show a significantly better fit to either one of the crustal and lithospheric mantle MT results.

- Overall, our MT results indicate that the lithosphere has strong variations in anisotropy and heterogeneity, both as a function of depth, and laterally. Additionally, our lithospheric results do not appear to be a result of LPO and thus give support for a dry lithosphere.

- Asthenospheric mantle MT results, although sparse, appear to be better correlated with plate motion directions, as well as shear wave splitting fast axis directions. The results promote a wet asthenosphere, with strongly developed LPO.

The SASE data from representative stations, as well as three permanent stations, were re-analysed for shear wave splitting. This analysis was undertaken using established methodologies and tested codes in order to gain a greater understanding of the results and to search for any indications of more complex anisotropy that may have been missed by the previous studies. Additionally, we have investigated further the correlation of shear wave splitting

results with plate motion and mantle flow models, as well as with tomography results from the SASE study. Below are the main results of the seismic re-analysis and investigation:

- Re-analysis of shear wave splitting results provide multi-event measurements consistent with those of previous authors (Silver *et al.*, 2001; Barruol & Ben Ismail, 2001).
- We find that while the splitting parameters plotted as a function of backazimuth do not suggest more complex anisotropy than a single horizontal layer, the data are also insufficient to reject this possibility. Waveform inversion that searches for parameters for two layer splitting was inconclusive.
- An important observation established in this study is that regions where there is good correlation between seismic fast axis directions and plate motion or mantle flow directions occur primarily where thick lithosphere is indicated by tomography models. This argues for a component of seismic anisotropy at the lithosphere/asthenosphere boundary, or within the asthenosphere. We suggest that this is a result of increased flow velocity below thick lithosphere.

Comparing the measured splitting parameters (fast axis direction and delay time) with the MT parameters (conductive direction and phase difference), we find no clear relationship. Additionally, there are no regions where these parameters agree significantly better or worse. While this may in some cases be due to seismic and electrical anisotropy being a result of different causes, we also suggest that an explanation for this lack of correlation is due to the different source regions of anisotropy. We propose a new model for the region, which explains both the seismic shear wave splitting and MT results. The proposed model (figures 7-16, 7-17) has an anisotropic, but heterogeneous, lithosphere on the cratonic region, with better ordered structures and anisotropy in the lithosphere of mobile belts. The lithosphere is underlain by anisotropic asthenosphere, as well as a strongly anisotropic region below the thicker cratonic keels in the region.

The stronger anisotropic region beneath the keel is required to explain the good correlation we observe over thick lithosphere between the splitting direction and the plate motion direction. It is possible that this might form due to increased flow velocity beneath the thick keel required in order to conserve momentum. If this is occurring, it is unlikely that there would not be any contribution in thinner parts of the lithosphere however, the contribution to anisotropy would probably be smaller in magnitude. The lithosphere is required to be anisotropic primarily due to xenolith studies, but also from surface wave studies. However,

our MT results advocate that large portions of the lithosphere are also strongly heterogeneous, an argument that has also been suggested in surface wave studies (Saltzer, 2002). We propose that the null splitting observations on the southeastern Kaapvaal craton are due to very strong heterogeneity in anisotropy resulting in severe scattering that can produce essentially a null observation (Saltzer *et al.*, 2000). The MT observations over the Namaqua-Natal mobile belt suggest coherent deformation that may align lithospheric LPO ≈90° to plate motion directions. We therefore appeal to the argument of Heintz & Kennett (2006) to explain the null splitting observations in this region. Additionally, the splitting directions over the Limpopo belt and northeastern Kaapvaal craton are predominantly aligned with surface deformational structures and not with plate motion direction, even though there is relatively thick lithosphere in this region. The severe deformation in this region may have produced a more well-ordered, less anisotropically heterogeneous region, which may result in shear wave splitting that tends to be weighted towards the upper portion of the anisotropic region. This is what we propose is occurring in the Limpopo belt and northeastern Kaapvaal craton. Thus, the model that we propose is not unnecessarily complex, with all the features required to support the observations in the region.

8.2 Future work and possible improvements

The study that we have conducted here can be extended and improved in a number of ways. Below, we summarise where extension and improvements may be made in order to reduce uncertainties and improve results obtained through this study:

- Of course, more stations and data will always be useful to gain further constraints. The main question is where these stations are located, and additionally whether a profile or grid of stations is preferable. Ideally the stations should be placed where there is poor coverage from existing profiles and also where poor data were obtained previously (only if there is reason to believe the results of a re-occupied station would be better for some reason). Profiles have the advantage for MT of having closer, more regular, station spacings which may be modelled using well developed 2D inversions, whereas a grid has the advantage of gaining broader and more uniform coverage. Ideally, given that the seismic study is an array, this aspect of the MT study may be better performed in an array with sites co-located with the seismic stations. Additionally, it would be very useful to have a SASE follow-up experiment extend further into Botswana and Namibia, as this is where we have far more MT coverage and better quality data. It would also be preferable for seismic stations to be left to record for longer periods

of time in order to gain a better backazimuthal distribution of splitting events. The AfricaArray research program will likely help in this regard.

- Another aspect to do with data collection that would improve this experiment, would be to have vertical magnetic field data collected at each site. This would substantially aid in determining whether regions that appear to be electrically anisotropic are a result of anisotropy, or a result of heterogeneity.

- In order to constrain further MT observations of the asthenosphere, it would be useful to return to areas where we have good penetration with long period MT systems during a sun spot maximum, in order to gain high quality data representative of asthenospheric depths.

- A drawback of shear wave splitting of teleseismic events, is that it has poor vertical resolution, something we try to counter by using MT. However, it may well be more appropriate to compare our MT data with surface wave anisotropy, as the latter has far better control on depth than teleseismic shear wave splitting. A drawback of this however is that you would lose the excellent horizontal resolution (in comparison to surface waves) afforded by the near-vertically travelling teleseismic waves. Nevertheless I feel this would be a worthwhile investigation.

- Future work on SAMTEX will include 2D and 3D inversion of the data, which will certainly provide some interesting results and further geological constraints (such as the size and shape of resistivity heterogeneities) for the region.

References

Agarwal, A K, & Weaver, J T. 2000. Magnetic distortion of the magnetotelluric tensor: a numerical study. *Earth Planets and Space*, **52**, 347–353.

Alsina, D., & Snieder, R. 1995. Small-scale sublithospheric continental mantle deformation: Constraints from SKS splitting observations. *Geophysical Journal International*, **123**, 431–448.

Aster, R. C., Shearer, P. M., & Berger, J. 1990. Quantitative measurements of shear wave polarizations at the Anza seismic network, Southern California: implications for shear wave splitting and earthquake prediction. *Journal of Geophysical Research-Solid Earth and Planets*, **95**(B8), 12,449–12,473.

Bahr, K. 1988. Interpretation of the magnetotelluric impedance tensor: regional induction and local telluric distortion. *Journal of Geophysics*, **62**, 119–127.

Bahr, K, & Simpson, F. 2002. Electrical Anisotropy Below Slow- and Fast-Moving Plates: Paleoflow in the Upper Mantel ? *Science*, **295**, 1270–1272.

Bailey, R C. 1970. Inversion of the geomagnetic induction problem. *Proceedings of the Royal Society of London*, **315**, 185 – 194.

Bailey, R.C., & Groom, R.W. 1987. Decomposition of the magnetotelluric impedance tensor wich is useful in the presence of channeling:. *Pages 154–156 of: 57th Annual International Meeting., Society of Exploration Geophysics, Expanded Abstracts.*

Barruol, G., & Ben Ismail, W. 2001. Upper mantle anisotropy beneath the African IRIS and Geoscope stations. *Geophysical Journal International*, **146**(2), 549–561.

Becker, T. W., Kellogg, J. B., Ekstrom, G., & O Connell, R. J. 2003. Comparison of azimuthal seismic anisotropy from surface waves and finite strain from global mantle-circulation models. *Geophysical Journal International*, **155**(2), 696–714.

Becker, T. W., Chevrot, S., Schulte-Pelkum, V., & Blackman, D.K. 2006. Statistical properties of seismic anisotropy predicted by upper mantle geodynamic models. *Journal of Geophysical Research*, **111**, B08309, doi:10.1029/2005JB004095.

Behn, M. D., Conrad, C. P., & Silver, P. G. 2004. Detection of upper mantle flow associated with the African Superplume. *Earth and Planetary Science Letters*, **224**(3-4), 259–274.

Ben-Ismaïl, W., Barruol, G., & Mainprice, D. 2001. The Kaapvaal craton seismic anisotropy: petrophysical analyses of upper mantle kimberlite nodules. *Geophysical Research Letters*, **28**(13), 2497–2500.

Beran, A., & Liboitzky, E. 2006. Water in Natural Mantle Minerals II: Olivine, Garnet and Accessory Minerals. *Reviews in Mineralogy and Geochemistry*, **62**, 169–191.

Blohm, E.K., Worzyk, P., & Scriba, H. 1977. Geoelectrical deep soundings in southern Africa using the Cabora Bassa power line. *Journal of Geophysics*, **43**, 665–679.

Bochannon, J. 2004. Earth Sciences seek niche apart from mining industry. *Science*, **304**, 380–381.

Bostick, F X. 1977. *A simple almost exact method of MT analysis.*

Bumby, A. J., Eriksson, P. G., van der Merwe, R., & Maier, W.D. 2001. The stratigraphic relationship between the Waterberg and Soutpansberg Groups in Northern Province, South Africa: Evidence from the Blouberg area. *South African Journal of Geology*, **104**, 205–216.

Cagniard, L. 1953. Basic theory of the magneto-telluric method of geophysical prospecting. *Geophysics*, **18**, 605 – 635.

Caldwell, T G, Bibby, H M, & Brown, C. 2004. The magnetotelluric phase tensor. *Geophysical Journal International*, **158**, 457–469.

Carlson, R. W., Grove, T. L., de Wit, M. J., & Gurney, J. J. 1996. Anatomy of an Archean craton: A program for interdisciplinary studies of the Kaapvaal craton, southern Africa. *EOS, Transactions of the American Geophysical Union*, **77**(29), 273, 277.

Carlson, R. W., Boyd, F. R., Shirey, S. B., Janney, P. E., Grove, T. L., Bowring, S. A., Schmitz, M. D., Dann, J. C., Bell, D. R., Gurney, J. J., Richardson, S. H., Tredoux, M., Menzies, A. H., Pearson, D. G., Hart, R. J., Wilson, A. H., & Moser, D. 2000. Continental growth, preservation and modification in southern Africa. *GSA Today*, **10**(2), 1–7.

Carney, J. N., Aldiss, D. T., & Lock, N. P. 1994. *The geology of Botswana*. Tech. rept. Private Bag 14, Lobatse, Botswana.

Chave, A D, & Jones, A G. 1997. Electric and magnetic field distortion decomposition of BC87 data. *Journal of Geomagnetism and Geoeletricity*, **49**, 767–789.

Chave, A D, & Smith, J T. 1994. On electric and magnetic galvanic distortion tensor decompositions. *Journal of Geophysical Reasearch*, **99**, 4669–4682.

Chave, A D, & Thomson, DJ. 2004. Bounded influence magnetotelluric response function estimation. *Geophysical Journal International*, **157**, 988–1006.

Chave, A D, Evans, R L, & Jones, A G. 2002. An Electromagnetic Experiment across the Kaapvaal craton and its bounding terranes. *Collaborative Research Proposal submitted to NSF*, 1–26.

Conrad, C. P., Behn, M. D., & Silver, P. G. 2007. Global mantle flow and the development of seismic anisotropy: Differences between the oceanic and continental upper mantle. *Journal of Geophysical Research*, B07317.

Corner, B., Durrheim, R. J., & Nicolaysen, L. O. 1990. Relationships between the Vredefort structure and the Witwatersrand basin within the tectonic framework of the Kaapvaal craton as interpreted from regional gravity and aeromagnetic data. *Tectonophysics*, **171**, 49–61.

Crampin, S. 1987. Geological and industrial implications of extensive-dilatancy anisotropy. *Nature*, **328**, 491–496.

Crampin, S, & Chastin, S. 2003. A review of shear wave splitting in the crack-critical crust. *Geophysical Journal International*, **155**, 221–240.

Crampin, S, & Peacock, S. 2005. A review of shear-wave splitting in the compliant crack-critical anisotropic Earth. *Wave Motion*, **41**, 57–77.

Crampin, S., & Zatsepin, S.V. 1995. Production seismology: the use of shearwaves to monitor and model production in a poro-reactive and interactive reservoir. *Pages 199–202 of: Proceedings of the 65th Annual International SEG Meeting, Expanded Abstracts.*

Cull, J P. 1985. Magnetotelluric soundings over a Precambrian contact in Australia. *Geophysical Journal of the Royal Astronomical Society*, **80**, 661–675.

Daines, M.J., & Kohlstedt, D.L. 1997. Influence of deformation on melt topology in peridotites. *Journal of Geophysical Research*, **102**(B5), 10,257–10,271.

Davis, W. J., Jones, A. G., Bleeker, W., & Grutter, H. 2003. Lithosphere development in the Slave craton: a linked crustal and mantle perspective. *Lithos*, **71**(2-4), 575–589.

de Beer, J. H., & Gough, D. I. 1980. Conductive structures in southernmost Africa: a magnetometer array study. *Geophysical Journal International*, **63**(Number 2), 479–495.

de Wit, M, & Horsfield, B. 2006. Inkaba yeAfrica project surveys sector of Earth from core to space. *EOS Transactions of the American Geophysical Union*, **87**(11), 113.

de Wit, M. J., Roering, C., Hart, R. J., Armstrong, R. A., de Ronde, C. E. J., Green, R. W. E., Tredoux, M., Peberdy, E., & Hart, R. A. 1992. Formation of an Archaean continent. *Nature*, **357**(6379), 553–562.

Debayle, E., & Kennett, B. L. N. 2000. The Australian continental upper mantle: Structure and deformation inferred from surface waves. *Journal of Geophysical Research*, **105**(B11), 25,423–25,450.

d'Erceville, E J, & Kunetz, G. 1962. The effect of a fault on the earths natural electromagnetic field. *Geophysics*, **27**, 651–665.

Do, V.C. 2006. *A study of seismic anisotropy in Ireland*. Ph.D. thesis, University College Dublin, Ireland, and Dublin Institute for Advanced Studies, Ireland.

Do, V.C., Readman, P.W., OReilly, B.M., & Landes, M. 2006. Shear-wave splitting observations across southwest Ireland. *Geophysical Research Letters*, **33**(L03309), 1–4.

Dziewonski, A. M., & Anderson, D. L. 1981. Preliminary reference Earth model. *Physics of the Earth and Planetary Interiors*, **25**(4), 297–356.

Eaton, D. W., Jones, A. G., & Ferguson, I. J. 2004. Lithospheric anisotropy structure inferred from collocated teleseismic and magnetotelluric observations: Great Slave Lake shear zone, northern Canada. *Geophysical Research Letters*, **31**(19), L19614.

Eaton, D.W., & Hope, J. 2003. Structure of the crust and upper mantle of the Great Slave Lake shear zone, northwestern Canada, from teleseismic analysis and gravity modeling. *Canadian Journal of Earth Science*, **40**, 1203–1218.

Egbert, G D. 1997. Robust multiple-station magnetotelluric data processing. *Geophysical Journal International*, **130**, 475–496.

Egbert, G D, & Booker, J R. 1986. Robust estimation of geomagnetic transfer functions. *Geophysical Journal of the Royal Astronomical Society*, **87**, 173–194.

Eggers, D E. 1982. An eigenstate formulation of the magnetotelluric impedance tensor. *Geophysics*, **47**, 1204–1214.

Eglington, B. M., & Armstrong, R. A. 2004. The Kaapvaal Craton and adjacent orogens, southern Africa: a geochronological database and overview of the geological development of the craton. *South African Journal of Geology*, **107**, 13–32.

Everett, M. 2005. What do electromagnetic induction responses measure? *The Leading Edge*, **24**(2), 154–157.

Feynman, R.P., Leighton, R.B., & Sands, M. 1964. *Mainly Electromagnetism and Matter*. The Feynman Lectures on Physics, vol. 2. Menlo Park: Addison-Wesley Publishing Company.

Fouch, M. J., & Fischer, K. M. 1996. Mantle anisotropy beneath northwest Pacific subduction zones. *Journal of Geophysical Research*, **101**(B7), 15,987–16,002.

Fouch, M. J., & Rondenay, S. 2006. Seismic anisotropy beneath stable continental interiors. *Physics of the Earth and Planetary Interiors*, **158**, 292–320.

Fouch, M. J., James, D. E., VanDecar, J. C., van der Lee, S., & Group, Kaapvaal Seismic. 2000a. Mantle seismic structure beneath southern Africa. *Page F834 of: AGU 2000 fall meeting, abstracts*.

Fouch, M. J., Fischer, K. M., Parmentier, E. M., Wysession, M. E., & Clarke, T. J. 2000b. Shear wave splitting, continental keels, and patterns of mantle flow. *Journal of Geophysical Research*, **105**(B3), 6255–6275.

Fouch, M. J., James, D. E., VanDecar, J. C., van der Lee, S., & Group, the Kaapvaal Seismic. 2004a. Mantle seismic structure beneath the Kaapvaal and Zimbabwe cratons. *South African Journal of Geology*, **107**, 35–46.

Fouch, M. J., Silver, P. G., Bell, D. R., & Lee, J. N. 2004b. Small-scale variations in seismic anisotropy beneath Kimberley, South Africa. *Geophysical Journal International*, **157**(2), 764–774.

Frederiksen, A.W., Ferguson, I.J., Eaton, D., S.-K., Miong, & Gowan, E. 2006. Mantle fabric at multiple scales across an ArcheanProterozoic boundary, Grenville Front, Canada. *Physics of the Earth and Planetary Interiors*, **158**, 240–263.

Freybourger, M., Gaherty, J. B., Jordan, T. H., & Group, Kaapvaal Seismic. 2001. Structure of the Kaapvaal craton from surface waves. *Geophysical Research Letters*, **28**(13), 2489–2492.

Gamble, T.G., Goubau, W.M., & Clarke, J. 1979. Magnetotellurics with a remote magnetic reference. *Geophysics*, **44**(1), 53–68.

Garcia, X, & Jones, A G. 2001. Decomposition of three-dimensional magnetotelluric data. *Pages 235–250 of:* Zhdanov, M S, & Wannamaker, P. E. (eds), *Three-Dimensional Electromagnetics*. Methods in Geochemistry and Geophysics, vol. 35. Elsevier.

Gatzemeier, A., & Tommasi, A. 2006. Flow and electrical anisotropy in the upper mantle: Finite-element models constraints on the effects of olivine crystal preferred orientation and microstructure. *Physics of the Earth and Planetary Interiors*, **158**, 92–106.

Good, N., & DeWit, M. J. 1997. The Thabazimbi-Murchison Lineament of the Kaapvaal Craton, South Africa: 2700 Ma of episodic deformation. *Journal of the Geological Society of London*, **154**(1), 93–97.

Gough, D. I., de Beer, J. H., & van Zijl, J. S. V. 1973. A Magnetometer Array Study in Southern Africa. *Geophysical Journal International*, **34**(4), 421–423.

Grant, K., Ingrin, J., Lorand, J.P., & Dumas, P. 2007. Water partitioning between mantle minerals from peridotite xenoliths. *Contributions to Mineralogy and Petrology*, **154**, 15–34.

Gripp, A. E., & Gordon, R. G. 1990. Current plate velocities relative to the hotspots incorporating the NUVEL-1 global plate motion model. *Geophysical Research Letters*, **17**(8), 1109–1112.

Gripp, A. E., & Gordon, R. G. 2002. Young tracks of hotspots and current plate velocities. *Geophysical Journal International*, **150**(2), 321–361.

Groom, R W, & Bahr, K. 1992. Corrections for near surface effects: Decomposition of the magnetotelluric impedance tensor and scaling corrections for regional resistivities: A tutorial. *Surveys in Geophysics*, **13**(4-5), 341–379.

Groom, R W, & Bailey, R C. 1989. Decomposition of Magnetotelluric Impedance Tensors in the Presence of Local Three-Dimensional Galvanic Distortion. *Journal of Geophysical Research (Solid Earth)*, **94**(B2), 1913–1925.

Groom, R W, Kurtz, R D, Jones, A G, & Boerner, D E. 1993. A quantitative methodology for determining the dimensionality of conductive structure from magnetotelluric data. *Geophysical Journal International*, **115**, 1095–1118.

Hamilton, M, Jones, A G, Evans, R L, Evans, S, Fourie, C J S, Garcia, X, Mountford, A, Spratt, J E, & Team, the SAMTEX. 2006. Electrical anisotropy of South African lithosphere compared with seismic anisotropy from shear-wave splitting analysis. *Physics of the Earth and Planetary Interiors*, **158**, 226–239.

Heintz, M, & Kennett, B.L.N. 2006. The apparently isotropic Australian upper mantle. *Geophysical Research Letters*, **33**, L15319.

Heise, W., & Pous, J. 2001. Effects of anisotropy on the two-dimensional inversion procedure. *Geophysical Journal International*, **147**, 610–621.

Heise, W., Caldwell, T.G., & Bibby, H.M. 2006a. 3D modelling of magnetotelluric phase tensor data from the Rotokawa geothermal field, Taupo Volcanic Zone, New Zealand. *18th Electromagnetic Induction Workshop*, Abstracts on CD ROM.

Heise, W., Caldwell, T.G., Bibby, H.M., & Brown, C. 2006b. Anisotropy and phase splits in magnetotellurics. *Physics of the Earth and Planetary Interiors*, **158**, 107–121.

Hess, H. H. 1964. Seismic anisotropy of the uppermost mantle under oceans. *Nature (London)*, **203**, 629–631.

Hirth, G. 2006. Protons lead the charge. *Nature*, **443**, 927–928.

Hirth, G., & Kohlstedt, D.L. 2003. Rheology of the upper mantle and the mantle wedge: A view from the experimentalists. *Pages 83–105 of:* Eiler, J. (ed), *Inside the Subduction Factory*. Geophysical Monograph Series, vol. 138. Washington, D.C.: AGU.

Hirth, G., Evans, R., & Chave, A. D. 2000. Comparison of continental and oceanic mantle electrical conductivity: Is the Archean lithosphere dry? *Geochemistry Geophysics Geosystems*, **1**, art. no.–0048.

Hoal, B. G., Hoal, K. E. O., Boyd, F. R., & Pearson, D. G. 1995. Age constraints on crustal and mantle lithosphere beneath the Gibeon kimberlite field, Namibia. *South African Journal of Geology*, **98**(2), 112–118.

Holtzman, B K, Kohlstedt, D L, Zimmerman, M E, Heidelbach, F, T., Hirage, & Hustoft, J. 2003. Melt segregation and strain partitioning: Implications for seismic anisotropy and mantle flow. *Science*, **301**, 1227–1230.

Hrouda, F., Pros, Z., & Wohlgemuth, J. 1993. Development of magnetic and elastic anisotropies in slates during progressive deformation. *Physics of the Earth and Planetary Interiors*, **77**, 251–265.

James, D. E., & Fouch, M. J. 2002. Formation and evolution of Archean cratons: insights from southern Africa. *Pages 1–26 of:* Fowler, C M R, Ebinger, C J, & Hawkesworth, C J (eds), *The Early Earth: Physical, Chemical and Biological Development*, vol. 199. Geological Society, London. Special Publication.

James, D. E., Fouch, M. J., VanDecar, J. C., van der Lee, S., & Group, Kaapvaal Seismic. 2001. Tectospheric structure beneath southern Africa. *Geophysical Research Letters*, **28**(13), 2485–2488.

James, D. E., Niu, F., & Rokosky, J. 2003. Crustal structure of the Kaapvaal craton and its significance for early crustal evolution. *Lithos*, **71**(2-4), 413–429.

Jelsma, H. A., de Wit, M. J., Thiart, C., Dirks, P. H. G. M., Viola, F., Basson, I. J., & Anckar, E. 2004. Preferential distribution along transcontinental corridors of kimberlites and related rocks of Southern Africa. *South African Journal of Geology*, **107**, 301–324.

Ji, S. C., Rondenay, S., Mareschal, M., & Senechal, G. 1996. Obliquity between seismic and electrical anisotropies as a potential indicator of movement sense for ductile shear zones in the upper mantle. *Geology*, **24**(11), 1033–1036.

Jiracek, G. R. 1990. Near-surface and topographic distortions in electromagnetic induction. *Surveys in Geophysics*, **11**, 163–203.

Johnson, S. D., Poujol, M., & Kisters, A.F.M. 2006. Constraining the timing and migration of collisional tectonics in the Damara Belt, Namibia: U-Pb zircon ages for the syntectonic Salem-type Stinkbank granite. *South African Journal of Geology*, **109**, 611–624.

Jones, A G. 1980. Geomagnetic induction studies in Scandinavia. *Jounal of Geophysics*, **48**, 181–194.

Jones, A G. 1983a. On the equivalence of the Niblett and Bostick transformations in the magnetotelluric method. *Journal of Geophysics*, **53**, 72–73.

Jones, A G. 1983b. The problem of current channelling: a critical review. *Geophysical Surveys*, **6**, 79–122.

Jones, A. G. 1986. Parkinson's pointers' potential perfidy! *Geophysical Journal of the Royal Astronomical Society*, **87**, 1215–1224.

Jones, A G. 1988. Static shift of magnetotelluric data and its removal in a sedimentary basin environment. *Geophysics*, **53**, 967–978.

Jones, A. G. 1999. Imaging the continental upper mantle using electromagnetic methods. *Lithos*, **48**(1-4), 57–80.

Jones, A G. 2006. Electromagnetic interrogation of the anisotropic Earth: Looking into the Earth with polarized spectacles. *Physics of the Earth and Planetary Interiors*, **158**, 281–291.

Jones, A G, & Groom, R W. 1993. Strike angle determination from the magnetotelluric impedance tensor in the presence of noise and local distortion: rotate at your peril! *Geophysical Journal International*, **113**, 524–534.

Jones, A G, & Spratt, J E. 2002. A simple method for deriving the uniform field MT responses in auroral zones. *Earth Planets and Space*, **54**, 443–450.

Jones, A. G., Lezaeta, P., Ferguson, I. J., Chave, A. D., Evans, R. L., Garcia, X., & Spratt, J. 2003. The electrical structure of the Slave craton. *Lithos*, **71**(2-4), 505–527.

Jones, A.G. 1992. Electrical conductivity of the continental lower crust. *Pages 81 – 143 of:* Fountain, D.M., Arculus, R.J., & Kay, R.W. (eds), *Continental Lower Crust*. Elsevier.

Jones, A.G., & Ferguson, I.J. 2001. The electric Moho. *Nature*, **409**, 331 – 333.

Jones, A.G., Chave, A.D., Auld, D., Bahr, K., & Egbert, G. 1989. A Comparison of techniques for magnetotelluric response function estimation. *Journal of Geophysical Research*, **94**(14), 14201–14213.

Jones, A.G., Ferguson, I.J., Chave, A.D., Evans, R.L., & McNeice, G.W. 2001. Electric lithosphere of the Slave craton. *Geology*, **29**(5), 423 – 426.

Jones, A.G., Evans, R.L., & Eaton, D.W. 2007. Velocity-conductivity relationships for mantle mineral assemblages in Archean cratonic lithosphere based on extremal bounds. *submitted to Lithos*.

Jones, F.W., & Price, A T. 1970. The Perturbations of Alternating Geomagnetic Fields by Conductivity Anomalies. *Geophysical Journal of the Royal Astronomical Society*, **20**, 317 – 334.

Jordan, T. H. 1975. The continental tectosphere. *Reviews of Geophysics*, **13**, 1–12.

Jordan, T.H. 1978. Composition and structure of the continental tectosphere. *Nature*, 544–548.

Jung, H., & Karato, S. 2001. Water-induced fabric transitions in olivine. *Science*, **293**(5534), 1460–1463.

Kaikkonen, P., Pernu, T., Tiikainen, J., Nozdrina, A.A., Palshin, N.A., Vanyan, L.L., & Yegorov, I.V. 1996. Deep DC soundings in southwestern Finland using the Fenno-Skan HVDC Link as a source. *Physics of the Earth and Planetary Interiors*, **94**, 275–290.

Kaminski, E., & Ribe, N. M. 2001. A kinematic model for recrystallization and texture development in olivine polycrystals. *Earth and Planetary Science Letters*, **189**(3-4), 253–267.

Kaminski, E., & Ribe, N. M. 2002. Timescales for the evolution of seismic anisotropy in mantle flow. *Geochemistry Geophysics Geosystems*, **3**(8), art. no.–1051.

Kaminski, E, Ribe, N. M., & Browaeys, J. T. 2004. D-Rex, a program for calculation of seismic anisotropy due to crystal lattice preffered orientation in the convective upper mantle. *Geophysical Journal International*, **158**, 744–752.

Kaneshima, S., Ando, M., & Kimura, S. 1988. Evidence from shear-wave splitting for the restriction of seismic anisotropy to the upper crust. *Nature (London)*, **335**(6191), 627–629.

Kao, D., & Orr, D. 1982. Magnetotelluric response of a uniformly stratified earth containing a magnetised layer. *Geophysical Journal of the Royal Astronomical Society*, **70**, 339–347.

Karato, S. 1990. The role of hydrogen in the electrical conductivity of the upper mantle. *Nature*, **347**, 272–273.

Karato, S, & Wu, P. 1993. Rheology of the upper mantel: a synthesis. *Science*, **260**, 771–778.

Kennett, B. L. N., & Engdahl, E. R. 1991. Traveltimes for global earthquake locations and phase identification. *Geophysical Journal International*, **105**, 429–465.

Key, R. M., & Ayres, N. 2000. The 1998 edition of the National Geological Map of Botswana. *Journal of African Earth Sciences*, **30**(3), 427–451.

Kind, R., Kosarev, G. L., Makeyeva, L. I., & Vinnik, L. P. 1985. Observations of laterally inhomogeneous anisotropy in the continental lithosphere. *Nature*, **318**(6044), 358–361.

Kneller, E.A., van Keken, P.E., Karato, S.-I., & Park, J. 2005. B-type olivine fabric in the mantle wedge: Insights from high-resolution non-Newtonian subduction zone models. *Earth and Planetary Science Letters*, **237**, 781–797.

Kwadiba, M. T. O. G., Wright, C., Kgaswane, E. M., Simon, R. E., & Nguuri, T. K. 2003. Pn arrivals and lateral variations of Moho geometry beneath the Kaapvaal craton. *Lithos*, **71**(2-4), 393–411.

Lahti, I, Korja, T, Kaikkonen, P, & Vaittinen, K. 2005. Decomposition analysis of the BEAR magnetotelluric data: implications for the upper mantle conductivity in the Fennoscandian Shield. *Geophysical Journal International*, **163**, 900–914.

Larsen, J C. 1977. Removal of local surface conductivity effects from low frequency mantle response curves. *Acta Geodaet. Geophysics et Montanist. Acad. Sci. Hung.*, **12**, 183–186.

LaTorraca, G A, Madden, T R, & Korringa, J. 1986. An analysis of the magnetotelluric impedance for three-dimensional conductivity structures. *Geophysics*, **51**, 1819–1829.

Lienert, B.R. 1979. Crustal electrical conductivities along the eastern flank of the Sierra Nevadas. *Geophysics*, **44**, 1830–1845.

Long, C., & Christensen, N. I. 2000. Seismic anisotropy of South African upper mantle xenoliths. *Earth and Planetary Science Letters*, **179**(3-4), 551–565.

Mackie, R L, Madden, T R, & Wannamaker, P E. 1993. Three-dimensional magnetotelluric modeling using finite difference equations - Theory and comparisons to integral equations solutions. *Geophysics*, **58**, 215–226.

Mackwell, S J, & Kohlstedt, D L. 1990. Diffusion of Hydrogen in Olivine: Implications for Water in the Mantle. *Journal of Geophysical Research (Solid Earth)*, **95**(B4), 5079–5088.

MacQueen, J.B. 1967. Some Methods for classification and Analysis of Multivariate Observations. *Pages 281–297 of:* LeCam, L.M., & Neyman, N. (eds), *Proceedings of the fifth Berkeley symposium on mathematical statistics and probability*, vol. 1. Berkeley, California: University of California Press.

Madden, T., & Nelson, P. 1986. A defense of Cagniard's magnetotelluric method. *In:* Vozoff, K (ed), *Magnetotelluric Methods*, vol. Reprint Series. Tulsa, OK: Society of Exploration Geophysics.

Mainprice, D., & Silver, P. G. 1993. Interpretation of SKS-waves using samples from the subcontinental lithosphere. *Physics of the Earth and Planetary Interiors*, **78**(3-4), 257–280.

Mainprice, D, Barruol, G, & Ismal, W B. 2000. The Seismic Anisotropy of the Earth's Mantle: From Single Crystal to Polycrystal. *Pages 237–264 of:* Karato, S, Forte, A M, Liebermann, R C, Masters, G, & Stixrude, L (eds), *Earth's Deep Interior, Mineral Physics and Tomography from the atomic to the global scale*. Geophysical Monograph Series, vol. 117. AGU, Washington, DC, United States.

Mareschal, M., Kellett, R. L., Kurtz, R. D., Ludden, J. N., Ji, S., & Bailey, R. C. 1995. Archean cratonic roots, mantle shear zones and deep electrical anisotropy. *Nature*, **375**(6527), 134–137.

Marson-Pidgeon, K, & Savage, M.K. 1997. Frequency-dependent anisotropy in the Wellington region, New Zealand. *Geophysical Research Letters*, **24**(24), 3297–3300.

Marti, A. 2006. *A Magnetotelluric Investigation of Geoelectrical Dimensionality and Study of the Central Betic Crustal Structure*. Ph.D. thesis, Universitat de Barcelona. 307 pp.

Maxwell, J.C. 1873a. *A Treatise on Electricity and Magnetism*. Vol. 1. Oxford at the Clarendon Press.

Maxwell, J.C. 1873b. *A Treatise on Electricity and Magnetism*. Vol. 2. Oxford at the Clarendon Press.

McCourt, S., & Vearncombe, J. R. 1992. Shear zones of the Limpopo Belt and adjacent granitoid-greenstone terranes: implications for late Archaean collision tectonics in southern Africa. *Precambrian Research*, **55**, 553–570.

McCourt, S., Kampunzu, A. B., Bagai, Z., & Armstrong, R. A. 2004. The crustal architecture of Archaean terranes in northeastern Botswana. *South African Journal of Geology*, **107**(Number 1/2), 147–158.

McNeice, G.W., & Jones, A G. 2001. Multisite, multifrequency tensor decomposition of magnetotelluric data. *Geophysics*, **66**, 158–173.

Mizukami, T, Wallis, S R, & Yamamoto, J. 2004. Natural examples of olivine lattice preferred orientaion patterns with a flow-normal a-axis maximum. *Nature*, **427**, 432–436.

Montagner, J. P., & Kennett, B. L. N. 1996. How to reconcile body-wave and normal-mode reference earth models. *Geophysical Journal International*, **125**(1), 229–248.

Nguuri, T. K., Gore, J., James, D. E., Webb, S. J., Wright, C., Zengeni, T. G., Gwavava, O., Snoke, J. A., & Group, Kaapvaal Seismic. 2001. Crustal structure beneath southern Africa and its implications for the formation and evolution of the Kaapvaal and Zimbabwe cratons. *Geophysical Research Letters*, **28**(13), 2501–2504.

Niblett, E R, & Sayn-Wittgenstein, C. 1960. Variation of electrical conductivity with depth by the magneto-telluric method. *Geophysics*, **5**, 998–1008.

Özalaybey, S., & Savage, M. K. 1994. Double-layer anisotropy resolved from S phases. *Geophysical Journal International*, **117**, 653–664.

Padilha, A L, Vitorello, I, Padua, M B, & Bologna, M S. 2006. Deep anisotropy beneath central-southeastern Brazil constrained by long period magnetotelluric data. *Physics of the Earth and Planetary Interiors*, **158**, 190–209.

Palacky, G.J. 1987. Resistivity characteristics of geologic targets. *In:* Nabighian, M.N. (ed), *Electromagnetic methods in applied geophysics*, vol. 1. Tulsa, OK: Society of Exploration Geophysics.

Park, J., & Levin, V. 2002. Seismic anisotropy: Tracing plate dynamics in the mantle. *Science*, **296**(5567), 485–489.

Parker, R. L. 1983. The magnetotelluric inverse problem. *Geophysical Surveys*, **6**, 5 – 25.

Parkinson, W.D. 1959. Directions of Rapid Geomagnetic Fluctuations. *The Geophysical Journal of the Royal Astronomical Society*, **2**(1), 1 – 14.

Parkinson, W.D. 1962. The Influence of continents and Oceans on Geomagnetic Variations. *Geophysical Journal of the Royal Astronomical Society*, **6**, 441 – 449.

Pek, J., & Verner, T. 1997. Finite-difference modelling of magnetotelluric fields in two-dimensional anisotropic media. *Geophysical Journal International*, **128**, 505–521.

Poe, B., Romano, C., Nestola, F., & Rubie, D. 2005. Electrical conductivity of hydrous single crystal San Carlos olivine (Abstract #MR41A-0895). *In: American Geophysical Union, Fall Meeting.*

Price, A T. 1962. The Theory of Magnetotelluric Methods when the source field is considered. *Journal of Geophysical Reasearch*, **67**, 1907 – 1918.

Price, A T. 1973. The theory of geomagnetic induction. *Physics of the Earth and Planetary Interiors*, **7**, 227–233.

Reeves, C. V., & Hutchins, D.G. 1982. A progress report on the geophysical exploration of the Kalahari in Botswana. *Geoexploration*, **20**, 209–224.

Richards, M L, Schmucker, U, & Steveling, E. 1982. Entzerrung der Impedanzkurven von magnetotellurischen Messungen in der Schwabischen Alb. *Pages 27–40 of: 9th Electromagnetic Deep Sounding Symposium.*

Ritter, O., Weckmann, U., Vietor, T., & Haak, V. 2003. A magnetotelluric study of the Damara Belt in Namibia - 1. Regional scale conductivity anomalies. *Physics of the Earth and Planetary Interiors*, **138**(2), 71–90.

Rodi, W., & Mackie, R.L. 2001. Nonlinear conjugate gradients algorithm for 2D magnetotelluric inversion. *Geophysics*, **66**, 174–187.

Rümpker, G., & Ryberg, T. 2000. New "Fresnel-zone" estimates for shear-wave splitting observations from finite-difference modeling. *Geophysical Research Letters*, **27**(13), 2005–2008.

Rümpker, G., & Silver, P. G. 1998. Apparent shear-wave splitting parameters in the presence of vertically varying anisotropy. *Geophysical Journal International*, **135**(3), 790–800.

Saltzer, R, Gaherty, J, & Jordan, T. 2000. How are vertical shear wave splitting measurements affected by variations in the orientation of azimuthal anisotropy with depth. *Geophysical Journal International*, **141**, 374–390.

Saltzer, R. L. 2002. Upper mantle structure of the Kaapvaal craton from surface wave analysis - a second look. *Geophysical Research Letters*, **29**(6), 17 1–4.

SAMTEX. 2004. (Southern African Magnetotelluric Experiment), MT data processing workshop held at the Dublin Institute for Advanced Studies, Dublin, Ireland. *1-14 March*.

SAMTEX. 2005. (Southern African Magnetotelluric Experiment), MT Modelling workshop held at the Dublin Institute for Advanced Studies, Dublin, Ireland. *16-27 May*.

Savage, M. K. 1999. Seismic anisotropy and mantle deformation: what have we learned from shear wave splitting? *Reviews of Geophysics*, **37**(1), 65–106.

Schmucker, U. 1970. Anomalies of Geomagnetic Variations in the Southwestern United States. *Bulletin of the Scripps Institute of Oceanography*, **13**.

Schmucker, U. 1973. Regional induction studies: a review of methods and results. *Physics of the Earth and Planetary Interior*, **7**, 365–378.

Schock, R N, Duba, A G, & Shankland, T J. 1989. Electrical conduction in olivine. *Journal of Geophysical reasearch*, **94**, 5829–5839.

Senechal, G., Rondenay, S., Mareschal, M., Guilbert, J., & Poupinet, G. 1996. Seismic and electrical anisotropies in the lithosphere across the Grenville Front, Canada. *Geophysical Research Letters*, **23**(17), 2255–2258.

Sheriff, R.E. 1999. *Encyclopedic Dictionary of Exploration Geophysics*. 3rd edn. Geophysical References Series 1. In America: Society of Exploration Geophysicists.

Shirey, S. B., Carlson, R. W., Richardson, S. H., Menzies, A., Gurney, J. J., Pearson, D. G., Harris, J. W., & Wiechert, U. 2001. Archean emplacement of eclogitic components into the lithospheric mantle during formation of the Kaapvaal Craton. *Geophysical Research Letters*, **28**(13), 2509–2512.

Shirey, S. B., Harris, J. W., Richardson, S. H., Fouch, M. J., James, D. E., Cartigny, P., Deines, P., & Viljoen, F. 2002. Diamond genesis, seismic structure, and evolution of the Kaapvaal-Zimbabwe craton. *Science*, **297**(5587), 1683–1686.

Sileny, J., & Plomerova, J. 1996. Inversion of shear-wave splitting parameters to retrieve three-dimensional orientation of anisotropy in continental lithosphere. *Physics of the Earth and Planetary Interiors*, **95**(3-4), 277–292.

Silver, P. G. 1996. Seismic anisotropy beneath the continents: Probing the depths of geology. *Annual Review of Earth and Planetary Sciences*, **24**, 385–432.

Silver, P. G., & Chan, W. W. 1988. Implications for continental structure and evolution from seismic anisotropy. *Nature*, **335**, 34–39.

Silver, P. G., & Chan, W. W. 1991. Shear wave splitting and subcontinental mantle deformation. *Journal of Geophysical Research*, **96**(B10), 16,429–16,454.

Silver, P. G., Gao, S. S., Liu, K. H., & the Kaapvaal Seismic Group. 2001. Mantle deformation beneath southern Africa. *Geophysical Research Letters*, **28**(13), 2493–2496.

Silver, P. G., Fouch, M. J., Gao, S. S., Schmitz, M., & the Kaapvaal Sesimc Group. 2004. Seismic anisotropy, mantle fabric and the magmatic evolution of Precambrian southern Africa. *South African Journal of Geology*, **107**(1-2), 45–58.

Silver, P.G., & Savage, M.K. 1994. The interpretation of shear-wave splitting parameters in the presence of two anisotropic layers. *Geophysical Journal International*, **119**(3), 949–963.

Simpson, F. 2001. Resistance to mantle flow inferred from the electromagnetic strike of the Australian upper mantle. *Nature*, **412**, 632–635.

Simpson, F, & Bahr, K. 2005. *Practical Magnetotellurics*. Cambridge: Cambridge University Press. 254 pp.

Simpson, F, & Tommasi, A. 2005. Hydrogen diffusivity and electrical anisotropy of a peridotite mantle. *Geophysical Journal International*, **160**, 1092–1102.

Sims, W.E., Bostick, F.X., & Smith, H.W. 1971. The estimation of magnetotelluric impedance tensor elements from measured data. *Geophysics*, **36**(5), 938–942.

Siripunvaraporn, W, & Egbert, G. 2000. An efficient data-subspace inversion method for 2-D magnetotelluric data. *Geophysics*, **65**(3), 791 – 803.

Siripunvaraporn, W, Egbert, G, Lenbury, Y, & Uyeshima, M. 2005. Three-dimensional magnetotelluric inversion: data-space method. *Physics of the Earth and Planetary Interiors*, **150**, 3–14.

Smith, J T. 1995. Understanding telluric distortion matrices. *Geophysical Journal International*, **122**, 219–226.

Smith, J T. 1997. Estimating galvanic-distortion magnetic fields in magnetotellurics. *Geophysical Journal International*, **130**, 65–72.

Spitz, S. 1985. The magnetotelluric impedance tensor properties with respect to rotations. *Geophysics*, **50**, 1610–1617.

Spratt, J E, Jones, A G, Muller, M R, Hamilton, M P, Miensopust, M, Garcia, X, Evans, R L, Fourie, C J S, Cole, P, Hutchins, D, T, Ngwisanyi, Evans, S F, Mountford, A Petit, W, & the SAMTEX Team. 2007. Structural dimentions and directionality of the Damara Mobile Belt and neighbouring terranes. *Pages CD–Rom of: SAGA 10th Biennial Meeting*. Wild Coast, South Africa: SAGA.

Stankiewicz, J., Chevrot, S., van der Hilst, R. D., & de Wit, M. J. 2002. Crustal thickness, discontinuity depth, and upper mantle structure beneath southern Africa: constraints from body wave conversions. *Physics of the Earth and Planetary Interiors*, **130**(3-4), 235–251.

Stettler, E. H., Prinsloo, J., Hauger, M. E., & du Toit, M. C. 1999. A crustal geophysical model for the Kheis tectonic province, South Africa based on magnetotelluric, reflection seismic, gravity and magetic data sets. *Pages 54–68 of: South African Geophysical Review*, vol. 3. Pretoria: South African Geophysical Association.

Stettler, E.H., Prinsloo, J., & Hauger, M.E. 1998. A geophysical transect between Avondale on the Kheis Tectonic Province and Keimoes on the Namaqua Metamorphic Province, South Africa. *Pages 83–95 of: South African Geophysical Review*, vol. 2. Pretoria: South African Geophysical Association.

Swift, C.M. 1967. A magnetotelluric investigation of an electrical conductivity anomaly in the Southwestern United States. *Pages 156 – 166 of:* Vozoff, K. (ed), *Magnetotelluric Methods*. Reprint Series, vol. 5. Tulsa, OK: Soc. Expl. Geophysics.

Tankard, A. J., Jackson, M. P. A., Eriksson, K. A., Hobday, D. K., Hunter, D. R., & Minter, W. E. L. 1982. *Crustal evolution of Southern Africa: 3.8 billion years of Earth history*. New York: Springer-Verlag.

Tikhonov, A.N. 1965. Mathematical basis of the theory of electromagnetic soundings. *USSR Comp. Math. Phys.*, **5**, 201 – 211.

Trampert, J., & van Heijst, H. J. 2002. Global azimuthal anisotropy in the transition zone. *Science*, **296**(5571), 1297–1299.

Uchida, T., & Ogawa, Y. 1993. Development of Fortran Code for Two-dimensional Magnetotelluric Inversion with Smoothness Constraint. *Geological Survey of Japan Open-File Report*, **205**, 1–21.

Utada, H, & Munekane, H. 2000. On galvanic distortion of regional three-dimensional magnetotelluric impedances. *Geophysical Journal International*, **140**, 385–398.

Valcke, S.L.A., Casey, M., Lloyd, G.E., Kendall, J.-M., & Fisher, Q.J. 2006. Lattice preferred orientation and seismic anisotropy in sedimentary rocks. *Geophysical Journal International*, **166**(2), 652–666.

Van Reenan, D. D., Roering, C., Ashwal, L. D., & de Wit, M. J. 1992. Regional geological setting of the Limpopo Belt. *Precambrian Research*, **55**(1-4), 1–5.

Van Zijl, J. S. V. 1969. A deep Schlumberger sounding to investigate the electrical structure of the crust and upper mantle in South Africa. *Geophysics*, **34**, 450–462.

Van Zijl, J. S. V. 1978. Deep electrical resistivity structure in southern Africa. *Transactions of the Geological Society of South Africa*, **81**, 129–142.

Van Zijl, J. S. V. 2006. A review of the resistivity structure of the Karoo Supergroup, South Africa, with emphasis on the dolerites: A study in anisotropy. *South African Journal of Geology*, **109**, 315–328.

Vauchez, A., Tommasi, A., Barruol, G., & Maumus, J. 2000. Upper mantle deformation and seismic anisotropy in continental rifts. *Physics and Chemistry of the Earth (A)*, **25**(2), 111–117.

Vinnik, L., & Montagner, J. P. 1996. Shear wave splitting in the mantle Ps phases. *Geophysical Research Letters*, **23**(18), 2449–2452.

Vinnik, L., Kosarev, G. L., & Makeyeva, L. I. 1984. Anisotropy of the lithosphere from the observations of SKS and SKKS. *Proc. Acad. Sci. USSR*, **78**, 1335–1339 (in Russian).

Vinnik, L., Kosarev, G. L., & Makeyeva, L. I. 1988. Azimuthal anisotropy of the lithosphere from observations of long period converted waves. *Page 221 (in Russian) of:* Nercesov, I.L. (ed), *Structure and Dynamics of the lithosphere According to Seismic data.*

Vinnik, L., Farra, V., & Romanowicz, B. 1989. Azimuthal anisotropy in the Earth from observations of SKS at GEOSCOPE and NARS broadband stations. *Bulletin of the Seismological Society of America*, **79**(5), 1542–1558.

Vinnik, L., Makeyeva, L. I., Milev, A., & Usenko, A. Y. 1992. Global patterns of azimuthal anisotropy and deformations in the continental mantle. *Geophysical Journal International*, **111**, 433–447.

Vinnik, L., Green, R. W. E., & Nicolaysen, L. O. 1995. Recent deformations of the deep continental root beneath southern Africa. *Nature*, **375**, 50–52.

Vinnik, L., Green, R. W. E., & Nicolaysen, L. O. 1996. Seismic constraints on dynamics of the mantle of the Kaapvaal craton. *Physics of the Earth and Planetary Interiors*, **95**(3-4), 139–151.

Vozoff, K. 1991. The magnetotelluric method. *Pages 641 – 712 of:* Nabighian, M.N. (ed), *Electromagnetic Methods in Applied Geophysics*, vol. 2. Tulsa, OK: Soc. Expl. Geophysics.

Wait, J.R. 1954. On the relation between telluric currents and the Earth's magnetic field. *Geophysics*, **19**, 281 – 289.

Wang, D., Mookherjee, M, Xu, Y, & Karato, S-I. 2006. The effect of water on the electrical conductivity of olivine. *Nature*, **443**, 977–980.

Wannamaker, P E. 2005. Anisotropy versus heterogeneity in continental solid earth electromagnetic studies: fundamental response characteristics and implications for physicochemical state. *Surveys in Geophysics*, **26**, 733–765.

Wannamaker, P E, Stodt, J A, & Rijo, L. 1987. A stable finite element solution for two-dimensional magnetotelluric modelling. *Geophysical Journal of the Royal Astronomical Society*, **88**, 277–796.

Ward, S.H., & Hohmann, G.W. 1987. Electromagnetic Theory for Geophysical Applications. *In:* Nabighian, M.N. (ed), *Electromagnetic methods in applied geophysics*, vol. 1. Tulsa, OK: Society of Exploration Geophysics.

Weaver, J T. 1963. The electromagnetic field with a discontinuous conductor with reference to geomagnetic micropulsations near a coastline. *Canadian Journal of Physics*, **41**, 484–495.

Weaver, J T, Agarwal, A K, & Lilley, F.E.M. 2000. Characterization of the magnetotelluric tensor in terms of its invariants. *Geophysical Journal International*, **141**, 321 – 336.

Weckmann, U., Ritter, O., & Haak, V. 2003. A magnetotelluric study of the Damara Belt in Namibia - 2. MT phases over 90°reveal the internal structure of the Waterberg Fault/Omaruru Lineament. *Physics of the Earth and Planetary Interiors*, **138**(2), 91–112.

Weckmann, U, Ritter, O, Jung, A, Branch, T, & de Wit, M. 2007. Magnetotelluric measurements across the Beattie magnetic anomaly and the Southern Cape Conductive Belt, South Africa. *Journal of Geophysical Research*, **112**, B05416, doi:10.1029/2005JB003975.

Weidelt, P. 1972. The inverse problem of geomagnetic induction. *Z. Geophysics*, **38**, 257–289.

Wessel, P., & Smith, W. H. F. 1991. Free software helps map and display data. *EOS, Transactions of the American Geophysical Union*, **72**, 445–446.

Wessel, P., & Smith, W. H. F. 1995. New version of the Generic Mapping Tools released. *EOS, Transactions of the American Geophysical Union*, **76**, 329.

Wiese, H. 1962. Geomagnetische Tiefentellurik. II. Die Streichrichtung der Untergrundstrukturen des elektrischen Widerstandes, erschlossen aus geomagnetischen Variationen (in German. *Geofis. Pura Appl.*, **52**, 83–103.

Wilson, J. F. 1990. A craton and its cracks: some of the behaviours of the Zimbabwe block from the Late Archaean to the Mesozoic in response to horizontal movements, and the significance of some of its mafic dyke patterns. *Journal of African Earth Science*, **10**, 483–501.

Wittlinger, G., & Farra, V. 2007. Converted waves reveal a thick layered tectosphere beneath the Kalahari super-craton. *Earth and Planetary Science Letters*, **254**, 404–415.

Wolfe, C. J., & Silver, P. G. 1998. Seismic anisotropy of oceanic upper mantle: Shear wave splitting methodologies and observations. *Journal of Geophysical Research*, **103**(B1), 749–771.

Wookey, J., & Kendall, J. M. 2004. Evidence of midmantle anisotropy from shear wave splitting and the influence of shear-coupled P waves. *Journal of Geophysical Research*, **109**(B07), B07309.

Wu, X., Ferguson, I.J., & Jones, A.G. 2002. Magnetotelluric response and geoelectric structure of Great Slave Lake shear zone. *Earth and Planetary Science Letters*, **96**, 35–50.

Yardley, G.S., & Crampin, S. 1991. Extensive-dilatancy anisotropy: Relative information in VSPs and reflection surveys. *Geophysical Prospecting*, **39**, 337–355.

Yoshino, Y, Matsuzaki, T, Yamashita, S, & Katsura, T. 2006. Hydrous olivine unable to account for conductivity anomaly at the top of the asthenosphere. *Nature*, **443**, 973–976.

Zhamaletdinov, A.A., Shevtsov, A.N., Korotkova, T.G., Efimov, B.V., Barannik, B.G., Kolobov, V.V., Prokopchuk, P.I., Kopytenko, Yu.A., Ismagilov, V.S., & Pesin, L.B. 2007. Deep sounding with industrial power lines in conjunction with MTS measurements. *Izvestiya Physics of the Solid Earth*, **43**(3), 259–265.

Zhang, S., & Karato, S. 1995. Lattice preferred orientation of olivine aggregates deformed in simple shear. *Nature*, **375**, 774–777.

APPENDICES

APPENDIX 1: Penetration estimates

Included in this appendix are graphs of the calculated periods corresponding to Niblett-Bostick (NB) penetration estimates for 35 and 45 km depth, for the profiles of the SAMTEX experiment.

Each plot shows the corresponding periods for 35 and 45 km, as + and -, respectively. The upper two lines on the plot indicate the decade of data selected for the crustal MT analysis. The lower two lines indicate the decade of data selected for the lithospheric mantle MT analysis. The NB depth estimates were calculated using the geometric mean of the apparent resistivity for the TE and TM modes.

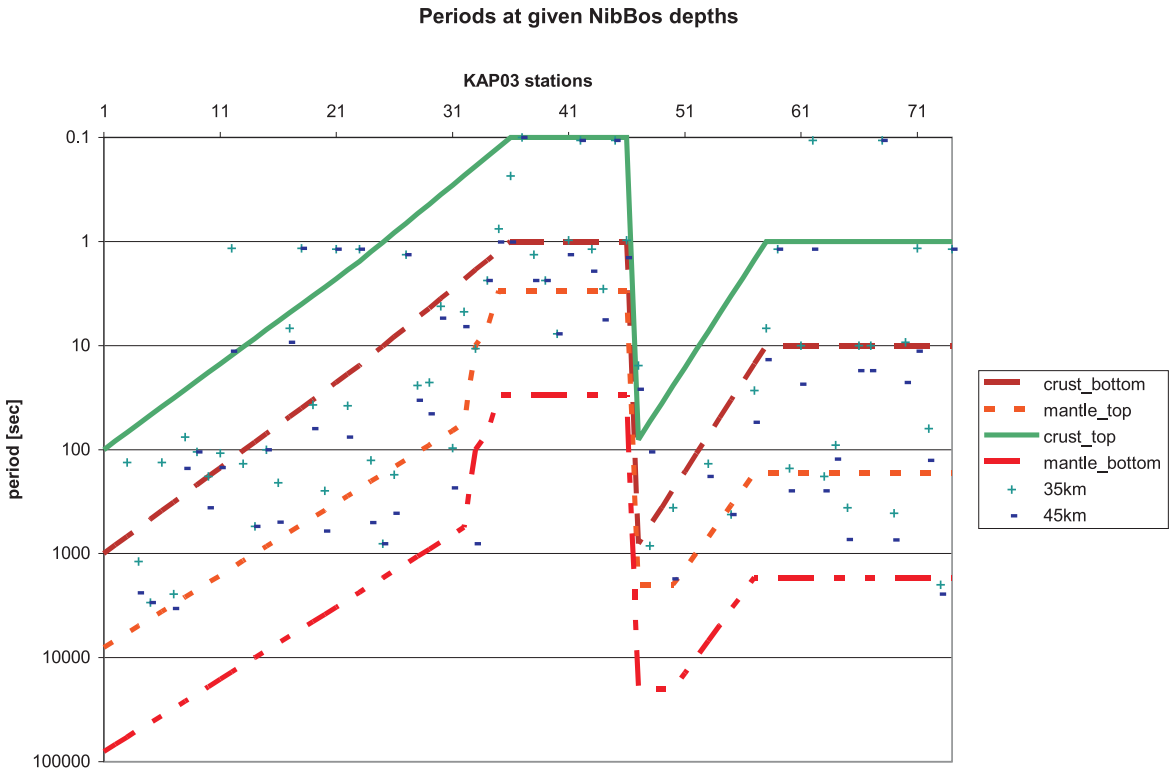
Periods at given NibBos depths
KAP03 stations
1
11
21
31
41
51
61
71
0.1
1
10
100
1000
10000
100000
period [sec]
crust_bottom
mantle_top
crust_top
mantle_bottom
35km
45km

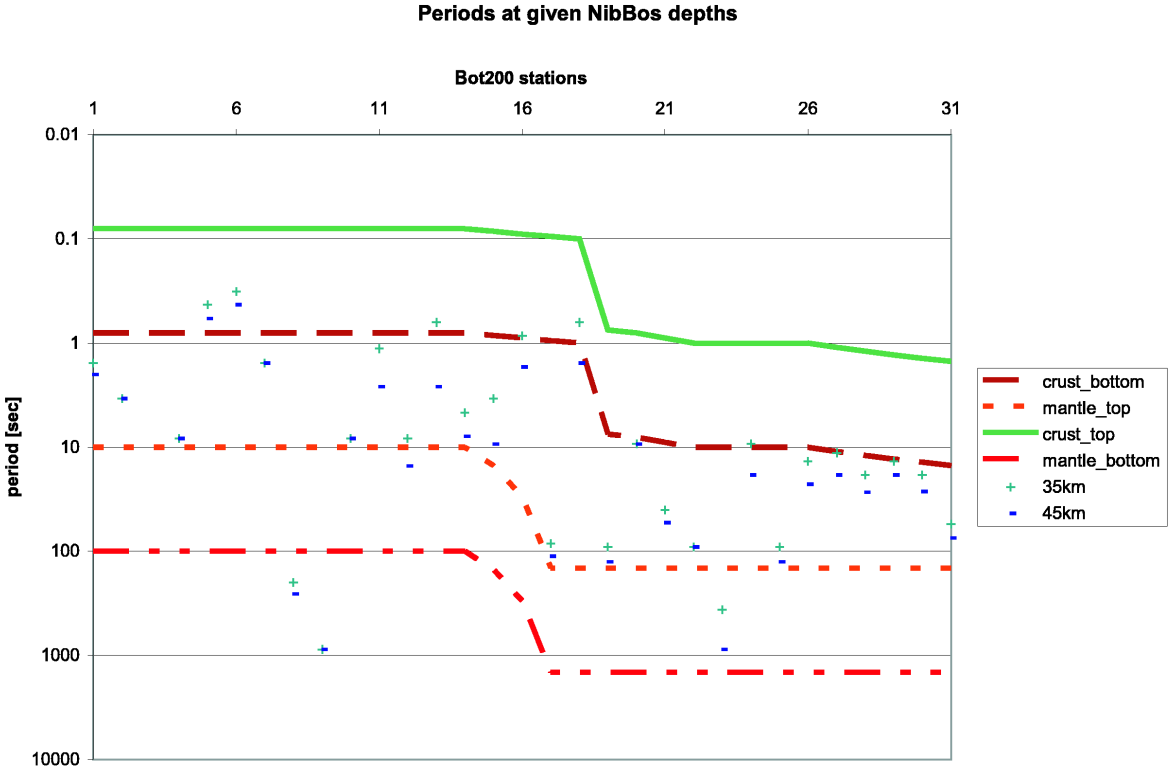
Periods at given NibBos depths
Bot200 stations
1
6
11
16
21
26
31
0.01
0.1
1
10
100
1000
10000
period [sec]
crust_bottom
mantle_top
crust_top
mantle_bottom
35km
45km

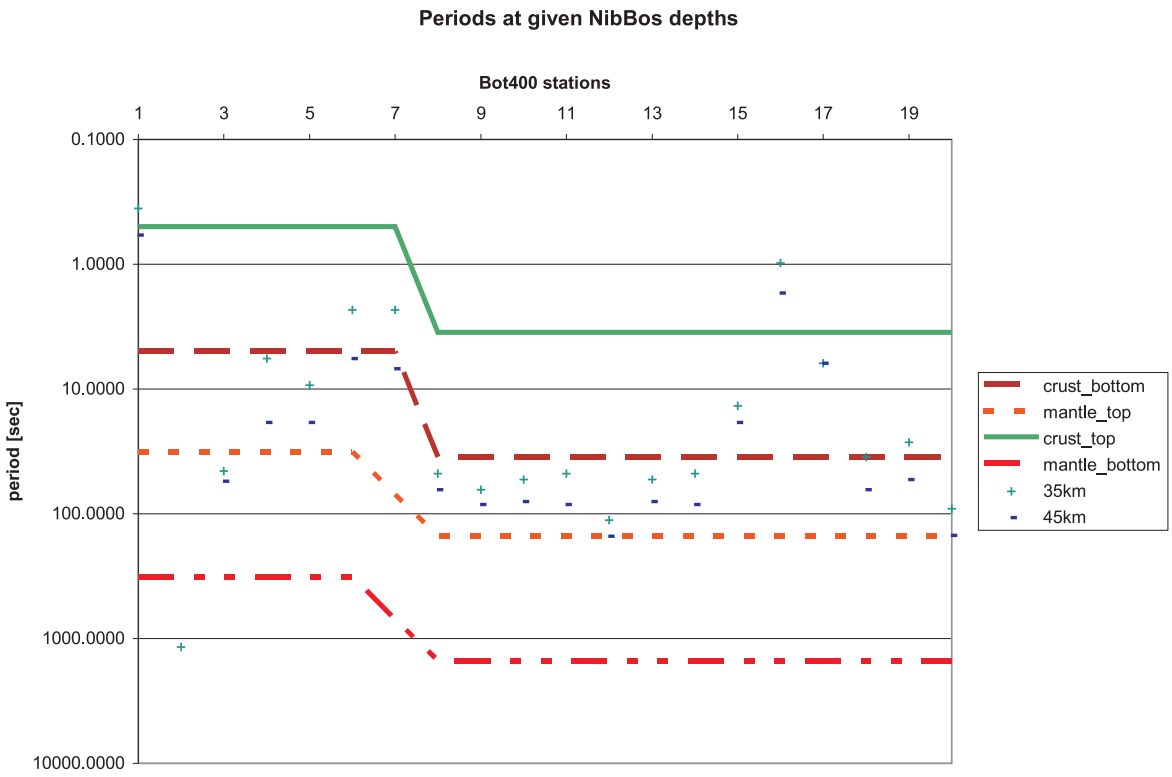
Periods at given NibBos depths
Bot400 stations
1
3
5
7
9
11
13
15
17
19
0.1000
1.0000
10.0000
100.0000
1000.0000
10000.0000
period [sec]
crust_bottom
mantle_top
crust_top
mantle_bottom
35km
45km

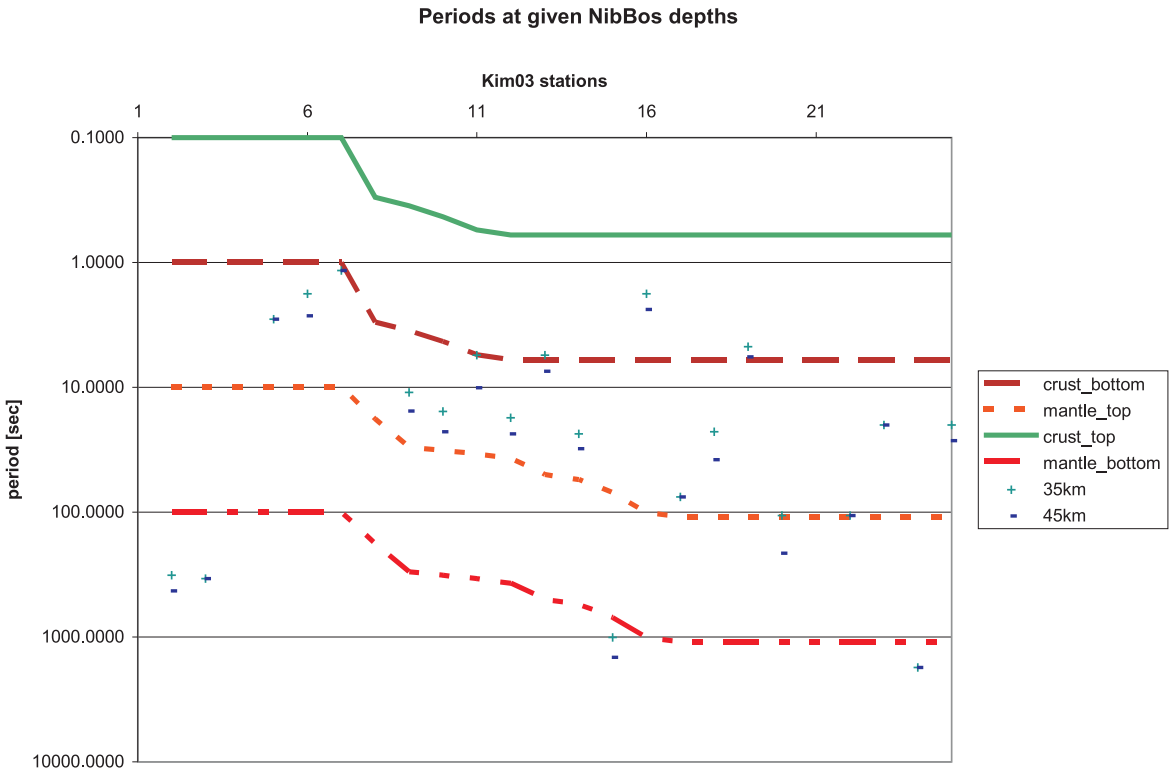
Periods at given NibBos depths
Kim03 stations
1
6
11
16
21
0.1000
1.0000
10.0000
100.0000
1000.0000
10000.0000
period [sec]
crust_bottom
mantle_top
crust_top
mantle_bottom
35km
45km

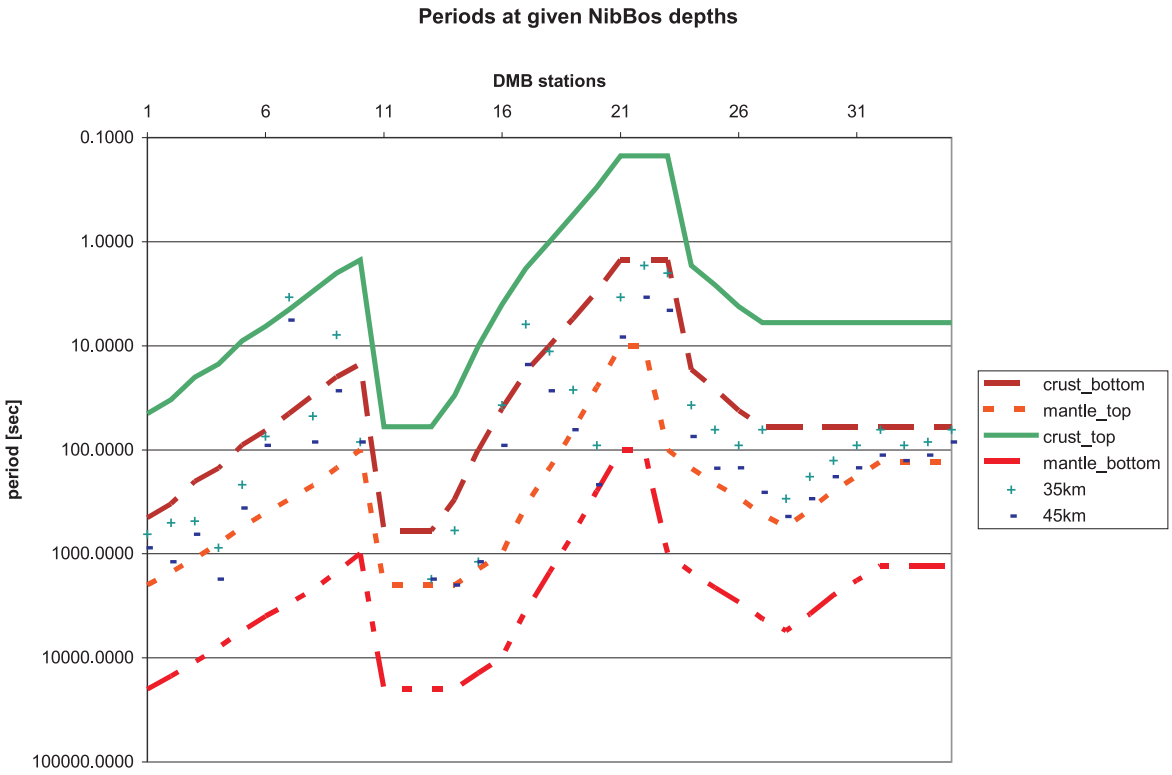
Periods at given NibBos depths
DMB stations
1
6
11
16
21
26
31
0.1000
1.0000
10.0000
100.0000
1000.0000
10000.0000
100000.0000
period [sec]
crust_bottom
mantle_top
crust_top
mantle_bottom
35km
45km

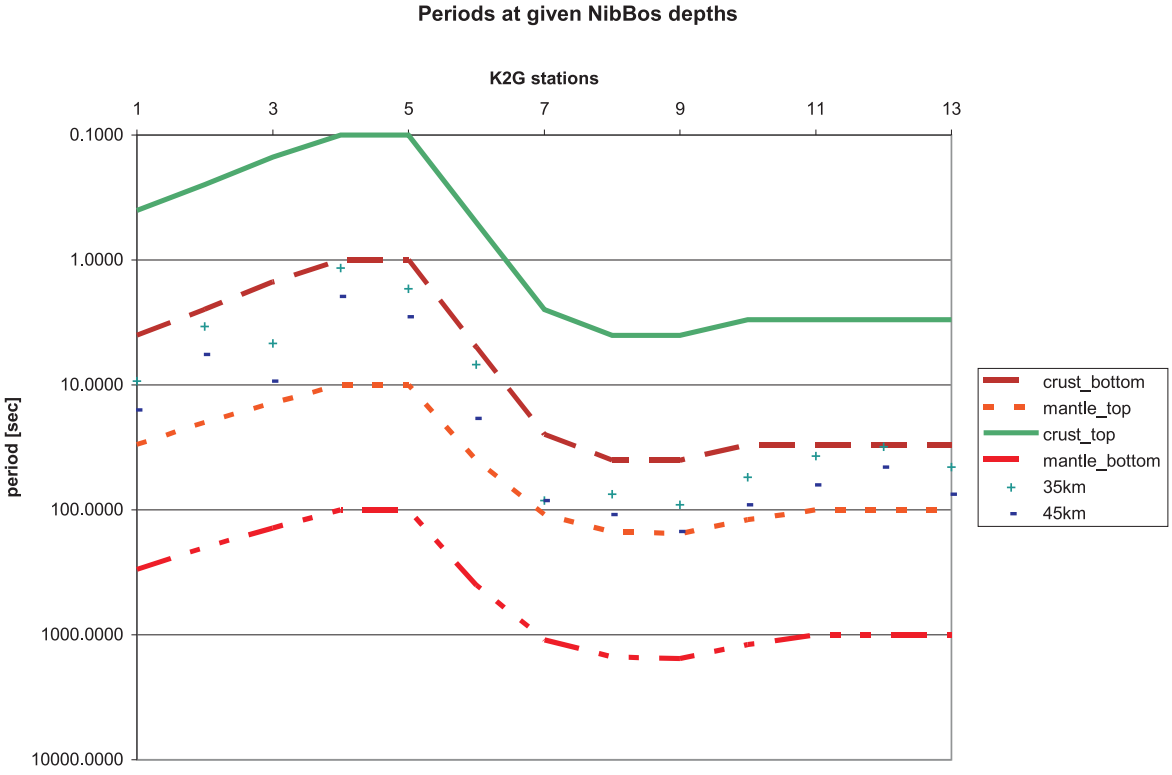
Periods at given NibBos depths
K2G stations
1
3
5
7
9
11
13
0.1000
1.0000
10.0000
100.0000
1000.0000
10000.0000
period [sec]
crust_bottom
mantle_top
crust_top
mantle_bottom
35km
45km

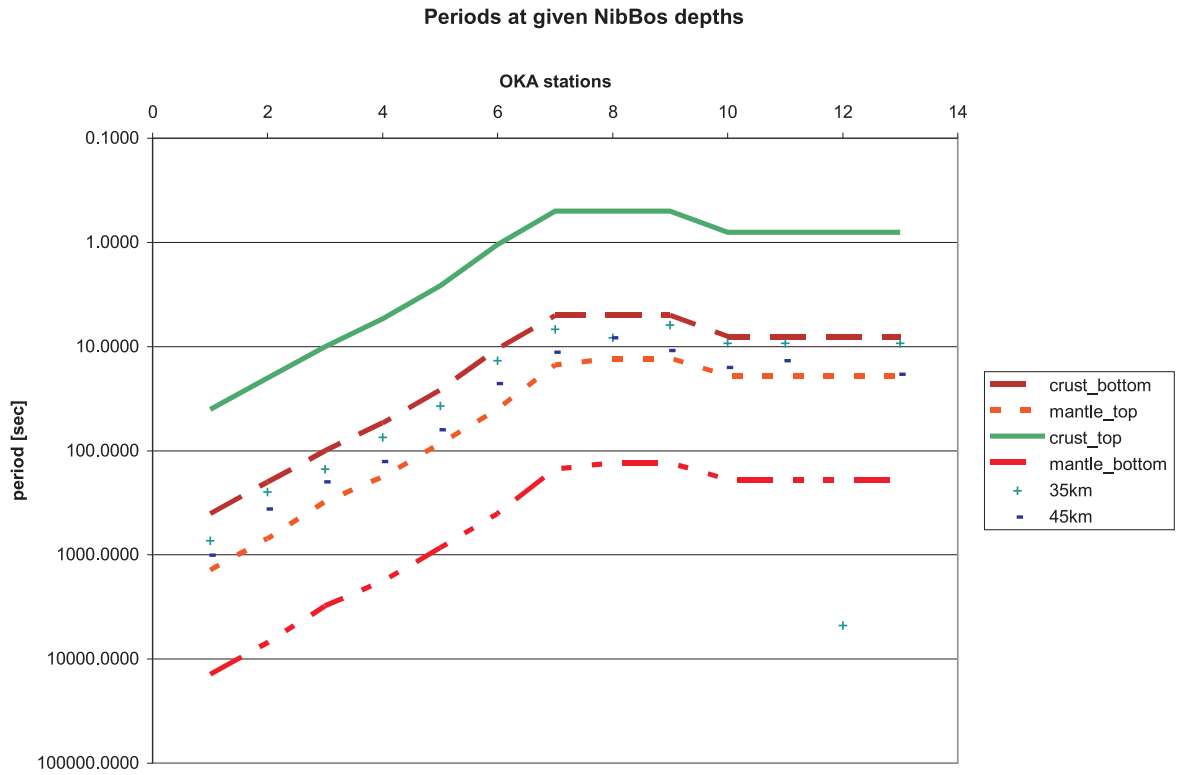
Periods at given NibBos depths
OKA stations
0
2
4
6
8
10
12
14
0.1000
1.0000
10.0000
100.0000
1000.0000
10000.0000
100000.0000
period [sec]
crust_bottom
mantle_top
crust_top
mantle_bottom
35km
45km

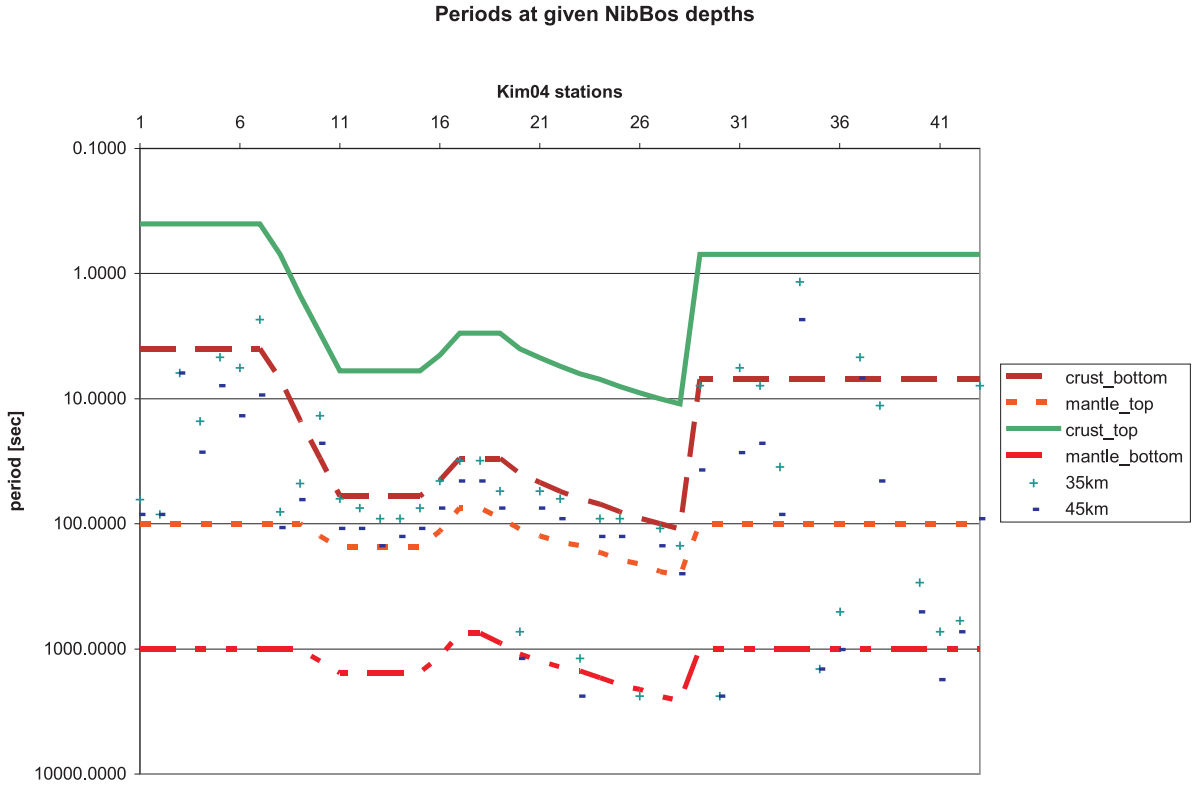
Periods at given NibBos depths
Kim04 stations
1
6
11
16
21
26
31
36
41
0.1000
1.0000
10.0000
100.0000
1000.0000
10000.0000
period [sec]
crust_bottom
mantle_top
crust_top
mantle_bottom
35km
45km

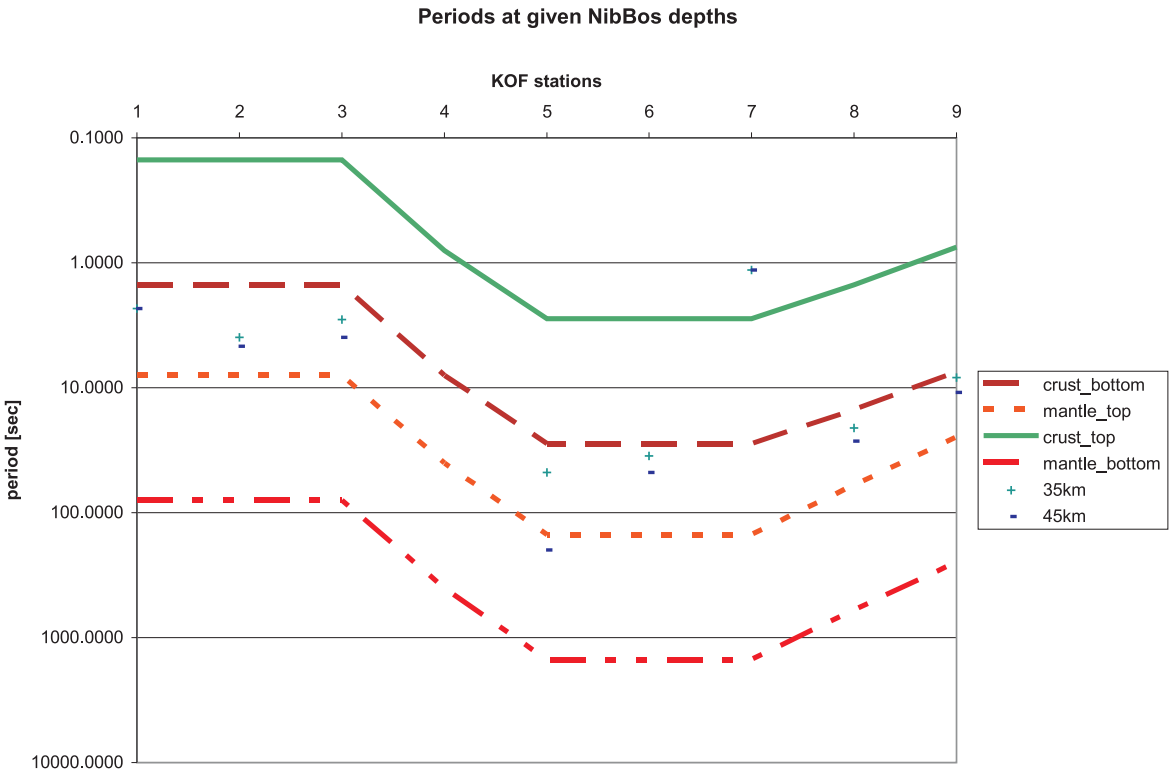
Periods at given NibBos depths
KOF stations
1
2
3
4
5
6
7
8
9
0.1000
1.0000
10.0000
100.0000
1000.0000
10000.0000
period [sec]
crust_bottom
mantle_top
crust_top
mantle_bottom
35km
45km

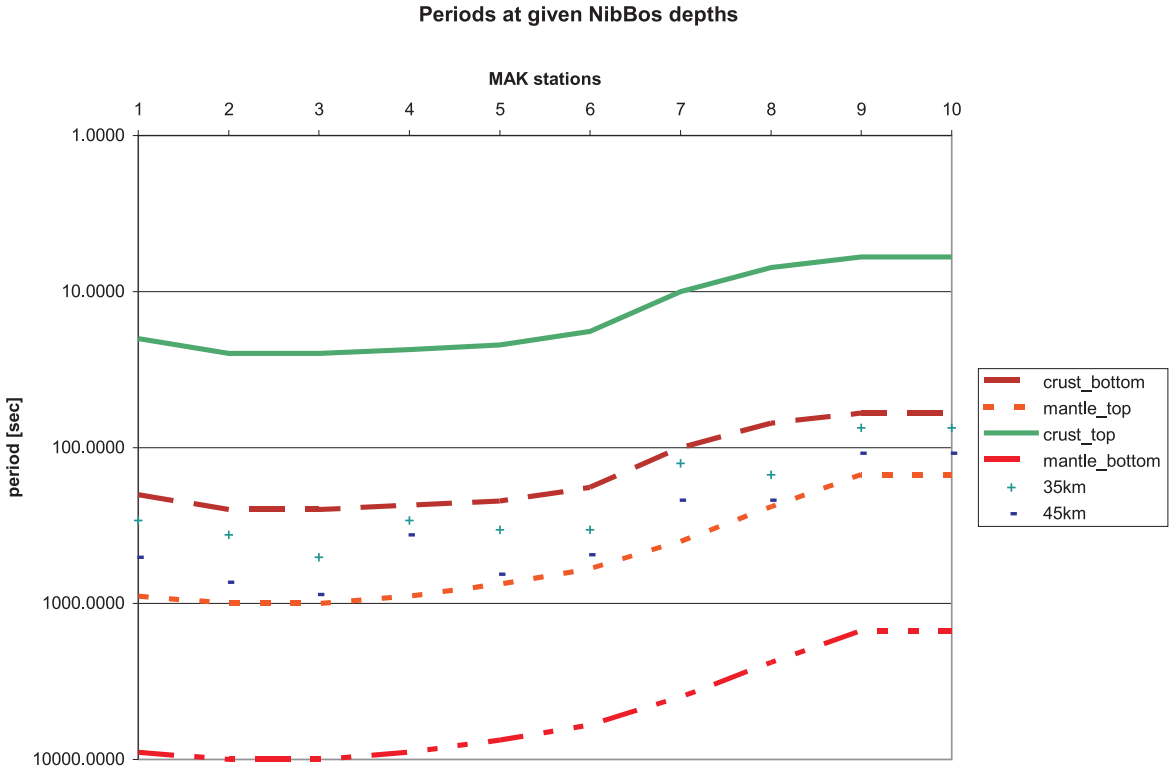
Periods at given NibBos depths
MAK stations
1
2
3
4
5
6
7
8
9
10
1.0000
10.0000
100.0000
1000.0000
10000.0000
period [sec]
crust_bottom
mantle_top
crust_top
mantle_bottom
35km
45km

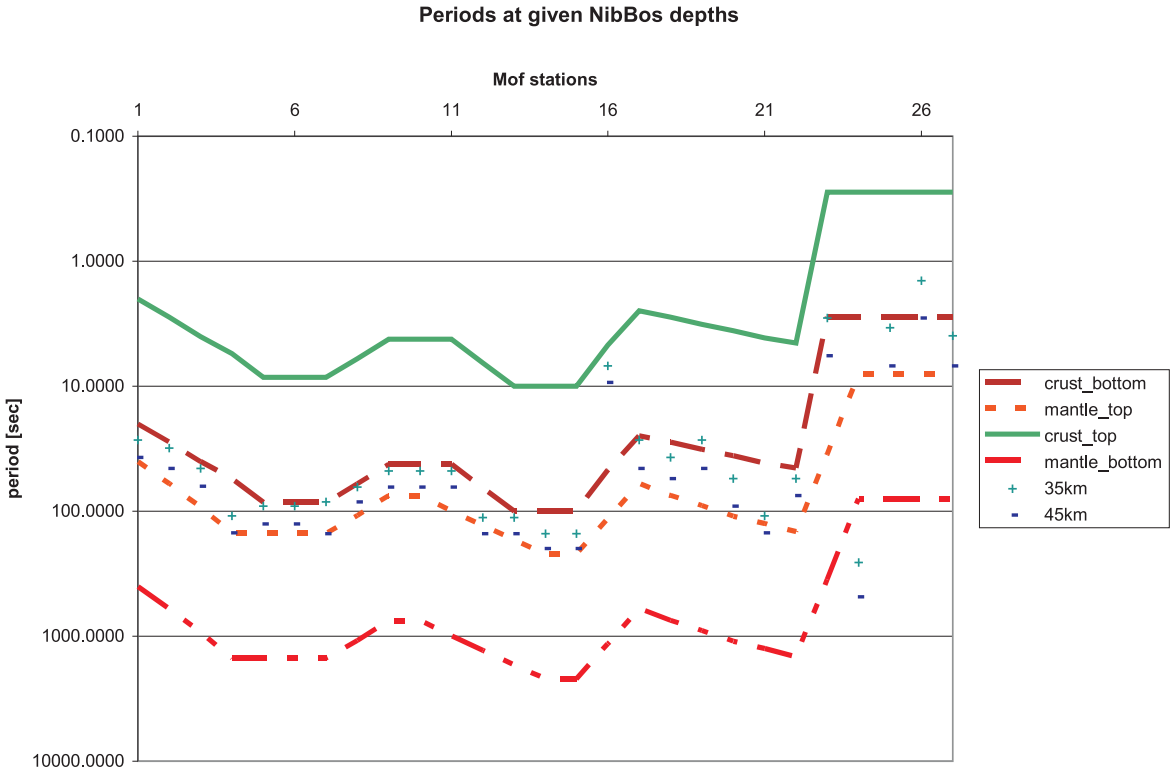
Periods at given NibBos depths
Mof stations
1
6
11
16
21
26
0.1000
1.0000
10.0000
100.0000
1000.0000
10000.0000
period [sec]
crust_bottom
mantle_top
crust_top
mantle_bottom
35km
45km

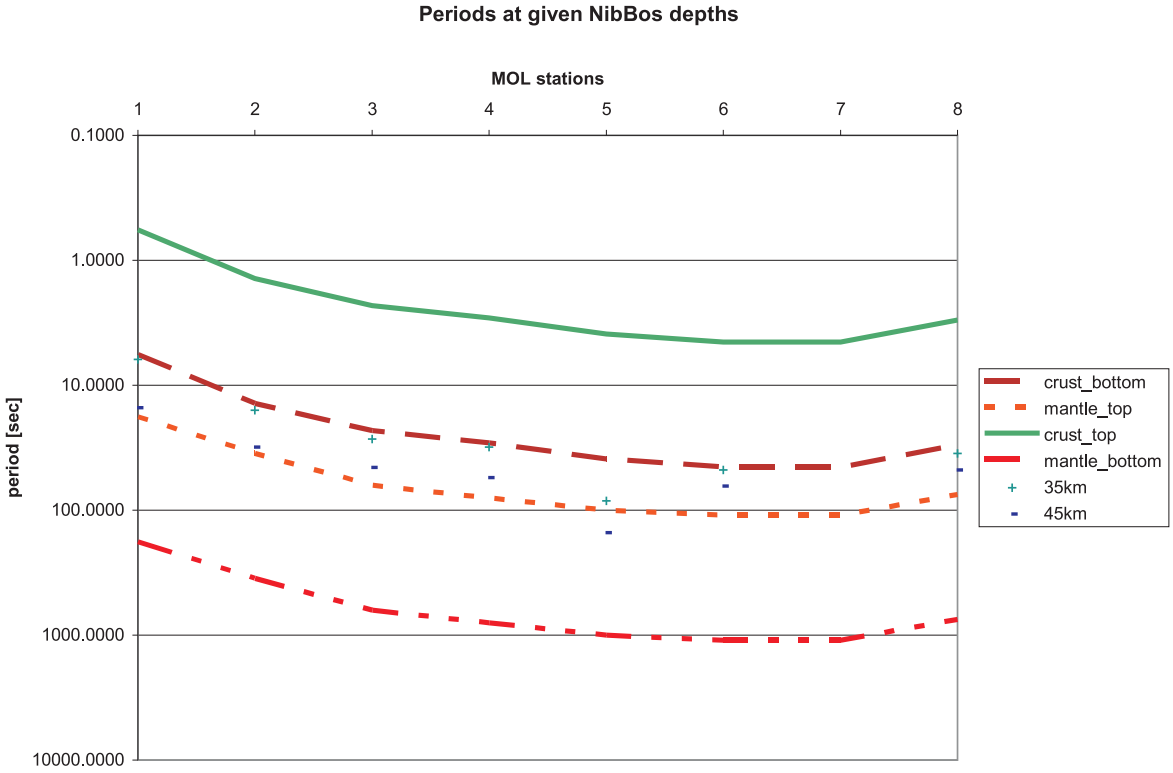
Periods at given NibBos depths
MOL stations
1
2
3
4
5
6
7
8
0.1000
1.0000
10.0000
100.0000
1000.0000
10000.0000
period [sec]
crust_bottom
mantle_top
crust_top
mantle_bottom
35km
45km

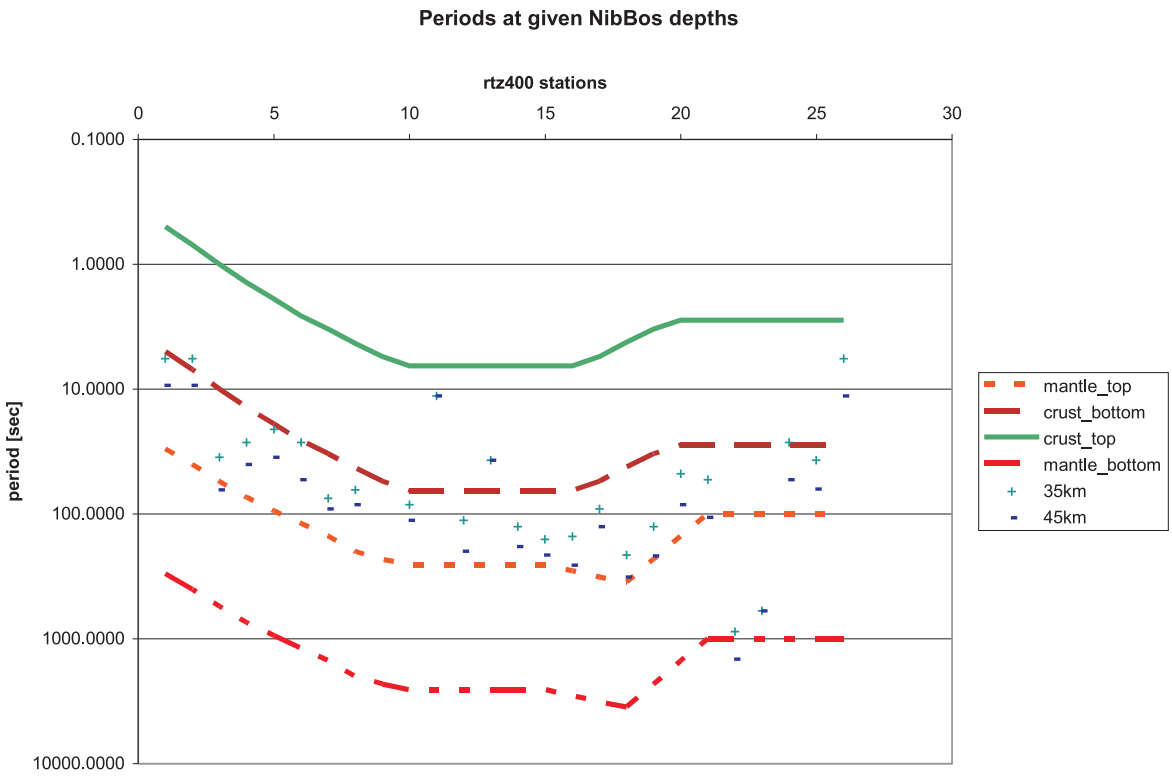
Periods at given NibBos depths
rtz400 stations
0
5
10
15
20
25
30
0.1000
1.0000
10.0000
100.0000
1000.0000
10000.0000
period [sec]
mantle_top
crust_bottom
crust_top
mantle_bottom
35km
45km

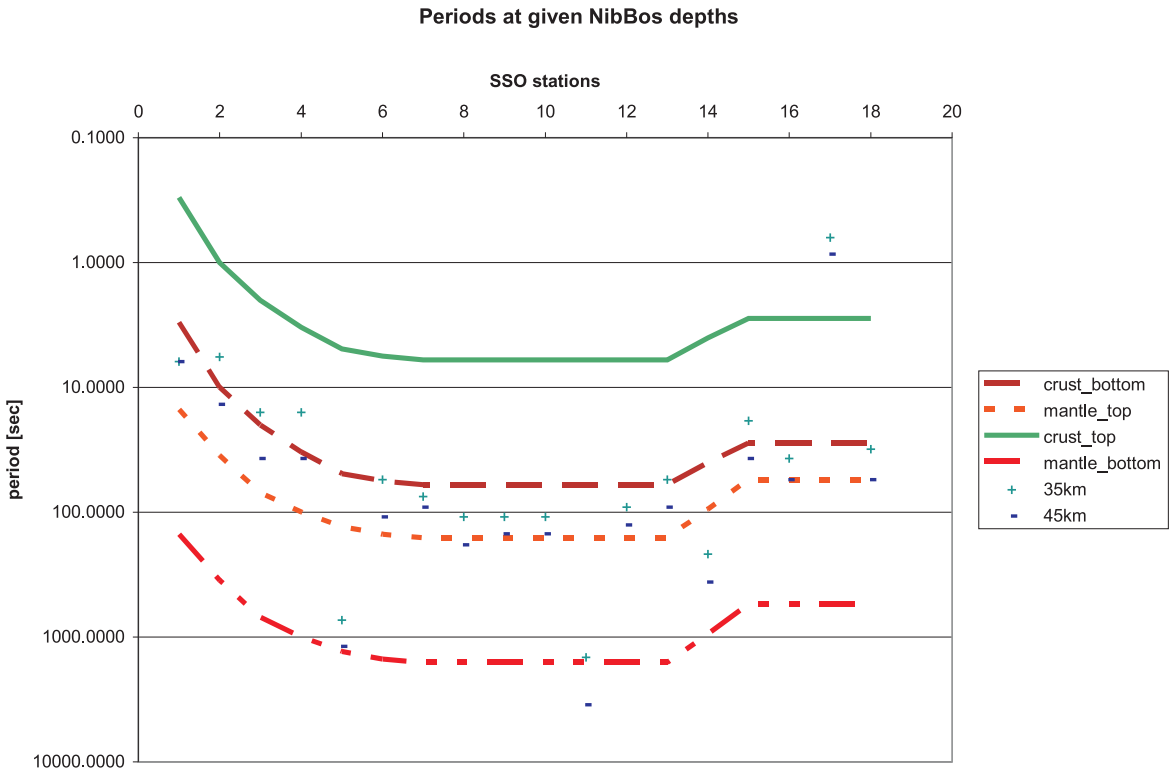
Periods at given NibBos depths
SSO stations
0
2
4
6
8
10
12
14
16
18
20
0.1000
1.0000
10.0000
100.0000
1000.0000
10000.0000
period [sec]
crust_bottom
mantle_top
crust_top
mantle_bottom
35km
45km

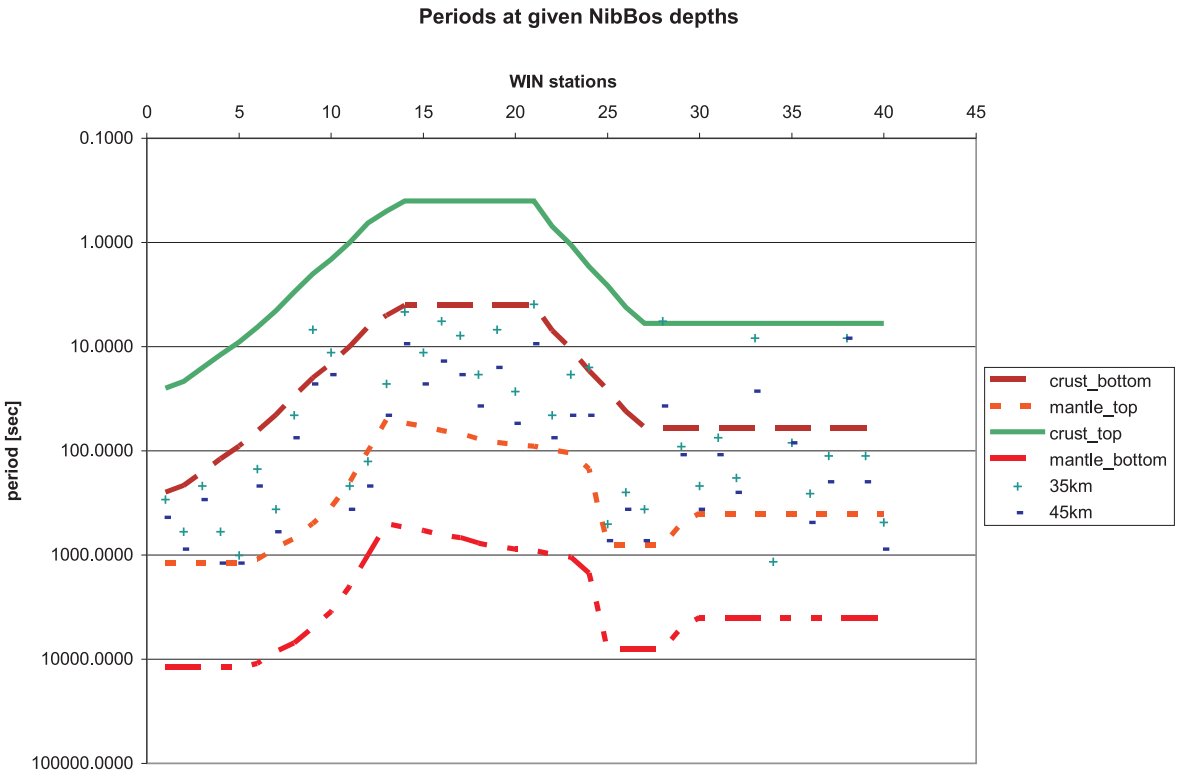
Periods at given NibBos depths
WIN stations
0
5
10
15
20
25
30
35
40
45
0.1000
1.0000
10.0000
100.0000
1000.0000
10000.0000
100000.0000
period [sec]
crust_bottom
mantle_top
crust_top
mantle_bottom
35km
45km

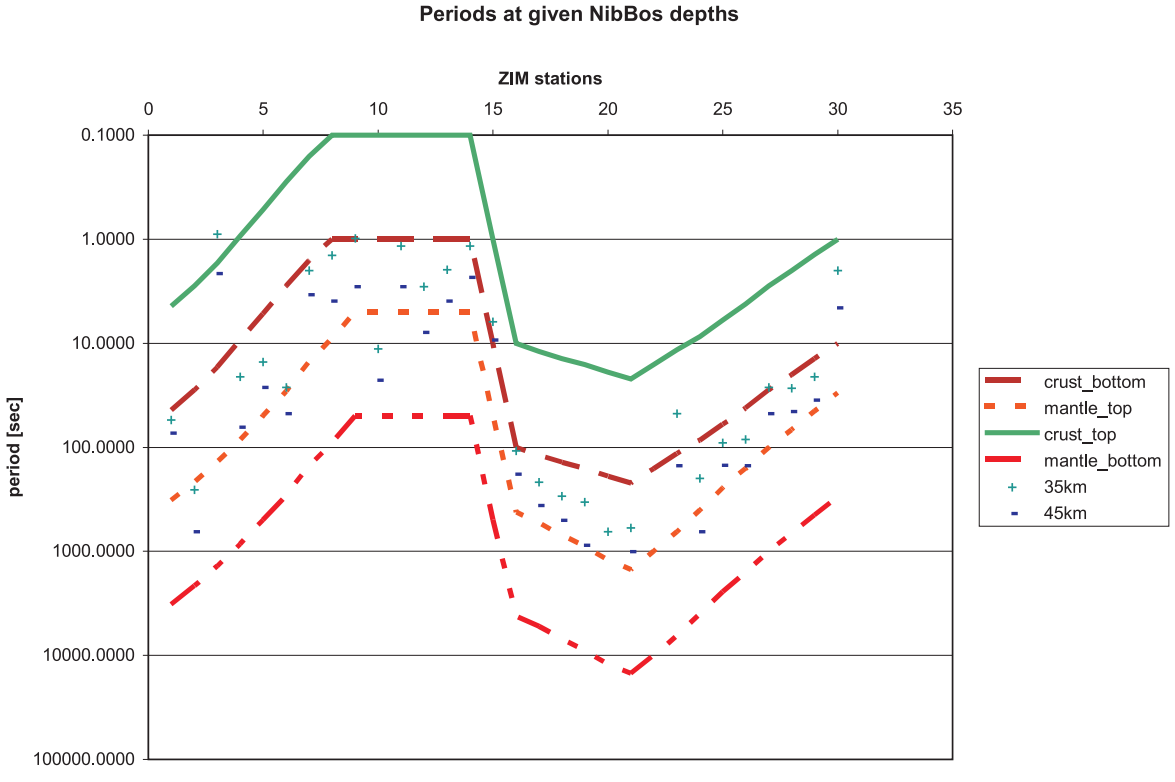
Periods at given NibBos depths
ZIM stations
0
5
10
15
20
25
30
35
0.1000
1.0000
10.0000
100.0000
1000.0000
10000.0000
100000.0000
period [sec]
crust_bottom
mantle_top
crust_top
mantle_bottom
35km
45km

APPENDIX 2: Asthenospheric MT analysis

In this appendix is a table describing the MT stations and periods used for the asthenospheric MT multi-site analysis.

Lat and *Long* are the central latitude and longitude positions of the stations used. *Angle* is the resulting conductive direction clockwise from north. *Length* is the phase difference, normalised to 30°. *Min T* and *Max T* are the minimum and maximum periods used in the multi-site GB analysis.

Lat	Long	Angle	Length	Min T	Max T	Stations utilised
-25.29	20.20	28.91	0.44	1700 s	2200 s	kim413, kim419, kim420, kim421, kim422, kim423, kim425
-24.21	23.44	179.94	0.19	900 s	1500 s	bot222, bot223, bot224, bot225, bot226, bot227, bot228, bot229, bot230, bot231
-23.39	19.08	144.25	0.51	3500 s	5200 s	dmb026, dmb030, dmb033
-22.27	21.70	17.62	0.38	950 s	1500 s	k2g002, k2g003, k2g004, k2g005, k2g006, k2g007
-23.30	22.43	32.55	0.75	2000 s	3000 s	k2g009, k2g010, k2g012, k2g013, k2g014
-27.09	25.39	41.81	0.58	200 s	400 s	kap037, kap038, kap039, kap044
-20.26	24.18	170.74	0.84	4000 s	5500 s	mof104, mof105, mof106
-24.46	22.47	29.56	0.24	3200 s	6500 s	rtz404, rtz407
-22.35	26.80	14.94	0.59	5500 s	9000 s	sso106, sso107, sso108, sso113
-22.14	20.82	22.23	0.78	2000 s	3000 s	win016, win017, win018, win020
-20.99	27.25	47.23	0.31	1700 s	3000 s	zim108, zim109, zim110, zim112

APPENDIX 3: SASE events

Here follows a list of seismic events that were used in the shear wave splitting analysis conducted on the SASE data at selcted stations.

Date	**Time**	**Latitude**	**Longitude**	**Depth**	**Magnitude**	**Delta**
1997-05-01	11:37:36	18.99	-107.35	33	6.9 Mw	134.25
1997-05-03	16:46:02	-31.79	-179.38	108.3	6.9 Me	116.46
1997-05-09	9:06:37	13.20	144.70	29	6 Mw	123.63
1997-05-11	22:16:14	-36.38	-97.70	10	6.5 Mw	95.14
1997-05-13	5:38:30	31.82	130.28	33	6.1 Mw	117.71
1997-05-15	18:01:33	-21.63	169.88	33	6 Mw	120.80
1997-05-21	14:10:26	-20.44	169.29	57	6.8 Me	121.46
1997-05-21	16:26:25	-18.90	175.95	33	6 Mw	126.16
1997-05-22	7:50:54	18.68	-101.60	70	6.5 Me	129.06
1997-05-22	13:21:36	18.92	121.34	33.9	6.1 Me	105.50
1997-05-25	23:22:33	-32.12	179.79	332.7	7.1 Mw	115.89
1997-05-27	8:00:29	-15.21	-173.33	14	6.4 Me	133.91
1997-05-27	6:10:32	-54.93	-136.17	10	6.1 Mw	95.30
1997-05-29	17:02:39	-35.96	-102.51	10	6.5 Mw	98.30
1997-06-09	7:24:12	-21.33	171.54	33	6 Mw	121.91
1997-06-10	21:53:55	-35.82	-108.14	10	6.5 Mw	101.59
1997-06-12	12:07:34	-5.95	147.03	33	6.1 Me	115.98
1997-06-24	23:04:53	-1.92	127.90	33	6.4 Me	101.85
1997-06-26	19:21:09	-49.69	-114.57	10	6.3 Mw	93.86
1997-07-06	20:13:37	16.16	-87.92	33	6.1 Mw	116.03
1997-07-09	19:24:13	10.60	-63.49	19.9	7 Me	92.23
1997-07-11	9:55:13	-5.70	110.80	574.4	6 Mw	85.04
1997-07-14	16:09:36	43.25	146.38	33	6.1 Me	132.16
1997-07-19	14:22:09	16.33	-98.22	33	6.9 Me	125.18
1997-07-31	21:54:21	-6.64	130.92	58.6	6 Me	102.12
1997-08-04	19:21:32	-15.21	-175.43	33	6 Mw	133.16
1997-08-04	18:53:59	-15.16	-175.27	33	6.1 Mw	133.27
1997-08-08	22:27:20	-15.48	-179.14	10	6.6 Mw	131.41

Date	Time	Latitude	Longitude	Depth	Magnitude	Delta
1997-08-10	9:20:31	-16.01	124.33	10	6.3 Mw	91.82
1997-08-13	4:45:05	25.03	125.77	55.3	6.2 Me	111.70
1997-08-15	7:37:49	-4.37	-105.70	10	6.3 Me	121.32
1997-08-17	20:11:11	-13.59	167.39	25.9	6 Mw	125.78
1997-08-29	6:54:00	-15.24	-175.58	33	6.5 Mw	133.08
1997-08-29	8:14:10	-3.56	144.36	22.8	6.6 Mw	115.12
1997-09-02	12:13:23	3.85	-75.75	198.7	6.8 Me	99.88
1997-09-03	6:22:44	-55.19	-128.99	10	6.1 Mw	93.57
1997-09-04	4:23:37	-26.57	178.34	624.7	6.8 Me	120.42
1997-09-10	12:57:07	-21.35	-174.39	10	6.1 Mw	127.81
1997-09-15	13:05:43	8.10	126.64	50.7	6.2 Me	105.45
1997-09-17	14:50:35	2.11	126.60	33	6 Me	102.64
1997-09-20	16:11:32	-28.68	-177.62	30	7 Mw	119.91
1997-09-26	15:48:34	-5.39	128.99	253.8	6 Mw	101.10
1997-09-30	6:27:25	31.96	141.88	10	6.2 Mw	127.25
1997-10-06	12:30:06	9.79	125.78	105.6	6.5 Me	105.44
1997-10-06	20:52:45	-9.30	158.69	33	6.1 Mw	122.95
1997-10-10	18:45:52	-9.32	158.73	33	6 Mw	122.97
1997-10-14	9:53:18	-22.10	-176.77	167.3	7.8 Me	126.31
1997-10-17	15:02:00	-20.89	-178.84	578.9	6 Me	126.66
1997-10-28	6:15:17	-4.37	-76.68	112	7.2 Me	96.81
1997-11-03	19:17:59	-6.74	129.02	215.6	6.1 Mw	100.45
1997-11-08	10:02:53	35.07	87.33	33	7.5 Me	87.21
1997-11-09	22:56:43	13.85	-88.81	176.4	6.5 Me	115.87
1997-11-10	23:06:44	31.19	140.49	86	6.2 Me	125.92
1997-11-15	7:05:17	43.81	145.02	161	6.1 Me	131.19
1997-11-15	18:59:24	-15.15	167.38	123.1	7 Me	124.57
1997-11-25	12:14:34	1.24	122.54	24	7 Me	98.65
1997-11-28	22:53:42	-13.74	-68.79	586	6.7 Me	85.50
1997-12-04	14:56:42	13.64	-90.66	80.5	6 Mw	117.42
1997-12-11	7:56:29	3.93	-75.79	177.5	6.4 Me	99.95
1997-12-16	11:48:30	16.11	-98.85	10	6 Mw	125.66
1997-12-18	15:02:00	13.84	-88.74	182.1	6.1 Me	115.81
1997-12-22	2:05:50	-5.50	147.87	179.3	7.2 Me	116.93
1997-12-22	10:03:45	13.74	-90.32	59.3	6.1 Mw	117.16
1998-01-01	6:11:23	23.91	141.91	95.6	6.4 Mb	125.12
1998-01-04	6:11:59	-22.30	170.91	100.6	7.5 Me	120.78
1998-01-10	4:54:25	-12.03	-72.07	33	6.4 Me	89.13
1998-01-10	8:20:06	14.37	-91.47	33	6.6 Mw	118.44
1998-01-12	16:36:20	-15.85	-179.38	23.4	6.7 Mw	130.98
1998-01-14	17:24:10	-15.73	-179.33	33	6.6 Mw	131.10

Date	Time	Latitude	Longitude	Depth	Magnitude	Delta
1998-01-27	2:14:13	-20.77	-179.18	642.8	6 Mw	126.63
1998-01-27	19:55:01	-22.54	179.05	611	6.3 Mw	124.32
1998-01-27	21:05:44	-22.41	179.04	610.1	6.5 Me	124.43
1998-01-31	23:30:42	-35.76	-97.06	10	6 Mw	95.14
1998-02-03	3:02:00	15.88	-96.30	33	6.4 Mw	123.31
1998-02-07	1:19:00	24.82	141.75	525.3	6.4 Me	125.27
1998-02-16	23:53:20	52.72	-33.68	10	6.8 Mw	94.69
1998-02-19	14:14:51	-4.48	129.08	33	6.5 Mw	101.63
1998-03-03	2:24:44	14.38	-91.47	62.8	6.2 Mw	118.44
1998-03-20	21:08:09	-50.01	163.11	10	6.7 Mw	94.26
1998-03-21	16:33:11	79.89	1.86	10	6.2 Mw	108.47
1998-03-29	19:48:16	-17.55	-179.09	537.2	7.2 Mw	129.57
1998-04-03	22:01:48	-8.15	-74.24	164.6	6.6 Me	92.86
1998-04-11	0:44:36	-23.64	-176.11	33	6.2 Me	125.11
1998-04-14	3:41:22	-23.82	-179.87	498.6	6.1 Me	123.60
1998-04-20	22:59:15	18.53	-101.20	67.3	6 Me	128.65
1998-04-27	18:40:39	-3.00	136.28	53	6.2 Me	108.58
1998-05-03	23:30:22	22.31	125.31	33	7.5 Mw	110.27
1998-05-10	6:05:59	13.68	-90.75	33	6.3 Me	117.51
1998-05-13	23:02:06	-5.15	151.71	61.4	6.6 Me	120.23
1998-05-14	18:56:23	40.25	143.25	33	6 Me	129.67
1998-05-15	5:58:06	14.18	144.88	154.1	6 Mw	124.20
1998-05-16	2:22:03	-22.23	-179.52	586.1	6.9 Me	125.18
1998-05-21	5:34:26	0.21	119.58	33	6.7 Mw	95.56
1998-05-23	17:44:48	8.14	123.73	657.8	6 Me	102.89
1998-05-27	15:27:16	-5.85	149.70	33	6 Me	118.21
1998-05-30	18:18:16	39.03	143.44	33	6.2 Me	129.68
1998-06-07	23:20:14	15.96	-93.78	86.6	6.3 Me	121.12
1998-06-16	9:35:12	-52.99	159.84	10	6.2 Mw	90.65
1998-06-20	20:24:45	-30.11	-177.93	57.4	6 Me	118.49
1998-07-09	14:45:40	-30.49	-178.99	129.5	6.9 Me	117.80
1998-07-16	11:56:36	-11.04	166.16	110.2	7 Me	126.92
1998-07-17	8:49:13	-2.96	141.93	10	7 Me	113.40
1998-07-18	16:41:19	-18.37	168.17	33	6.1 Me	122.50
1998-07-19	15:58:39	-21.84	-175.79	72.1	6 Mw	126.89
1998-07-24	18:44:04	21.25	122.02	33	6.1 Mw	107.05
1998-07-25	2:39:23	-13.61	166.87	43.5	6.3 Me	125.44
1998-07-29	18:00:30	-2.69	138.90	33	6.7 Me	110.97
1998-07-31	12:41:00	-21.61	169.82	33	6.1 Mw	120.78
1998-07-31	12:48:04	-21.64	169.92	33	6 Mw	120.81
1998-08-04	18:59:20	-0.59	-80.39	33	7.2 Me	101.88

Date	Time	Latitude	Longitude	Depth	Magnitude	Delta
1998-08-05	12:54:26	-54.67	-135.52	10	6.2 Mw	95.42
1998-08-20	6:40:56	28.93	139.33	440.5	7.1 Me	124.38
1998-08-23	5:36:13	14.70	120.05	70.1	6.1 Me	102.58
1998-08-23	13:57:15	11.66	-88.04	54.6	6.7 Me	114.26
1998-08-28	12:40:59	-0.15	125.02	66.2	6.1 Me	100.18
1998-08-30	1:48:09	17.09	148.13	33	6.3 Me	128.23
1998-09-02	8:37:30	5.41	126.76	50	6.8 Me	104.33
1998-09-07	0:39:30	-36.24	-97.71	10	6.1 Mw	95.24
1998-09-14	4:43:29	-34.75	-107.98	10	6.1 Mw	102.29
1998-09-15	8:35:52	-5.62	151.64	83	6.3 Me	119.89
1998-09-21	6:52:41	0.26	122.47	147.4	6 Mw	98.13
1998-09-21	12:09:40	-13.57	166.79	33	6.4 Me	125.41
1998-09-22	1:16:55	11.82	143.15	9.2	6 Me	121.68
1998-09-28	13:34:30	-8.19	112.41	151.6	6.6 Mw	85.31
1998-09-28	19:23:23	3.84	126.41	30.1	6.2 Mw	103.28
1998-10-03	11:15:43	28.51	127.62	226.6	6.2 Me	114.47
1998-10-08	4:51:43	-16.12	-71.40	136.2	6.1 Mb	86.62
1998-10-09	11:54:36	11.32	-86.45	68.7	6 Me	112.71
1998-10-10	16:32:19	-0.40	119.84	33	6 Me	95.50
1998-10-11	23:36:22	-56.91	-142.62	10	6.3 Mw	94.34
1998-10-28	16:25:04	0.84	125.97	33	6.6 Mw	101.48
1998-11-08	7:25:49	-9.14	121.42	33	6.4 Me	92.71
1998-11-09	5:38:44	-6.92	128.95	33	7 Me	100.29
1998-11-09	5:30:14	-6.95	129.02	33	6.7 Me	100.34
1998-11-14	15:03:12	-14.95	167.37	115.1	6 Me	124.72
1998-11-15	2:44:12	-21.59	-176.50	149.1	6.3 Me	126.88
1998-11-18	15:48:41	-3.32	130.77	33	6 Mw	103.66
1998-11-19	15:39:19	22.61	125.78	10	6.3 Mw	110.79
1998-11-24	23:54:46	-16.52	-174.75	223.2	6.1 Mw	132.20
1998-11-25	18:05:26	-7.86	158.62	47.9	6.2 Me	123.86
1998-11-29	14:10:32	-2.07	124.89	33	7.7 Mw	99.15
1998-12-06	0:47:13	1.25	126.20	33	6.6 Me	101.88
1998-12-14	19:35:27	-15.06	167.31	139.9	6 Mw	124.60
1998-12-16	0:18:45	31.29	131.29	41.6	6 Mw	118.37
1998-12-16	17:45:05	1.12	126.18	33	6.2 Mw	101.80
1998-12-26	15:39:08	-1.36	123.64	33	6.1 Mw	98.39
1998-12-27	0:38:27	-21.63	-176.38	144.3	6.9 Me	126.88
1999-01-05	8:32:47	-18.50	-174.07	33	6 Mw	130.59
1999-01-12	8:49:21	-5.42	151.68	42.6	6 Me	120.04
1999-01-19	3:35:34	-4.60	153.24	114.1	7 Me	121.78
1999-01-24	0:37:05	30.62	131.09	33	6.4 Me	118.01

Date	Time	Latitude	Longitude	Depth	Magnitude	Delta
1999-01-24	7:01:58	-21.13	-174.66	33	6.1 Me	127.93
1999-01-25	18:19:17	4.46	-75.72	17	6.4 Me	100.14
1999-01-28	18:24:25	-4.58	153.66	101	6.4 Me	122.12
1999-02-03	1:13:58	-20.31	-174.37	33	6.3 Me	128.80
1999-02-06	21:47:59	-12.85	166.70	90.1	7.3 Me	125.90
1999-02-06	17:45:24	19.20	121.27	33	6 Mw	105.56
1999-02-13	14:45:13	-3.56	144.83	10	6.2 Mw	115.52
1999-02-14	21:12:25	-15.51	168.00	10	6 Me	124.66
1999-02-22	1:00:33	-21.45	169.68	33	6.4 Me	120.84
1999-02-23	7:27:56	0.20	119.54	33	6.2 Me	95.52
1999-02-25	18:58:29	51.60	104.86	10	6 Me	106.60
1999-03-04	8:52:02	5.40	121.94	33	7.1 Me	100.06
1999-03-07	20:35:44	-15.77	-179.53	33	6.1 Mw	130.98
1999-03-21	16:16:02	55.90	110.21	10	6 Mw	111.12
1999-03-31	5:54:42	5.83	-82.62	10	7 Me	106.86
1999-04-01	21:36:21	-4.36	152.71	33	6.2 Mw	121.50
1999-04-02	17:05:47	-19.90	168.19	10	6.2 Mw	121.29
1999-04-03	6:17:18	-16.66	-72.66	87.2	6.8 Me	87.43
1999-04-03	10:10:31	13.17	-87.63	38.4	6 Mw	114.55
1999-04-05	11:08:04	-5.59	149.57	150	7.4 Me	118.25
1999-04-06	8:22:14	-6.53	147.01	33	6.4 Mw	115.63
1999-04-08	13:10:34	43.61	130.35	565.7	7.1 Me	120.63
1999-04-09	12:16:02	-26.35	178.22	621.2	6.2 Me	120.57
1999-04-11	16:50:39	-6.00	148.50	58.3	6 Me	117.14
1999-04-13	10:38:48	-21.42	-176.46	164.2	6.8 Me	127.05
1999-04-20	19:04:08	-31.89	-179.04	95.7	6.5 Mw	116.48
1999-04-26	18:17:26	-1.65	-77.78	172.6	6 Me	99.08
1999-05-05	22:41:30	14.36	-94.67	33	6.3 Me	121.26
1999-05-08	22:12:46	14.21	-91.95	39.2	6.1 Mw	118.79
1999-05-10	20:33:02	-5.16	150.88	138	7.1 Me	119.56
1999-05-11	1:00:41	-36.10	-110.64	10	6 Mw	102.72
1999-05-12	17:59:22	43.03	143.84	102.7	6.2 Mw	130.30
1999-05-16	0:51:20	-4.75	152.49	73.7	7.1 Me	121.09
1999-05-16	15:25:54	-2.64	138.22	59.2	6.4 Me	110.42
1999-05-17	10:07:56	-5.17	152.88	27	6.6 Me	121.15
1999-05-18	4:19:53	-5.65	148.53	127.3	6.1 Mw	117.38
1999-05-22	10:08:54	-20.73	169.88	33	6.1 Mw	121.54
1999-06-06	7:08:06	13.90	-90.77	33	6.3 Mw	117.62
1999-06-15	20:42:06	18.39	-97.44	70	7 Me	125.27
1999-06-18	10:55:26	5.51	126.64	33	6.4 Me	104.27
1999-06-21	17:43:05	18.32	-101.54	68.7	6.3 Mw	128.87

Date	Time	Latitude	Longitude	Depth	Magnitude	Delta
1999-06-26	22:05:29	-17.96	-178.19	590.4	6 Mw	129.58

Appendix 4: Permanent station events

Here follows a list of seismic events that were used in the shear wave splitting analysis conducted on the permanent stations in the region (BOSA, SUR, LBTB).

Date	**Time**	**Latitude**	**Longitude**	**Depth**	**Magnitude**	**Delta**	**Backazimuth**
1991-03-01	17:30:26	10.94	-84.64	196.5	6.1 Mb	110.95	270.41
1991-08-14	12:53:26	54.39	-169.30	274.8	6.1 un	151.97	18.25
1992-07-12	11:08:55	41.46	142.03	63.8	6 Mb	128.86	57.91
1992-10-22	9:04:23	-30.23	-177.21	26.3	6.6 Ms	118.60	158.17
1993-05-06	13:03:18	-8.47	-71.49	572.8	6.1 un	90.31	259.33
1993-05-25	23:16:43	55.02	-160.51	36.8	6.2 Mb	152.76	7.36
1993-10-11	13:07:30	-17.85	-178.73	554.5	6 un	129.46	150.55
1993-11-19	1:43:24	54.29	-164.16	30.3	6.4 Ms	153.07	12.33
1993-12-14	6:31:19	-20.70	-173.45	30.6	6.1 Ms	128.71	157.78
1994-01-10	15:53:50	-13.34	-69.45	596	6.9 un	86.25	256.05
1994-04-10	17:36:57	14.72	-92.00	100.1	6 un	119.05	270.73
1994-06-16	18:41:28	-15.25	-70.29	199.5	6 un	86.08	253.99
1994-08-02	14:17:52	52.43	158.04	144.7	6 Mb	138.57	41.97
1994-08-08	21:08:32	24.72	95.20	121.7	6.1 un	86.86	58.82
1994-10-16	5:10:01	45.75	149.17	116.6	6.8 un	134.10	52.62
1995-02-05	22:51:05	-37.76	178.75	21.1	7.5 Ms	110.37	158.07
1995-05-06	1:59:07	24.99	95.29	117.5	6.4 Mb	87.08	58.64
1995-06-29	7:45:10	48.79	154.45	64.1	6 un	137.27	47.92
1995-08-19	21:43:32	5.14	-75.58	119.6	6.6 Mw	100.33	269.35
1995-09-16	1:03:37	-6.32	155.21	151	6.1 Me	122.26	117.83
1995-10-01	17:06:03	29.31	139.04	430.8	6.1 Mw	124.24	71.86
1995-10-20	19:21:29	18.71	145.54	224.8	6.1 Mw	126.55	86.30
1996-01-17	10:06:47	-4.40	140.07	109.1	6.1 Me	111.07	106.48
1996-02-28	9:44:11	1.76	126.05	115.5	6.4 Me	101.99	93.65
1996-05-03	3:32:47	40.77	109.66	26	6 Mw	105.20	51.08
1996-08-02	12:55:29	-10.77	161.45	33	6.9 Mw	123.91	126.52
1996-09-14	13:10:54	-10.88	165.99	72.7	6.4 Me	126.93	130.44
1996-09-28	14:10:42	10.04	125.37	234.8	6.3 Me	105.19	85.85

Date	Time	Latitude	Longitude	Depth	Magnitude	Delta	Backazimuth
1996-12-22	14:53:28	43.21	138.92	226.5	6.5 Me	126.74	55.37
1997-03-26	2:08:57	51.28	179.53	33	6.7 Mw	150.56	33.19
1997-04-12	9:21:56	-28.17	-178.37	183.6	6 Mw	120.14	156.20
1997-09-02	12:13:23	3.85	-75.75	198.7	6.8 Me	99.88	268.11
1997-11-09	22:56:43	13.85	-88.81	176.4	6.5 Me	115.87	271.33
1997-11-28	22:53:42	-13.74	-68.79	586	6.7 Me	85.50	256.01
1997-12-22	2:05:50	-5.50	147.87	179.3	7.2 Me	116.93	112.13
1998-01-10	8:20:06	14.37	-91.47	33	6.6 Mw	118.44	270.61
1998-05-27	20:41:38	52.24	159.53	60.1	6 Mw	139.49	41.86
1998-07-16	11:56:36	-11.04	166.16	110.2	7 Me	126.92	130.72
1998-09-14	23:16:47	51.62	-173.15	33	6.1 Mw	153.26	25.77
1998-10-03	11:15:43	28.51	127.62	226.6	6.2 Me	114.47	69.03
1998-10-08	4:51:43	-16.12	-71.40	136.2	6.1 Mb	86.62	252.71
1998-11-14	15:03:12	-14.95	167.37	115.1	6 Me	124.72	134.91
1998-11-25	18:05:26	-7.86	158.62	47.9	6.2 Me	123.86	121.75
1998-12-14	19:35:27	-15.06	167.31	139.9	6 Mw	124.60	134.95
1998-12-27	0:38:27	-21.63	-176.38	144.3	6.9 Me	126.88	155.07
1999-01-28	8:10:05	52.89	-169.12	67.2	6.6 Me	153.37	19.62
1999-03-08	12:25:49	52.06	159.52	56.6	7 Me	139.55	42.13
1999-04-20	19:04:08	-31.89	-179.04	95.7	6.5 Mw	116.48	157.28
1999-05-10	20:33:02	-5.16	150.88	138	7.1 Me	119.56	113.78
1999-05-18	4:19:53	-5.65	148.53	127.3	6.1 Mw	117.38	112.69
1999-08-28	12:40:06	-1.29	-77.55	196.4	6.3 Me	99.05	262.64
1999-12-07	21:29:49	-15.91	-173.98	137.7	6.4 Me	133.04	154.86
2000-02-26	8:11:48	13.80	144.78	132.2	6.2 Me	123.95	91.34
2000-03-03	22:09:14	-7.32	128.49	141.9	6.4 Me	99.70	102.87
2000-06-07	21:46:56	26.86	97.24	33	6.3 Mw	89.55	58.06
2000-06-14	23:01:15	-17.90	176.21	33	6 Mw	127.15	145.33
2000-08-15	4:30:09	-31.51	179.73	357.7	6.6 Me	116.43	156.05
2000-10-04	14:37:44	11.12	-62.56	110.3	6.2 Me	91.68	280.81
2000-11-13	15:57:22	42.49	144.77	33	6 Me	130.96	56.85
2000-12-20	16:49:43	-9.23	154.35	33	6.6 Mw	119.77	119.80
2000-12-21	2:41:23	-5.35	154.13	386.7	6 Mw	122.03	116.18
2001-01-19	1:12:52	15.40	-92.72	93.2	6 Mw	119.96	271.11
2001-02-26	5:58:22	46.82	144.53	392	6.1 Mw	130.85	51.20
2001-04-28	4:49:53	-18.06	-176.94	351.8	6.9 Mw	129.97	152.62
2001-06-03	2:41:57	-29.67	-178.63	178.1	7.2 Mw	118.67	156.65
2001-08-21	6:52:06	-36.81	-179.58	33	7.1 Mw	111.75	158.95
2001-12-09	18:15:03	0.00	122.87	156.3	6.1 Mw	98.36	93.66
2002-01-16	23:09:52	15.50	-93.13	80.2	6.4 Mw	120.37	271.03
2002-03-19	22:14:15	-6.49	129.90	148.1	6.1 Mw	101.33	102.86

Date	Time	Latitude	Longitude	Depth	Magnitude	Delta	Backazimuth
2002-05-25	5:36:32	53.82	-161.12	33	6.4 Mw	153.90	8.72
2002-08-02	23:11:39	29.28	138.97	426.1	6.3 Mw	124.17	71.87
2002-08-12	2:59:24	-19.51	169.04	112.2	6 Mw	122.08	139.72
2002-09-07	8:14:20	-20.28	-176.04	209.9	6 Mw	128.26	154.76
2002-10-12	20:09:11	-8.30	-71.74	534.3	6.9 Mw	90.61	259.36
2002-10-14	14:12:44	41.17	142.25	61.4	6.1 Mw	128.99	58.30
2002-10-16	10:12:21	51.95	157.32	102.4	6.2 Mw	138.30	42.83
2003-03-11	7:27:33	-4.69	153.24	40.2	6.8 Mw	121.72	114.95
2003-04-27	22:57:45	-8.20	-71.59	559.9	6 Mw	90.53	259.52
2003-06-16	22:08:02	55.49	160.00	174.8	6.9 Mw	138.56	37.08
2003-07-21	13:53:58	-5.48	148.85	189.6	6.4 Mw	117.74	112.74
2003-07-27	6:25:32	47.15	139.25	470.3	6.8 Mw	127.26	50.55
2003-08-21	12:12:50	-45.10	167.14	28	7.2 Mw	99.85	153.86
2003-09-26	20:38:22	41.99	144.58	33	6 Mw	130.79	57.49
2003-09-29	2:36:53	42.45	144.38	25	6.5 Mw	130.67	56.88
2003-10-15	2:19:44	-17.82	-178.70	582.6	6 Mw	129.49	150.57
2003-12-25	14:21:15	-34.95	-178.25	34.6	6 Mw	113.87	159.25
2003-12-29	1:30:55	42.42	144.61	33	6.1 Mw	130.84	56.93
2004-04-14	1:54:09	55.23	162.66	51.3	6.2 Mw	140.04	36.58
2004-07-08	10:30:49	47.20	151.30	128.5	6.4 Mw	135.44	50.51
2004-10-08	8:27:54	-10.95	162.16	36	6.8 Mw	124.28	127.25
2004-11-07	2:02:26	47.95	144.48	474	6.2 Mw	130.79	49.72
2004-11-11	10:02:47	42.14	144.34	32.8	6.1 Mw	130.63	57.27
2004-12-13	15:23:41	13.39	-89.37	62.3	6 Mw	116.17	270.59
2005-02-14	23:38:09	41.73	79.44	22	6.1 Mw	86.76	37.33
2005-03-17	13:37:37	15.14	-91.38	197.4	6.1 Mw	118.67	271.46
2005-09-21	2:25:08	43.89	146.15	103	6.1 Mw	132.00	55.10
2005-12-23	21:47:28	-1.39	-77.52	192.9	6.1 Mw	98.97	262.57
2006-03-05	8:07:57	-20.12	-175.66	205.8	6.1 Mw	128.54	155.09
2006-04-30	8:17:35	-15.10	167.44	127.7	6.1 Mw	124.64	135.09
2006-05-22	13:08:03	54.27	158.45	197	6.2 Mw	138.19	39.24
2006-06-11	20:01:26	33.13	131.15	140	6.3 Mw	118.78	65.33
2006-07-08	20:40:01	51.21	-179.31	22	6.6 Mw	151.12	32.34
2006-09-29	13:08:26	10.88	-61.76	53	6.1 Mw	90.87	280.97
2006-12-12	15:48:03	3.73	124.68	213.5	6.3 Mw	101.71	91.23

APPENDIX 5: Published manuscript

This appendix was published as a paper in the journal: Physics of the Earth and Planetary Interiors

Hamilton, M.P., Jones A.G., Evans, R.L., Evans, S.F., Fourie, C.J.S., Garcia, X., Mountford, A., Spratt, J.E., and the SAMTEX MT Team. 2006. Electrical anisotropy of South African lithosphere compared with seismic anisotropy from shear-wave splitting analyses. *Physics of the Earth and Planetary Interiors*, **158**, 226-239.

Electrical anisotropy of South African lithosphere compared with seismic anisotropy from shear-wave splitting analyses

Mark P. Hamilton[1,2], Alan G. Jones [1], Rob L. Evans [3], Shane Evans [4], C.J.S. Fourie [5], Xavier Garcia [1], Andy Mountford [6], Jessica E. Spratt [1], the SAMTEX MT team [7]

[1]Dublin Institute for Advanced Studies, 5 Merrion Square, Dublin 2, Ireland
[2]University of the Witwatersrand, School of Geosciences, Private Bag 3, Johannesburg, South Africa
[3]Woods Hole Oceanographic Institution, Department of Geology and Geophysics, Clark South 172, 360 Woods Hole Road, Woods Hole, MA 02543-1542, USA
[4]De Beers Group Services, Private Bag X01, Southdale 2135, South Africa
[5]Council for Geoscience, 280 Pretoria Street, Silverton, Pretoria, South Africa
[6]Rio Tinto Mineral Exploration Inc., P.O. Box 695, 7th Floor Castlemead, Lower Castle Street, Bristol BS99 1FS, UK
[7]Other members of the SAMTEX team are: Louise Collins, Clare Horan, Gerry Wallace, Dublin Institute for Advanced Studies; Alan Chave,Woods Hole Oceanographic Institution; Marisa Adlem, Kobus Raath, Edgar Stettler, Raimund Stettler, Council for Geoscience; Mark Muller, Sue Webb, University of the Witwatersrand.

Abstract

Electrical anisotropy in southern Africa, inferred from the analysis of magnetotelluric (MT) data recorded as part of the Southern African MT Experiment (SAMTEX), is compared with seismic anisotropy inferred from an SKS shear-wave splitting study in the same region. Given the vastly varying penetration depths in the survey area, electrical anisotropy is derived in terms of approximate depth, rather than frequency. Electrical anisotropy directions for crustal depths (<35 km) show more distinct variability than those for upper mantle depths, and, not surprisingly, appear to be strongly related to large-scale geological structures. Our results for upper lithospheric mantle depths (>45 km) are not consistent with the fast-axis directions inferred from the SKS analyses. Upper mantle electrical results appear to be mostly a consequence of the geometry of large-scale geological structures and provide evidence that some crustal structures are distinct at depth, while others seem to be confined to the crust. Our results indicate that the causative region for the seismic anisotropy in the lithospheric mantle has either a correspondingly weak electrical anisotropic signature, or is more prominent at greater lithospheric depths than those we investigate here.

Keywords: Anisotropy; Magnetotellurics; Geoelectric strike; Shear-wave splitting; Southern Africa

Introduction

The Kaapvaal craton in southern Africa is one of the most extensively studied Archean cratons in the world, largely due to the vast economic resources of the region (principally diamonds and gold), yet the formation mechanism, structure, and evolution of the craton and its surrounding terranes have still not been conclusively resolved; basic, fundamental questions remain unanswered. The Southern African Seismic Experiment (SASE), part of the Kaapvaal Craton Project (Carlson *et al.*, 1996, 2000), was conducted in southern Africa from 1997 to 1999 (Fig. -1), with the aim of investigating the seismic structure of the region. Broadband seismic stations were deployed on the Kaapvaal craton, part of the Zimbabwe craton, and on the surrounding mobile belts, and the results have been widely reported (Carlson *et al.*, 2000; James *et al.*, 2001; James & Fouch, 2002;

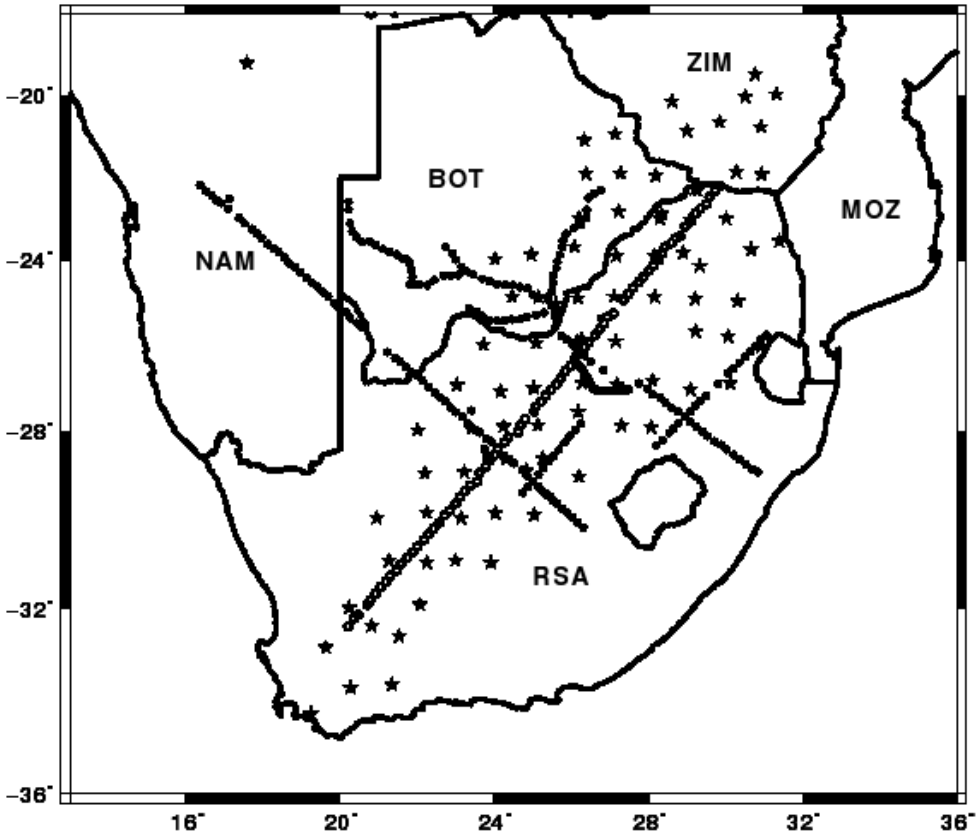

Figure -1: *Southern Africa with the Southern African Seismic Experiment (SASE) station locations represented by stars and the Southern African Magnetotelluric Experiment (SAMTEX) station locations from phases I and II represented as circles. Open circles denote the SAMTEX profile discussed in this paper. BOT: Botswana. MOZ: Mozambique. NAM: Namibia. RSA: Republic of South Africa. ZIM: Zimbabwe.*

Silver *et al.*, 2001, 2004).

Initiated in 2003, the Southern African Magnetotelluric (MT) Experiment (SAMTEX) is being conducted by a consortium comprising academic, industry and government partners representing five countries from around the world (South Africa, Botswana, Namibia, Ireland and the USA). When completed, it will be the most extensive land-based MT study yet performed, and to date includes the collection of MT sounding data with broadband (≈0.002 s to ≈6000 s) magnetotelluric (BBMT) instruments at more than 330 sites (Fig. -1), and long period (20 s to ≈10,000 s) magnetotelluric (LMT) instruments at approximately one-third of the BBMT sites to enhance depth penetration. The total length of the profiles is well over 5000 km, with BBMT stations spaced at nominally 20 km separation, and LMT stations spaced at 60 km (every third BBMT site), over a wide variety of geological terranes (Fig. -2).

The survey is being conducted in order to gain insight into the electrical structure of the crust and lithospheric mantle beneath the cratons of southern Africa, and their surrounding terranes, and, from that knowledge, to infer Archean and Proterozoic processes of formation and deformation. Unfortunately, due to logistical and security concerns we have been unable to extend the MT

data acquisition into Zimbabwe, as originally planned, for complete comparison with the SASE results, and have instead expanded the experiment northwest into Namibia and Botswana and to the southeast of the main acquisition corridor (Fig. -1). As is the experience from other cratonic studies (e.g., the Slave craton in northern Canada, (Davis *et al.*, 2003), where electromagnetic, geochemical, and seismic results combined to give new insight into the understanding of the upper mantle of the region), it is expected that the combined results of SASE and SAMTEX, taken together with the superb geochemical and geological information, will complement each other and add considerably to our inferences of the tectonic history of southern Africa, and thereby to our understanding of Archean tectonic processes.

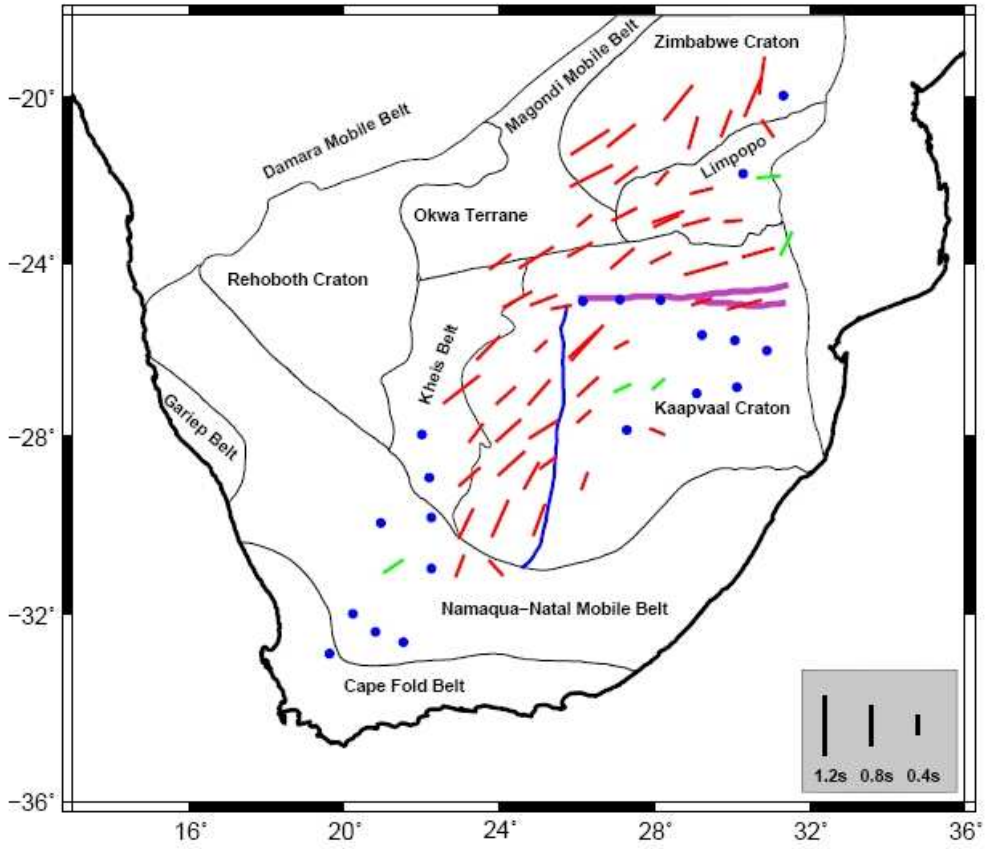

Figure -2: *Results from the shear-wave splitting measurements (fast polarisation directions) made by Silver* et al. *(2001), overlying a tectonic outline. High quality data are plotted in red, low quality in green, and stations with undetectable splitting in blue. Thabazimbi-Murchison Lineament (TML), as plotted by Silver* et al. *(2001), is represented as purple lines. Blue line: the NS trending ColesburgMagnetic Lineament (CML).*

One important component of the SASE data analyses was the shear-wave splitting study conducted by Silver *et al.* (2001), further discussed by Silver *et al.* (2004). Derived SKS seismic anisotropy shows clear differences in splitting parameters over the various cratons and terranes, and was inferred to result from fossil anisotropy in the lithospheric mantle. In this paper we present electrical anisotropy results determined for the same region, compare them with the seismic anisotropy results of Silver *et al.* (2001) and Silver *et al.* (2004), and consider what further insights may be obtained using this facet of the MT method.

Geological setting

The Archean Kaapvaal craton as a whole is composed of various granite-greenstone terrains, and is bounded to the south and west by Proterozoic mobile belts (Namaqua-Natal mobile belt and the Kheis belt), to the east by the Lebombo monocline (Jurassic in age), and to the north by the Neoarchean Limpopo mobile belt (de Wit *et al.*, 1992). At its surface, the Kaapvaal craton can be divided into Archean subdomains (de Wit *et al.*, 1992), and it has been suggested that some of these subdomains are also distinct at upper mantle depths within the deep lithospheric keel, or tectosphere (Jordan, 1975), typically found beneath Archean cratons. In the SASE data the Kaapvaal cratonic keel is in the form of a high velocity mantle zone observed by James *et al.* (2001) through tomographic analyses of P-wave and S-wave delay times. The eastern part of the craton is host to the oldest known sections (≈3.5 Gyr), some of which may represent the remnants of ancient oceanic lithosphere, whereas the more western sections of the craton are generally younger in age (de Wit *et al.*, 1992). In contrast to the general ENE-WSW trend in the east of the craton, the western section of the Kaapvaal craton, to the west of the Colesburg Magnetic lineament (CML, Fig. -2) shows a distinctively NS trend both geologically and geophysically, e.g., the Amalia and Kraaipan greenstone belts as well as the CML itself (Corner *et al.*, 1990; de Wit *et al.*, 1992).

The Limpopo belt (late Archean in age), separates the Kaapvaal and Zimbabwe cratons (Fig. -2), and can be divided into three different zones; the northern marginal zone, central zone, and southern marginal zone (de Wit *et al.*, 1992). There is a large system of roughly ENE-WSW trending ductile shear zones that accommodated crustal shortening during the Limpopo Orogeny (McCourt & Vearncombe, 1992). The Thabazimbi-Murchison Lineament (TML, Figs. -2, -6 and -7), a deformation belt with a long-lived tectonic history, is one such feature roughly 25 km wide that stretches for approximately 500 km across the Kaapvaal craton (Good & DeWit, 1997). The TML appears to be an important controlling structure for the SKS shear-wave splitting results and, to a lesser degree, for the MT results.

Seismic anisotropy (shear-wave splitting)

The following is intended as a brief description of shear-wave splitting; for more complete reviews of the methodology see Silver (1996) and Savage (1999). A seismic shear wave that passes through a seismically anisotropic medium is split into different polarization directions that have differing propagation velocities. The so-called SKS shear-wave splitting studies utilise nearvertical wave paths of seismic energy from teleseismic events that pass through the core, and they provide us with a means of indirectly measuring the deformation in the crust and mantle. The method has been used in many studies worldwide, particularly since the early 1990s (see review by Savage (1999)). In shear-wave splitting studies the measured splitting parameters are the fast polarisation direction (ϕ_S) indicating the orientation of deformation, and the delay time (δt) between the perpendicularly polarised fast and slow arrivals, indicating the magnitude of deformation in the horizontal plane (Silver, 1996). This method provides good lateral resolution, but has no intrinsic vertical resolution – the anisotropy could reside anywhere on the path from the core-mantle boundary to the surface.

Seismic anisotropy in the upper mantle is predominantly interpreted to arise from the preferred orientationof anisotropic crystals as result of mantle deformation caused by past and present geological processes (Silver, 1996). Olivine, being the most abundant phase in the upper mantle, is an anisotropic crystal whose orientation is strain dependent, known as lattice preferred orientation

(LPO), and is expected therefore to reflect these deformational processes. Vinnik *et al.* (1992) correlate absolute plate velocity directions with the fast direction of seismic anisotropy in the upper mantle, and suggest that the dominant cause of the observed SKS anisotropy is due to recent and present-day flow in the mantle, though this hypothesis does not always appear to be consistent with observations (e.g., Silver *et al.*, 2001). The diametrically opposed counter-hypothesis is that of Silver & Chan (1988) and Silver & Chan (1991), who suggest that SKS anisotropy is dominantly a response to fossil, or frozen in, crystal alignment created at the time of primary lithospheric formation. There are further complexities to these arguments that have been explored in more recent work (e.g., Jung & Karato, 2001; Holtzman *et al.*, 2003) and suggest that the alignment depends significantly on the region being studied. Jung & Karato (2001) show that the addition of large amounts of water to olivine (e.g. in subduction zones) can change the relation between flow geometry and seismic anisotropy. Additionally, Holtzman *et al.* (2003) demonstrate that the presence of melt weakens the alignment of the olivine fast axis (also know as the a axis, or [1 0 0] axis), and where the melt segregates to form networks of shear zones it may even cause the alignment to be at 90° to the shear direction. Neither of these mechanisms, however, is expected to be operative in Archean or Proterozoic aged lithosphere.

Silver *et al.* (2001) inferred single-layer seismic anisotropy from shear-wave splitting at 79 sites in southern Africa of the SASE deployment. They divided the results from the analyses into three categories: well constrained stations that showed resolvable splitting, stations that did not exhibit detectable splitting, and stations that were poorly constrained (Fig. -2). Overall, where splitting was observed, delay-times are small (typically 0.6 s) compared to world averages (1-2 s). Silver et al. (2001, 2004) showed that the absolute plate motion (APM) of southern Africa does not explain the polarization directions (ϕ) that are derived, contrary to the Vinnik *et al.* (1992) hypothesis, but rather that the orientation direction of the anisotropy (fast polarisation direction) is more closely aligned with the strike of known Archean aged deformational structures of the Kaapvaal craton. The depth of the anisotropic region was concluded to be confined to the lithospheric mantle, with (a) the lack of correlation of the anisotropy directions with APM models resulting in the asthenosphere being excluded as a causative region and with (b) conversions at the crust-mantle boundary being exploited to exclude crustal effects. There appears to be strong differences in both the splitting parameters between early and late Archean regions of the craton, as well as between on and off craton regions. These results provide support for the hypothesis that mantle deformation is preserved from events as far back as the age of the Earth's earliest continental cratonic fragments.

Electrical anisotropy

Gaining an understanding of the geoelectric dimensionality and directionality in a dataset is the first step in the analysis of MT data, and enhances our understanding of the electrical anisotropy, in the broadest sense of the term including micro and macro anisotropy as well as lateral heterogeneity, of the survey region. In a similar manner to the SKS approach, electrical anisotropy is represented by the direction of maximum conductivity (ϕ_E), which is either parallel or perpendicular to the regional strike direction (see below for discussion). The processed MT responses are in the form of a frequency-dependent 2×2 complex impedance tensor, the elements of which can be transformed into magnitudes, scaled as apparent resistivities, and phases. In most situations, the most important tensor elements are the off-diagonal ones which relate the horizontal magnetic field components to their perpendicular electric field components. For a one-dimensional (1-D) Earth, the diagonal terms are zero and the off-diagonal terms are equal to each other (except for a sign

difference). For a two-dimensional (2-D) Earth, in strike coordinates the diagonal terms are zero and the off-diagonal terms are different from each other. When the impedance tensor cannot be validly described by either of these, then the Earth is three-dimensional (3-D), or is 1-D or 2-D but with galvanic distortion effects (see below). In addition to a magnitude relationship, akin to apparent resistivity in DC methods, we derive the phase of an impedance tensor element, which is the phase lead of the electric field over the magnetic field. In 2-D when in strike coordinates, where the phase difference ($\delta\theta$) between the two off-diagonal elements of the impedance tensor is small it implies there is little lateral heterogeneity in the subsurface, i.e., almost 1-D, compared with a larger phase difference, which is indicative of 2-D or 3-D regional structures.

In MT soundings local, small-scale conductivity heterogeneities cause distortions of primarily the electric field, and deform the response produced by the underlying, regional geoelectric structures. In the ideal, distortion-free 2-D case the diagonal elements of the impedance tensor would be zero when rotated to the appropriate strike direction; though with experimental data, this is rarely, if ever, the case. The distortions can be practically (though not entirely separately) viewed as inductive and galvanic effects. The inductive effect is a result of the time-varying magnetic field that induces currents, which, if flowing in closed loops, will in turn result in a secondary magnetic field that adds to the primary magnetic field (Jones, 1988; Jiracek, 1990). Where there are local conductivity heterogeneities in the subsurface, flux through the boundaries of these heterogeneities by the regional current results in the build-up of charge at these boundaries (Price, 1973; Jones, 1983a) as a consequence of Ohm's Law. These charges create a secondary electric field that distorts the regional current flow in that area. Where the distorting inhomogeneity is small relative to the scale size of the experiment, this effect is known as galvanic distortion. Such distortion may also be caused by topography near the measurement location (Jiracek, 1990). Galvanic distortion effects persist to the longest periods, whereas the effect of near-surface inductive distortions decreases in proportion to the regional inductive response with increasing period (Jones & Groom, 1993; Chave & Smith, 1994; Chave & Jones, 1997; Smith, 1997; Agarwal & Weaver, 2000). At sufficiently long periods, where "sufficient" is defined by the inductive scale length of the distorting structures, except for unusual cases of intense distortion to the regional current density, the horizontal magnetic field components are largely unaffected (Groom & Bailey, 1989; Chave & Jones, 1997; Caldwell *et al.*, 2004), and the distortion effect is almost entirely limited to the electric field.

There are a number of methods that are used for galvanic distortion analysis of MT data; accordingly there are also a number of reviews on the subject of how to address the problem (e.g., Jiracek, 1990; Groom & Bahr, 1992; Groom *et al.*, 1993; McNeice & Jones, 2001). Two of the more commonly used methods are Bahr (1988), and Groom & Bailey (1989), both of which are 2-D extensions of the 1-D approach of Larsen (1977). Richards *et al.* (1982) were the first to propose this approach for handling galvanic distortions of the electric field from 2-D regional structures. Unfortunately, their paper is rather inaccessible, with the result that those authors have not received the recognition due for their insight.

Both the Bahr and Groom-Bailey (GB) methods recover parameters from the magnetotelluric impedance tensor, and assume that the regional conductivity structure that we are attempting to resolve is either 1-D or 2-D, but not 3-D. Utada & Munekane (2000) and Garcia & Jones (2001) considered 3-D galvanic distortion of EM fields from 3-D regional structures, and proposed methods for its examination, but application of these approaches is not yet routine. The parameters that are obtained from the GB approach (the so-called twist, shear, and anisotropy tensors) are a consequence of a matrix factorisation of the distortion tensor and partially describe the effects of distortion. The GB approach has the distinct advantage over Bahr's parameterisation, and that of

Smith (1995), Smith (1997), and earlier factorizations (Eggers, 1982; Spitz, 1985; LaTorraca *et al.*, 1986), in that the parameterisation is in terms of determinable and indeterminable parts, rather than a complex (and, for some factorisations, unknown) mix of the two. In our analysis we use the extended GB approach of McNeice & Jones (2001), where a minimum is sought in order to find the appropriate regional geoelectric strike direction and telluric distortion parameters for a range of frequencies at each site.

Phase tensor analysis is another, more recently developed, method of determining the dimensionality of the subsurface conductivity distribution (Caldwell *et al.*, 2004). The phase relationships that are contained in the impedance tensor are shown by Caldwell *et al.* (2004) to be a second-rank tensor. This second-rank phase tensor, contained within the impedance tensor, is nonsymmetric in the 3-D case and has a third coordinate invariant, which is a distortion-free measure of asymmetry found in the regional magnetotelluric response. We have used this method in order to compare with the results obtained through the GB approach.

There are a number of suggested causes for electrical anisotropy that gives rise to the regionally observed effect; however, as yet there is little consensus on the causative phenomenon. Hydrogen diffusion has been proposed as a mechanism for reducing electrical resistivity of mantle materials (Karato, 1990; Hirth *et al.*, 2000), and recent laboratory studies are showing that minor (a few hundred ppm) amounts ofwater are sufficient to raise the electrical conductivity of olivine by several orders of magnitude (Poe *et al.*, 2005). Anisotropic hydrogen diffusivity in olivine crystals (the most abundant mineral in the upper mantle) has been suggested as an explanation for electrical anisotropy, with the [100] axis of the olivine crystal having the highest rate of diffusion, therefore being the more conductive (Schock *et al.*, 1989; Mackwell & Kohlstedt, 1990); however, this effect is thought to account for only about a third of the average measured values at most (Simpson & Tommasi, 2005). This indicates that there must be other factors, larger in magnitude of effect compared with the olivine crystal scale, which contribute to the overall electrical conductivity that we are observing. One such possibility would be interconnectivity of a conductive mineral phase (e.g., graphite) along grain boundaries, and therefore along foliations and lineations, referred to as shape-preferred orientation (Mareschal *et al.*, 1995); see Jones (1992), for a more complete discussion in this regard]. Saline fluid-filled cracks are another possibility that has been suggested and is one that would likely affect both seismic and electrical anisotropy; however, this would most likely be a mechanism valid only in the crust.

It must be noted that from MT data alone it is virtually impossible to discriminate between the response to a 2-D structure (heterogeneity), such as a fault in the lower crust, and the response due to 2-D anisotropy that is of a scale not resolvable by the technique. The difference between the two can however be observed in the response of the vertical magnetic field (Cull, 1985; Mareschal *et al.*, 1995; Jones, 1999). More detailed discussions on the topic of heterogeneity versus anisotropy and some of the problems that anisotropy poses are described by Heise & Pous (2001) and in the recent review by Wannamaker (2005).

The symbiotic relationship

One of the most problematic areas for seismic SKS analysis is vertical resolution, caused by the use of seismic waves with near-vertical ray paths and long wavelengths for analysis. The advantage of using such ray paths is that, depending on the quantity and quality of the data that are

collected, horizontal resolution within the lithosphere can be exceptionally good (<50 km, (Savage, 1999)). However, without additional information vertical resolution is extremely poor. Conversely, the magnetotelluric (MT) method has intrinsic vertical dependency due to the skin depth phenomenon, which assures penetration at any depth depending on the period and resistivity (ρ) of the subsurface. In theory, to penetrate deeper into the Earth, all one needs to do is to measure at sufficiently longer periods, although at great depths source field geometry needs to be taken into account (e.g., Jones & Spratt, 2002), and the exponential sensitivity of impedance skin depth results in a decrease in resolution with depth, thereby also causing a loss of vertical resolution with depth.

Although these two methods, SKS shear-wave splitting and MT, do not measure the same physical properties, in certain cases it may be the case that they are essentially measuring a different response of the same causative effect. As an example of this, Ji *et al.* (1996) noted a directional obliquity between MT and seismic anisotropy results, and suggested that the cause for this was the differing directions of lattice-preferred (LPO) and shape-preferred (SPO) orientations of mantle minerals. They used this obliquity result to suggest that a combination of both MT and SKS results could be employed to determine the sense of movement of transcurrent ductile shear zones in the upper mantle. They concluded that although the direct cause of the anisotropy was different for the two methods, they were a result of the same tectonic feature. Following up on this hypothesis, Eaton *et al.* (2004) conducted an experiment across a highly sheared region, the Great Slave Lake shear zone of northern Canada. They correlated MT anisotropy with seismic (SKS and SKKS) anisotropy to constrain the depth location of the seismic anisotropy using approximately collocated teleseismic and magnetotelluric observations. They noted that in their study region there was no systematic obliquity observed between the MT and seismic results, but suggested that this may be because of the intense deformation of the Great Slave Lake shear zone resulting in parallel axes for the C (shear band) and S (foliation fabric) strain ellipses.

Another recent MT/SKS comparison study by Padilha *et al.* (2006) has shown that in parts of the survey area (central south-eastern Brazil) where there is significant electrical anisotropy, a close correlation of shear-wave splitting results and MT strike results can be made, also without any systematic obliquity. They deduce from their study that lithospheric and sublithospheric deformation is vertically coherent with the surface tectonic trends in this region, which requires strong crust-mantle coupling across the Moho and is indicative of the lack of a lower crustal rheologically weak layer. From these studies it is clear that MT is indeed an exquisitely complementary method to seismic methods for mantle imaging (Jones, 1999); however, the use of both methods together for combined interpretations is still in its infancy, and certainly the implications of the correlations are immature.

There are a number of suggested causes for electrical and seismic anisotropy, some of which have been discussed earlier. The explanation most readily used for upper mantle seismic anisotropy is strain-induced LPO of olivine crystals (see reviews by Silver (1996), and Savage (1999), and references therein). In the lower crust, aligned saline fluid-filled cracks may account for anisotropy, and would affect both seismic and electrical results, but this does not readily explain observations of lithospheric mantle anisotropy. There does not appear to be a general consensus on the causes of electrical anisotropy, largely because there are insufficient observations, and those made to date are highly area dependent implying a combination of causes. For example, in a highly ordered upper mantle it is possible that anisotropic hydrogen diffusivity is a contributing factor, but this is unlikely to be either the dominant factor or the sole cause. Even when present it likely will result in an electrical anisotropy factor no greater than about 3–4. Thus, to aid us in the meaningful

interpretation of seismic and MT observations of anisotropy we must rely heavily on geological knowledge, such as geochemical and petrological results.

MT data analysis

Data from the main SAMTEX Kaapvaal craton profile, from Southerland in the southwest of South Africa to Messina at the South Africa-Zimbabwe border (Fig. -1), have been analysed for anisotropy using the McNeice & Jones (2001) distortion decomposition code, and the results compared with applying phase tensor analysis (Caldwell *et al.*, 2004). This survey line, the first to be undertaken in the SAMTEX program, is almost 1500 km in length and extends over important and diverse geological terranes, including the Kaapvaal craton (mainly the western section), the Limpopo belt, and the Namaqua-Natal mobile belt. As could be expected due to the length of the survey, data quality is variable, with the southwest of the line producing the highest quality responses, while sites near Kimberley were the lowest quality, being seriously affected by DC train noise.

Due to the large scale of the survey it is necessary to consider that penetration over the various regions will differ significantly; for example depth penetration at long periods on the Karoo Basin and on the Bushveld Complex is highly attenuated due to their high upper crustal conductivity compared with other regions. In order to gain a quantitative understanding of this issue, we estimated the frequency for penetration to given depths using Niblett-Bostick (Niblett & Sayn-Wittgenstein, 1960; Bostick, 1977; Jones, 1983b) depth estimates (Fig. -3) and inductive response functions, also known as C response functions (Schmucker, 1970; Jones, 1980). The real part of the C response function, related to MT impedance by a factor of $1/\omega\mu$, was shown to be the depth of maximum eddy current flow by Weidelt (1972), and is a measure of the depth of investigation. Three-dimensional structures that may influence the C responses are assumed to be sufficiently long at the depth of investigation such that they may be interpreted as being 2-D; additionally the decomposition analysis determines whether a 2-D assumption is valid. The penetration information in Fig. -3 was calculated using Niblett-Bostick estimates (which are almost identical to the C response function estimates) on distortion-removed data in order to minimize the influence of distortion on the calculations. Static shift effects are not corrected by distortion analysis and can influence depth estimates by the square root of their value (e.g., Jones, 1988), definitely not as severe as on apparent resistivity data. Notwithstanding the possible presence of static shift effects, there are clearly regional trends visible in the data. Note the significance of this figure (Fig. -3); electromagnetic waves penetrating to 35 km in the crust are at periods of 1000 s or greater at the southern (stations 1–30 on the Karoo Basin) and north-central (stations 46–56 on the conductive Bushveld Igneous Complex) sites, at periods of 2 s or less in the centre (stations 30–45 in the centre of the Kaapvaal craton) of the profile, and at periods of 30 s or less at the northern end of the profile (stations 57–75, NE Kaapvaal craton and Limpopo mobile belt). Clearly, a map of geoelectric strikes from these stations at one particular period would be meaningless, as depth penetration varies significantly along the profile. The effect is a direct consequence of the large variation of the parameter that EM studies are sensing, namely electrical resistivity, which ranges over many orders of magnitude (see, e.g. Jones, 1992), and contrasts sharply with the small (less than 10%) variations in seismic parameters. From these results it is clear that either the line must be split into sections and analysed separately, or the data must be analysed for given depths, as opposed to given frequencies, in order to make interpretation of any resulting strike map meaningful. Jones (2006) raises this caution and shows examples from three other regions of the world where one must give consideration to penetration depth.

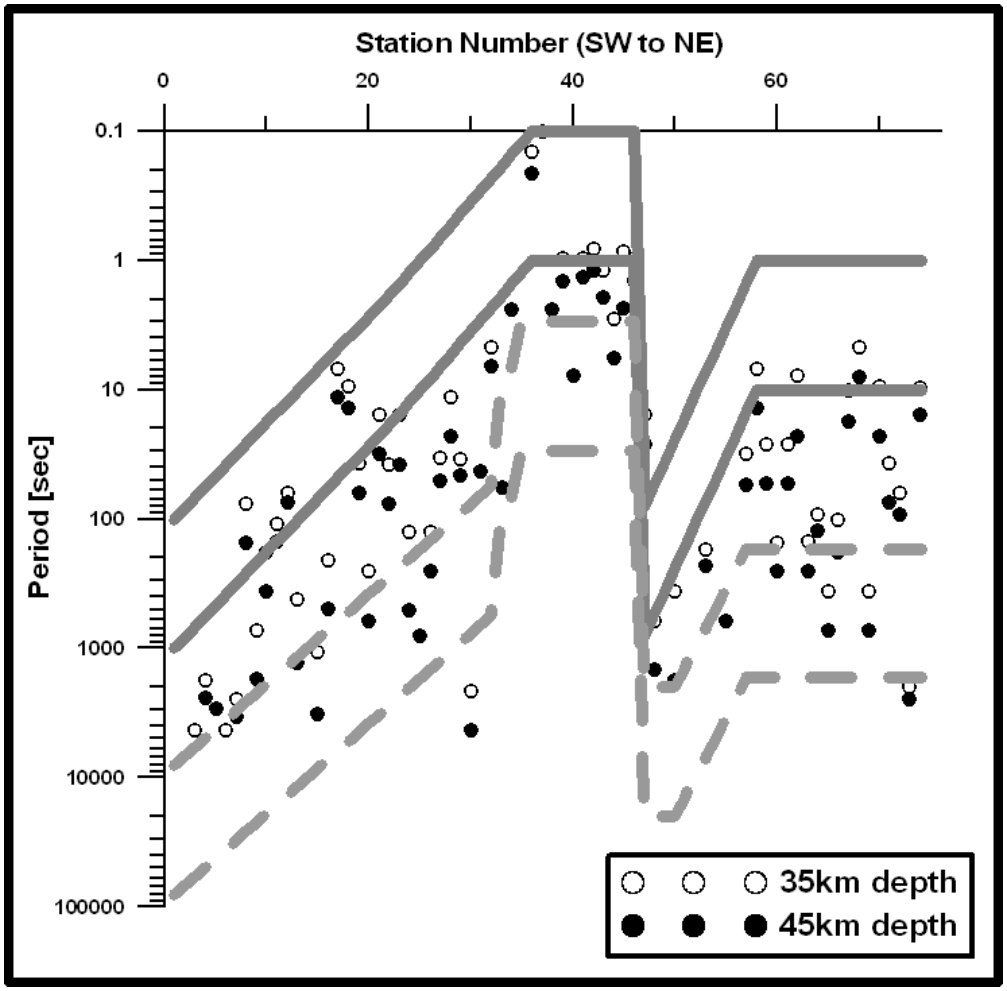

Figure -3: *The corresponding period (averaged between the two modes) for depths of 35 km and 45 km determined using Niblett-Bostick depth estimation on distortion-removed data. This gives an indication of the variation in penetration depth along the profile. Note the sudden drop in penetration around station 48 as we move onto the very conductive Bushveld Igneous Complex (BIC). The period decade between the two solid lines indicates the frequencies used to estimate the strike directions for crustal depths, while the period decade between the two dashed lines indicates the frequencies used to estimate the strike directions for upper mantle depths.*

Crustal thickness, as defined by the seismic results (Nguuri *et al.*, 2001; Stankiewicz *et al.*, 2002; James *et al.*, 2003), varies from ≈35–40 km below the craton, to ≈45–50 km below the Proterozoic regions where the Moho is also more complex. In order to gain strike directions representative of the crust and upper mantle, while avoiding complex structures at the crust-mantle boundary, we selected a one-decade wide period band for the crust (between the two solid lines on Fig. -3) and the upper mantle (between the two dashed lines on Fig. -3). One decade wide bands were selected so as not to bias any one site with more or less data than another. These sites were then each analysed twice (separately for each frequency band) using the single site GB approach (Groom & Bailey, 1989) for a range of frequencies, as implemented by McNeice & Jones (2001), in order to determine two regional geoelectric strike estimates for each site, one representative of the crust and

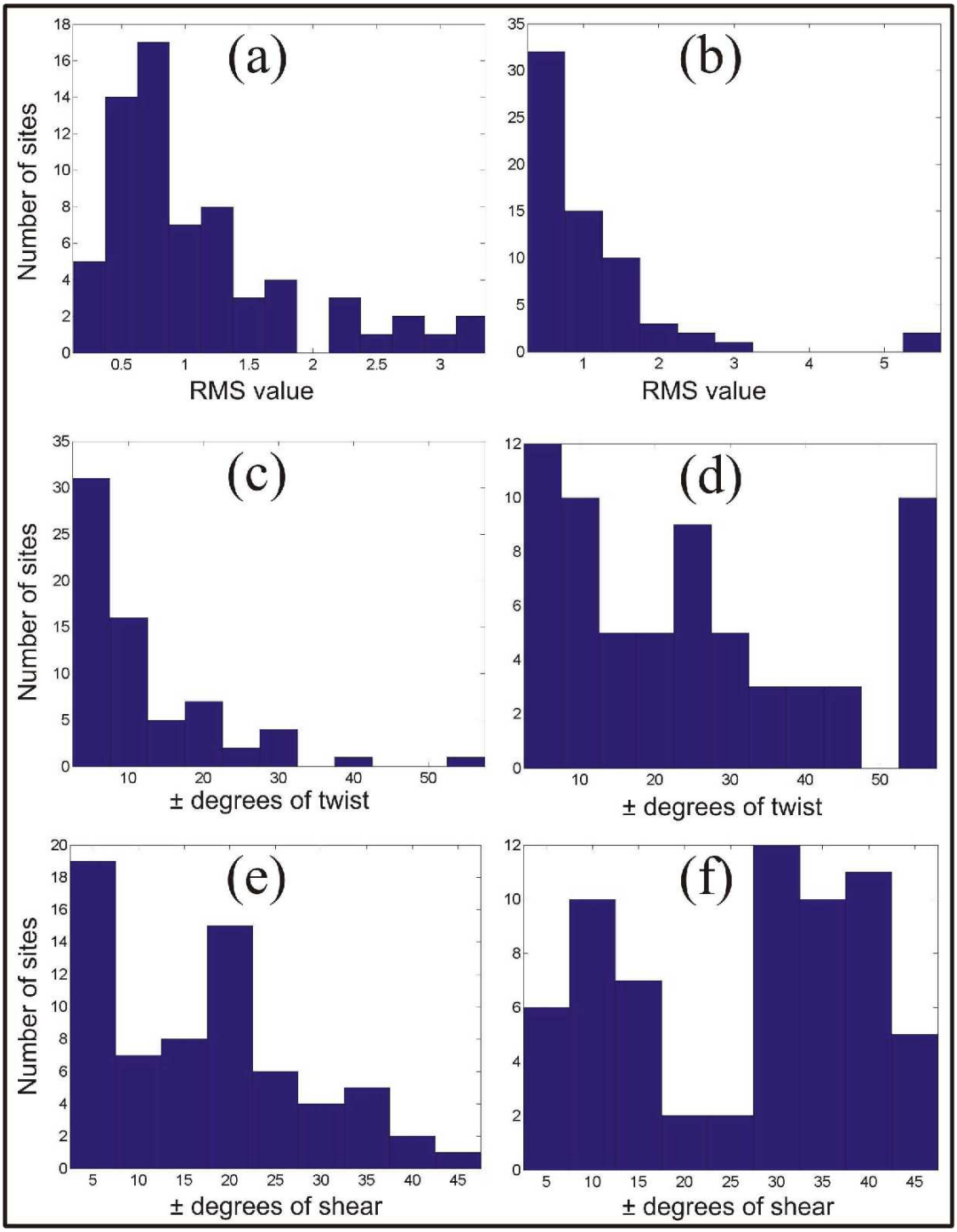

Figure -4: *Histograms displaying results from Groom-Bailey (GB) decomposition analyses. Displayed are: (a, b) the average RMS values, (c, d) the average (positive or negative) twist (in degrees), and (e, f) the average (positive or negative) shear (in degrees), for all the sites. Histograms for the crustal band are on the left (a, c, e), and for the upper mantle band on the right (b, d, f).*

one representative of the upper mantle. Data were analysed with an assumed error floor of 2° for the phase and equivalent 7% for apparent resistivity. The average calculated RMS values from the unconstrained, one-decade wide GB decomposition for most sites were in the range between one and three for both the crustal and upper mantle analyses. The average twist values were mostly within the range ±30°, and the shear values were generally slightly higher falling within the range ±40°. Both the twist and shear values were slightly higher at the longer periods (upper mantle band), where the signal to noise ratios are worse. The average RMS, twist, and shear results for all the sites, are displayed in Fig. -4 (crustal results on the left and mantle results on the right), which shows that the majority of the data have reasonably low distortion values compared to what can often be observed on shield regions e.g., Fennoscandian Shield (Lahti *et al.*, 2005). For these data, the direction chosen to display as geoelectric "strike" was taken as the more conductive direction of the two. This direction was reasonably consistent with that found using the phase tensor approach (Caldwell *et al.*, 2004), as is to be expected for high-quality, low noise, lowdistortion data. The GB approach proves itself superior in the presence of higher noise and/or higher distortion (e.g., Jones & Groom, 1993; McNeice & Jones, 2001).

However, the more conductive direction is not necessarily the strike direction of 2-D structures. Consider the TE and TM apparent resistivity curves for a simple two quarter-space fault model (e.g., d'Erceville & Kunetz, 1962; Weaver, 1963; Price, 1973), schematically drawn in Fig. -5. On the resistive side of the fault the TE mode apparent resistivity is the more conductive (lower resistivity), so its direction is taken, which is correctly the strike direction of the fault as the TE electric field is parallel to strike. Conversely, on the conductive side of the fault (shaded side in Fig. -5), the TM mode apparent resistivity is the more conductive, so its direction is taken, which is perpendicular to strike. Herein we are concerned only with the more conductive direction and its correlation with the faster shear velocity direction. It is important to appreciate that we are not using these conducting directions to define geological strike for a 2-D interpretation.

The geoelectric strike directions for the crust (<35 km) and upper lithospheric mantle (>45 km) are shown as red lines in Figs. -6 and -7, respectively, together with the terrane subdivision of southern Africa from potential field data. The lines are scaled by the maximum phase difference in the frequency band analysed, as a proxy for the amplitude of anisotropy. Some sites were omitted from the plot if either there were no data at sufficiently long periods, or if the data at the periods analysed were very poor (high noise content or large error bars). The geoelectric upper mantle strike results (Fig. -7) fall within the probable causative region of the seismic anisotropy, which was confined through inferences of the seismic results. On Fig. -7 are also plotted the seismic anisotropy results of Silver *et al.* (2001) for comparison.

Discussion

Bearing in mind the physics of the model described in Fig. -5, the crustal MT results (Fig. -6) display some interesting and satisfying, though obviously complex, features. The more conductive directions at the southwestern craton boundary are parallel to the boundary on the Namaqua-Natal mobile belt (NN), but upon moving onto the craton the directions change abruptly to be nearly perpendicular to the NN. This behaviour is consistent with Fig. -5, implying that the Kaapvaal craton crust is more conducting than the Namaqua-Natal crust, and is what we would expect if large-scale 2-D geologic features were responsible for the electrical structure. Similar orthogonal relationship patterns can be observed at the Colesburg Magnetic Lineament (CML, blue line on Fig.

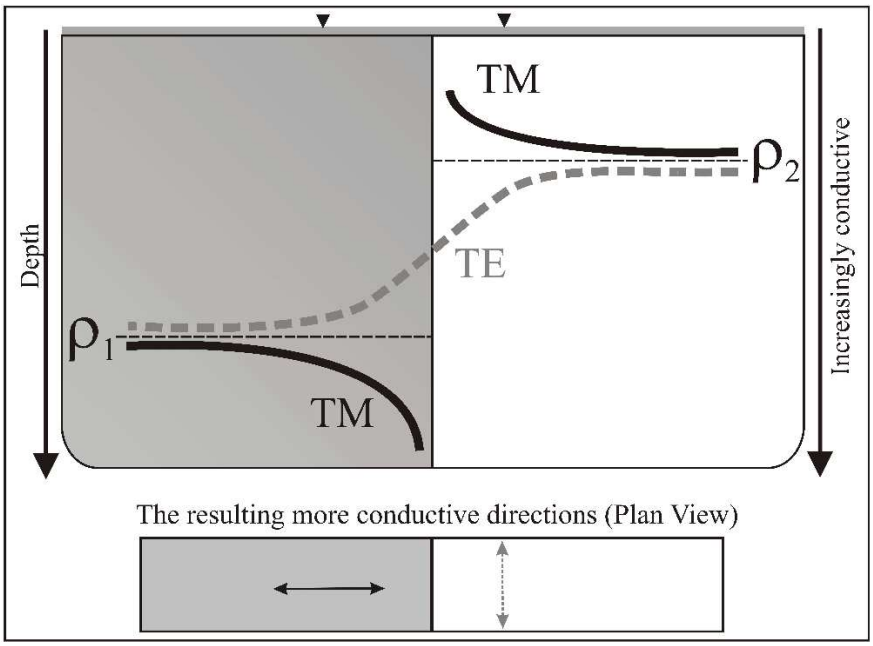

Figure -5: *Schematic diagram portraying the MT response at one frequency to the two quarter-space fault model with the more conductive side shaded grey. The variations of the TE and TM modes across the fault for a given frequency are shown. On the more conductive side of the fault, the TM mode apparent resistivity is the more conductive, whereas on the resistive side of the fault the TE mode apparent resistivity is the more conductive. This results in the more conductive directions being parallel to the geological strike on one side of the fault (the resistive side), and perpendicular on the other (the conductive side).*

-6), the Thabazimbi-Murchison Lineament (TML, purple line on Fig. -6), as well as at the Kaapvaal craton-Limpopo belt boundary. The results to the immediate SW of the TML are complex, and are probably a result of the influence of the conductive Bushveld Igneous Complex (BIC). At first glance, the result from the site on the end of the profile in the SW seems anomalous; however, it may be that this site is being affected by a response from the Cape Fold belt (CFB), although no data were collected further towards and onto the CFB to confirm this.

The upper mantle MT results (Fig. -7, red lines) do not correlate well with those from shear-wave splitting (Fig. -7, green lines). The close azimuthal correlations between geoelectric strike and seismic fast-axis directions noted by other authors (e.g., Eaton *et al.*, 2004; Padilha *et al.*, 2006) are not observed in our data, nor do we see a constant obliquity between the two results, as observed by Ji *et al.* (1996). A few sites, particularly those around the TML and to the SW of the profile, do show distinctly similar directions to the seismic results; however, overall the results are far too inconsistent to draw any reliable conclusions about their correlation. The same effect of Fig. -5, although not as clear as in the crustal results, can be observed at the craton boundaries, indicating that these features are distinct at upper mantle depths and that there is probably strong coupling between the crust and upper mantle. Results near the TML do not show the same effect, suggesting that this feature is confined to the crust. A similar argument could be applied for the CML, although the results in this region are confusing and seem to lack any discernible order. Unfortunately the site furthest to the SW that seemed to respond to the CFB in the crustal analysis did not have data at sufficiently long periods to probe upper mantle depths and consequently we

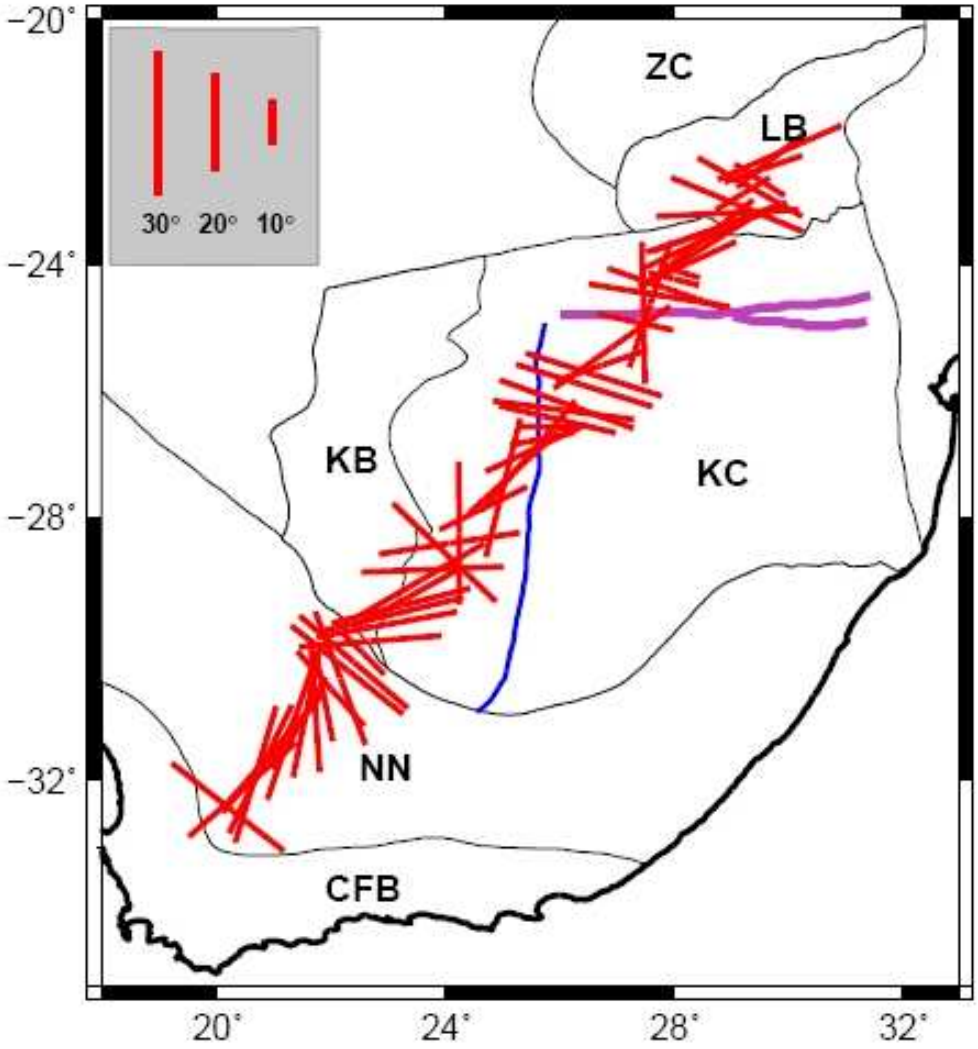

Figure -6: *Electrically more conductive directions (in red), scaled by maximum phase difference, for the crust. ZC: Zimbabwe craton. KC: Kaapvaal craton. LB: Limpopo belt. NN: Namaqua-Natal mobile belt. CFB: Cape Fold belt. KB: Kheis and Proterozoic fold and thrust belt. Purple lines: the E-W trending Thabazimbi-Murchison Lineament (TML), as plotted by Silver* et al. *(2001). Blue line: the N-S trending Colesburg Magnetic Lineament (CML).*

can make no further judgement on this. A noteworthy feature is the N-S geoelectric directions for the northeast-most stations. There is no correlation between these sites and the surface geological trends of the Limpopo belt, nor the surrounding seismic fast-axis directions. However, to the north the seismic fast-axis directions do follow the same N-S trend. This effect was attributed by Silver *et al.* (2001) to the Great Dyke of Zimbabwe, which has a general N-S trend across the country. Is it possible the electrical response to this massive feature is sensed at further distances than the seismic response? An answer to this question can only come through future MT measurements in Zimbabwe.

Our crustal geoelectric strike results are clearly a result of large-scale geological structures.

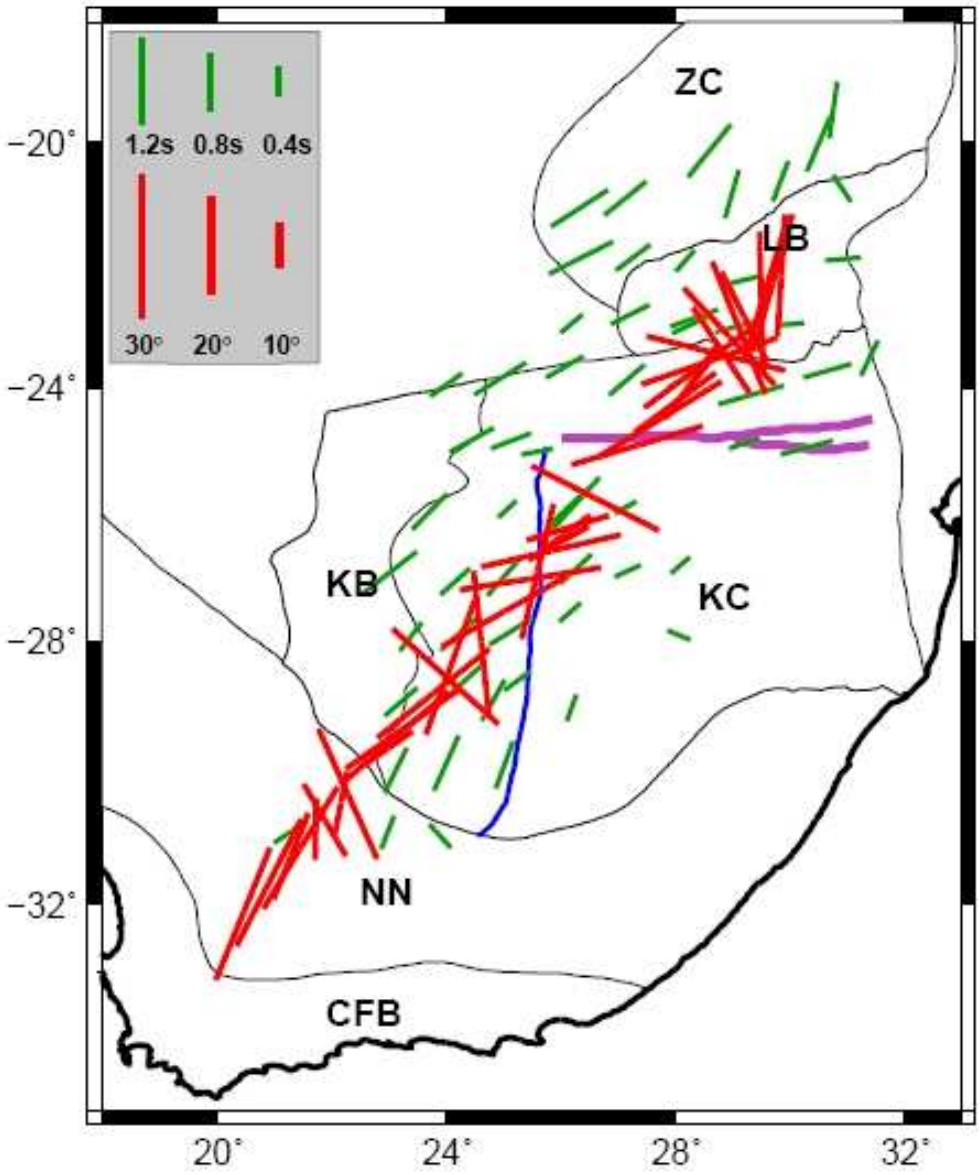

Figure -7: *Electrical more conductive directions (in red), scaled by maximum phase difference, for the lithospheric upper mantle, and the shear-wave splitting results (both high and low quality results plotted in green, but sites with no detectable splitting omitted). ZC: Zimbabwe craton. KC: Kaapvaal craton. LB: Limpopo belt. NN: Namaqua-Natal mobile belt. CFB: Cape Fold belt. KB: Kheis and Proterozoic fold and thrust belt. Blue line: the N-S trending ColesburgMagnetic Lineament (CML). Purple lines: the E-W trending Thabazimbi-Murchison Lineament (TML), as plotted by Silver* et al. *(2001).*

The upper mantle MT anisotropy direction results show little correlation with the seismic SKS anisotropy results. We observe rather large phase differences, of the order of 20° or more, that are difficult to achieve with the low order of anisotropy expected from hydrogen diffusion in aligned olivine grains.Were these large phase differences caused by the response to an interconnecting conductive mineral phase along lineation or foliation planes, we would expect the results to correlate better with the seismic results, if not exactly, then with a constant obliquity such as observed by Ji

et al. (1996). Following this reasoning, there are a fewpossible explanations for the upper mantle MT results we observe: either the effect of the large-scale 2-D geological structure is "hiding" the lesser magnitude effect due to preferentially aligned crystals or an interconnecting mineral phase; perhaps there is no corresponding electrical response to the cause of the seismic shear-wave splitting results; or the causative layer of the seismic response could reside deeper in the lithosphere, beyond the depths that we are sensing.

Our MT profile is located mainly across the younger western section of the Kaapvaal craton, and thus at this stage we are unable to draw any conclusions as to whether we see similar variations in on-craton geological regions to those observed by the shear-wave splitting results. The phase differences do not appear to show any correlation between the different geological regions, though trends are expected to appear when the newer SAMTEX data, continuing into other regions of the craton and into more of the surrounding geological provinces, have been analysed. Analyses of data from the surrounding areas are bound to yield some interesting outcomes that will be integrated with the Kaapvaal Craton Project.

Conclusions

Our crustal electrical anisotropy results are quite instructive, and rather satisfying. They appear to be strongly related to large-scale geological structures both at craton and surrounding terrane boundaries as well as within the craton itself. Some of these features such as the TML are confined to the crust, while others such as the craton boundaries are distinct at upper mantle depths.

The electrical results for the upper lithospheric mantle do not appear to correlate well with the shear-wave splitting results for the same region. Thus, if aligned olivine is the cause of the observed seismic anisotropy, it is not the cause of the observed electrical anisotropy. We conclude that the cause of the electrical response at these depths is dominantly as a result of large-scale geological structures, although there may be contributions smaller in magnitude from preferential crystal alignment or interconnecting mineral phases.

Acknowledgements

We would like to thank the whole SAMTEX Team, comprising many enthusiastic organisations and individuals, without whose colossal and unrelenting efforts this project would never have been possible. Especially we wish to thank the project financial sponsors, namely the National Science Foundation's Continental Dynamics program, the Council for Geoscience, Science Foundation Ireland, De Beers Group Services and Rio Tinto Mineral Exploration. Further details on the SAMTEX project and its participants can be found at http://www.dias.ie/~mh/SAMTEX.html.

We would like to thank Professors Andreas Junge, David W.S. Eaton, and an anonymous reviewer for their reviews and comment on the submitted paper. We would also like to thank S.J. Webb and K. Garcia for helpful reviews on the early version of the paper, and M. Moorkamp and C.K. Rao for their useful discussions during the preparation of this manuscript. All maps were produced using the program GMT (Wessel & Smith, 1991, 1995), with some of the geological digitising obtained from S.J. Webb.